SANDIA REPORT

SAND2015-20766
Unlimited Release
Printed January 2015

Light Initiated High Explosive Driven Flyer Plate Impulse Generation Technique For Material and Structural Response

Wayne Gary Rivera

Prepared by
Sandia National Laboratories
Albuquerque, New Mexico 87185 and Livermore, California 94550

Sandia National Laboratories is a multi-program laboratory managed and operated by Sandia Corporation, a wholly owned subsidiary of Lockheed Martin Corporation, for the U.S. Department of Energy's National Nuclear Security Administration under contract DE-AC04-94AL85000.

Issued by Sandia National Laboratories, operated for the United States Department of Energy by Sandia Corporation.

Available to DOE and DOE contractors from
U.S. Department of Energy
Office of Scientific and Technical Information
P.O. Box 62
Oak Ridge, TN 37831

Telephone: (865) 576-8401
Facsimile: (865) 576-5728
E-Mail: reports@adonis.osti.gov
Online ordering: http://www.osti.gov/bridge

Available to the public from
U.S. Department of Commerce
National Technical Information Service
5285 Port Royal Rd.
Springfield, VA 22161

Telephone: (800) 553-6847
Facsimile: (703) 605-6900
E-Mail: orders@ntis.fedworld.gov
Online order: http://www.ntis.gov/help/ordermethods.asp?loc=7-4-0#online

SAND2015-20766
Unlimited Release
Printed January 2015

Light Initiated High Explosive Driven Flyer Plate
Impulse Generation Technique For Material and Structural Response

Wayne Gary Rivera
6615, Active Response and Denial, MS0783

Sandia National Laboratories
P.O. Box 5800
Albuquerque, New Mexico 87185-MSXXXX

Abstract

The objective for this research has been to develop a method to induce a high frequency, large amplitude shock pulse into materials and structures as an above-ground laboratory simulation of an exo-atmospheric cold x-ray induced blow-off event. This work builds on the successes of direct-spray Light Initiated High Explosive impulse delivery technique, in order to drive a flyer to a desired impact velocity to induce the proper combined material and structural response of the target.

The reported development focuses on flyer velocity from explosive initiation to target impact to flyer rebound. A comprehensive derivation of an analytical model to predict flyer velocity as a function of explosive deposition and flyer properties is presented. One-and two-dimensional test series were conducted to evaluate impulse delivery and impact pressure, as well as target material and structural response. Experimental results show good agreement in flyer velocity between that predicted by the developed theory and that inferred by impulse delivery. A definitive material response was measured in each of the one-dimensional targets. The structural strain response measured in the ring experiments showed excellent agreement with both the predicted flyer performance and the analytical strain solution for a cosine distributed impulsive loading.

This work has focused on the utilization of analytical, hydrocode, and test analysis to confirm that a LIHE driven flyer impulse technique can be an effective simulation of a cold x-ray blow-off event. It is shown that a thin metallic flyer plate can be explosively accelerated to impact a target with sufficient energy to generate an impulsive load which induces both structural and material response in a test item.

ACKNOWLEDGMENTS

To my family for their infinite patience and support.

The author would like to express sincere appreciation to the following individuals and organizations for their help and support in the development of the Light Initiated High Explosive flyer technique. Robert Benham for his wisdom, guidance, and vision to develop “the most comprehensive solution.” He is the father and greatest champion of LIHE impulse testing, and it has been an honor to have the opportunity to work with this truly great engineer. Dr. Ken Eckelmeyer for his mentoring and tutelage in the field of metallurgy and analysis techniques. The Sandia LIHE Team, Lloyd Bonzon, Mike Skaggs, Tim Covert, Ed Mulligan, John Liwski, and Dan Dow for their support and patience in this endeavor. The Sandia Optical Metallography Lab, including Charlie Robino, Mark Reece, Alice Kilgo, and Robert Wright, whose help in providing access to their laboratory, as well as sample preparation and partial analysis of the many material samples, was instrumental in this work. Sandia National Laboratories (SNL) who supported this work by providing funding, materials, equipment, and facilities.

A special thanks is extended to the reviewers of this dissertation, Dr. Todd Simmermacher and Dr. Michael Kaneshige. Their extensive review of the text, theory, and experimental results has been essential in the writing of this document.

And finally, the author would like to thank Dr. Osman Inal for his advice, encouragement, and direction during a time of transition from an Engineering Mechanics focus to a Materials Engineering curriculum. His insight has been instrumental in achieving this very lofty honor of PhD.

CONTENTS

FIGURES

TABLES

NOMENCLATURE

List of Symbols

A	Area
ρ_A	Density, Areal (Mass of explosive per unit area, typically mg/cm^2)
ρ_{HE}	Density, Explosive
ρ	Density, Material
α	Decay Constant
e	Energy
$\sqrt{2E}$	Gurney Velocity
γ	Ideal Gas Constant
I_{sp}	Impulse, Specific
$I_{sp\text{-}coupon}$	Impulse, specific (generated by explosive deposited on coupon)
$I_{sp\text{-}infinite}$	Impulse, specific (generated by explosive deposited on infinite surface)
m	Mass, Explosive
m_f	Mass, Flyer
c	Mass, Metal
x	Position
P	Pressure
R_f	Rebound Factor
Z	Shock Impedance
s	Slope
C_0	Sound Speed
t_{HE}	Thickness, Explosive
t_f	Thickness, Flyer
t	Time
k	Velocity Fraction
V_f	Velocity, Flyer
V_{in}	Velocity, Incoming
V_{out}	Velocity, Outbound

u	Velocity, Particle
U	Velocity, Shock
Vol	Volume, Trapped Air
f	Flyer Subscript
T	Target Subscript

List of Abbreviations

AFB	Air force base
EOS	Equation of state
GUI	Graphical user interface
H-W	Humphres-Winter analytical ring structural response solution
LIHE	Light initiated high explosive
MDF	Mild detonating fuse
MEMS	Micro-electrical-mechanical-system
PETN	Pentaerythritol tetranitrate explosive
RLC	Resistance, inductance, capacitance (Typically RLC circuit)
ROF	Explosive Rods-Over-Foam impulse generation technique
SASN	Silver acetylide-silver nitrate explosive
SBPA	Small bank pendulum apparatus
SELT	Sheet-Explosive-Loading-Technique
SNL	Sandia National Laboratories
SPLAT	Spray-Lead-At-Target Impulse generation technique
TNT	Trinitrotoluene explosive
TTF	Thermal treatment facility to dispose of excess SASN explosive

FORWARD

This report was authored by Wayne Gary Rivera in 2006 and submitted to the Department of Materials and Metallurgical Engineering at the New Mexico Institute of Mining and Technology in Socorro, NM in partial fulfillment of the requirements for the degree of Doctor of Philosophy in Mechanical Engineering. At the time of publication, this report documented the relevant theory, model development, and data collected in support of these activities. The report was correct, with the exception of minor errata, based on the contemporary knowledge as of publication. Since this initial publication, research and development has continued on the explosively driven flyer plate impulse generation technique advancing the theory, model development, and supporting data collection. This report is being republished as a Sandia Laboratories report to ensure its accessibility to Sandia researchers. Although minor errata have been corrected in this current publication, no effort has been made to update the original flyer plate theory, modeling, and data presented by Dr. Rivera.

Timothy Covert
EM Simulations and Fabrication
Sandia National Laboratories

1. INTRODUCTION

1.1. Overview

The simulation of an impulse load generated by an exo-atmospheric, cold x-ray deposition on a structure, as a result of a nuclear detonation, has been of interest for over forty years. Because this nuclear event is very difficult and costly to recreate, extensive work has been done to understand the mechanisms by which the environment can be simulated by conventional means. These efforts have included theoretical, computational, and experimental regimes, resulting in varying degrees of success. Ideally, any simulation would be comprehensive in simulating four parameters relative to x-ray loading: stress wave temporal distribution, amplitude, simultaneity, and spatial distribution. The measure of the ability of a simulation technique to duplicate these four parameters is referred to as the "load fidelity" of the method. Due to the diverse, highly energetic nature of the environment, compromises are often made to excite specific responses without exciting others. Combined response simulation, where the material and structural responses are investigated simultaneously, is desirable whenever possible.

Impulse generation techniques for large, semi-complex test items have included several explosive methods as well as surface impact by magnetically accelerated flyer plates. Typically, surface detonation of an explosive product cannot recreate the peak pressure and duration required to adequately excite the material response characteristics of the test structure surface as a cold x-ray deposition would. In certain circumstances explosives can simulate the delivered impulse to excite the proper structural response of the test item. Conversely, flyer plate techniques, under the right conditions, have the ability to simulate both pressure pulse shape (amplitude and duration) and delivered impulse.

Much of the cold x-ray deposition research has been fully documented, and is available for reference, though most of these techniques require a fair degree of hands-on experience and learning to successfully implement. As a result, many of the techniques investigated in the past are no longer available or are currently unachievable. At this time, only one facility in the United States, the SNL Light Initiated High Explosive (LIHE) Facility, exists to conduct impulse testing on full scale exo-atmospheric structures. The charter of this facility is to conduct impulse testing to excite the structural response of a test item by detonating a thin layer of explosive, spray deposited on surfaces of interest, using specialized processes and procedures (see Chapter 3). While the direct spray LIHE technique has been used extensively, it does not deliver the proper pressure pulse to excite the material response of the sprayed surfaces as an actual cold x-ray deposition would.

1.2. Motivation

The desire to develop a comprehensive, high-fidelity, above-ground simulation of the exo-atmospheric cold x-ray induced blow-off impulse on space structures and component materials is high. Traditionally, impulse simulation has been accomplished by several methods, including underground nuclear testing, magnetically accelerated flyer plate (Mag-Flyer) testing, and various explosively generated techniques such as Explosive Rods-Over-Foam, and Light Initiated High Explosives [59]. Many of these techniques have focused on the structural response of the item being tested due to the difficulty of reproducing the precise pressure pulse shape, amplitude, and duration experienced in an actual exo-atmospheric event.

Three techniques have been shown to excite both structural and material responses in the test item by sufficiently reproducing the desired pressure pulse. These are a nuclear underground test, the magnetically accelerated flyer plate technique, and an explosively driven flyer plate technique. Currently, nuclear underground testing is at a halt, and the final Mag-Flyer testing facility to conduct large-scale testing in the United States is no longer in service. Initial investigations into the explosively driven flyer capability were conducted in the 1970s, 80s, and 90s with very promising results, but the researchers are no longer available, leaving significant gaps in implementation capability. Therefore, there is no currently available test technique to excite a combined material and structural response in an above-ground simulation of a cold x-ray deposition on a test item.

The present work aims to redevelop and extend the capability to achieve a high fidelity combined material and structural response using aspects of the current LIHE technique and flyer plate methods to drive a metallic flyer plate to the proper impact conditions.

1.3. Background Concepts

Of particular interest to this work is the environment which is being simulated, the cold x-ray induced blow-off, a the explosive driving of metal. The following sections provide a brief introduction to these topics. Further details can be found in the literature review of Chapter 2, and in numerous references listed in the Bibliography section.

1.3.1. Cold X-Ray Induced Surface Loading

Cold X-ray induced surface loading is the result of an exo-atmospheric nuclear event where relatively cold x-rays are absorbed in a thin layer of an exposed surface. For an axi-symmetric body of revolution, the impulse from a side-on exposure to the incident

x-ray field will vary approximately as the cosine of the azimuthal angle. The peak deposition is at the 0º location and falls to zero at plus and minus 90º. The opposite side of the body will receive no load.

If the absorbed x-ray intensity is sufficiently high, the deposition can cause the surface material to instantaneously heat up and vaporize. The vaporization of the surface and resulting vapor expansion create a shock which travels through the thickness of the material, impulsively loading the structure. The shock wave can cause degradation of material properties, delamination of material layers, and spall [59]. The severity of the material response is a function of the combination of materials, pressure amplitude, and pulse shape.

The expansion of the vapor from the surface of the body imparts a change in momentum to the structure in a very short time frame, generally on the order of a few microseconds. If this loading duration is shorter than approximately ¼ cycle time of the highest response frequency of interest, the load is considered impulsive [59]. If impulsive, the pressure pulse shape (amplitude and duration) is of little consequence to the structural response as long as the amplitude of impulse (area under the pressure-time curve) is correct and satisfies the ¼ cycle time requirement. This impulsive exterior loading will cause dynamic loads to be imparted throughout the structure.

The interaction between stress wave damage due to material response (material property degradation, delamination, spall, etc.) and impulsive structural response is often referred to as “combined response.” Each of these individual or combined effects can alter the designed response of the structure, affecting its performance.

1.3.2. Explosively Driven Metal

Much study has been dedicated to the understanding of driving metals to high velocities using explosives. These studies have included the propulsion of metallic fragments from bomb casings to the driving of explosively formed projectiles to impact a target. Multiple geometries and explosive configurations have been considered and studied. Generally, these studies deal with relatively thick layers of metal (with respect to the explosive charge) in order to achieve a desired result, such as penetration of a target. Much of this study has involved the work of R.W. Gurney [42] who developed a model in the 1940s to predict the initial velocity of metal fragments driven by an explosive charge [24].

It has been accepted that the properly designed impact from a thin metallic flyer plate onto a target surface sufficiently recreates the pressure pulse from an exo-atmospheric event [31]. Mag-Flyer facilities have implemented this technique in the past with success, though as stated above, are no longer available to the impulse community. An alternative to the magnetically accelerated flyer is an explosively accelerated flyer plate configured to induce the same high-amplitude, short duration shock pulse into a test item.

Typically, it is difficult to use explosives to drive very thin flyers without significant damage and deformation to the flyer material. It will be shown that the light initiated explosive silver acetylide-silver nitrate (SASN) can effectively and predictably generate the driving forces to propel a thin metallic flyer to velocities adequate to induce a desired material and/or structural response without flyer damage. This primary explosive has approximately 20% of the output of TNT, and can be spray deposited onto a surface in very thin layers, which is required to effectively control the characteristics of

the explosive/flyer/target interaction. To accommodate the impact simultaneity requirement, the explosive is nearly simultaneously initiated over a large surface area by an intense flash of light, driving the entire flyer towards the target.

Because the SASN explosive is a highly sensitive primary explosive, special facilities must be employed to implement the reported explosively driven flyer plate test method. The SNL LIHE Facility is uniquely qualified to work with this highly specialized explosive. The standard LIHE simulation involves spraying the SASN explosive directly on the surface of the test item to create a desired impulsive load on the test structure [1, 11, 19, 53]. The standard direct spray LIHE test does not generate the desired peak pressure and duration required to match an actual radiation deposition, although the impulse area under the pressure-time curve is identically matched to produce the same impulsive load to the structure being tested.

1.4. Scope

Primarily through experiment, the work presented here aims to redevelop and expand the capability to explosively drive a thin metallic flyer plate to a high velocity capable of nearly simultaneously creating a large-amplitude, short-duration pressure pulse over a surface area. The ultimate goal is to field a technique to predictably exercise both material and structural responses in a target structure. The reported work builds on the LIHE direct spray test technique, using established explosive spraying and handling procedures.

The experiments conducted in the current flyer development have been in cooperation and coordination with existing spray operations at the SNL LIHE Facility between June 2004 and March 2005. Explosive deposition for each of the eight spray

operations encompassing this work were determined by requirements external to this research. For this reason, development of the modern flyer techniques is independent of a desired pressure pulse, and instead focuses on determination of flyer performance, material response, and structural response based on the achieved explosive depositions for each experiment case. Definable flyer parameters, such as flyer and target materials and standoff gap, have been chosen based on material availability and expected explosive depositions.

The research presented focuses on one and two-dimensional flyer motion, shock physics, and Gurney assumptions, and utilizes analytical, hydrocode, and experimental analysis to investigate the hypothesis: Can a SASN driven flyer technique prove effective for simulation of a cold x-ray blow-off event?

1.5. Objectives

The road to implementation of a high fidelity, LIHE driven flyer capability was started in the late 1960s and continued through the early 1990s. To bring the theory and analysis to a modern understanding and implementation, three distinct objectives are set forth for the presented research:

1. Redevelop and expand the theory required to utilize silver acetylide-silver nitrate explosive to drive a metallic flyer to impulsive loading velocities and impact pressures using analytical and computer modeling techniques.
2. Implementation of a one-dimensional LIHE driven flyer to generate high-frequency, high-amplitude shock pulses into different material samples. This series will focus on flyer motion, delivered impulse, and target material response. Material response parameters investigated include the spall characteristics of

plastic materials, generation of a shock-hardened area of a metallic material, and any changes in metallic grain structure.

3. Implementation of a two-dimensional LIHE driven flyer series on a ring structure to generate a predictable and measured structural response.

1.6. Chapter Summary

The reporting of the present research is broken into eleven chapters and three appendices. Chapter 2 provides a synopsis of previous work done in the field of impulse loading in over thirty years of research, development, and implementation. Chapter 3 details the steps required to conduct a LIHE experiment, relating to both direct spray and flyer testing. Chapter 4 discusses the theoretical considerations required to implement the LIHE driven flyer. Chapter 5 reports the results of an explosive calibration activity to determine the explosive characteristics required to complete the analytical flyer solution. Chapters 6, 7, and 8 discuss the redevelopment and implementation of the flyer capability. Chapters 9 and 10 discuss the flyer experimental results. Chapter 11 summarizes the conclusions from this research and makes recommendations for further work. Test fixture design drawings are given in Appendix A. And finally, extensive test data for each experiment are given in Appendices B and C.

1.7. Units

This work utilizes "taps" as the community-accepted measure of impulse per unit area (specific impulse). The basic units of impulse are pressure-time per area, and will be reported in taps wherever possible. The conversion from taps to more common CGS units is

$$1 \cdot tap = 1 \cdot \frac{dyn \cdot \sec}{cm^2} \tag{1.1}$$

Pressure is measured in units of bar, and generally reported in kbar, where

$$1 \cdot bar = 10^6 \cdot \frac{dyn}{cm^2} \tag{1.2}$$

The units convention for this work will generally be reported in CGS (centimeter, gram, second) units. Because a portion of the work actually utilizes USCS (United States Customary System—inch, pound, second) units, these will be reported in parenthesis following the CGS units when applicable. A notable exception to this convention is the reporting of explosive deposition in terms of "areal density", weight of explosive per area, which will always be reported as mg/cm^2, which is the convention used at the LIHE facility for this factor.

2. LITERATURE REVIEW

This chapter aims to discuss some of the work and results of previous investigations pertaining to the research at hand. On the topic of exo-atmospheric, cold x-ray deposition, a great deal of work has been performed to investigate and field test techniques that adequately simulate a nuclear environment in a conventional way. The interest in this topic started in the early 1960s when computer processing power was cumbersome and inefficient to use. For this reason, the majority of the documented work has focused on experimental and theoretical research with some correlation with computational results of the day.

Today, computing power is readily available to the research community. In order to predict and analyze the response of a structure to an input loading, dynamic structural codes and shock physics hydrocodes are employed. SNL has designed, written, and implemented a number of these codes including CTH [57], a three-dimensional shock physics code, and SALINAS [21], a three-dimensional structural response code. Lawrence Livermore Laboratories developed a one-dimensional shock physics hydrocode named KOWIN [23] which has been used extensively in this research. The details of the development of these codes are not presented here.

2.1. Experimental

Impulse testing has been of interest since the early 1960s [59], and has utilized multiple techniques to induce a high-frequency, large amplitude pressure pulse into a test item. These range from very complicated and expensive high-fidelity nuclear underground tests to relatively simple low-fidelity above-ground techniques like the Explosive Rods-Over-Foam method. Many of these techniques were quite novel in

concept such as the “SELT” (sheet explosive loading technique) and “SPLAT” (spray lead at target) techniques.

The sheet explosive loading technique was first introduced in the early 1960s and was the first of the impulse simulation methods [59]. The SELT method utilized long strips of DuPont Detasheet explosive (~80% PETN, 20% plastic binder) laid over a 1.2 cm (0.47”) thick layer of foam neoprene rubber which was in turn laid over the test item [31]. The explosive strips were initiated simultaneously at one end, with the detonation running the length of the strip at approximately 730,000 cm/s (287,400 in/s). The purpose of the neoprene attenuation layer was to lower the peak pressures at the test item surface. This method failed the surface load simultaneity and pressure amplitude requirements and was not well suited to conduct impulses at lower ranges.

The Rods-Over-Foam (ROF) technique [59, 71] utilizes 0.089 cm (0.035”) diameter extruded PETN rods arranged in parallel paths over a layer of (typically) polyurethane or melamine foam to impart a quasi-impulsive load to a structure. The explosive product is somewhat flexible and has the consistency of a fine spaghetti pasta, allowing semi-complex shapes to be loaded. Each rod is initiated at one end, with the detonation running the length of the rod at a velocity of approximately 720,000 cm/s (283,464 in/s). As adjacent shocks from the detonating rods travel through the foam, they coalesce to a somewhat planar shock wave at the test item surface, although local pressure peaks often form between rods due to the complex shock interactions within the foam layer. The ROF method is considered a low-fidelity technique because the pressure pulse amplitude falls far short of the actual blow-off event and the pressure duration is approximately 20 times longer than the desired pulse width. In addition, because the

explosive detonation must sweep along the surface of the test item, the loading cannot be considered simultaneous; but for larger items, the loading occurs at a rate that satisfies the ¼ cycle time requirement, making the load impulsive to the structure.

The SPLAT technique [59] utilized lead sheathed mild detonating fuse (MDF) explosive rods positioned adjacent to each other above the test item at a specified distance. The MDF was typically manufactured by swaging lead around a core of PETN explosive, producing a finished product that had the appearance and working properties of lead solder. As the MDF detonation traveled the length of each rod, the lead sheath fractured into fine particles moving away from the center detonation. A portion of the lead from each strand impacted the target surface, delivering impulse by linear superposition of the momenta of impact of individual spray clouds [31]. Like the ROF method, the SPLAT technique does not provide simultaneous loading; and due to the obvious lead contamination reasons, this technique is not environmentally friendly.

Magnetically driven flyer plates were developed in the mid-1960s and the LIHE method in the early 1970s. While these impulse delivery methods were direct competitors, they are actually quite dissimilar techniques in practice. The two techniques provided most of the impulse testing capabilities through the early 1990s, when all of these facilities were mothballed or closed. The discussion presented in this chapter will focus on these two methods as the most relevant to the work at hand. The first section will discuss the magnetically accelerated flyer plate technique in general terms since the concepts used by individual researchers are similar in practice. (The mathematical concepts are well documented by Curran, et al., [31], Farber, et al., [35], and Walling [86] and are not presented here.) The second will provide an overview of the Light

Initiated High Explosive flyer work done previous to this investigation. Because the direct spray LIHE technique has been extensively utilized in the recent development of the LIHE driven flyer plate technique, Chapter 3 will describe the direct spray process in detail. It is shown that both of these summarized methods have their advantages and disadvantages, and the need for an effective combination of the two is warranted.

2.1.1. The Magnetically Accelerated Flyer Plate

Magnetically accelerated flyer plate testing, often referred to as "Mag-Flyer," has been conducted since the mid-1960s to simulate the cold x-ray deposition environment [58, 59]. A number of organizations have operated large Mag-Flyer facilities (with approximately 400-500 kJ energy capacities) in the 40 year lifespan of the technique. These include EG&G in Bedford, MA (for Sandia); SNL and the Air Force Weapons Laboratory (Kirtland AFB), both in Albuquerque, NM; and Kaman Sciences (for the Navy) in Colorado Springs, CO. Each of these facilities have been dismantled or closed, with the Kirtland facility being mothballed in early 2005. Other smaller "facilities" have been developed with the ability to test material samples or impart impulsive like loading to small test items such as MEMS devices. One such system (designed and fabricated by the author) [74], utilizing a 10kV-300J capacitor bank capable of throwing a 1.27 cm by 6.35 cm (0.5" by 2.5") flyer, is currently in use at the Sandia Shock and Vibration Lab testing accelerometer assemblies.

Typically, the Mag-Flyer technique drives a soft aluminum or copper flyer plate, usually on the order of 0.013 cm (0.005") to 0.076 cm (0.030") thick, to impact a target surface at velocities capable of inducing a large-amplitude, high-frequency pressure pulse. During the initial setup, the flyer is separated from another parallel conductive surface (often called a backstrap) by a thin insulating layer. Current from a discharging

capacitor bank is channeled through the flyer and back through the backstrap (or vice-versa) in a manner which assures that the current in the two plates is flowing in parallel and opposite directions. A repulsive Lorentz force is induced between the flyer and backstrap, which drives the two plates apart. The magnetic pressure driving the flyer is usually on the order of several kilobars, is generally less than the yield strength of the flyer material, and is at its peak within a few microseconds from start [19]. A basic diagram of the backstrap and flyer configuration is given in Figure 2.1.

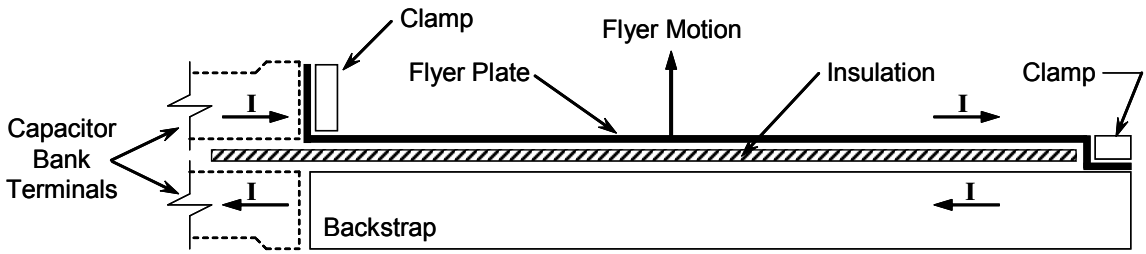

Figure 2.1: Typical Mag-Flyer Configuration [31]

The repulsive pressure generated by the Lorentz forces drives both the flyer and the backstrap apart at velocities relative to the mass of each component. By making the backstrap more massive than the flyer, the flyer accelerates away from the backstrap, and towards the target surface, at a significantly higher velocity, than if the two were of comparable mass.

For a typical application, the capacitor bank required to drive the flyer is a relatively high-energy and low-inductance. Banks on the order of 50kV-500kJ have been used in the past. The capacitor bank and load normally form an under-damped RLC circuit which results in a decaying sinusoidal current discharge [59]. The driving pressure from the Lorentz forces is proportional to the square of the current per unit width of the flyer and backstrap assembly. As a result, the decaying ring-down current accelerates the flyer with a decreasing series of pressure pulses. A typical Mag-Flyer driving pressure is

given in Figure 2.2. Because the driving pressure is not constant, the acceleration of the flyer is not constant, resulting in a stepped velocity profile, shown in Figure 2.3. Given this result, very special attention must be paid to the spacing of the flyer with respect to the target to achieve the desired flyer velocity at impact, taking into account the effect of the trapped air between the flyer and target.

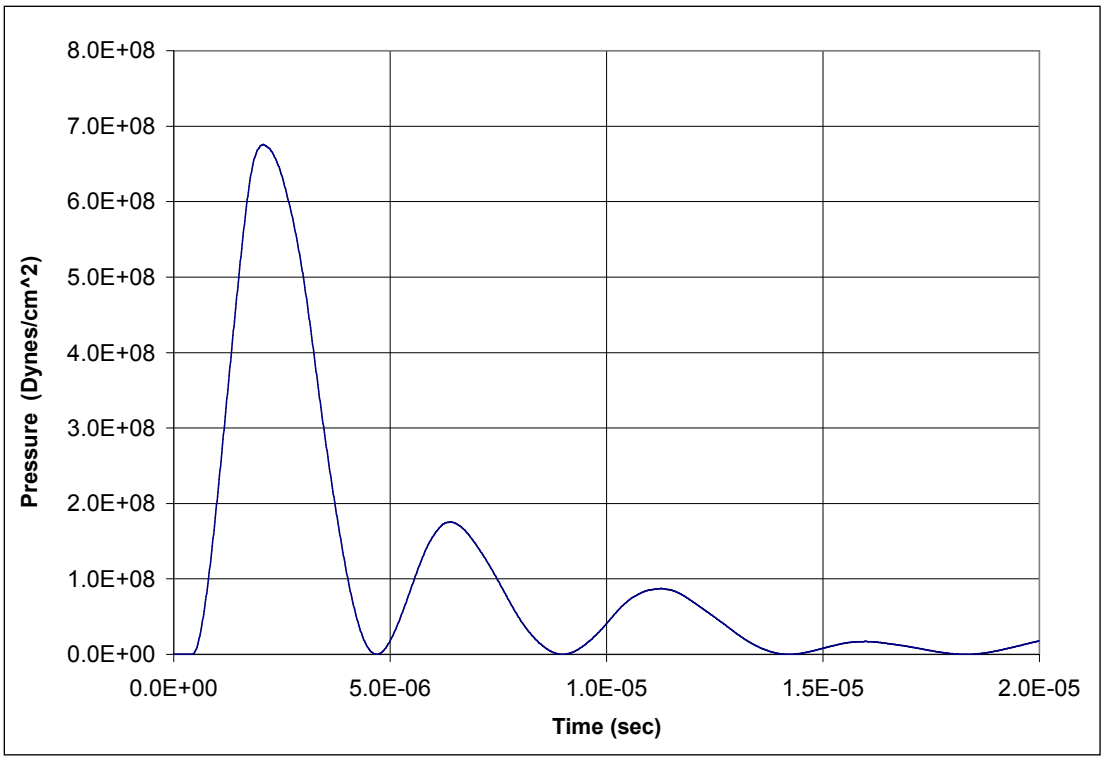

Figure 2.2: Typical Mag-Flyer Driving Pressure [19]

The stepped velocity profile can be avoided by using the "crowbar" method. This technique requires that special circuitry be employed between the capacitor bank and flyer/backstrap to terminate the current at the first peak. The circuitry effectively places an electrical short across the flyer/backstrap, causing the current to decay in a quasi-exponential manor. The pulsating acceleration characteristic associated with a sinusoidal current discharge is eliminated, resulting in a simplified velocity profile.

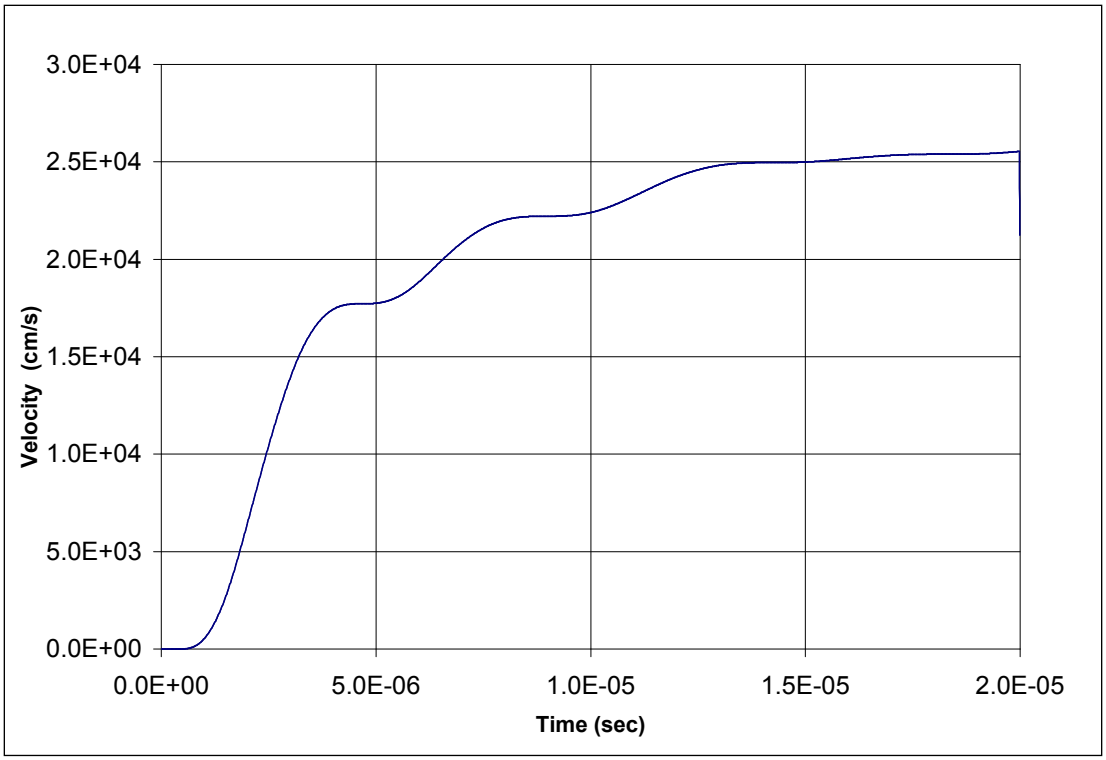

Figure 2.3: Typical Mag-Flyer Velocity Profile [19]

The driving magnetic force accelerates the flyer toward the target surface, compressing the trapped air between the flyer and target, as depicted in Figure 2.4. This air increases in pressure as the volume between the flyer and the target decreases, effectively acting like an air spring to transfer the energy of the flyer to the target. The flyer "impacts" the target and imparts a pressure pulse commensurate with the shock properties of the flyer/target materials, the flyer velocity, and the volume and dynamics of the trapped air. Shortly after impact, within a few microseconds, the flyer will rebound away from the target, at a velocity corresponding to the specific test conditions and materials. The total impulse delivered to the test item is a function of the change in flyer velocity (incoming and outgoing) and the mass of the flyer.

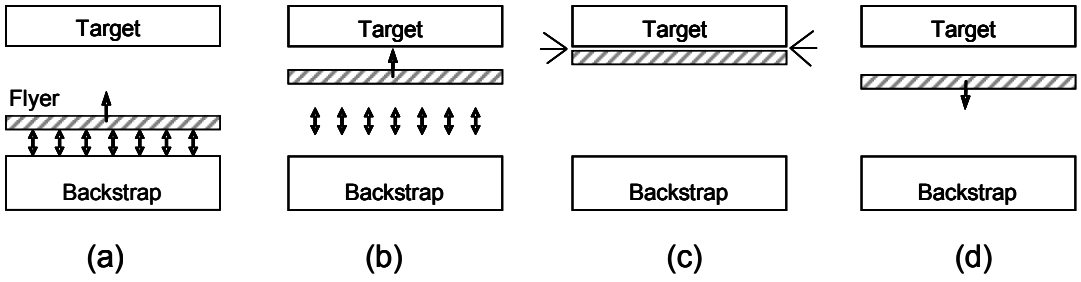

Figure 2.4: Mag-Flyer Impact and Rebound

The primary advantage of the Mag-Flyer technique is that the flyer plate is capable of exciting both the structural and material response of the test item by nearly matching the pressure pulse of the actual x-ray deposition. In addition, by choosing the proper materials and impact velocity, shaping of the pressure pulse to achieve a desired result is possible within certain limitations. The primary disadvantage is that magnetically driven flyer plate operations are relatively difficult. The extremely precise positioning of the test item with respect to the flyer and backstrap, in order to achieve the desired impact velocity, requires experience and is difficult to master. Meagher emphasizes the difficulty involved in implementing a successful Mag-Flyer program [59]: "Preparation of the inserts for dielectric switches and insulation lay-ups between the flyer and backstrap are both art forms which require practice."

2.1.2. Light Initiated High Explosives

Direct spray light initiated high explosives have been used since the early 1970s as an established impulse loading technique for complex shapes and structures [1, 9, 10, 11, 14, 44, 51, 53, 54, 59, 67]. This technique is accomplished by initiating a sprayed-on layer of the silver acetylide-silver nitrate explosive by an extremely bright light source. This direct spray method has the ability to produce the desired impulse load and loading simultaneity, but does not recreate the pressure pulse generated by the actual event. Thus,

the technique provides a good loading to produce the appropriate structural response, but does not have the capability to excite the desired material response of the target surface.

The first work on light initiation of explosive was documented in 1951 by J. Eggert [87] who studied the physical chemistry of the detonation processes. He reported at least sixteen solid compounds, including silver acetylide-silver nitrate, which could be initiated by an intense flash of light from gas-discharge tubes. The first investigations into using a light initiated explosive product, in this case lead azide, were reported in 1964 by Roth [87]. In 1965, Nevil and Hoese reported the initial experiments with spray deposited SASN to impulsively load a structure [87]. Further research to characterize the SASN explosive for impulse loading was done under Sandia direction in the late 1960s [87], leading to a number of interesting conclusions. These included that SASN could be manufactured easily in the lab environment with readily available chemical constituents, is non-detonable when stored in acetone, and can be "safely" spray deposited by hand. The implication here is that the spraying of SASN does not require remote handling operations. It must be noted and emphasized that this is in fact an incorrect assumption and remote handling is required. Additionally, it was found that SASN is more sensitive to light initiation than most other primary explosives, and that dying the SASN explosive further improved the detonation qualities 1.

The concept of using an explosive charge to drive a thin metallic flyer to simulate the cold x-ray deposition environment is not new to the research at hand. It was recognized in the late 1960s that even though the direct spray LIHE technique could impart a desired impulse to a structure, it could not simulate the specific pressure pulse required to excite the material and structural combined response of an actual cold x-ray

deposition. Simple experiments were conducted as early as 1969 to show the ability of the SASN explosive to drive a thin metallic flyer 1. These early experiments, though marginally successful, effectively generated interest in further pursuing the technology.

2.1.2.1 Southwest Research Institute

Southwest Research Institute (SwRI) conducted multiple investigations in the mid- to late-1960s into the potential capabilities of light initiated explosives 1. Some of this work was funded and directed by Sandia Labs for direct use involving impulse testing of strategic weapons systems. Other work was done during this time to investigate other uses such as explosive forming and explosive welding, both utilizing elements of the explosively driven flyer process. Other work done during this time included studies into the shock loading of brittle materials (acrylic resin), improvement of light initiation qualities (by dying the explosive), and enhancement of the explosive properties by the addition of secondary explosives to the formulation process. SwRI documented its flyer research in 1971 [5], focusing on small scale flat experiments utilizing the SASN explosive to drive aluminum and Mylar® flyers to impact a target.

2.1.2.2 Sandia National Laboratories

During the time that the LIHE facility was in operation between 1972 and 1992, a number of LIHE driven flyer experiments were conducted. Robert Benham, the facility test engineer, embraced the idea that the LIHE facility could successfully combine the LIHE direct spray techniques with explosively driven flyer plates to generate combined response experiments. He reported initial investigations into the driving of small flat aluminum flyers with SASN explosive onto pressure gages [13]. The results from this early investigation were preliminary in nature, but started the work at SNL to expand the method to larger and two-dimensional test items. In 1987, Benham reported on combined

response impulse testing using SASN spiked with the secondary explosive PETN [16]. This flyer plate testing resulted in flyer velocities approximately 100,000 cm/s (39,370 in/s) to impact ring targets with sufficient peak pressure to cause catastrophic material damage, most notably spall. The major leap from previous LIHE flyer work, other than the development of a greater power light initiated explosive product, was that the explosive deposition on the flyer was pseudo-cosine distributed to cause a cosine distributed impulse load to the structure.

Goolsby and Benham [39] reported in the early 1990s on work to further refine the LIHE driven flyer concepts. Work was done on understanding the techniques required to measure flyer/target impact pressure with thin film carbon pressure gages. In this work, the one-dimensional hydrocode WONDY [50] was used to quantify the differences between expected pressures and measured pressure data. It was shown that the presence of the gage between the aluminum flyer and the aluminum target resulted in a lower measured impact pressure than if the gage were not present. A further test series in July of 1991 [38] was conducted to extend the hydrocode validation to softer materials with an aluminum flyer impacting Teflon and Lucite targets. The culmination of the work done in 1991, shortly before the facility was mothballed, was a flyer/ring experiment conducted with the standard formulation SASN at a significantly lower impulse loading than the experiments run in 1987. Finally, in 2003, Benham, Rivera, Skaggs, and Goolsby [19] published a paper study on the engineering differences between magnetically driven flyer plates and explosively driven flyer plates in conjunction with the LIHE facility being reopened from mothball status.

Up to this point, each of the light initiated explosively driven flyer experiments have added complexity and understanding to the technique. But as of 1991, a complete analytical/experimental solution had not been achieved. In Goolsby's 1991 ring experiment, efficiency factors were employed in the design process that required the experience and job knowledge of the experimenters to determine flyer velocity and explosive performance. The present work has aimed to take the next step in the development in the LIHE driven flyer process by eliminating these efficiency factors in the design process, and replacing them with quantified terms indicative of the physics of the situation.

2.1.3. Material Response Studies

The interest in materials exposed to shock loading is extremely large, and work in the field is extensive. There are entire conferences dedicated to the shock compression of condensed matter [80] where leaders in the field regularly report cutting edge research. The areas of this research span the fields of modeling, experimental work, and analytical derivation in topics from planetary physics to molecular studies of material interactions to macroscopic mechanical properties of solids under shock loading. The entire scope of this field is far too broad to adequately describe here. A subset of this field is the experimental work on the material response of solids under impact loading. Of specific interest to this project is the work done in the field of material response induced by flyer impact and the mechanisms required to generate spall.

In the area of impulse testing, much work has been done on composite materials. With multiple mag-flyer facilities in operation from the 1960s through the early 1990s, much of this work involved the impact of one-, two-, and three-dimensional structures to ascertain the surface material damage generated by a thin flyer impact. Farber, Seman,

and Ciolkosz [35] discussed, in 1969, an extensive series of one- and two-dimensional mag-flyer induced impulse experiments for combined response. These experiments varied target and flyer materials, as well as impact pressure pulse amplitude and duration to determine target damage at each combination of factors. A secondary objective was to determine the difference between material response and combined response (using ring structures) on the damage threshold. These tests are representative of the types of flyer impact experiments that were conducted within the impulse community, and directly address the need of a test technique to induce combined response in target structures.

An applicable use of a flyer impact experiment to induce a quantifiable material response was conducted by Shirey [82] in 1972. Here, an explosively driven, relatively thick flyer was used to shock harden a beryllium-copper material sample. The 0.062" thick steel flyer was driven by a thick (in comparison to a sprayed layer of SASN) layer of Detasheet explosive. Of interest here is the work done to calculate the impact pressure at the flyer/target interface, as well as the concepts of a flyer impact induced shock hardening of the target material. Shirey utilized an early computer code to calculate impact pressure in the target based on the Hugoniot and material properties of the flyer and target. The hardness results of the beryllium-copper (Be-Cu) study may have been useful to the present study as a basis for comparison, but unfortunately Be-Cu could not be chosen as a sample material due to health safety concerns.

Also of interest to the present study is the generation of material spall due to mechanical impact. Again, multiple sources and references were found during the literature search on this relatively broad topic. Two excellent discussions on spall mechanisms and phenomena are given by Curren, Seaman, & Shockey [30] as well as

Meyers & Aimone [61]. Both of these documents were published in journal form in the mid-1980s, and describe in detail the micro and macro structural phenomena that led to the generation of dynamic spall in materials. Both make extensive correlation with controlled experimental data and provide a comprehensive reference on the topic.

In 1968, Thurston and Mudd [83] sought to develop a spallation criteria for use in numerical calculations. Their experimental work focused on solid metallic materials (copper and aluminum) as well as sandwiched composite (copper/aluminum/copper) test specimens. The results were a spall criteria model based on an empirical correlation of induced spall tension in terms of the static tensile strength of the metallic material. This document also provides a good graphical discussion on the shock mechanisms required to induce spall in a target material.

in 1987, Grady [40] formulated two conditions which placed constraints on the processes of dynamic spall in condensed materials. The first condition was reported as a "horizon" condition which established a domain of communication, within which spall must be independent of the surrounding environment. The second condition was an energy condition, requiring that the potential and kinetic energy associated with the tensile loading process exceed the fracture energy of the material. Grady used these conditions to establish specific analytic expressions for spall properties. His developed theory was compared to experiments in solid aluminum and liquids (within the range of Newtonian fluid behavior), although liquid experimental data was sparse. His conclusion was that spall is dominated by surface energy at low strain rates and viscous dissipation at high rates.

2.2. Theoretical

Much theoretical work has been done to understand the physics involved in both the Mag-Flyer technique and the LIHE technique. The details of that work are beyond the scope of this work, but are presented in a number of excellent references. *The Tutorial Handbook on X-Ray effects on Materials and Structures*, by Curran, et al., [31] provides a good introduction and reference for many of the impulse delivery methods described above, including Mag-Flyer theory and the direct spray LIHE techniques. Walling [86] also provides a good description of the Mag-Flyer theory in conjunction with ring experiments, circa 1970. Benham published "An initiation and Gas Expansion Model for the Light-Initiated Explosive Silver Acetylide-Silver Nitrate" [14] in 1980, providing an excellent description of the detonation physics behind the LIHE process.

2.2.1. Simple Ring Structural Response

Because the analytical solution of a cosine distributed impulsive loading on a thin metallic cylindrical shell is integral to the research at hand, a discussion on the details of its application is given here. This solution was published in the proceedings of the AIAA Fifth Annual Structures and Materials Conference in April of 1964 by J.S. Humphreys and R. Winter [45]. Their solution was further updated and corrected by M.J. Forrestal, M.J. Sagartz, and H.C. Walling in the September 1973 issue of the AIAA Journal, though the solution is commonly referred to as the Humphreys-Winters (H-W) Solution [36]. This largely analytical and mathematical solution utilized traveling wave solutions for membrane stresses, modal solutions for both membrane and bending stresses, and shell theory to describe the dynamic structural response of a cylinder or ring to a cosine distributed side pressure pulse, depicted in Figure 2.5. The H-W solution has proven to be

an excellent diagnostic for impulse loading techniques, and has been used extensively by Benham since its inception [16, 17].

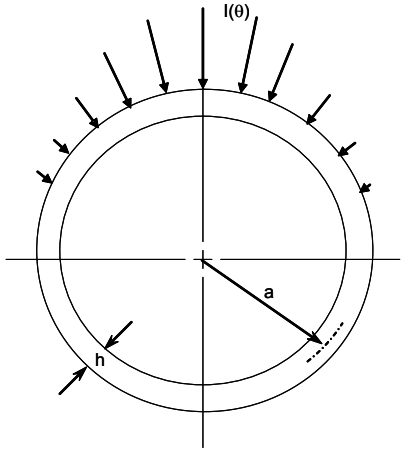

Figure 2.5: Cosine Loading of a Simple Ring Structure

The structural response equations presented by Forrestal, Sagartz, and Walling are divided into the membrane response σ_m,

$$\frac{\sigma_m \cdot h}{I \cdot c} = \frac{1}{\pi} \cdot \sin(\tau) - \frac{1}{(2)(2)^{1/2}} \cdot \sin\left[(2)^{1/2} \cdot \tau\right] \cdot \cos(\theta) + \frac{2}{\pi} \cdot \sum_{n=2,4}^{\infty} \frac{(-1)^{n/2}}{(n^2-1)(n^2+1)^{1/2}} \cdot \sin\left[(n^2+1)^{1/2} \cdot \tau\right] \cos(n\theta) \tag{2.1}$$

and the bending response σ_b,

$$\frac{\sigma_b \cdot h}{I \cdot c} = \frac{2 \cdot (3)^{1/2}}{\pi} \cdot \sum_{n=2,4}^{\infty} \frac{n \cdot (-1)^{n/2}}{(n^2-1)(n^2+1)^{1/2}} \cdot \sin\left[\frac{n \cdot (n^2-1)}{2 \cdot (3)^{1/2} (n^2+1)^{1/2}} \cdot \frac{h \cdot \tau}{a}\right] \cdot \cos(n\theta) \tag{2.2}$$

Here, h is the ring wall thickness, I is the impulse level, τ is a non-dimensionalized temporal term, comprised of the sound speed, c, time, t, and the ring mean radius, a,

$$\tau = \frac{c \cdot t}{a} \tag{2.3}$$

The squared sound speed c is a function of the modulus of elasticity, E, material density, ρ, and Poisson's ratio, v,

$$c^2 = \frac{E}{\left[\rho \cdot \left(1 - \nu^2\right)\right]} \tag{2.4}$$

making the assumption that the ring remains within the elastic range, equations (2.1) and (2.2) can be manipulated by dividing by the modulus of elasticity to reflect membrane,

$$\varepsilon_m = \frac{\sigma_m}{E} = \frac{I \cdot c}{\pi \cdot h} \cdot \sin(\tau) - \frac{I \cdot c}{h \cdot (2)(2)^{1/2}} \cdot \sin\left[(2)^{1/2} \cdot \tau\right] \cos(\theta) + \frac{2 \cdot I \cdot c}{\pi \cdot h} \cdot \sum_{n=2,4}^{\infty} \frac{(-1)^{n/2}}{\left(n^2 - 1\right)\left(n^2 + 1\right)^{1/2}} \cdot \sin\left[\left(n^2 + 1\right)^{1/2} \cdot \tau\right] \cos(n\theta) \tag{2.5}$$

and bending strains,

$$\varepsilon_b = \frac{\sigma_b}{E} = \frac{2 \cdot I \cdot c \cdot (3)^{1/2}}{\pi \cdot h} \cdot \sum_{n=2,4}^{\infty} \frac{n \cdot (-1)^{n/2}}{\left(n^2 - 1\right)\left(n^2 + 1\right)^{1/2}} \cdot \sin\left[\frac{n \cdot \left(n^2 - 1\right)}{2 \cdot (3)^{1/2}\left(n^2 + 1\right)^{1/2}} \cdot \frac{h \cdot \tau}{a}\right] \cdot \cos(n\theta) \tag{2.6}$$

The combined strain response at the surface of the ring is simply the combination of equations (2.5) and (2.6). The subtraction of bending strain from membrane strain results in the strain at the inner surface of the ring, and the addition of the bending and membrane strains results in the strain at the outer surface. Because it is logistically easier to measure strain on the inner surface of the ring, the combined response as measured by a strain gage is

$$\varepsilon_{gage} = \varepsilon_m - \varepsilon_b \tag{2.7}$$

The infinite series terms in equations (2.5) and (2.6) correspond to modal frequencies of the vibrating ring. Generally two or three terms of the infinite series are sufficient for comparison to test data.

Sebrell and Lobitz [80] investigated imperfections in cosine loadings to determine the effect on the structural response of a simple ring structure. This study was to ascertain the effectiveness of several of the different impulse loading techniques. Their reported

results showed that the simulation was acceptable if an approximate cosine load distribution was achieved and τ of equation (2.3) is less than or equal to unity. In essence, this says that a precise, simultaneously applied cosine load is not necessarily required for acceptable results, but should be strived for in order to achieve optimal results.

2.2.2. Explosive Driving of Metal

In the 1940s, R.W. Gurney [42] investigated the expansion of metal cylinders driven by an explosive contained within the cylinder walls at the US Army Ballistic Research Laboratory in Aberdeen, MD [49]. His model described the initial velocity of the fragments produced by the expanding cylinder driven by the detonation of the explosive charge. This model relies on a partition of the explosive energy between the driven metal wall and the gases driving it. The result is a relationship between the terminal metal velocity, the explosive energy, and the ratio of the mass of the driven metal to that of the loaded explosive charge [24]. Gurney applied his analysis approach to multiple loading configurations including cylindrical, spherical, symmetrical sandwich, unsymmetrical sandwich, and open face sandwich. The sandwich configurations refer to planar geometries where the explosive charge is sandwiched between two layers of metal. In the case of the open-face sandwich, a planar layer of explosive is in contact with a single layer of metal.

Though relatively simple, Gurney's model is effective in predicting metallic particle motion as a result of an explosive detonation. The current flyer research extensively utilizes Gurney's work to predict the motion of the flyer.

3. THE LIHE PROCESS

The direct spray LIHE test technique is an integral part of this investigation. The current chapter details each of the processes and steps that go into conducting a successful LIHE test. The detail provided is sufficient for general insight, but is not adequate to conduct a test without additional knowledge, process understanding, and experience. It should be noted and emphasized that silver acetylide-silver nitrate, though relatively low in explosive output, is a highly sensitive primary explosive, and special facilities and procedures are required to safely work with this energetic material. The process for formulating the explosive, spraying a test item, and conducting a test are summarized in the following sections.

There are multiple steps required to complete a LIHE test. These include designing the spray deposition profile, programming a robot arm to apply the explosive, formulation of the explosive, spraying of the explosive, verifying the load distribution, conditioning of the explosive, firing the explosive using a capacitor bank powered light source, and cleanup. Ultimately, the goal of a LIHE test is to subject a test item to a specified impulse in the proper distribution. The load distribution generally corresponds to the geometry and orientation of the test item to the simulated x-ray deposition. A spray design process is used to determine the number and location of spray passes over the test item to achieve the proper explosive distribution. Often times, a single test will require hundreds of spray passes in numerous locations, and take many hours to complete the spraying process alone.

3.1. Explosive Spray Design

In many ways, the process for spraying SASN suspended in acetone onto a surface is similar to spraying a common paint onto a surface. Spray preparation, formulation, coverage area, spray pattern, and deposition thickness are all important factors in a successful application, but in the case of a LIHE spray, the "paint" is a primary explosive. The typical setup of the spray gun forms the spray fan distribution into an oval shape, approximately 33 cm (13") long and 10 cm (4") wide. The distribution of explosive within the fan is approximately normally distributed. By overlapping multiple adjacent spray passes, the explosive layer is built up locally to achieve the overall desired deposition.

Silver acetylide-silver nitrate deposition characteristics were documented by Mathews in 1981 [51], including the effects of spray gun distance, gun angle to the spray surface, and robot arm velocity. These characteristics have been captured in computer program form to allow the test engineer to "design" the spray profile to achieve the desired loading distribution on the sprayed surfaces. Prior to mothballing the facility in 1992, the design process was cumbersome due to the available computing power of the day. A typical design at that time could take days to complete. The modern incarnation of the computer design code is highly interactive and allows the designer to quickly vary each of the spray parameters to create an optimal spray profile. These improvements in modern computing allow a typical design to take only hours to complete. An example screen capture from the LIHE Flat Spray Design program graphical user interface (GUI) is shown in Figure 3.1 [82]. Of interest in the figure shown is the main portion of the screen where a graphical representation of the impulse delivered (red line) for the explosive deposition is generated. The particular deposition shown is the result of 23

spray passes at each of twelve overlapping spray positions at a nominal gun velocity of 12.7 cm/s (5.0 in/sec). In this example case, a constant explosive deposition is maintained over 40.6 cm (16.0 in), dropping off to zero on either side.

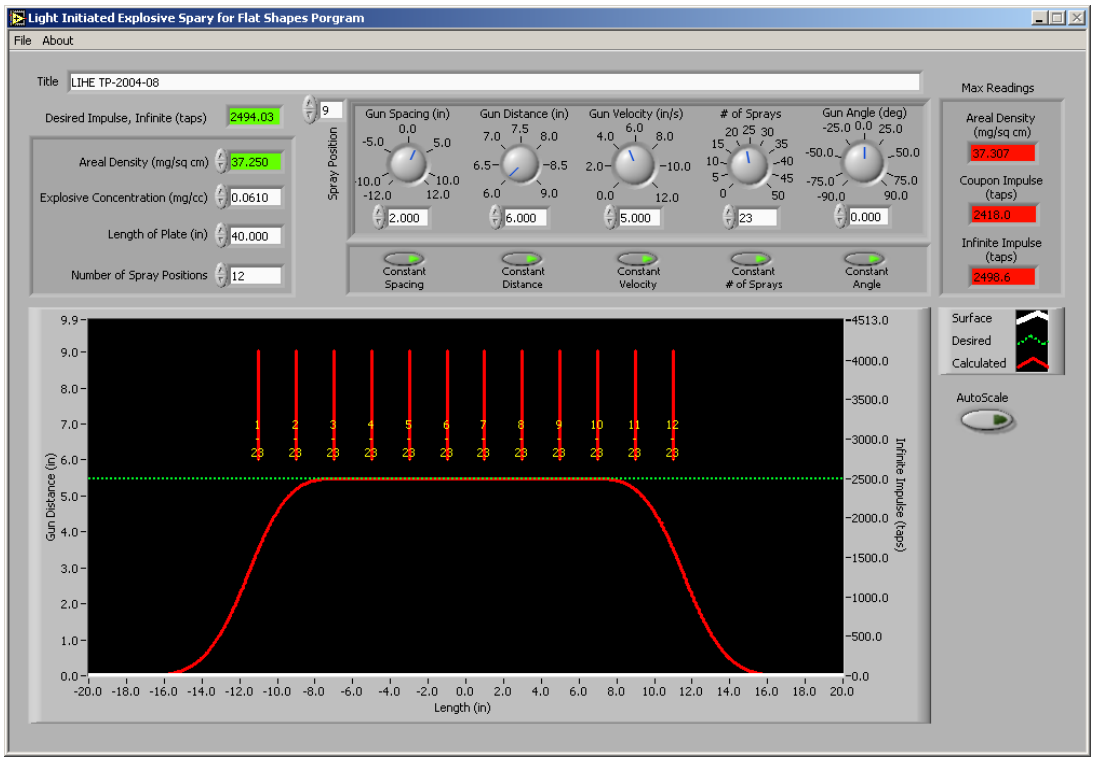

Figure 3.1: LIHE Design Code GUI

3.2. Viton Rubber Application

Prior to the application of explosive, a thin layer of viton rubber is spray deposited onto the spray surface. The viton layer acts as a binding agent between the SASN explosive and the spray surface. Viton is dissolved in acetone to form a solution with a specific gravity of 0.80. The solution is then sprayed onto the test item surface, with a spray gun similar to that of the explosive spray, to an areal density between 0.50 and 1.0 mg/cm^2. The acetone carrier evaporates quickly after contact with the target surface, leaving the thin layer of viton.

As the initial layers of SASN are sprayed onto the spray surface, the acetone carrier of the explosive slurry dissolves a portion of the viton on the surface. A layer of viton mixed with SASN is created as the acetone quickly evaporates. This effect greatly enhances the ability of the explosive to adhere to the spray surfaces. But, since the viton is not an energetic material, excess mixing of SASN and viton will decrease the explosive output. For this reason, control of the viton deposition on the surface is critical.

3.3. The SASN Explosive Formulation Process

The formulation process requires four distinct steps to complete: Test preparation, formulation, washing, and preparation for spray. Generally these steps, as well as the spray process itself, are completed in a single six to ten hour day. Operations require a minimum team of two with intimate knowledge of the LIHE process, test objectives, and specialized knowledge of explosive chemistry and robotics.

3.3.1. Preparation of the Spray Booth

Again, because the SASN explosive is extremely sensitive, it is necessary to prepare the formulation/spray area for remote operation and cleanup. The explosive is formulated and sprayed in a 3.7 m by 3.5 m by 3.5 m (12’ by 11.5’ by 11.5’) environmentally controlled blast chamber, shown in Figure 3.2, capable of withstanding a detonation of up to several pounds of SASN explosive (many times greater than the typical amount of explosive formulated). Operations are monitored though a 27.9 cm (11”) thick PMMA and LEXAN® layered window, and controlled using master/slave manipulators and remote controlled systems. Because personnel cannot enter the spray booth during and after explosive is formulated, all materials, chemicals, and hardware must be in place before formulation begins. Figure 3.3 shows the spray booth through the protective window during handling operations.

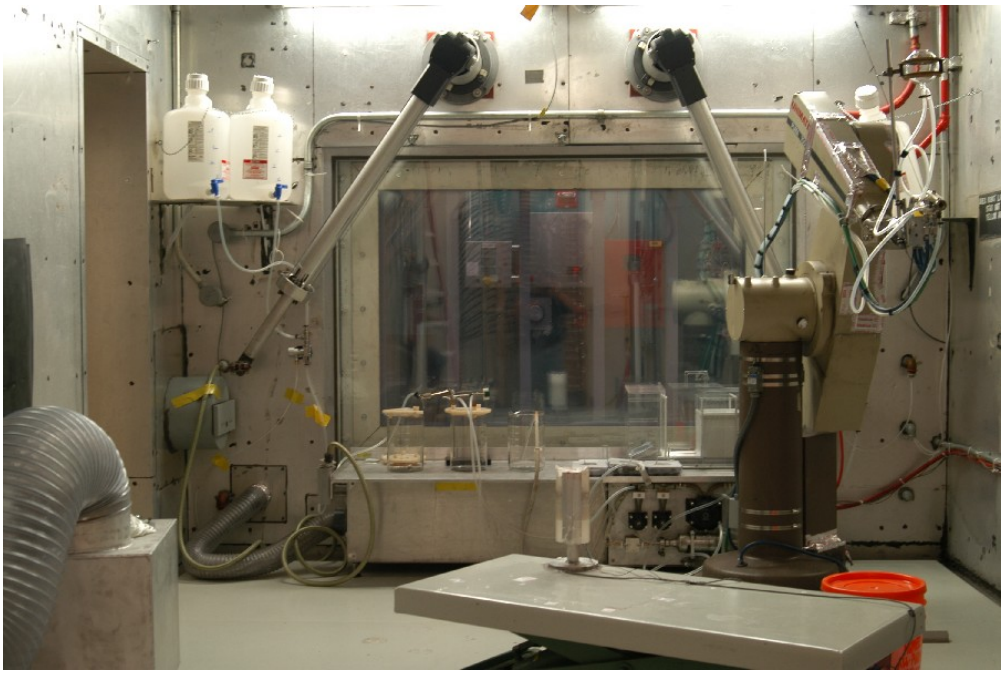

Figure 3.2: Environmentally Controlled Spray Booth

Figure 3.3: Remote Handling Operations Using Master/Slave Manipulators

3.3.2. Explosive Formulation

The SASN explosive formulation has been relatively unchanged since a stable process was developed in the early 1970s [9]. The process for making the explosive starts with silver nitrate crystals dissolved in a liquid solvent. A precipitation process is employed in which acetylene gas is dispersed through the silver nitrate/solvent solution. The silver nitrate reacts with the acetylene gas as follows:

$$3AgNO_3 + C_2H_2 \rightarrow Ag_2C_2 \cdot AgNO_3 + 2HNO_3$$

The silver acetylide-silver nitrate ($Ag_2C_2 \cdot AgNO_3$) settles out as a white precipitate, seen in Figure 3.4, and the nitric acid (HNO_3) remains mixed with the solvent which does not participate in the reaction. The nitric acid effectively decreases the explosive output of the SASN, so it must be removed from the solution.

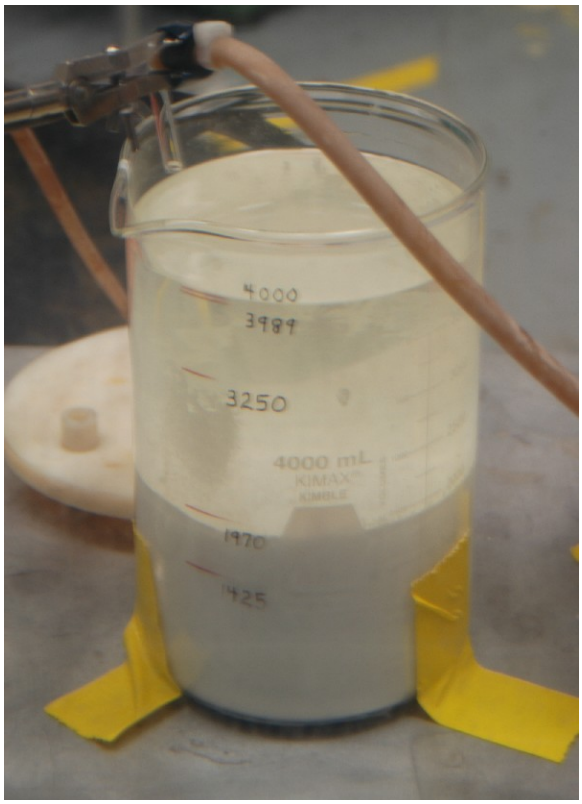

Figure 3.4: SASN Explosive Settling During Formulation

3.3.3. *Explosive Washing*

The explosive is washed with acetone, to remove the excess nitric acid and any other impurities. This is done by adding a predetermined amount of acetone to the solution, stirring, letting the explosive settle to the bottom of the beaker, and then removing the supernatant liquid. This washing step is conducted several times to reduce the nitric acid content to an acceptable level. The stirring and settling steps are shown in Figure 3.5 (a) and (b) respectively.

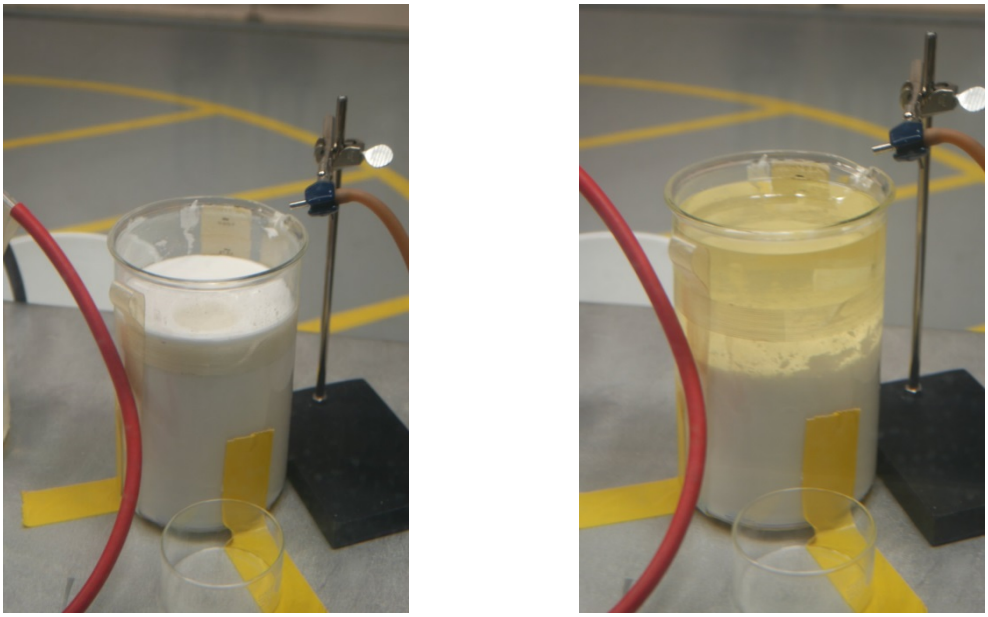

(a) Explosive Stirring (b) Explosive Settling

Figure 3.5: Explosive Washing Process

3.3.4. *Preparation For Spraying*

The explosive is pumped from the formulation beaker through Latex tubing by a peristaltic pump to the spray gun, to a vacuum break, and then pumped back to the formulation beaker by a second peristaltic pump. The vacuum break (glass globe above the spray gun in Figure 3.7) assures a constant pressure at the spray gun nozzle regardless of vertical robot position. Atomizing air is supplied to the spray gun to form the spray

into the oval shaped fan distribution. A fluid density/flow meter is also located in the circuit which monitors the explosive/acetone slurry for explosive concentration which directly corresponds to the explosive deposition on the spray surface. Figure 3.6 shows the PUMA 760 robot spraying explosive on a flat target on a horizontal trajectory.

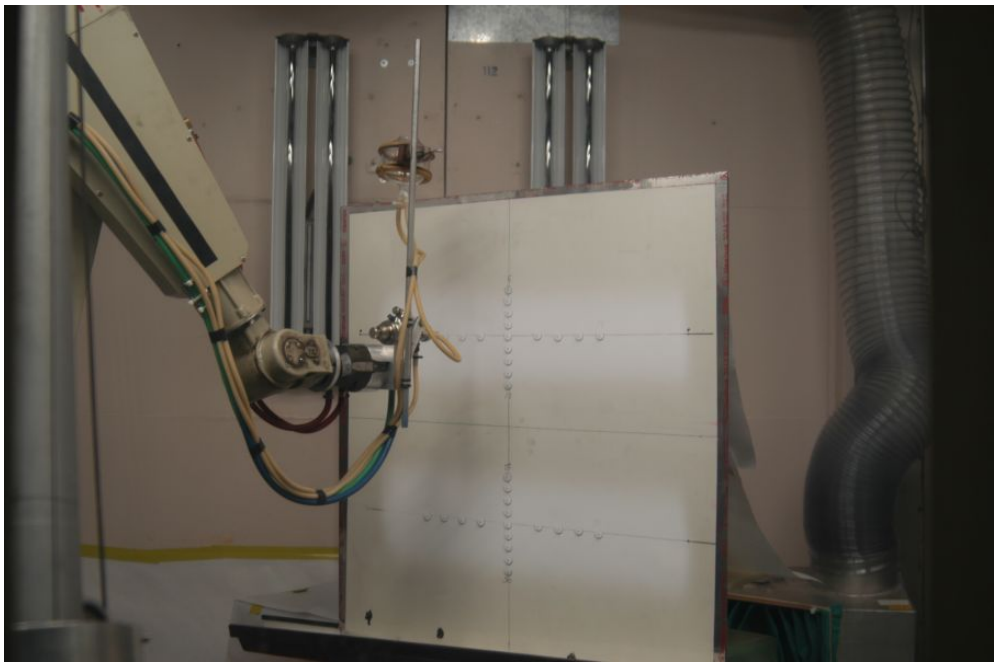

Figure 3.6: One-Dimensional Explosive Spray Operations

3.4. Robotic Positioning and Spray

A computer controlled six-axis PUMA 760 robotic arm is used to precisely position the spray gun over the test item surface [67]. The PUMA 760 is an eighties era robot, which was used extensively in the automotive industry. It utilizes a sequential programming language called VAL II, similar to BASIC or FORTRAN, which was designed specifically for this type of robot arm. Typically, robot programs are written for specific tasks and spray surface configurations. As part of the test preparation, the robot is "taught" points of interest on the test item. These points are used within the robot control program to vary the spray gun position and velocity to accomplish the proper explosive deposition and distribution, as determined by the design process.

The explosive is pumped as a suspension in acetone to the spray gun for application to the test item. The spray gun used in the LIHE process is a conventional type Binks Model 61 spray gun, specially modified to maintain a constant pressure (controlled by the vacuum break) in the fluid chamber. When directed to start spraying, the spray gun atomizes the explosive/acetone mixture directed at the spray surface. The explosive/acetone travels through an air gap of approximately six inches and is then deposited on the spray surface, where the remaining acetone evaporates leaving only explosive. Because it takes approximately 40 seconds for each spray pass to "dry" (evaporate the remaining acetone carrier), it is necessary to pay special attention to stagger overlapping spray passes in order to minimize the time required to complete an entire test item.

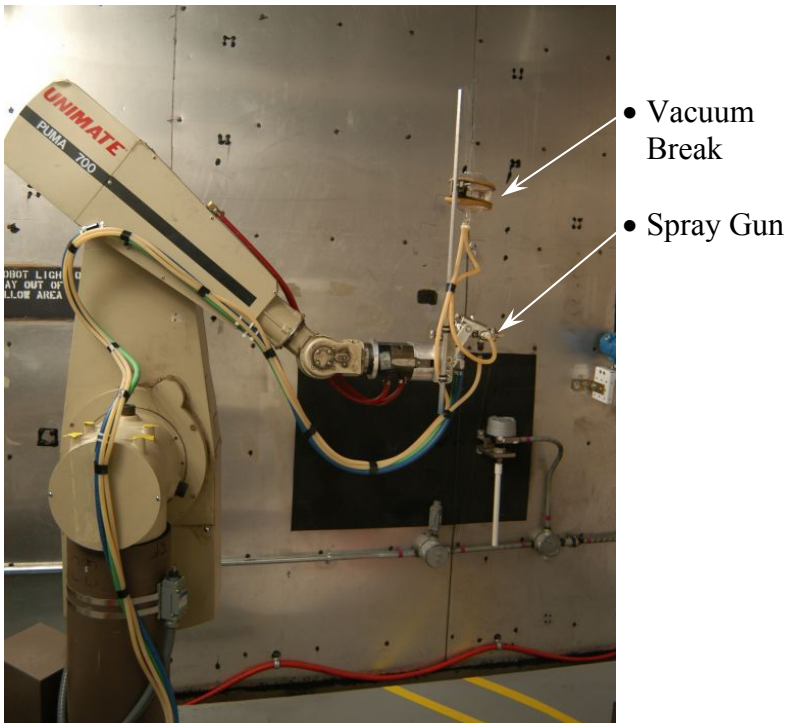

Figure 3.7: PUMA 760 Robot Arm

3.5. Load Distribution

The primary method used to verify that the explosive applied to the test item matches the designed load distribution is coupon weighing. The measure of explosive deposition on a sprayed surface is areal density, defined as the mass of explosive divided by the area which it is deposited on, given in units of mass per area (mg/cm^2), and denoted ρ_A.

With the coupon diagnostic technique, small Kovar® coupons, typically 1.905 cm (0.75") diameter, are magnetically attached to the sprayed surface. After a number of spray passes have been completed, a coupon can be remotely removed from the test item and weighed on a digital scale. The difference between the tare weight of the coupon and weight of the coupon with explosive implies the explosive deposition and is directly related to the delivered impulse to the sprayed surface. Once this measurement has been made, the coupon can be returned to the sprayed surface for additional explosive deposition and future measurements, if necessary.

3.6. "Sun-Tanning" of the Explosive

Exposure of the SASN to ultraviolet light causes the surface of the explosive to darken. It is believed that the sun-tanning process slightly decreases the sensitivity of a very thin surface layer of the SASN, while increasing the efficiency of energy absorption from the light source, thus sensitizing the total explosive layer to the initiating flash of light. This effect greatly enhances the number of detonation points on the surface of the test item when exposed to the energized light array, resulting in greater detonation simultaneity.

As mentioned in Chapter 2, it was found in the early 1970s that dying the explosive resulted in a better energy transfer from the light array 1. The sun-tanning

process effectively accomplishes the same task without adding additional chemicals to the formulation. Exposure to ultraviolet light was originally accomplished by focusing sun light on the explosive surface with mirrors, hence "sun-tanning" of the explosive. To improve repeatability, ultraviolet lights replaced the sun and mirror technique in the mid-1970s.

Sun-tanning is done after the explosive has been sprayed and dried on the test item, and before moving the test item to its firing position in front of the light array. Typically, the explosive is exposed to the ultraviolet light for a minimum of five minutes, and the surface turns from a white color to a burnt cream color. Upon completion of the sun-tanning process, the test unit or coupon is positioned in front of the light array for detonation. Figure 3.8 pictures a group of coupons being sun-tanned by exposure to ultraviolet lights.

Figure 3.8: Sun-Tanning of SASN on 1.905 cm (0.75") Diameter Coupons

3.7. Light Array

The light array is a capacitor bank powered flash source, capable of causing a nearly simultaneous detonation of the SASN explosive on the surface of the test item [44]. It is believed that the actual mechanism for detonation is that the intense flash transfers thermal energy to the explosive surface causing multiple hot spots within the explosive layer (on the order of hundreds per square centimeter), which in turn sets off

the explosive adjacent to each hot spot [53]. The result is a detonation that is nearly simultaneous over the coated surface of the test item.

The LIHE facility has two light arrays that can be configured to initiate the SASN explosive. The large bank light array, shown in Figure 3.9 (a), is powered by a 40kV-208kJ capacitor bank, and is generally used to initiate the explosive deposited on large test items. This array is divided into five modules and can be discharged in any combination of modules to accommodate test item size and orientation. Typically, each module generates a peak current of ~150,000 amps. The small light array, shown in Figure 3.9 (b), is powered by a 10kV-300J capacitor bank and is used for testing of coupons and small test items. The small light array is considered a single module, generating a peak current of ~24,000 amps, and cannot be reconfigured.

(a) Large Bank Light Array

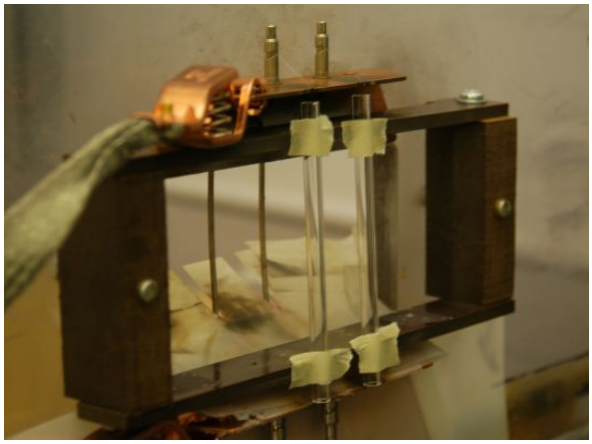

(b) Small Bank Light Array

Figure 3.9: Large and Small Bank Light Arrays

In both arrays, electrical energy is sent to an array of tungsten wires [0.0076 cm (0.003”) in diameter and 61.0 cm (24”) long for the large light array and 0.0051 cm

(0.002”) in diameter and 7.6 cm (3”) long for the small light array], each wire strung within a clear quartz tube. Investigations have shown that quartz tubing results in better detonation characteristics than regular glass or Pyrex [44]. When the capacitor bank is discharged through the tungsten, the wires vaporize leaving an electrical arc through the plasma contained by the quartz tubing. The discharge in both capacitor banks is characterized by a critically damped RLC circuit. This arc becomes the light/heat source for the SASN explosive, transferring energy through the quartz to the explosive surface. A coupon detonation is shown in Figure 3.10, where the small light array is energized and the explosive on the coupon has been detonated, imparting an impulse to the ballistic pendulum mass.

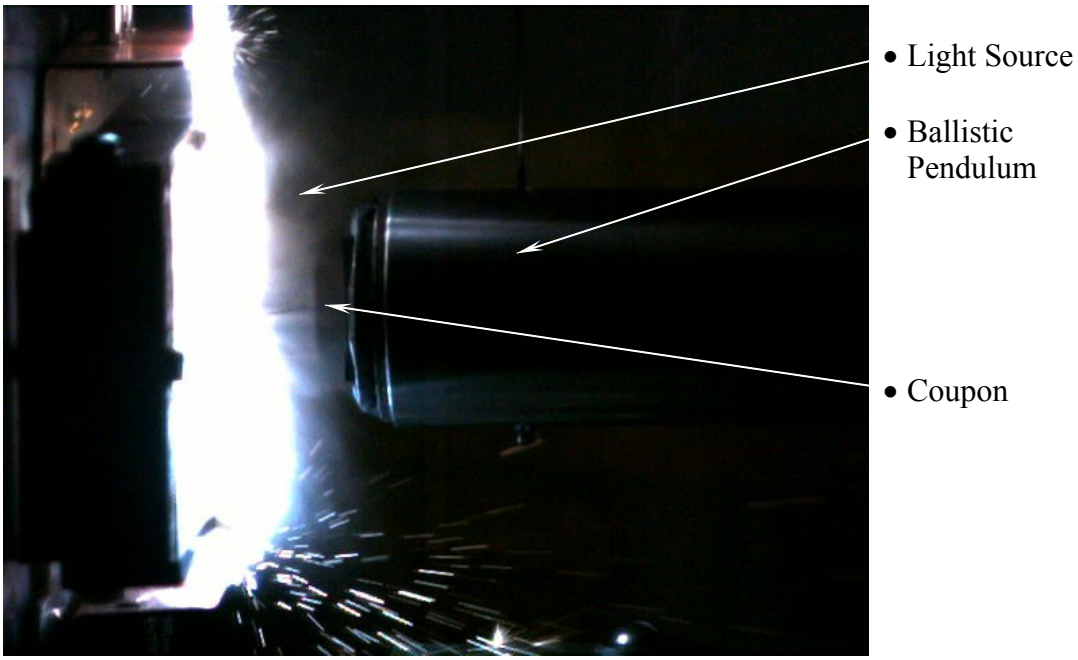

Figure 3.10: Small Bank Light Array Firing a 1.905 cm (0.75”) Coupon

3.8. Test Diagnostics

A number of test diagnostics are employed to quantify the delivered impulse to the test item. The most accurate indication of impulse delivered is a measurement of rigid

body motion of the test item. Three methods are used to determine rigid body motion when fired on the large array: displacement gages, flash x-ray, and high speed photography. Comparison of measurements taken by the these three methods can be made to an analytical solution to either verify the design impulse, or calculate the actual delivered impulse. When firing test samples on the small bank pendulum apparatus (SBPA) using the small light array, a non-contact eddy current displacement gage is used to measure rigid body motion of the horizontal single pendulum mass.

Additionally, thin film carbon pressure gages can be applied directly to the surface of the test item (before spraying of the explosive). This measurement will provide an estimate of the local pressure-time loading history at the test surface. By integrating the pressure time history, impulse can be determined. The gages can also be used for detonation simultaneity or time of arrival measurements.

3.9. Test Cleanup

After a test has been conducted, a thorough cleaning of the spray booth and test area is required. To remove any excess explosive or explosive residue, both areas are washed down with water to render any explosive present non-detonable (while wet) and manually cleaned. The wash water is channeled through multiple filters to catch any explosive residue not collected by other means. These filters are then removed and sent to a New Mexico Environmental Department permitted onsite thermal treatment facility (TTF) to dispose of any explosive waste. Any of the explosive/acetone mixture that was not used during the spray is pumped to the TTF and treated. In addition, any explosive contaminated solids, such as paper or Mylar® masking, are also removed to the TTF for disposal. The developed procedures assure that at the beginning of the spray/test process,

no SASN explosive is present at the facility, and the same is true when the test is completed.

4. THEORETICAL CONSIDERATIONS

The development and implementation of a LIHE driven flyer to excite both material and structural response in a target requires the assembly of analytical work from several previous researchers. These include Hugoniot relationships discussed by Cooper [24] and the work of Gurney [42, 49] for the explosive driving of metals, as well as simple models for trapped air compression by Baker, et al. [5]. This analysis will primarily focus on Gurney and Hugoniot relations as they relate to the explosively driven flyer velocity and impact. Additional discussion on the effect of trapped air between flyer and target, as well as flyer rebound away from the target surface is presented. The present chapter discusses the steps necessary to build an analytical model to predict flyer/target impact conditions for a given set of test parameters.

A note about symbols and nomenclature in the following analysis: the work of several authors has been tapped to develop this analysis. Each have used their own nomenclature to describe different methods and physical quantities, some of which have become standard within the shock and impulse communities. Invariably, conflicting nomenclature schemes have been used that require clarification for use in this investigation. Every attempt will be made to use the standard nomenclature whenever possible, though in order to maintain consistency and foster clarity, some variables representing common quantities are standardized. Table 4.1 lists the variables presented and used in this chapter with their corollary variables from other analyses.

Table 4.1: Variable Nomenclature

Physical Quantity	Variable Used	Hugoniot	Gurney	Air Comp.	Rebound
Area	A	-	A	A	-
Density, Areal	ρ_A	-	ρ_A	-	-
Density, Explosive	ρ_{HE}	-	ρ_{HE}	-	-
Density, Material	ρ	ρ	ρ	-	-
Decay Constant	α	α	-	-	-
Energy	e	e	-	-	-
Gurney Velocity	$\sqrt{2E}$	-	$\sqrt{2E}$	-	-
Ideal Gas Constant	γ	-	-	γ	-
Impulse Specific	I_{sp}	I_{sp}	I_{sp}	-	I_{sp}
Mass, Explosive	m	-	M	-	-
Mass, Flyer	m_f	-	-	m_f	m_f
Mass, Metal	c	-	C	-	-
Position	x	-	-	x	-
Pressure	P	P	-	P	-
Rebound Factor	R_f	-	-	-	R_f
Shock Impedance	Z	Z	-	-	-
Slope	s	s	-	-	-
Sound Speed	C_0	c_0	-	-	-
Thickness, Explosive	t_{HE}	-	t_{HE}	-	-
Thickness, Flyer	t_f	h_f	t_f	-	t_f
Time	t	t	-	t	-
Velocity Fraction	k	-	-	-	k
Velocity, Flyer	V_f	v_f	V	&	V_f
Velocity, Incoming	V_{in}	-	-	-	V_{in}
Velocity, Outbound	V_{out}	-	-	-	V_{out}
Velocity, Particle	u	u	-	-	-
Velocity, Shock	U	U	-	-	-
Volume, Trapped Air	Vol	-	-	Vol	-
Flyer Subscript	f	f	f	f	f
Target Subscript	T	T	T	T	T

4.1. Geometry and Basic Assumptions

The LIHE driven flyer problem can be physically defined, in the one-dimensional case, as a rigid target separated from a thin flyer plate by a relatively small air gap, with a layer of SASN explosive in intimate contact with the flyer. A simple schematic for this configuration is given in Figure 4.1 (a). As the explosive is initiated by the light array the flyer is driven towards the target compressing the entrapped air [Figure 4.1 (b)]. The flyer

impacts the target surface imparting a shock pulse into both target and flyer alike [Figure 4.1 (c)]. Finally, the flyer rebounds away from the target, returning the induced impact pressure at the target surface to zero [Figure 4.1 (d)].

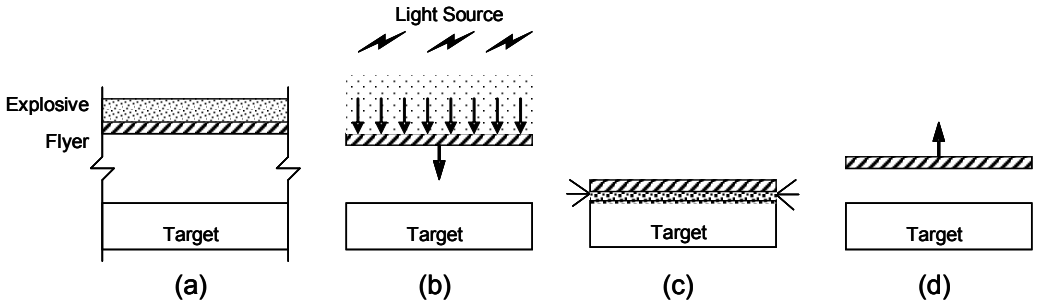

Figure 4.1: One-Dimensional Flyer Configuration

For initial analysis and derivation, the flyer is chosen to be a thin metallic sheet, infinite in two directions, and the trapped air between the flyer and target is initially assumed to be negligible. It is understood that this trapped air assumption is not correct, and additional analysis, found in Sections 4.5 and 4.6, will add an air cushion effect to the discussion. The SASN explosive is considered to be a uniform thickness and is assumed to detonate simultaneously over its surface. The explosive imparts a simultaneous driving pressure over the surface of the flyer which quickly drives the flyer to a terminal velocity prior to impact.

4.2. Hugoniot Analysis

When two materials collide in a planar fashion, Hugoniot analysis can be used to determine the impact conditions at the collision interface. Cooper [24] provides an excellent derivation and application of the Hugoniot relations, the details of which are not given here beyond the concepts directly applicable to this study.

Three Rankine-Hugoniot jump equations, based on the conservation of mass, momentum, and energy, are derived for the jump condition between un-shocked and

shocked material at a moving shock front. These relations utilize five basic parameters involved in describing a traveling shock condition: pressure (P), shock velocity (U), particle velocity (u), density (ρ), and specific internal energy (e). The subscripts 0 and 1 refer to the states just in front of and just behind the shock front, respectively. These jump relations provide the basis for shock behavior and interaction and are generally given in the following form:

Mass: $$\frac{\rho_1}{\rho_0} = \frac{U - u_0}{U - u_1} \tag{4.1}$$

Momentum: $$P_1 - P_0 = \rho_0 \cdot (u_1 - u_0) \cdot (U - u_0) \tag{4.2}$$

Energy: $$e_1 - e_0 = \frac{P_1 u_1 - P_0 u_0}{\rho_0 \cdot (U - u_0)} - \frac{1}{2}\left(u_1^2 - u_0^2\right) \tag{4.3}$$

4.2.1. Flyer/Target Impact

As two materials collide, the Hugoniot relations indicate material pressure as a function of the parameters: pressure (P), particle velocity (u), material density (ρ), sound speed (C_0) and slope of the shock velocity vs. particle velocity curve (s). The equation of state (EOS) parameters (density, sound speed, and slope of the U-u line) can usually be found in tabular form for many common materials. The subscripts f and T are used in this analysis to describe the various conditions in the flyer and target respectively.

Prior to impact, the flyer material is in an unshocked state at zero pressure ($P_{0f} = 0$), and moving towards the target at an initial velocity V_f. Because the entire flyer is assumed to be moving at the same initial velocity, the particle velocity of the flyer material is equal to the flyer velocity ($u_{0f} = V_f$). The target material is stationary with an initial particle velocity of zero ($u_{0T} = 0$) and is also in an unshocked state with a material pressure of zero ($P_{0T} = 0$). Utilizing the Pressure-Particle Velocity Hugoniot, the shock

pressure traveling into the target and flyer materials are calculated by equations (4.4) and 4.5) respectively:

Target: $$P_{1T} = \rho_{0T} \cdot C_{0T} \cdot u_1 + \rho_{0T} \cdot s_T \cdot u_1^2 \tag{4.4}$$

Flyer: $$P_{1f} = \rho_{0f} \cdot C_{0f} \cdot (u_{0f} - u_1) + \rho_{0f} \cdot s_f \cdot (u_{0f} - u_1)^2 \tag{4.5}$$

The impact pressure (P_1) and particle velocity (u_1) must be the same for both the flyer and target at the interface to preserve the conservation conditions. The impact pressure is found by equating the pressure equations (4.4) and (4.5), solving for particle velocity, (u_1), and inserting back into either of the pressure equations to yield the impact pressure for both flyer and target. Graphically, the interface pressure is the intersection of the flyer and target Hugoniot curves. The initial velocity of the flyer is represented on the Pressure vs. Particle Velocity plane by the point (u_{0f}, 0), and because the target is initially stationary, its initial "velocity" is represented by the origin (0, 0). Figure 4.2 shows the graphical Hugoniot intersection for an impact of an aluminum flyer ($V_f = u_{0f} =$ 20,000 cm/s) and a stationary PMMA target. In this example, the calculated interface pressure is 5.37 kbar, with a corresponding particle velocity for both materials of 16,320 cm/sec at the interface. Note that, at the velocities of interest to this study, the Hugoniot curves are nearly linear.

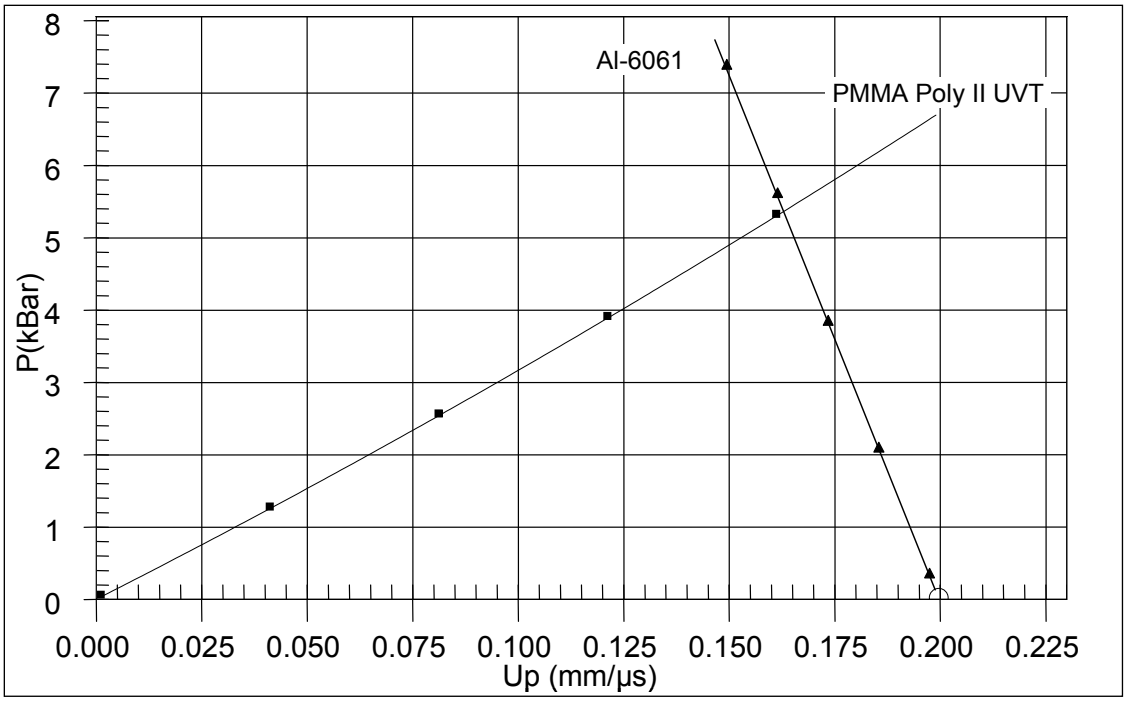

Figure 4.2: Al Flyer and PMMA Target Hugoniot at u_0 = 20,000 cm/s

4.2.2. Shock Impedance

The slope of the Hugoniot is a function of the material shock impedance, which can be approximated by the product of the material density and shock velocity, denoted

$$Z = \rho_0 \cdot U \approx \rho_0 \cdot C_0 \tag{4.6}$$

It is known that shock speed and material density increase with pressure, but can be approximated as being constant for weak shock calculations. In addition, the shock velocity, U, and material sound speed, C_0, are nearly equal for the relatively weak shock states encountered at the velocities of interest to this study.

Three flyer/target impedance mismatch conditions exist for the flyer problem, each of which having the effect of changing the pressure pulse duration and shape. In this ideal case analysis, no trapped air exists between the flyer and target. These three conditions are $Z_f > Z_T$, $Z_f = Z_T$, and $Z_f < Z_T$.

4.2.2.1 Flyer Impedance Greater than Target Impedance ($Z_f > Z_T$)

The condition where the shock impedance of the flyer is greater than the target is the more complicated of the three conditions. This impact scenario will result in the flyer remaining in contact with the target, with the pressure ringing down to zero as a function of the flyer thickness and impedance. At impact, a compressive shock wave travels into the target and back through the flyer. As the shock reaches the rear free surface of the flyer, it reverses direction and travels back towards the impact surface as a tensile stress. Because, in this scenario, the impedance of the target is less than that of the flyer, the tensile shock once again reverses sign and direction at the impact surface, resulting in a new, lower pressure, shock state in both the target and flyer materials. This process continues in both until the reverberating shock in the flyer is attenuated to zero or the original compressive shock in the target returns from a free surface as a tensile stress, separating the target from the flyer. Assuming a sufficiently thick target to avoid the latter situation, the pressure ring down at the surface is governed by the Hugoniot interactions at each stress state represented in Figure 4.3.

The idealized stepped pressure pulse shape is calculated using the pressure at each stress state, the flyer thickness, and shock velocity through the flyer. The transit time required for each shock state transit cycle through the flyer is found by the relation

$$t_{transit} = \frac{2 \cdot t_f}{U_f} \approx \frac{2 \cdot t_f}{C_{0f}} \tag{4.7}$$

where t_f is the thickness of the flyer. The ring down results in a stepped pressure profile, shown in Figure 4.4, which approximates an exponential pressure decay. In reality, nonlinearities in the material equations-of-state would smooth the abrupt steps in the pressure profile in this analysis [31].

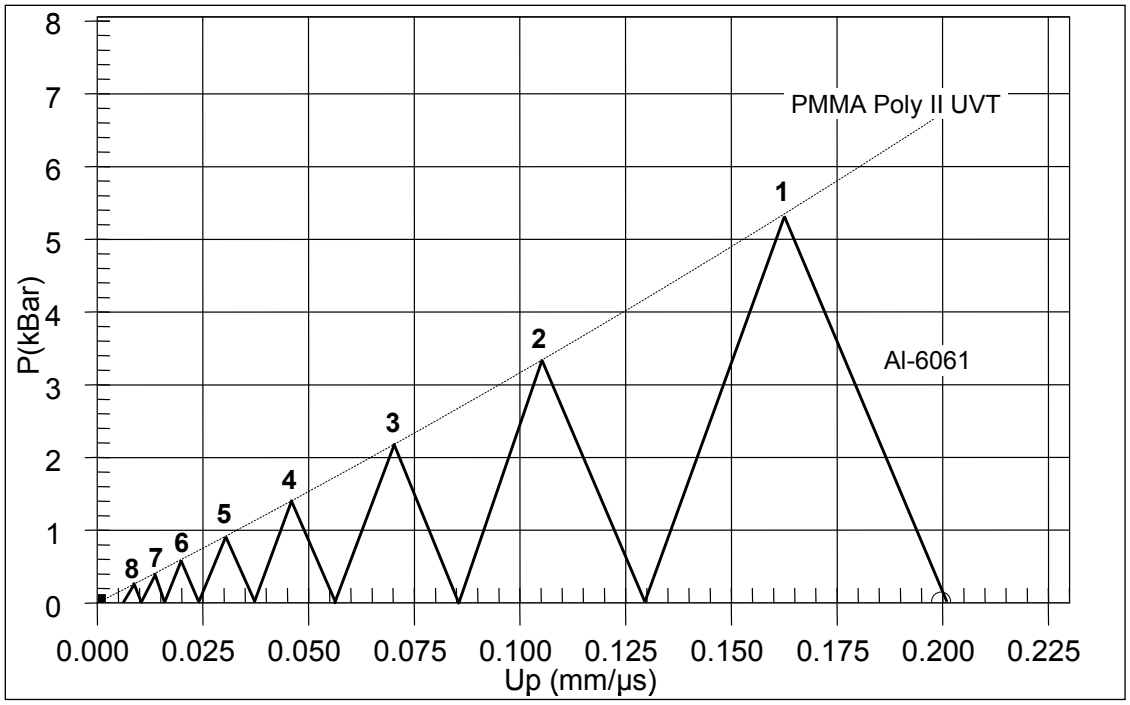

Figure 4.3: High Impedance Flyer Ring Down

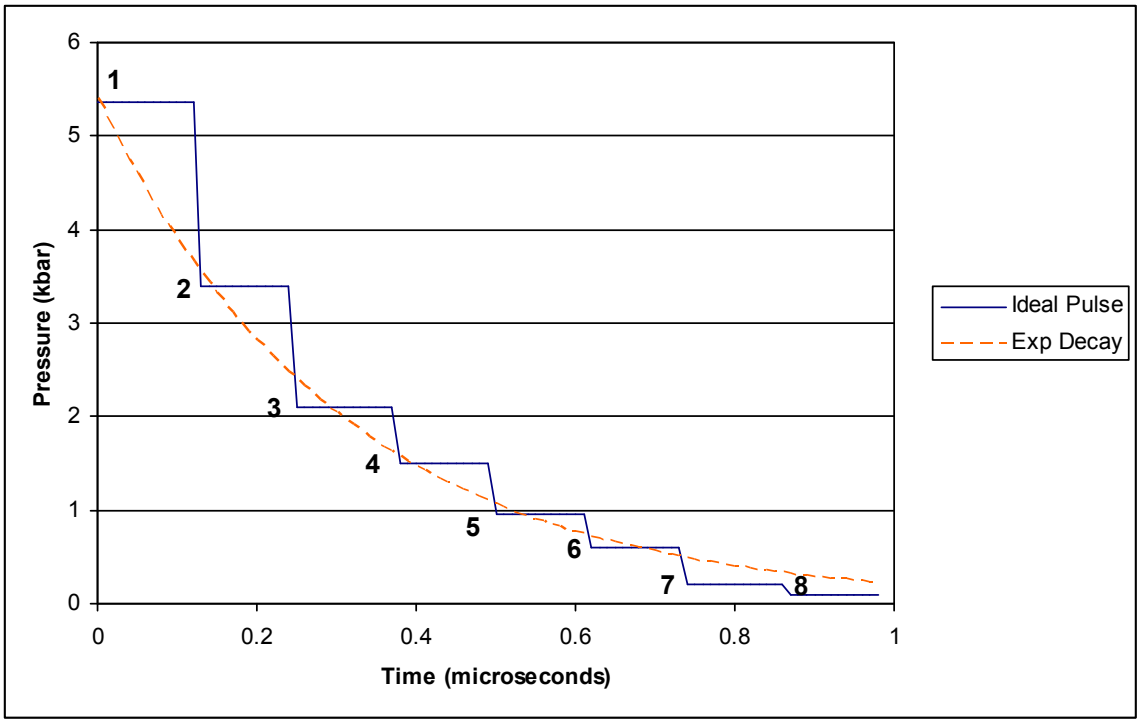

Figure 4.4: Idealized Pressure Pulse Shape for $Z_f > Z_T$

4.2.2.2 Flyer Impedance Equal to Target Impedance ($Z_f = Z_T$)

The situation where the impedance for the flyer and target are equal, the Hugoniot equations will indicate an impact pressure corresponding to a particle velocity ½ of the flyer velocity (u_0 = ½ V_f), when calculated by equations (4.4) or (4.5). The Pressure-Particle Velocity plot (Figure 4.5) shows the intersection of the symmetric Hugoniot curves for the identical flyer and target materials. For this scenario, there will be no pressure ring down because the flyer separates from the target after one shock transit cycle through the flyer due to the impedance match at the impact interface. The idealized pressure pulse will be a square wave, shown in Figure 4.6, of the initial impact amplitude, again calculated by equation (4.4) or (4.5), and a duration corresponding to one transit cycle of the shock wave through the flyer material using equation (4.7).

In the example shown in Figure 4.5, an aluminum flyer impacts an aluminum target with a flyer velocity of 20,000 cm/sec. The calculated Hugoniot impact pressure is 14.82 kbar, with a corresponding particle velocity of 10,000 cm/sec.

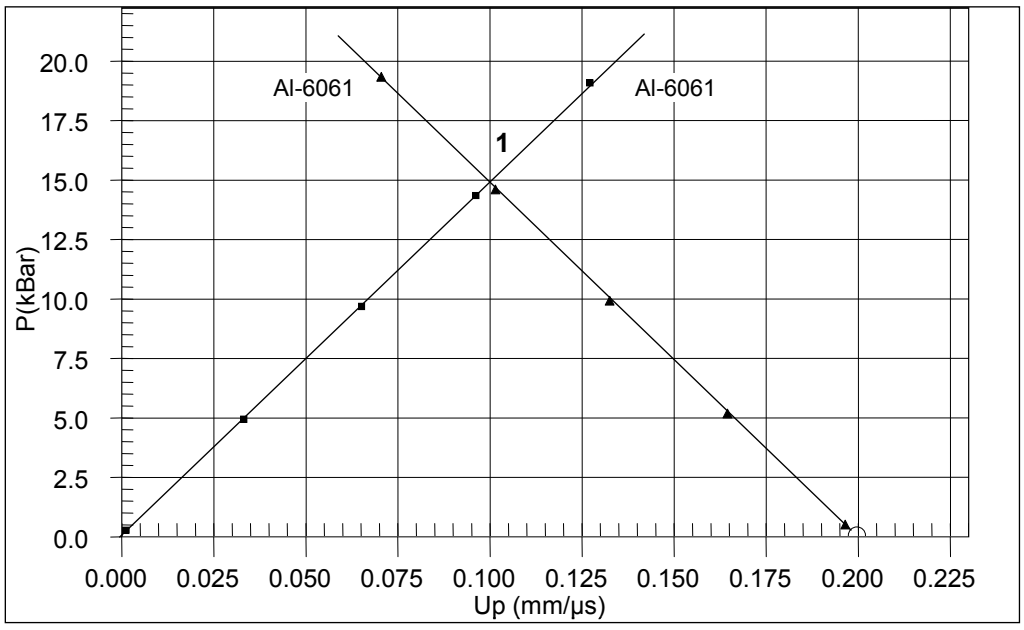

Figure 4.5: Al Flyer and Target Hugoniot Intersection at u_0 = 20,000 cm/s

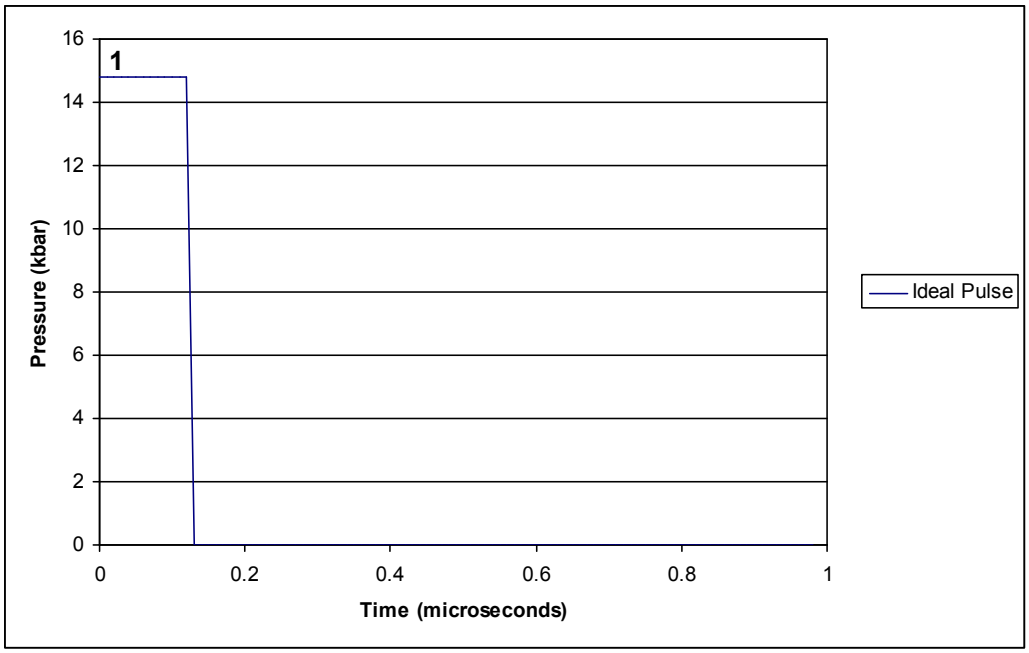

Figure 4.6: Idealized Pressure Pulse Shape for $Z_f = Z_T$

4.2.2.3 Flyer Impedance Less than Target Impedance ($Z_f < Z_T$)

Much like the situation where the flyer and target are of the same impedance, when the shock impedance of the target is greater than that of the flyer, only one shock transit cycle will take place in the flyer before separating from the target. The Hugoniot intersection for this situation generally results in a high peak pressure due to the increased slope of the target Hugoniot curve. The intersection on the P-U_p plane for this scenario is shown in Figure 4.7, where the interface particle velocity is shown to be lower than in the previous scenarios, with the impact pressure significantly higher.

In the example shown in Figure 4.7, an aluminum flyer traveling at 20,000 cm/sec impacts a 304 stainless steel target. The result is an impact pressure of 21.29 kbar with a corresponding particle velocity of 5,780 cm/sec.

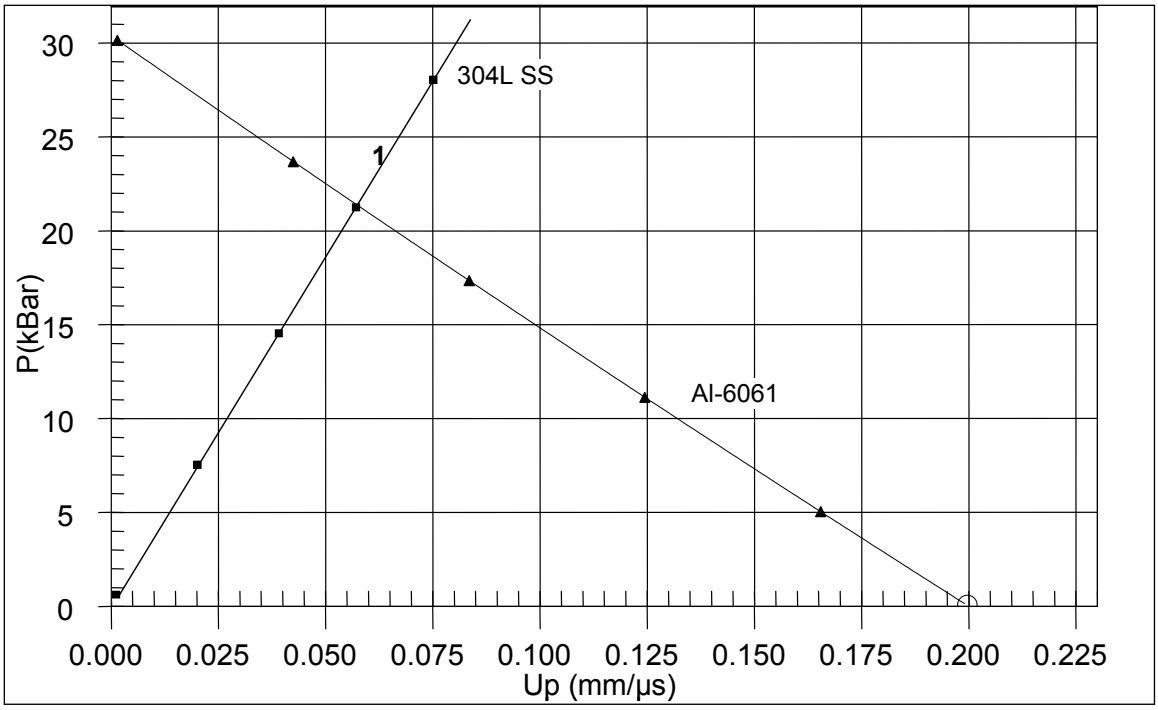

Figure 4.7: Al Flyer and 304 SS Target Hugoniot Intersection at u_0 = 20,000 cm/s

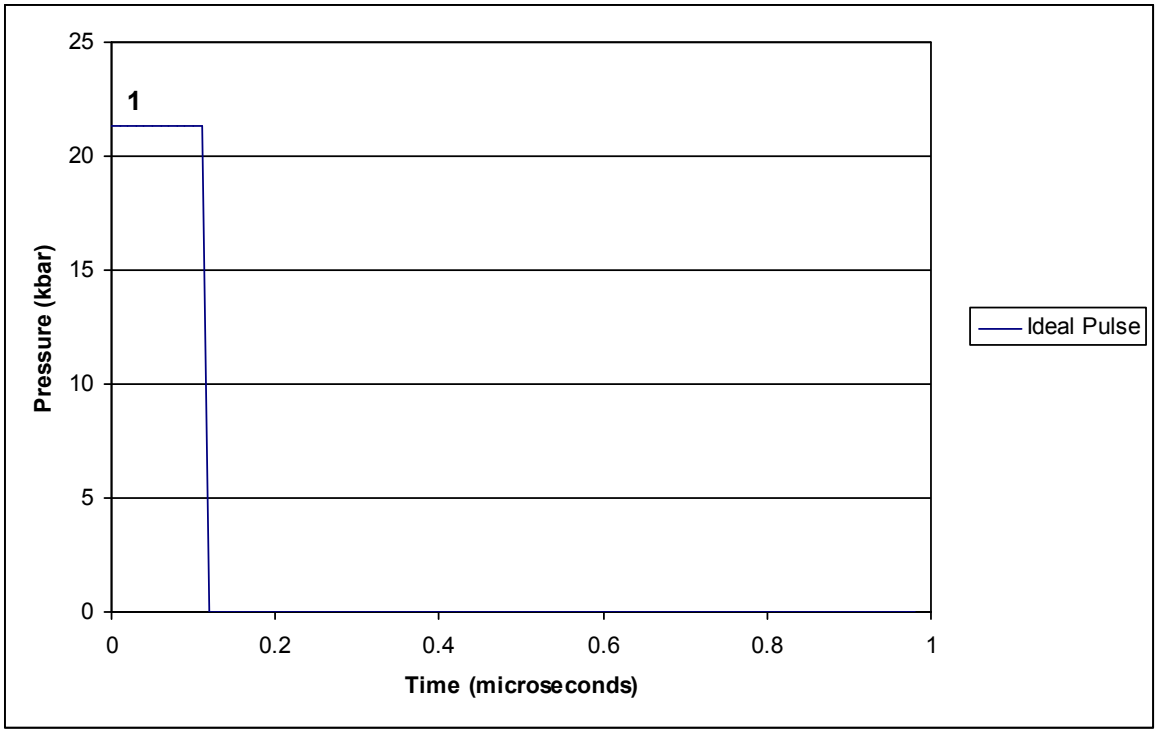

Figure 4.8: Idealized Pressure Pulse Shape for $Z_f < Z_T$

In comparing the three examples given, it can be seen that with a constant flyer velocity and material, pressure increases as the target impedance increases. In these examples, the pressure varies from 5.37 kbar for a soft PMMA target to 21.29 kbar for a relatively harder 304 stainless steel target.

4.3. Flyer Plate Design

A flyer experiment can be designed to create a desired pressure pulse by working with multiple variables, including flyer thickness, flyer material, and impact velocity. The starting point to designing a flyer impact experiment begins with a desired or specified pressure pulse. A common simulation of cold x-ray deposition is an exponentially decreasing pressure pulse of the form

$$P(t) = P_{\max} e^{-\alpha \cdot t} \tag{4.8}$$

where P_{max} is the peak pressure amplitude, α controls the rate of exponential decay, and t is time. The shape of this pulse is similar to a triangle pressure pulse that one might encounter with a direct exposure to an explosive detonation, though it is extremely difficult to match all of the impulse and pressure requirements with direct application of explosive. Because the pulse shape is exponentially decreasing, a higher shock impedance flyer material to target material is often desirable to achieve the ring down pressure pulse.

A method for determining the impact velocity necessary to induce a peak pressure is to utilize the impedances of the flyer and target materials. The required idealized (no trapped air) flyer impact velocity is found using the relationship of material impedances and desired pressure

$$V_f = P_{\max} \left[\frac{Z_f + Z_T}{Z_f \cdot Z_T} \right] \tag{4.9}$$

With the flyer velocity to induce the desired peak pressure now known, the flyer thickness can be determined. It can be shown using the definitions of specific impulse that flyer properties are related to the desired pressure function by

$$I_{sp} = \Delta(mV) = \rho_f \cdot t_f \cdot V_f = \int_0^\infty P(t)dt \tag{4.10}$$

where t_f is the thickness of the flyer. Equation (4.10) can be solved for flyer thickness yielding the relationship

$$t_f = \frac{1}{\rho_f \cdot V_f} \cdot \int_0^\infty P(t)dt \tag{4.11}$$

For the example common pressure pulse given in equation (4.8), equation (4.11) becomes

$$t_f = \frac{P_{\max}}{\rho_f \cdot V_f} \cdot \int_0^\infty e^{-\alpha \cdot t} dt \tag{4.12}$$

Assuming that the exponential decay variable α is a constant, equation (4.12) reduces to

$$t_f = \frac{P_{\max}}{\rho_f \cdot V_f} \cdot \left(\frac{1}{\alpha}\right) \tag{4.13}$$

To calculate the idealized stepped pressure pulse shape, an iterative process is required to determine the Hugoniot ring down pressures, discussed in Section 4.2.2. The cycle transit time of the shock wave through the flyer thickness is approximated by equation (4.7). The pressure pulse shape can then be compared to that of the desired pressure pulse using the analysis also developed in Section 4.2.2.

4.4. Gurney Flyer Analysis

The work of R.W. Gurney [24, 49] has been used extensively to predict the terminal velocity of explosively driven metal. This theory is readily applied to multiple standard explosive charge configurations, such as cylindrical or spherical explosive/metal

assemblies, which use well characterized explosive types. But non-standard applications of the theory require additional work for proper implementation.

Gurney developed analytical relationships between the final driven metal velocity, the explosive energy, and the ratio of the mass of the driven metal to that of the explosive charge for multiple geometries. It is desired to use the Gurney relations as a function of flyer thickness, flyer density, and SASN areal density (explosive deposition) to predict the driven velocity of the flyer plate. The present discussion will use the Gurney model to develop the basis for the SASN driven flyer experimental design and analysis.

4.4.1. Gurney Assumptions

The following assumptions are made regarding the derivation of the Gurney velocity coefficient, $\sqrt{2E}$, as a function of flyer thickness, t_f, flyer density, ρ_f, and explosive areal density, ρ_A, for SASN explosive:

1. An unsymmetrical sandwich configuration, or more commonly "open-face sandwich" configuration, shown in Figure 4.9, is assumed for this problem. This configuration is characterized by an explosive charge in intimate contact with a metallic flyer plate with no tamping of the explosive layer.

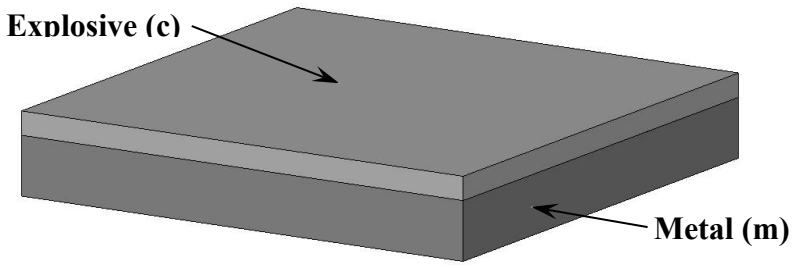

Figure 4.9: Open Face Sandwich Configuration

2. To determine the Gurney velocity coefficient specific to silver acetylide-silver nitrate, a metal mass orders of magnitude greater than the explosive mass will be

assumed. This assumption takes into account the physical configuration of the SBPA used to calibrate the explosive, where a thin explosive layer accelerates a large stainless steel pendulum mass.

3. To determine the predicted thin metal flyer velocity, the flyer mass and explosive mass are of approximately the same order of magnitude.

4. A unit area is assumed.

4.4.2. Gurney Velocity Coefficient

Gurney shows that for an "open-face sandwich," the equation to determine flyer velocity, V_f, is

$$\frac{V_f}{\sqrt{2E}} = \left[\frac{\left(1 + 2\frac{m}{c}\right)^3 + 1}{6 \cdot \left(1 + \frac{m}{c}\right)} + \frac{m}{c} \right]^{-1/2} \tag{4.14}$$

where $\sqrt{2E}$ is the Gurney velocity coefficient, m is the unit mass of the metal, and c is the unit mass of the explosive charge. Typically, the Gurney velocity coefficient is a function of explosive type and density, and is often available in table form in explosive publications [24]. Because SASN is not a common explosive type, nor is it typically used to drive metal, a published Gurney velocity is not available. Instead, a Gurney velocity relationship specific to sprayed SASN is developed.

The assumption that the flyer mass is much greater than the explosive mass is required to develop the approximation for $\sqrt{2E}$ in terms of explosive deposition (areal density). This assumption approximates the actual calibration process for the SASN explosive, where small Kovar® coupons are sprayed with explosive and fired on a heavy ballistic pendulum. The mass of the pendulum is many orders of magnitude greater than the mass of explosive. The very thin layer of SASN deposited on the coupon drives the massive metal pendulum mass to an initial velocity. After multiple coupons are fired on

the SBPA, a calibration curve that plots the impulse delivered as a function of the areal density of the explosive is statistically generated. A detailed description of the calibration process is given in Chapter 5.

Given the explosive/pendulum mass difference assumption, equation (4.14) reduces through a series of steps to the approximation

$$V_f = \sqrt{2E} \cdot \left(\frac{3}{4}\right)^{1/2} \cdot \frac{c}{m} \tag{4.15}$$

Additionally, it is known that the product of specific impulse and area ($I_{sp} \cdot A$) equates to the change in momentum of the pendulum mass (ΔmV). Because the initial velocity of the pendulum mass is zero, this relation is reduced to the mass of the pendulum times the final velocity of the pendulum. The resulting relationship between specific impulse and velocity becomes

$$I_{sp} \cdot A = m \cdot V_f \tag{4.16}$$

Rearranging equation (4.16), the relationship of metal mass to impulse, area, and flyer velocity is

$$m = \frac{I_{sp} \cdot A}{V_f} \tag{4.17}$$

The mass of the explosive (c) relates to the areal density of the explosive (ρ_A) by

$$c = \rho_{HE} \cdot t_{HE} \cdot A = \rho_A \cdot A \tag{4.18}$$

where ρ_{HE} is the explosive density, and t_{HE} is the explosive thickness. Inserting equations (4.17) and (4.18) into (4.15), the relationship for flyer velocity becomes

$$V_f = \sqrt{2E} \cdot \left(\frac{3}{4}\right)^{1/2} \cdot \frac{I_{sp} \cdot A}{V_f \cdot \rho_A \cdot A} \tag{4.19}$$

Rearranging and simplifying, the resulting relation for the Gurney velocity coefficient becomes

$$\sqrt{2E} = \frac{I_{sp}}{\rho_A} \cdot \sqrt{\frac{4}{3}} \tag{4.20}$$

which is independent of flyer velocity, flyer mass, as well as pendulum mass. The explosive calibration curve, developed in Chapter 5, will yield a relation between specific impulse and areal density, to be used in equation (4.20).

4.4.3. Thin Metallic Flyer Velocity

Inserting equation (4.20) into equation (4.14), the flyer velocity as a function of specific impulse, areal density, and metal mass/explosive mass ratio is found as

$$V_f = \left[\frac{I_{sp}}{\rho_A} \cdot \sqrt{\frac{4}{3}}\right] \cdot \left[\frac{\left(1 + 2\frac{m}{c}\right)^3 + 1}{6 \cdot \left(1 + \frac{m}{c}\right)} + \frac{m}{c}\right]^{-1/2} \tag{4.21}$$

It is known that the mass of the flyer is

$$m = \rho_f \cdot t_f \cdot A \tag{4.22}$$

Again, where ρ_f is the flyer density, t_f is the flyer thickness and A is the flyer area. Combining equation (4.22) with equation (4.18), the mass ratio m/c becomes

$$\frac{m}{c} = \frac{\rho_f \cdot t_f}{\rho_A} \tag{4.23}$$

Using equations (4.21) and (4.23), the flyer velocity is found to be

$$V_f = \left[\frac{I_{sp}}{\rho_A} \cdot \sqrt{\frac{4}{3}}\right] \cdot \left[\frac{\left(1 + 2\frac{\rho_f \cdot t_f}{\rho_A}\right)^3 + 1}{6 \cdot \left(1 + \frac{\rho_f \cdot t_f}{\rho_A}\right)} + \frac{\rho_f \cdot t_f}{\rho_A}\right]^{-1/2} \tag{4.24}$$

This is the velocity to which the flyer will be accelerated by the explosive for a given flyer material, flyer thickness, explosive areal density, and impulse delivered to the flyer

by the explosive layer. It will be seen in Chapter 5 that a two-part equation will result that quantifies the specific impulse as a function of the deposition of the SASN explosive.

4.5. The Air Cushion Effect

The expression derived in equation (4.24) predicts the driven velocity of the flyer for a given set of parameters. Unless the flyer plate experiments are carried out in a vacuum, air will be trapped between the flyer and the target, decelerating the flyer and decreasing the impact velocity. The presence of the trapped air layer will impede the flyer's movement and modify the "ideal" impact conditions by applying a pressure increase to both flyer and target by air compression prior to impact. The entrapped air will essentially reduce the peak pressure, round off the pulse shape, and increase the pulse width. In the purely one-dimensional sense, the trapped layer of air would not allow the flyer to impact the target surface at all. Instead, the air would be compressed to a very high pressure with minimal thickness, keeping the flyer at some final distance away from the target. In reality, the flyer and target are not precisely planar, and some flyer to target interaction is inevitable.

To estimate the effect of trapped air on the impact pressure of the flyer onto the target a simplified model, shown in Figure 4.10, can be used [5]. If the flyer is assumed to be a frictionless piston, the trapped air, being compressible and ideal, undergoes an isentropic compression. It is assumed that the target is massive and does not move in the time frames being investigated (x_2 is constant).

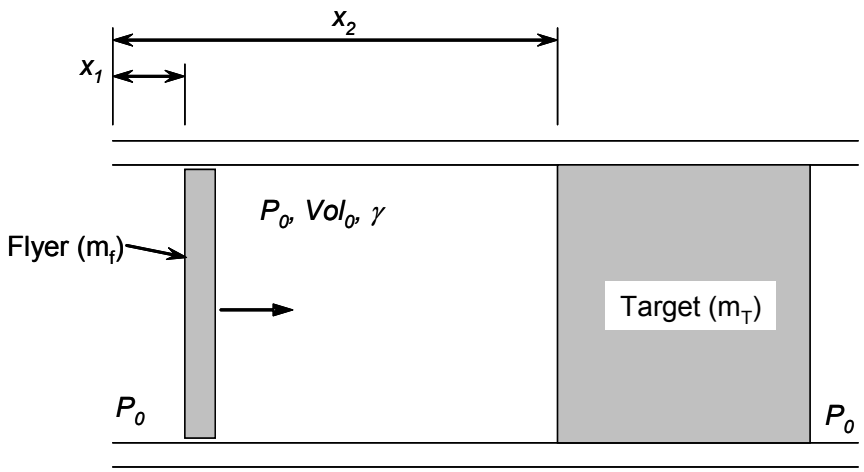

Figure 4.10: Simplified Model for Flyer Impact Including Entrapped Air

If the analysis is started with the ideal gas law,

$$P \cdot Vol^{\gamma} = P_0 \cdot Vol_0^{\gamma} \tag{4.25}$$

it can be shown that the pressure between the flyer and the target is a function of the initial pressure and the relative positions of the flyer and target, i.e.,

$$P = P_0 \cdot \left[\frac{x_2}{x_2 - x_1} \right]^{\gamma} \tag{4.26}$$

Applying Newton's second law of motion ($F = ma$), it can be shown that the motion of the flyer plate, x_1, is described by the differential equation

$$\ddot{x}_1 = \frac{P_0 \cdot A}{m_f} \cdot \left[1 + \left(\frac{x_2}{x_2 - x_1} \right)^{\gamma} \right] \tag{4.27}$$

where initial pressure (P_0), area (A), flyer mass (m_f), stationary target position (x_2), and the ratio of heat capacities for an ideal gas ($\gamma = 1.67$) are known quantities. Equation (4.27) is most easily solved by numerically integrating to determine the flyer velocity and position as a function of time. Additionally, the pressure between the flyer and the target, as a function of position, x_1, is also found using equation (4.26).

Because numerical analysis to quantify the effect of trapped air between the flyer and target is required, this study will utilize the one-dimensional hydrocode KOWIN [23] to predict the flyer motion and induced pressure into the target. This code effectively replaces the analytical approach discussed in this section, by taking into account the gas compression mechanics as well as shock physics of the flyer impact on the target. KOWIN is used extensively in this study to estimate the rebound factor (see Section 4.6) for the various sets of flyer parameters. While KOWIN has the ability to simulate explosively driven flyers, its material libraries do not include the silver acetylide-silver nitrate explosive. As a result, the simulations will require an assumption of initial flyer velocity, which is similar to the approach required by the piston analysis discussed above.

4.6. The Effect of Flyer Rebound on Delivered Impulse

The previous discussion regarding trapped air between the flyer and target demonstrates that a layer of air will be compressed to a high pressure and minimal volume as the flyer travels towards the target. Once the flyer's energy has been transferred to the air in the compression process, a reverse reaction will take place. The high pressure air will act like a compressed spring and push the flyer away from the target surface. Without the presence of air, rebound would occur when the impedance of the flyer is higher than that of the target, as discussed in section 4.2.2 The rebound motion of the flyer will achieve a final outbound velocity that is some fraction of the original incoming velocity due to energy losses in the system such as heat transfer or deformation of flyer and target materials.

The impulse delivered to a target is a direct function of the change in momentum of the flyer. It can be shown that the impulse delivered to the target is a function of the change in velocity of the flyer using the basic definition of total impulse,

$$\left(I_{sp}A\right)_T = \Delta\left(mV\right)_f = m_f\left(V_0 - V_1\right)_f \tag{4.28}$$

Assigning the incoming velocity to V_0 and the outgoing velocity, in the negative direction, to V_1 , equation (4.28) is rewritten as

$$\left(I_{sp}A\right)_T = \Delta\left(mV\right)_f = m_f\left(V_{in} + V_{out}\right)_f \tag{4.29}$$

As said above, the outgoing velocity will be some fraction of the incoming velocity. Assigning the variable *k* to that fraction, equation (4.29) becomes

$$\left(I_{sp}A\right)_T = \Delta\left(mV\right)_f = m_f\left(V_{in} + k \cdot V_{in}\right) \tag{4.30}$$

Collecting terms:

$$\left(I_{sp}A\right)_T = \Delta\left(mV\right)_f = m_f \cdot V_{in}\left(1 + k\right) \tag{4.31}$$

Here, a rebound factor R_f is defined as

$$R_f = \left(1 + k\right) \tag{4.32}$$

Substituting equation (4.32) into (4.31), the equation is simplified to

$$\left(I_{sp}A\right)_T = m_f V_{in} R_f \tag{4.33}$$

Again, from equation (4.22), the mass of the flyer known as

$$m = \rho_f \cdot t_f \cdot A \tag{4.34}$$

Inserting equation (4.34) into (4.33), and realizing that the incoming velocity is the same as the flyer velocity ($V_{in} = V_f$), the specific impulse delivered to the target is given as a function of flyer density, flyer thickness, incoming flyer velocity and rebound factor,

$$I_{sp} = \rho_f \cdot t_f \cdot V_f \cdot R_f \tag{4.35}$$

As discussed in the previous section, the hydrocode KOWIN is used to predict an outgoing flyer velocity, and thus the rebound factor, for a given set of flyer parameters. The rebound factor for the analysis of the experimental results would ideally be

calculated from measured incoming and outgoing flyer velocities. Unfortunately, these measurements are difficult to make under the engineering conditions presented by an explosively driven flyer. Due to this difficulty, KOWIN is used for both prediction and verification purposes.

4.7. Formulation of an Engineering Design Model

The assembly of the presented analyses in this chapter are necessary for the formulation of an analytical model to be used in the engineering design of a flyer experiment. In general, eight steps are necessary to design an experiment, assuming that a desired impulse and pressure pulse are given:

1. Impact Condition Analysis: The first step is to analyze the required pressure pulse and impact conditions. Peak pressure and pulse shape are of special interest at this time. Can the desired pressure pulse shape be achieved? Is the peak pressure achievable? Use of the analysis in Section 4.2 is beneficial in the determination of the impedance matching to achieve the desired pulse. This is the point where the first approximation of flyer material is chosen based on the pulse shape and physical test constraints.

2. Flyer Velocity: Based on the material impedances, the approximate required flyer velocity is determined using the analysis and results from Section 4.3

$$V_f = P_{\max}\left[\frac{Z_f + Z_T}{Z_f \cdot Z_T}\right] \tag{4.36}$$

3. Flyer Thickness: The next step is to "design" the flyer plate thickness to match the pressure pulse requirements as discussed in Section 4.3. Here, the flyer thickness is defined by the calculated flyer velocity, assumed flyer material density, and the integral of the desired pressure as a function of time

$$t_f = \frac{1}{\rho_f \cdot V_f} \cdot \int_0^{\infty} P(t)dt \tag{4.37}$$

4. Explosive Deposition: The use of the Gurney analysis in Section 4.4 to determine the required explosive deposition to achieve the required flyer velocity for the flyer thickness and material density using the basic equation

$$V_f = \left[\frac{I_{sp}}{\rho_A} \cdot \sqrt{\frac{4}{3}}\right] \cdot \left[\frac{\left(1 + 2\frac{\rho_f \cdot t_f}{\rho_A}\right)^3 + 1}{6 \cdot \left(1 + \frac{\rho_f \cdot t_f}{\rho_A}\right)} + \frac{\rho_f \cdot t_f}{\rho_A}\right]^{-1/2} \tag{4.38}$$

5. Air Gap: An offset air gap between the flyer and target must be chosen. Due to the air cushion effect, it is generally desired to minimize this gap within the constraints of allowing the flyer to accelerate to terminal velocity and physical testing requirements, such as handling.

6. Determine the Flyer Rebound: The next step is to determine the approximate effect of the flyer rebound from the target surface. As discussed, the rebound directly affects the pulse shape and delivered impulse. Numerical analysis, and preferably hydrocode analysis, is required for this step.

7. Calculate Delivered Impulse: With the flyer material, thickness, velocity, and rebound all calculated, the delivered impulse is determined via the discussion from Section 4.6. The specific impulse is determined by the relation

$$I_{sp} = \rho_f \cdot t_f \cdot V_f \cdot R_f \tag{4.39}$$

8. Comparison and Iteration: At this point, the flyer material and thickness has been chosen, the impact velocity and required explosive deposition determined, an air gap between flyer and target chosen, a rebound factor calculated, and the specific impulse determined. All of these combine to predict an impact pressure, pulse shape, and

delivered impulse, which must be compared to the desired input loading. If there are differences between what is predicted and what is required, iteration is necessary. If a recalculation is required, the work done to this point is useful as a starting point for the input to Step 1.

The explosively driven flyer impulse test design is further complicated when a two-dimensional impulse profile is required. In the case where a cosine distributed impulse loading on a cylindrical surface is called for, the flyer velocity and gap will be varied to achieve the proper loading at each location around the circumference. This situation will also require a varying explosive deposition on the flyer surface. This loading situation requires a fair amount of iteration in order to finalize a test design.

5. EXPLOSIVE CHARACTERIZATION

As observed in the derivation of the Gurney equations for driving a thin flyer, a keen understanding of the explosive performance is required. Specifically, the ratio of specific impulse (I_{sp}) to areal density (ρ_A) is integral to the implementation of the Gurney solution presented in the previous chapter, as well as the LIHE process in general.

5.1. Silver Acetylide-Silver Nitrate Characteristics

Silver acetylide-silver nitrate (SASN) is a primary explosive formulated specially for the purposes of the Light Initiated High Explosive facility. This explosive is extremely sensitive and cannot be transported to or from the facility, and must be formulated on site. As the moniker "light initiated" suggests, the SASN is capable of being initiated by an extremely bright flash of light, as well as other traditional methods of initiation such as friction or impact. Due to the extremely sensitive nature of this explosive, nearly all explosive operations require remote handling and special procedures for safe conduct.

The explosive is white in color when spray deposited on a surface, which turns to a burnt cream color when exposed to ultraviolet light. The solid density of the SASN compound is 5.34 g/cm^3, with a detonation velocity of 445,000 cm/sec (175,197 in/sec) [14]. But in actuality, the sprayed explosive is somewhat "fluffy" in nature, resulting in a density that is significantly lower than solid (with a decreased detonation velocity). For the sprayed product, the approximate mass density is 0.6 g/cm^3 with the reported sweeping detonation velocity between 60,000 cm/s (23,622 in/sec) 1 and 120,000 cm/s (47,244 in/sec) [14]. It is believed that the actual detonation velocity is closer to the latter. In general, the explosive output of the sprayed SASN is considered to be 20% of explosive output of TNT.

5.2. Explosive Initiation

Throughout this investigation, the SASN explosive is described as "light initiated", due to the light array method in which the detonation is started. In reality, the initiation process is likely thermal in nature and not photo-chemical. Thermal energy is transferred from the electrical arc created by the discharging capacitor bank at the light array to the explosive surface. The thermal initiation temperature of the explosive is ~235ºC, which is easily achieved with a properly functioning light array. The explosive area is bathed with thermal energy from the light array, causing a nearly simultaneous detonation over the entire sprayed surface. As will be seen in the two-dimensional results in Chapter 10, a malfunctioning array can, and will, directly affect the initiation of the explosive and the performance of the LIHE driven flyer.

Experiments have shown that when the SASN explosive is initiated on a surface by the light array technique, a random pattern of detonation points is apparent on the spray/detonation surface. The density of the detonation points is greatly enhanced by the sun-tanning process discussed in Section 3.6. Typically, the detonation will expand away from the detonation point in a hemispherical manner through the thickness of the explosive. For surfaces that are not sun-tanned and have relatively few detonation points per square centimeter, it is evident that a sweeping detonation wave originates at each detonation point and runs along the surface until colliding with detonation waves from adjacent initiation points. It is desired to have a high detonation point density to decrease the sweeping detonation distance, and thus decrease the time required to explosively load the surface. In short, as the initiation point density is increased, a better loading simultaneity is achieved.

5.3. Explosive Calibration to Determine I_{sp} as a Function of ρ_A

To determine the impulse to areal density relationship for the current formulation of the SASN explosive, a calibration test series has been undertaken. While the performance characteristics of the SASN have been reported in the past [9, 10, 14], and the process to formulate the explosive has been kept as constant as possible, it is understood that today's chemicals, equipment, and personnel may combine to produce a difference in the formulation. The purpose of this calibration series has been to either confirm a consistent explosive calibration curve, or create a new curve corresponding to the modern processes and constituents.

5.3.1. Calibration Spray Operations

To accomplish the explosive calibration for this investigation, three formulation and spray activities were conducted. Each of these tests involved formulating a 275 gram batch of explosive, using chemical constituents currently available. This explosive product was sprayed on a target consisting of two non-overlapping horizontal rows of 1.905 cm (0.75") diameter Kovar® coupons (see Figure 3.6). To vary the level of explosive deposition (areal density) for the calibration, several coupons were removed from the target after a specified number of spray passes, resulting in a range of areal densities for further explosive testing.

The calculation of areal density requires the measurement of the weight of explosive deposited over a known area. Each coupon was weighed during the spray process (on spray day) to determine if the weight of explosive deposition was adequate for further investigation. If not, the coupon was returned to the spray target surface for additional spray passes. After the spray process was complete, each coupon was conditioned in the spray booth overnight to assure that all of the acetone carrier had

evaporated from the spray surface and only SASN explosive remained. The overnight conditioning required that the coupons remain at a nominal 26.7ºC (80ºF), and ~20% relative humidity. This overnight "drying" is an established process for conditioning the explosive for an explosive test. After conditioning, the coupons were reweighed to determine their "dry" weight, then were removed from the spray booth and taken to the location of the small bank light array for testing.

5.3.2. Small Bank Pendulum Apparatus (SBPA)

The SBPA, consisting of a single degree-of-freedom ballistic pendulum assembly, a 10kV-300J capacitor bank, a small two-wire light array, and an eddy current displacement gage, is shown in Figure 5.1. The pendulum mass is positioned in front of the light array allowing for a 2.5 cm (1.0") spacing between the explosive surface of the coupon, magnetically held to the pendulum, and the light source. The non-contact eddy current displacement gage measures the movement of the pendulum mass, with a 0.0025 cm (0.001") resolution, and is recorded on a digital oscilloscope for conversion to impulse.

To detonate the explosive deposited on the coupon, the capacitor bank is discharged through the two 0.0051cm (0.002") diameter tungsten wires, enclosed in quartz tubing, of the small bank light array. The rapid absorption of energy into the explosive layer from the light array causes a nearly simultaneous detonation over the explosively covered surface of the coupon. The explosive detonation drives the pendulum mass to an initial velocity proportional to the explosive deposition on the coupon. The resulting motion of the simple pendulum is sinusoidal, and decays with time. A typical pendulum displacement trace is shown in Figure 5.2. The period of the pendulum is independent of explosive charge and is fixed by the length of cable supporting the

pendulum mass. Figure 5.2 is annotated with the labels 1, 2, and 3, which correspond to the three displacement peaks that are used to determine the initial velocity of the pendulum and impulse delivered from the explosive.

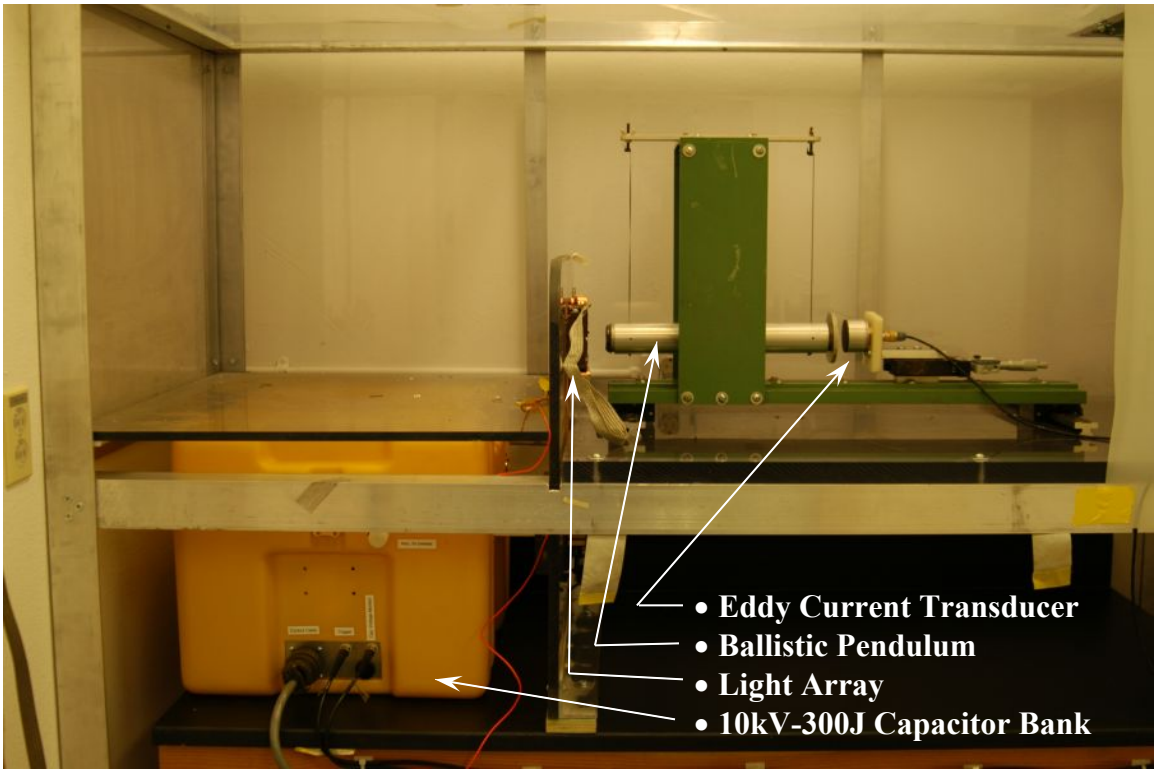

Figure 5.1: Small Bank Pendulum Apparatus

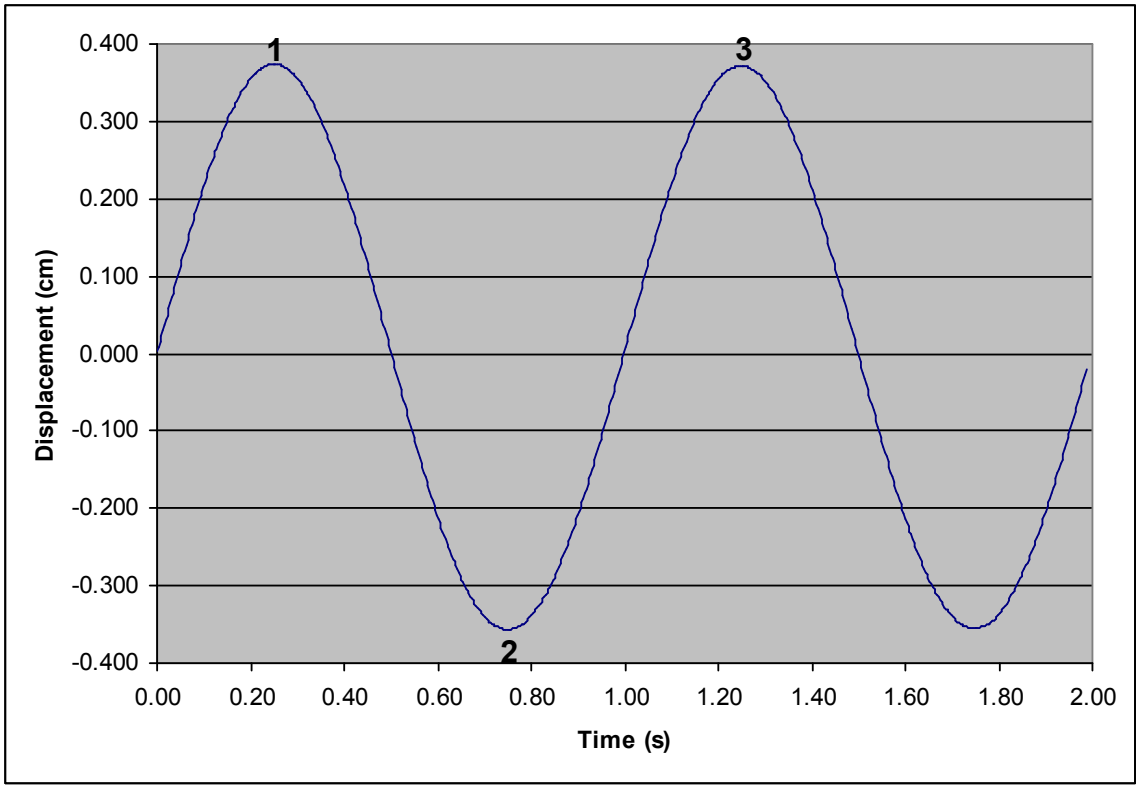

Figure 5.2: Pendulum Mass Displacement

In order to determine the impulse delivered by the explosive areal density for each coupon, it was required to determine the initial velocity (V_0) of the pendulum mass. A quick and straightforward method for determining V_0 is to calculate the initial slope of the displacement vs. time history of the pendulum mass. This calculation is simply the ratio of the change in displacement over the change in time

$$V_0 = \frac{\Delta x}{\Delta t} \tag{5.1}$$

It is understood that a finite mass cannot instantaneously accelerate from standstill to a finite velocity. Thus, care is taken to determine V_0 after a very short (~0.005 sec) acceleration phase.

With the initial velocity calculated, the specific impulse is calculated by

$$I_{sp} = \frac{m_p \cdot V_0}{A_{coupon}} \tag{5.2}$$

where I_{sp} is the specific impulse in taps (dyn · sec/cm^2), m_p is the mass of the pendulum, V_0 is the initial velocity, and A_{coupon} is the area of the coupon. Due to the very small times and distances encountered in this calculation, it is prone to relatively large round off error, and is generally used as a first look and check of the a more robust impulse calculation presented below.

A second, and generally more reliable, method for determining pendulum initial velocity is also used. This method assumes that the damped motion of the pendulum follows the simple pendulum equation

$$x = X \cdot e^{-\alpha \cdot t} \cdot \sin(\omega \cdot t) \tag{5.3}$$

Here, x is the horizontal displacement of the mass as a function of time, X is the un-damped sinusoidal amplitude, α is the exponential decay rate, ω the pendulum frequency, and t is time. By measuring two peaks (time and amplitude) of the sinusoidal motion of the pendulum, denoted 1 and 2 in Figure 5.2, the decay rate and frequency of the pendulum are found using the equations

$$\alpha = \ln\left[\frac{x_1}{-x_2}\right] \cdot \frac{1}{t_2 - t_1} \tag{5.4}$$

and

$$\omega = \frac{\pi}{t_2 - t_1} \tag{5.5}$$

where x_1 and x_2 are absolute values of the amplitude of peaks, corresponding to the times t_1 and t_2 respectively. Three values of un-damped amplitude are generally calculated

corresponding to displacement peaks 1, 2, and 3, then averaged. Assigning the index notation i = 1 to 3, and rearranging equation 5.3 to solve for un-damped amplitude,

$$X_i = \frac{x_i}{e^{-\alpha t_i} \cdot \sin(\omega \cdot t_i)} \tag{5.6}$$

The initial velocity of the pendulum mass is then calculated by

$$V_0 = \frac{\sum_1^3 X_i}{3} \cdot \omega \tag{5.7}$$

Impulse is calculated by equation (5.2) using the initial velocity calculated with equation (5.7). While this method to determine initial velocity is believed to be more accurate than the initial slope method [equation (5.1)], error may be introduced into the analysis due to the possibility of late time forces, such as a blast reflection, affecting the movement of the pendulum. For this reason, special care is taken to observe any deviation from the ideal sinusoidal motion, which may invalidate the displacement data.

5.3.3. Explosive Calibration Operations

Three formulation/spray activities were completed for the calibration, resulting in coupon areal densities between 10.6 and 41.4 mg/cm^2. A total of 60 coupons were tested on the SBPA (over the three sprays). The specific impulse versus areal density data from these tests are shown in Figure 5.3. The dotted lines represent error bounds from a measurement error analysis of the coupon weighing and firing process [9]. It is known from the previous facility calibration that the explosive calibration curve changes from quadratic to linear at a point of approximately 22.5 mg/cm^2.

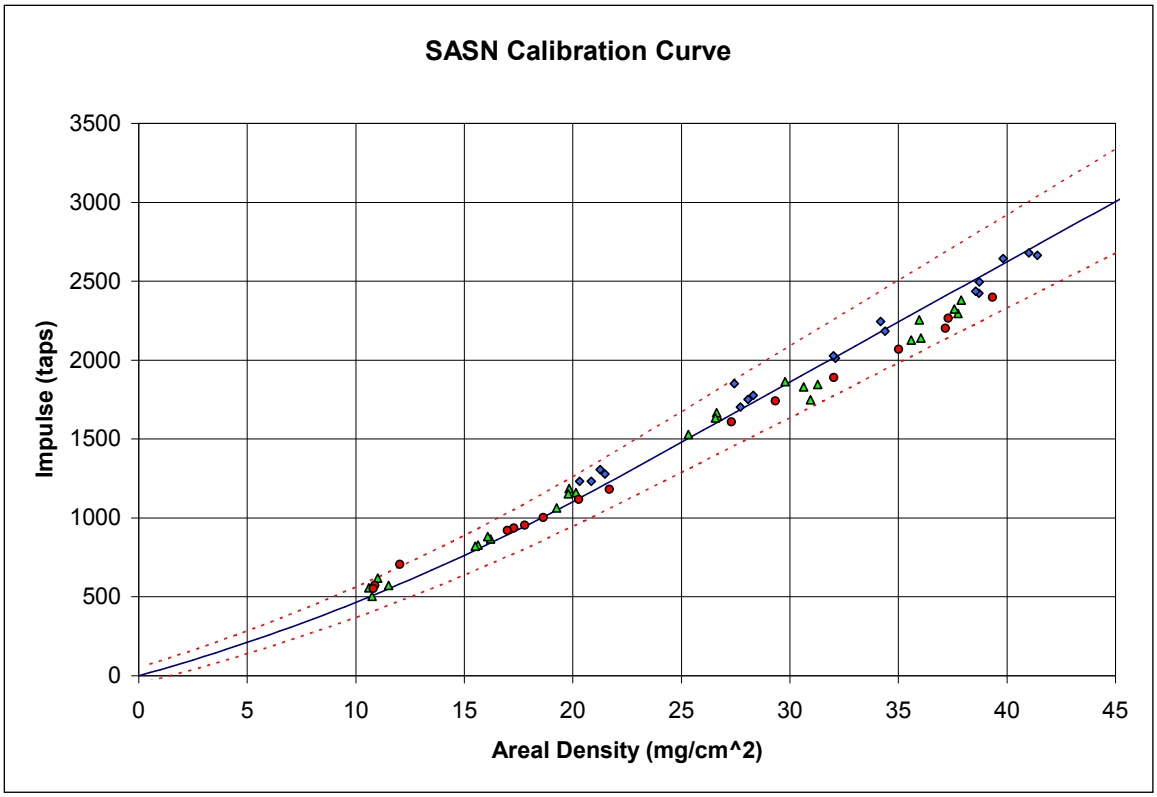

Figure 5.3: Specific Impulse versus Areal Density for Sprayed SASN

A linear regression has been fit to the data between densities 22.5 and 41 mg/cm^2, yielding the calibration equation

$$I_{sp} = 76.26 \cdot \rho_A - 427.06 \tag{5.8}$$

where the specific impulse (I_{sp}) is in units of taps, and the areal density (ρ_A) in units of mg/cm^2. This result matches the calibration curve, in this areal density region, used at the facility in the past. Because only a few coupons were tested below the 22.5 mg/cm^2 level, and a good correlation between the explosive output data above the 22.5 mg/cm^2 level was observed, the quadratic calibration curve from 0 to 22.5 mg/cm^2 previously reported at the facility [73] is assumed to be correct. This relation is given as

$$I_{sp} = 0.86 \cdot \rho_A^2 + 37.95 \cdot \rho_A \tag{5.9}$$

5.4. "Coupon" to "Infinite" Impulse

Equations (5.8) and (5.9) have been experimentally derived to describe the impulse yielded by a specified areal density of explosive deposited on a 1.905 cm (0.75") diameter coupon. But the boundary conditions of a coupon sprayed with a layer of explosive driving a large mass are somewhat different than a larger semi-infinite area driving a flyer or plate. Edge effects from the circumference of the coupon cause a small portion of the explosive energy to be driven perpendicular to the measured impulse from the coupon. This effect reduces the impulse delivered to the pendulum in the calibration process. As the areal density increases, so does the actual thickness of the explosive layer, which increases the fraction of explosive energy lost due to the edge effects. This effect is called explosive stacking, illustrated in Figure 5.4. It is therefore necessary to introduce the concept of "infinite impulse" versus "coupon impulse." Work has been done in the past that quantifies the degradation of impulse from the edge effect of the coupon [12, 49, 54]. This work has focused on the work of Baum [7] involving the loss of energy due to edge effects.

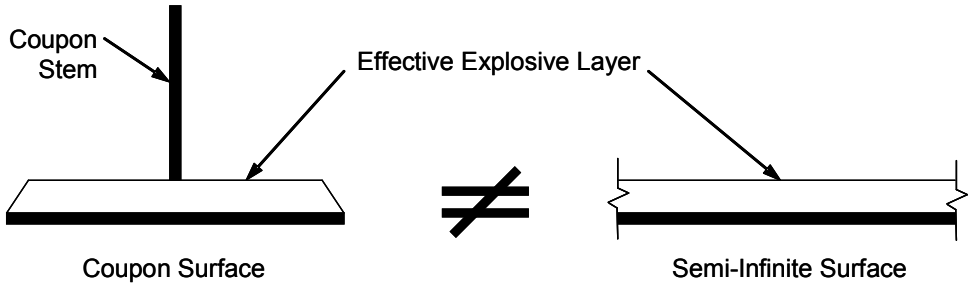

Figure 5.4: Explosive Stacking

For the specific geometry of the 1.905 cm (0.75") diameter coupon, the transfer function from coupon impulse to infinite impulse, as a function of areal density [54] is estimated by the function

$$I_{sp-Infinite} = \frac{I_{sp-coupon}}{1 - 0.5\left(\frac{\rho_A}{571.5}\right) + 0.08333\left(\frac{\rho_A}{571.5}\right)^2} \tag{5.10}$$

where the specific impulse (I_{sp}) is in units of taps, and the areal density (ρ_A) in units of mg/cm^2. Figure 5.5 plots equation (5.10), and graphically compares the difference between infinite impulse and coupon impulse. As can be seen, the specific impulse delivered over a large surface is greater than that delivered over a small surface. For a semi-infinite explosive deposition area, the explosive stacking effects are small compared to those from the calibration process, and are generally neglected. Although, as the sprayed area decreases for the same explosive deposition, the effect of stacking increases. For this reason, special attention must be paid to the flyer and target size to reduce, wherever possible, this effect.

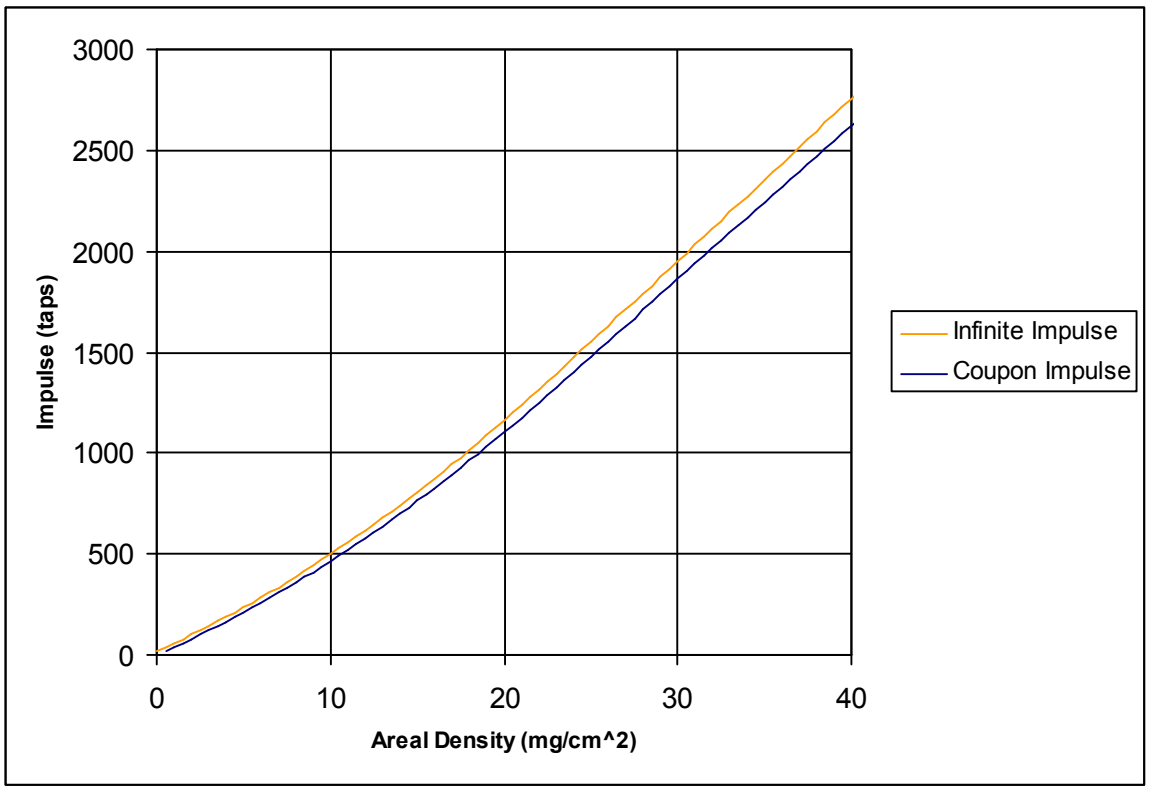

Figure 5.5: Infinite and Coupon Impulse as a Function of Areal Density

5.5. Velocity as a Function of Areal Density

Equations (5.8), (5.9), and (5.10) are substituted into equation (4.24) of the previous chapter to yield a two part flyer velocity equation as a function of explosive areal density, flyer thickness and density: For $\rho_A \geq 22.5$ mg/cm^2 flyer velocity is calculated by

$$V = \left[\frac{76.26 \cdot \rho_A - 427.06}{\left(1 - 0.5 \cdot \left(\frac{\rho_A}{571.5}\right) + 0.0833 \cdot \left(\frac{\rho_A}{571.5}\right)^2\right) \cdot \frac{\rho_A}{1000}} \cdot \sqrt{\frac{4}{3}} \right] \cdot \left[\frac{\left(1 + 2 \cdot \frac{\rho_{f \cdot t_f}}{\rho_A}\right)^3 + 1}{6 \cdot \left(1 + \frac{\rho_{f \cdot t_f}}{\rho_A}\right)} + \frac{\rho_{f \cdot t_f}}{\rho_A} \right]^{-\frac{1}{2}} \tag{5.11}$$

And for $\rho_A < 22.5$ mg/cm^2 flyer velocity is similarly calculated by

$$V = \left[\frac{0.86 \cdot \rho_A^{\,2} - 37.95 \cdot \rho_A}{\left(1 - 0.5 \cdot \left(\frac{\rho_A}{571.5}\right) + 0.0833 \cdot \left(\frac{\rho_A}{571.5}\right)^2\right) \cdot \frac{\rho_A}{1000}} \cdot \sqrt{\frac{4}{3}} \right] \cdot \left[\frac{\left(1 + 2 \cdot \frac{\rho_{f \cdot t_f}}{\rho_A}\right)^3 + 1}{6 \cdot \left(1 + \frac{\rho_{f \cdot t_f}}{\rho_A}\right)} + \frac{\rho_{f \cdot t_f}}{\rho_A} \right]^{-\frac{1}{2}} \tag{5.12}$$

where the areal density of explosive (ρ_A) in units of mg/cm^2, flyer bulk density (ρf) in units of mg/cm^3, flyer thickness (t_f) in units of cm, and velocity (V) in units of cm/s. Equations (5.11) and (5.12) are the basis for the SASN driven thin metallic flyer plate, and are used extensively to design and analyze the experimental portion of this investigation. These equations, as presented, are given in terms of infinite impulse, which is the likely boundary condition for larger flyer plate experiments, like the ring experiments discussed in Chapters 7, 8, and 10. Under the scenario of a very small LIHE driven flyer, the coupon impulse can be used to predict flyer velocity. Comparing the difference in flyer velocity between coupon and infinite impulse, Figure 5.6 shows a

slightly higher flyer velocity per explosive deposition for the infinite impulse curve than the coupon impulse. The figure shows the driven flyer velocity for an aluminum flyer 0.033 cm (0.013") thick.

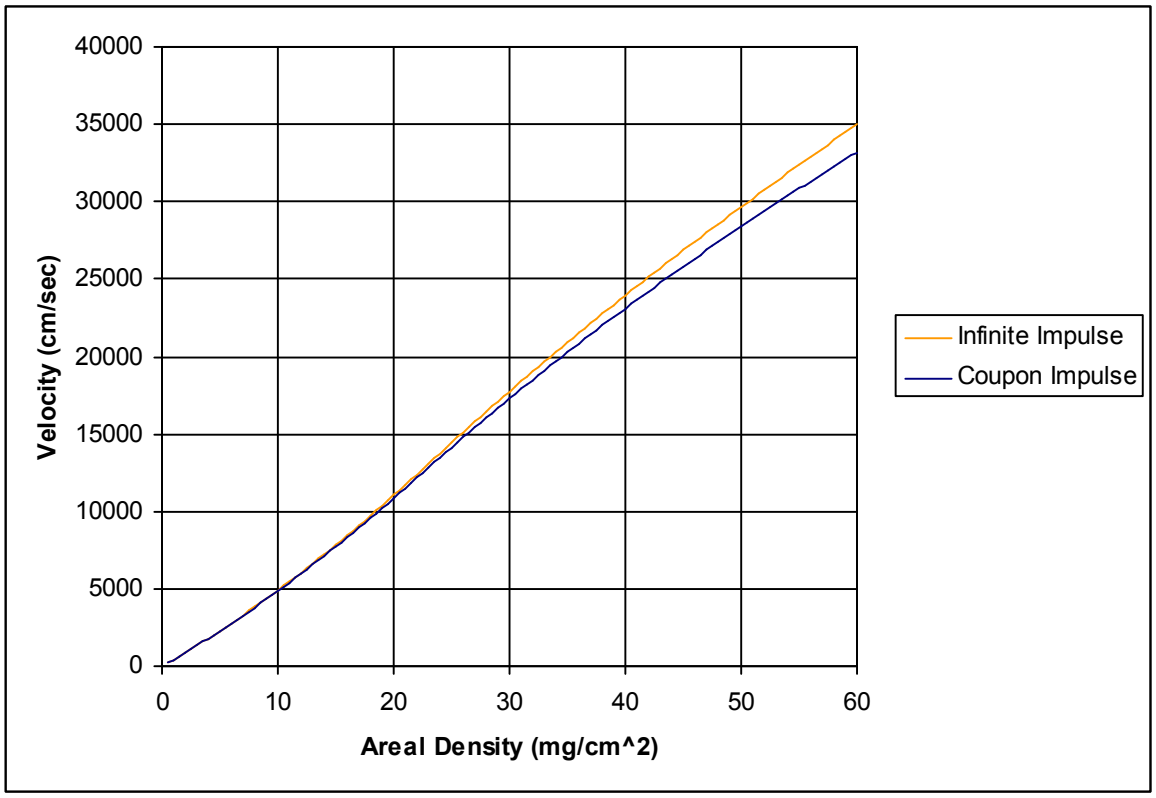

Figure 5.6: 0.033 cm Thick Flyer Velocity for Infinite and Coupon Impulse

6. DEVELOPMENT OF THE ONE-DIMENSIONAL FLYER

The extension to the Gurney analytical solution presented in Chapters 4 and 5 was the first step in the design and implementation of a LIHE driven flyer. These results suggest that silver acetylide-silver nitrate explosive can predictably drive a thin metallic flyer plate to velocities of interest for this study. But, there are still a number of steps required to successfully design, conduct, and analyze a flyer experiment. The design phase of a one-dimensional, explosively-driven flyer experiment is presented in the current chapter. This discussion will include the calculation of the minimum flyer offset from the target, choice of materials, flyer and target design, and explosive charge, as well as an introduction to the instrumentation used for test analysis.

The major focus for this one-dimensional portion of the flyer development is to physically design the experimental technique to create a high amplitude, short duration, impact pressure pulse at a target surface. The objectives of this design are to investigate material response of a target plate, impulse delivery by the flyer, and the logistics and feasibility of a LIHE driven flyer technique. The design of these experiments had to accommodate a number of constraints imposed by the ongoing LIHE test and spray activities external to this study. These included the spray pattern, available space, explosive handling limits, and initiation constraints.

The proper design of the flyer experiment is an iterative process taking into account desired structural and material response, pressure pulse characteristics, as well as other engineering and logistics issues, such as material availability, compatibility, and cost. Due to the logistical nature of this investigation, flyer experiments were designed with a variable explosive loading in mind, utilizing a constant flyer material and

thickness. The basic assumptions in the design of the one-dimensional flyer and target assembly are as follows:

1. Explosive depositions will range between 35 and 50 mg/cm^2.
2. Explosive initiation will take place on the SBPA. This results in a target/flyer assembly size constraint.
3. Total explosive deposition can be no greater than 1.0 gram (0.0022 lb) for each experimental sample. This results in a flyer area constraint.
4. Each experimental sample must be handled by the master/slave manipulator grips inside of the spray booth after spray activities have concluded. Again resulting in a target/flyer assembly size constraint.

6.1. Flyer/Target Assembly Overview

To accommodate the objectives of the one-dimensional portion of this investigation, a flyer/target assembly was developed. Specifics of this assembly are discussed in the following sections, but a brief overview is given here to aid the reader through the chapter. The assembly is made up of a material target, an offset spacer, a main flyer layer, and a flyer support layer. The different layers are bonded together with spray adhesive and transfer tape forming an assembly which suspends the flyer impact surface approximately 0.20 cm (0.079”) from the target surface. As the explosive layer is detonated, the flyer support shears at the edges of the offset spacer window, allowing the flyer to accelerate towards the target. Figure 6.1 shows an exploded view of the flyer assembly.

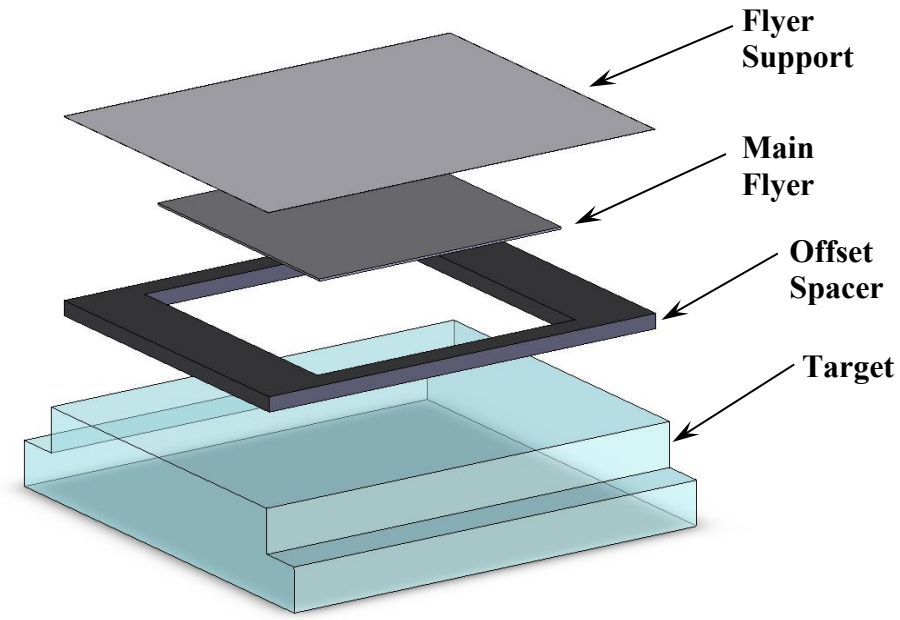

Figure 6.1: One-Dimensional Flyer Experimental Assembly

6.2. Flyer Offset

A small offset gap between the initial position of the flyer and the target is required to give the flyer time and space to accelerate from rest to the driven terminal velocity. Ideally, this gap would contain a vacuum to avoid the cushion effect of trapped air between the flyer and target which, as seen in Chapter 4, results in lower peak pressures and longer duration pulses. Unfortunately a vacuum gap is generally not feasible, even for small flyer experiments.

Work has been done to determine the minimum space required to accelerate the flyer to terminal velocity [59]. Again, starting with the basic equations for impulse presented in Chapter 4,

$$I_{sp} A = \Delta\left(m_f V_f\right) = m_f \left(V_1 - V_0\right) \tag{6.1}$$

and

$$I_{sp} = \int_0^t P(t)dt \tag{6.2}$$

and a representative SASN generated pressure pulse (shown in Figure 6.2 below), the velocity profile and associated displacement of a SASN driven flyer can be numerically calculated.

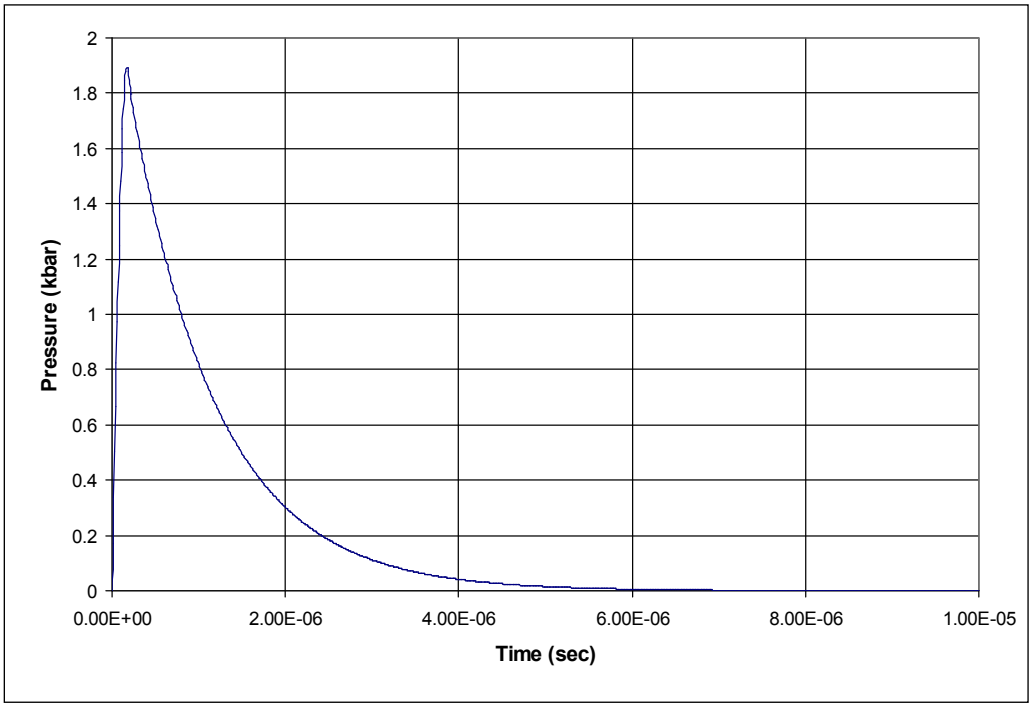

Figure 6.2: SASN Generated Pressure Pulse (Detonation in Contact with Al) [19]

This analysis assumes an initially stationary flyer with no target or corresponding trapped air. Since the flyer (of mass m_f) is initially at zero velocity, the change in momentum term in equation (6.1) becomes

$$I_{sp} A = m_f V_f \tag{6.3}$$

The mass of the flyer is a function of the material density and the volume (product of thickness and area) and given by the relation

$$m_f = \rho_f t_f A \tag{6.4}$$

Substituting equation (6.4) into (6.3), the specific impulse becomes a function of flyer density, flyer thickness and velocity, independent of area,

$$I_{sp} = \rho_f t_f V_f \tag{6.5}$$

Rearranging equation (6.5), the flyer velocity as a function of specific impulse is given by

$$V_f = \frac{I_{sp}}{\rho_f t_f} \tag{6.6}$$

Recognizing that the specific impulse, as a function of time is given by equation (6.2), equation (6.6) becomes

$$V_f(t) = \frac{\int_0^t P(t)dt}{\rho_f t_f} \tag{6.7}$$

Because there is no common analytic function for the SASN generated pressure pulse shape and amplitude, a numerical integration scheme is used to determine velocity and displacement for the generalized pressure pulse in Figure 6.2. Integrating the entire pressure pulse and substituting into equation (6.7) yields the terminal velocity of the flyer. A time-history of the flyer velocity is calculated by evaluating the integral at times (or time steps) of interest. The flyer displacement history is calculated by integrating the flyer velocity history. The flyer velocity and the displacement curves for the given explosive pressure pulse, as a function of time, are given in Figure 6.3 and Figure 6.4 respectively. Of course, this result is a function of the given pressure pulse which will change in amplitude with changes in areal density and spray surface material. The flyer velocity and displacement profiles will vary with these changes. The duration of the pressure pulse will change only slightly with changing explosive deposition. The result is that the time to reach terminal velocity is relatively independent of deposition. The point

to be made here is that the flyer acceleration is a direct function of the explosive generated pressure applied and will decrease to zero as the pressure decreases to zero.

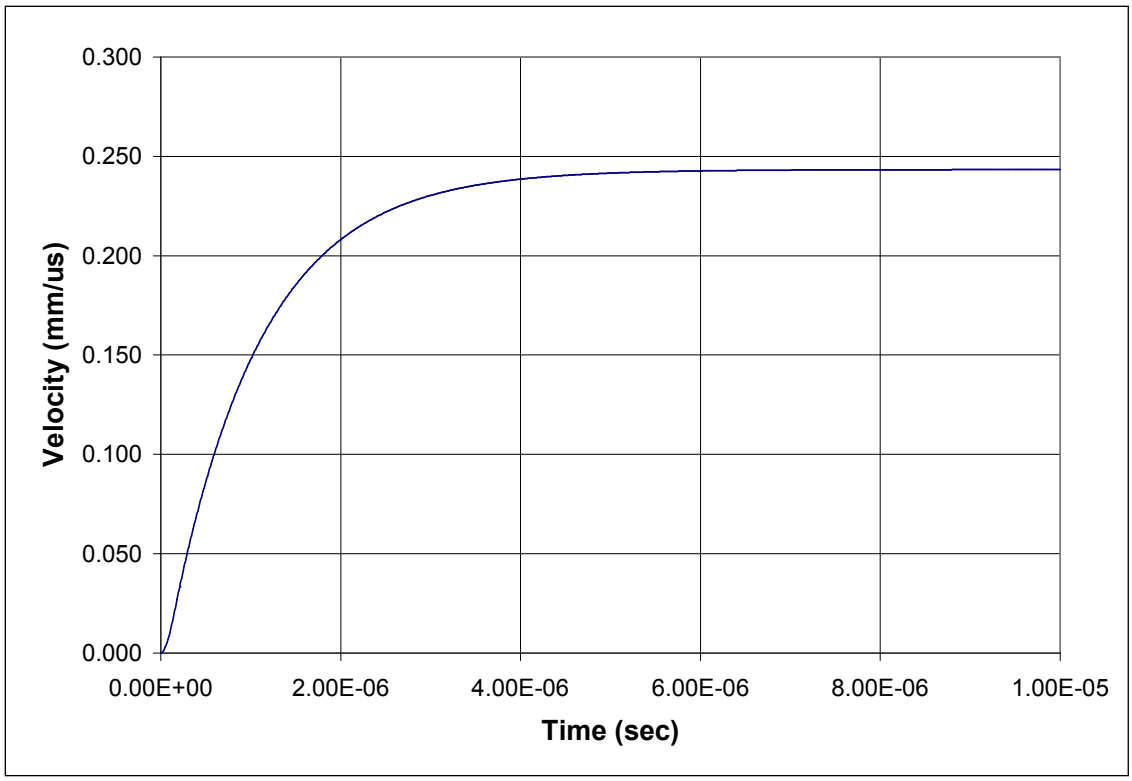

Figure 6.3: Flyer Velocity Profile from a General SASN Pressure Pulse [19]

It is observed in Figure 6.3 that, for this general configuration, ~99% of the terminal velocity of the flyer is achieved within 5 μs, which corresponds in this example to 0.098 cm (0.038") of travel. This analysis suggests that a minimum offset distance of ~0.10 cm (0.039") is required to achieve terminal velocity for a typical pressure pulse in the range of explosive depositions expected in this study. Of interest is the observation that the flyer can impact at any time, within reason, after the 5 μs acceleration phase with approximately the same velocity, therefore making the offset distance tolerance between flyer and target less stringent than if the flyer was still in the acceleration phase at the desired impact velocity.

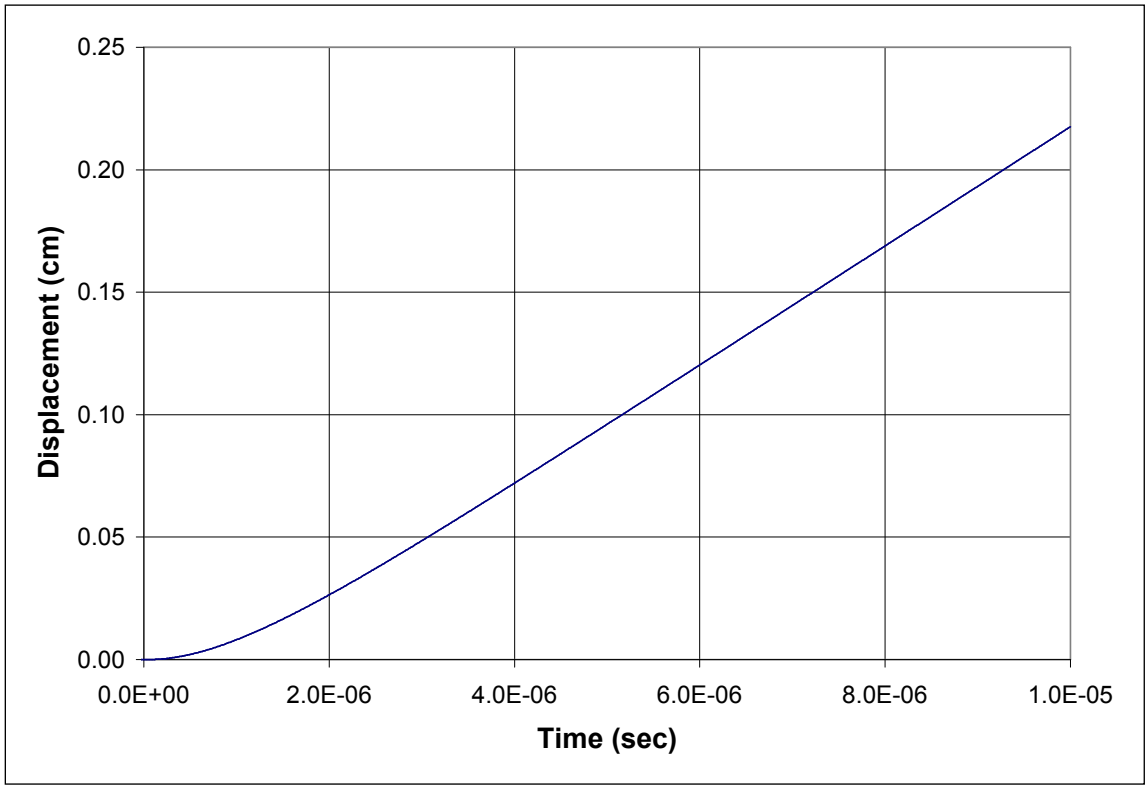

Figure 6.4: Flyer Displacement from a General SASN Pressure Pulse [19]

As stated above, this analysis assumes no target or trapped air, which is obviously not the case for the present investigation. It was shown in Section 4.5 that the impact velocity and resulting pressure is reduced by the presence of the trapped air. This effect must be taken into account in order to fully understand the transfer of energy from the flyer to the target. In general, it is desirable to have a minimum amount of trapped air, while still allowing the flyer to reach full velocity before impact.

To accommodate the wide range of expected explosive densities in this study, an offset distance of 0.20 cm (0.079") was chosen. An offset spacer plate, shown in Figure 6.5 was used to achieve this gap. This piece was wire EDM manufactured to the dimensions of the target and flyer (given in subsequent sections) out of 0.24 cm (0.094" or 3/32") stock aluminum plate.

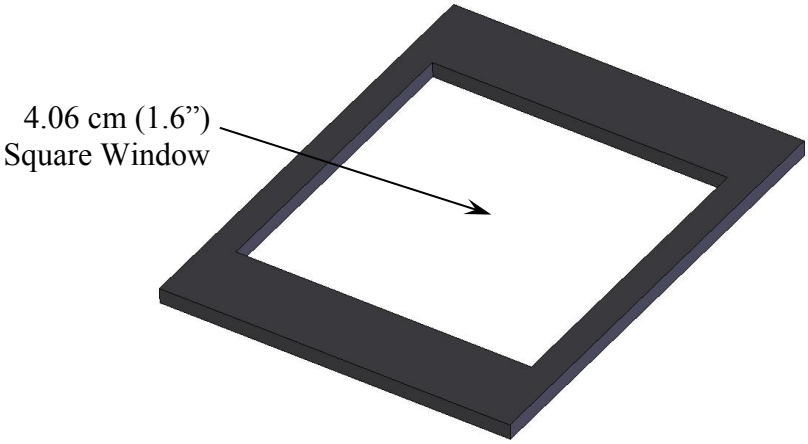

Figure 6.5: 0.24 cm (0.094”) Thick Offset Spacer

6.3. Flyer Material and Design

The choice of flyer material depends on a number of experimental considerations. It was observed in Chapter 4 that the shock properties of the flyer design greatly affect the impact pressure, pulse shape, and flyer rebound. A relatively strong material was required because the flyer cannot be destroyed, or significantly altered in shape by the explosive detonation. Aluminum’s physical characteristics are a good match for the project at hand due to its strength, density, and well understood shock properties. Aluminum’s light weight was preferred to other metallic materials due to availability, material compatibility, and that a given explosive deposition will drive an aluminum flyer to a relatively high velocity, potentially creating large peak impact pressures at the target surface.

Traditionally, aluminum flyer plates used in impulse applications have been the 1100 alloy, which has a density of 2.71 g/cm^3 (0.098 lb/in^3). 1100 Aluminum is a virtually pure alloy consisting of 99.9% aluminum with only trace amounts of copper, manganese, and zinc [22, 56]. Using the explosive calibration and expanded Gurney

equations (5.11) and (5.12) from Chapter 5, the flyer velocity is plotted in Figure 6.6 for aluminum flyer thicknesses between 0.0203 cm (0.008") and 0.0356 cm (0.014") as a function of areal density, up to 60 mg/cm^2. It is evident that thinner, and hence lighter, flyer plates will have an incrementally higher terminal velocity for any given areal density.

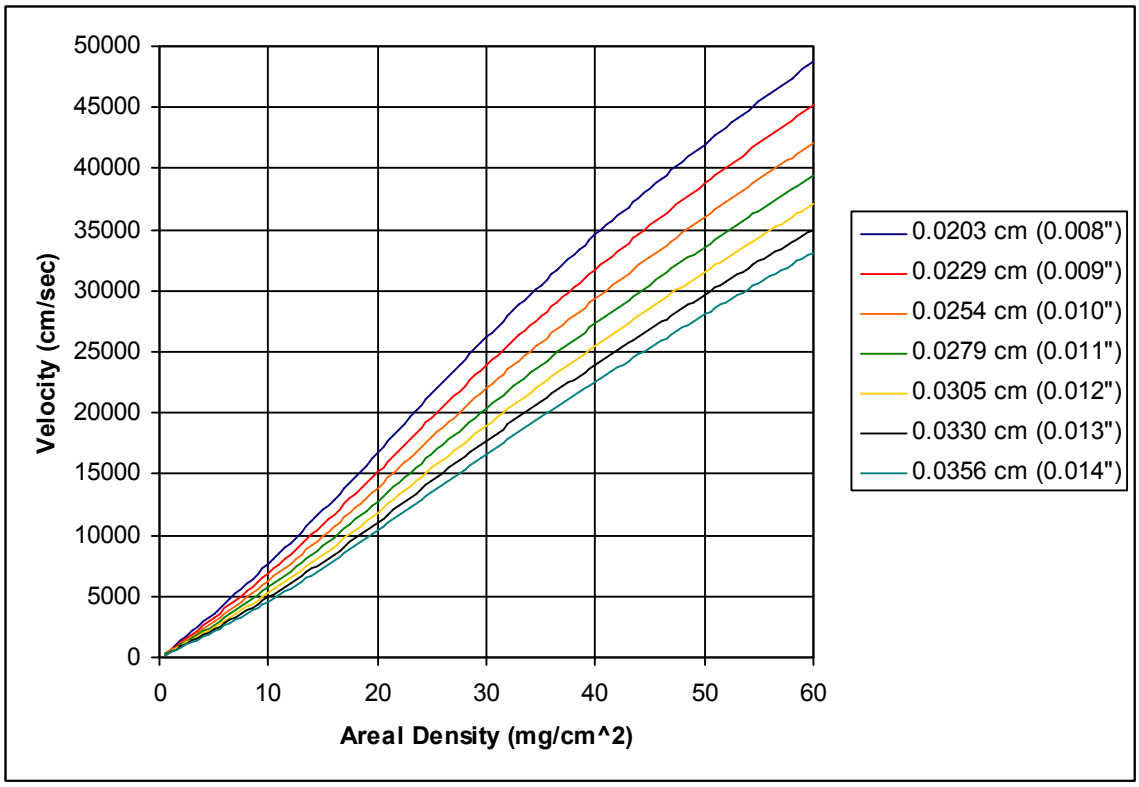

Figure 6.6: Flyer Velocity as a Function of SASN Areal Density.

For engineering considerations, the flyer plate itself was designed as a composite of two layers of aluminum foil. The purpose of this composite assembly was to provide a structure to rigidly suspend the flyer over the target at a known offset, as well as provide a weak portion of that structure to allow the flyer to accelerate unimpeded after the explosive detonation.

The first layer, in contact with the explosive, was a very thin aluminum foil [0.0018 cm (0.0007”) thick] glued to the offset spacer. The second aluminum layer [3.81 cm (1.50”) square and 0.030 cm (0.012”) thick] made up the majority of the flyer thickness and is smaller in area than the 4.06 cm by 4.06 cm (1.6” by 1.6”) spacer window. The two layers were coupled with a thin coating of spray adhesive. The flyer thickness used in calculations and analysis, made up of the two flyer layers, was 0.033 cm (0.013”).

The intent of the flyer design was that when the explosive was initiated, the thin foil of the flyer assembly would be sheared along the window edge of the standoff spacer, allowing the remaining flyer assembly to accelerate unimpeded towards the target. Figure 6.7 shows the general makeup of the composite flyer assembly.

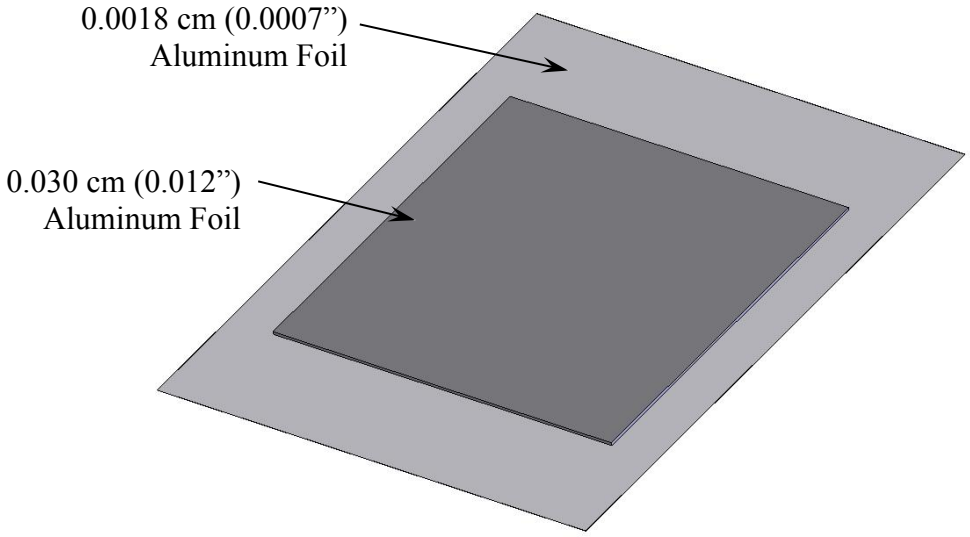

Figure 6.7: Composite Flyer Assembly (Impact Side Up)

6.4. Target Materials and Design

The list of potential target materials for this investigation was quite large. As stated in the project scope and objectives (Section 1.4), the aim of this work was to develop the flyer technique to excite both material and structural response in an impacted target. But for this investigation, a specific material response was not required. Instead, it was desired to achieve a difference in material characteristics, such as a change in hardness or the generation of internal spall, in a number of target materials. It was desired to work with target materials that would exhibit noticeable, qualitative, and quantitative material responses.

Eight materials were chosen for the one-dimensional experiments. These materials are PMMA (Plexiglas), polycarbonate (LEXAN®), 1100 aluminum, 6061-T651 aluminum, C110 copper, nickel 200, and 304 and 316 stainless steels. Each of these materials are commercially available, well characterized, and show potential to exhibit varying levels of material response to the flyer impact. Table 6.1 gives the shock properties required for Hugoniot analysis for each of the materials used in this investigation.

Table 6.1: One-Dimensional Test Sample Materials [24, 56]

Material	Density (g/cm^3)	Sound Speed (km/s)	S
PMMA (Plexiglas®)	1.18	2.49	1.69
Polycarbonate (LEXAN®)	1.19	2.25	1.55
6061-T651 Aluminum	2.70	5.35	1.34
1100 Aluminum	2.71	5.35	1.34
304 Stainless Steel	7.89	4.57	1.49
316 Stainless Steel	7.89	4.58	1.49
Nickel 200	8.90	4.58	1.465
C110 Copper	8.93	3.94	1.489

PMMA (polymethyl methacrylate) is a light weight thermoplastic, often referred to as acrylic or by the trade names Plexiglas® or Lucite®. The PMMA material used for

this study was manufactured by Polycast Technology Corporation under the trade name POLY II® UVT. PMMA is a transparent, relatively brittle, easily machined plastic. The reported impact strength of PMMA (Izod Milled Notch test) is 0.35-0.40 ft-lb/in [69]. Extensive gas gun experimentation [18, 55] has been done to characterize this particular brand and formulation of PMMA in the 19 to 69 kbar range. Matthews [55] lists a PMMA tensile strength of 62.1-75.8 MPa (9000-11,000 psi) with a density of 1.19 g/cm^3 (0.043 lb/in^3).

The polycarbonate sheet used for this study was manufactured by GE Plastics under the trade name LEXAN® 9034. GE characterizes LEXAN® as an amorphous engineering thermoplastic with high levels of mechanical, optical, electrical, and thermal performance [37]. LEXAN®, as well as other brands of polycarbonate sheet, is widely used in large numbers of structural and product applications due to its strength and durability. In addition, polycarbonate sheet is used extensively in the explosives and ballistics community where its impact and shatter resistant properties are required. The reported impact strength for LEXAN® 9034 (Izod Milled Notch test) is 12-16 ft-lb/in [56]. LEXAN® was chosen for this study as a plastic material with similar strength properties to PMMA, but with a superior impact resistance to acrylic sheet [37]. The reported tensile strength for the LEXAN® used is 62.1 MPa (9000 psi) with a density of 1.20 g/cm^3 (0.043 lb/in^3) [56].

The two types of aluminum used in this investigation, 6061-T651 and 1100, were chosen for different purposes in the test matrix. 6061-T651 aluminum is a common structural alloy with well characterized physical and shock properties. Its primary purpose in this study was impact pressure and impulse delivery analysis. There is little

difference in shock properties between 1100 and 6061 aluminums, and they can generally be thought of as interchangeable for the shock related portion of the analysis. In contrast, the 1100 aluminum targets were used in the material response portion of the study. The mechanical strength of aluminum can be enhanced by cold-work and alloying, and in some cases heat-treatment, although the 1100 alloy is not heat-treatable for an increase in strength [22]. In the annealed state, the yield strength of 1100 Al is reported as 35 MPa (5000 psi) with an ultimate tensile strength of 90 MPa (13,000 psi) [22].

Two types of stainless steel were utilized for material targets: 304 and 316. Both of these stainless steels are characterized by high chromium content, excellent corrosion resistance, and are austenitic in microstructure. 316 is manufactured with 1%-2% molybdenum, less carbon, slightly less chromium, and slightly more nickel than 304. Austenitic stainless steels were chosen for this study due to the possibility that the cold-work, caused by the flyer impact, would be sufficient to induce a change in the surface material of the target. Austenitic stainless steels cannot be hardened by heat treatment, and are hardened and strengthened by cold-work [22]. In the annealed state, the yield strength of 304 stainless is 205 MPa (30,000 psi) and the ultimate strength is 515 MPa (75,000 psi) [22]. For 316 stainless, the yield strength is 170 MPa (25,000 psi) with an ultimate strength of 485 MPa (70,000 psi) [22].

C110 Copper, which also goes by the nomenclature electrolytic tough pitch or C11000 copper, is nearly pure copper. It is characterized by being very soft and ductile, and difficult to machine. Much like the austenitic stainless steel samples, most copper alloys cannot be hardened or strengthened by heat-treatment, but improvement of these mechanical properties by cold-working is possible [22]. In the annealed state, C110

copper has a tensile yield strength of 69 MPa (10,000 psi) and an ultimate tensile strength of 220 MPa (32,000 psi) [22]. In addition, the stock material for the copper target samples was plated with a thin layer of silver to avoid any potential chemical incompatibilities between the SASN and exposed copper.

Nickel and its alloys are highly resistant to corrosion in many applications, including high temperature and corrosive aqueous environments [51]. Nickel has been used extensively in the chemical processing, food processing, and the electronics industry, where the need for end-product purity is required. The form of commercially available nickel is fully austenitic [51], and generally magnetic in all tempers and in temperatures to about 204°C (400°F) [62, 22]. Much like the stainless steel and copper targets, nickel is not hardened by heat treatment, but can be strengthened and hardened by cold-working [62]. Nickel 200 is a nearly pure alloy with a composition of 99.5% nickel with trace amounts of carbon, manganese, and silicon [51]. In the annealed state, nickel 200 has a tensile yield strength of 148 MPa (21,500 psi) and an ultimate tensile strength of 462 MPa (67,000 psi) [51].

The design of the one-dimensional target is a 6.35 cm by 6.35 cm by 1.27 cm thick (2.5” by 2.5” by 0.5” thick) plate with 0.64 cm (0.25”) grooves on either side to interface with a target holder on the SBPA. The design of the target, pictured in Figure 6.8, accommodated each of the size constraints discussed earlier in the chapter. The two material exceptions to this target design are the C110 copper and the nickel 200 samples where 1.27 cm thick stock material was not available. Instead, a 6.35 cm by 6.35 cm by 0.64 cm thick (2.5” by 2.5” by 0.25” thick) plate with no grooves was used. Detailed descriptions, dimensions, and drawings of the target structures are given in the appendix.

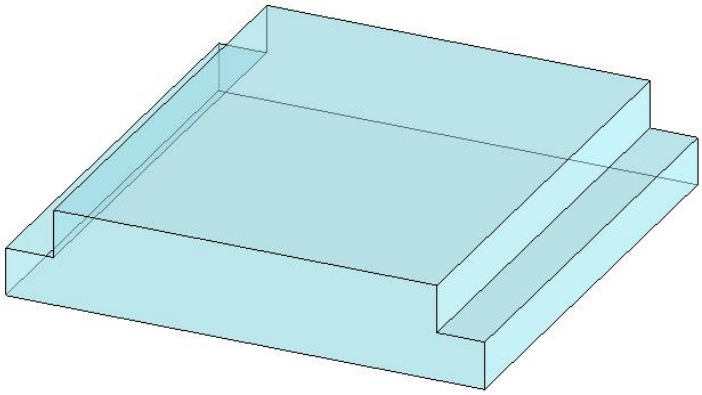

Figure 6.8: One-Dimensional Target

6.5. Explosive Deposition

As discussed earlier, the explosive deposition achieved on each of the one-dimensional samples was determined by objectives external to this study. Fortunately, the resulting explosive depositions, of approximately 35 to 50 mg/cm^2, were of the appropriate level to achieve the project goals. Each of the flyer/target assemblies is sprayed as part of a vertical, flat, overlapping spray pattern. The resulting explosive deposition is considered uniform over the flyer surface. Aluminum masks were employed to allow explosive deposition only on the 3.81 cm (1.50") square area of the flyer.

Two methods were used to evaluate the areal density of the explosive deposited on the flyer surface. The first utilized the coupon measurement technique described in section 5.3.1, where 1.905 cm (0.75") diameter Kovar$_{®}$ coupons were weighed on a digital scale to determine the weight of explosive deposited on the surface of the coupon. The presence of a coupon on the flyer surface during detonation would greatly disrupt the driving forces acting on the flyer. For this reason, coupons were placed adjacent to the flyer surface (in this case on the aluminum mask) for an inferred deposition on the flyer.

The second method attempted to directly weigh the explosive deposited on flyer surface after spray operations were complete. This measurement was much more difficult to perform than the coupon technique because the entire flyer/target assembly had to be remotely placed on the digital scale inside of the spray booth. In addition, this measurement was somewhat prone to error because the amount of explosive deposited on the flyer was a small fraction of the total assembly weight. For example, at a deposition of 50 mg/cm^2, the amount of explosive present on the flyer is 0.725 grams, as compared to the weight of the stainless steel target assembly of 375 grams, the explosive percentage of the total weight in this case was a mere 0.2%. For these reasons, the coupon measurement technique was preferred.

6.6. Impulse Delivery and Flyer Velocity Measurement

Ideally, flyer velocity and displacement would be measured directly using a laser based VISAR (velocity interferometer system for any reflector) system [6], or similar optical method. Unfortunately, the equipment and personnel necessary for this direct measurement were not available for this investigation. Flyer velocity was instead indirectly measured as a linear component of the total impulse delivered by the flyer impact. The flyer velocity is related to the total impulse delivered by the equation

$$V_f = \frac{I \cdot A}{\rho_f t_f R_f} \tag{6.8}$$

Again, the rebound factor (R_f) is estimated numerically through KOWIN calculations for the estimated flyer velocity from the measured explosive areal density.

With the flyer parameters (material, thickness, and area) defined, the total delivered impulse was measured using the same techniques as the coupon impulse delivery described in chapter 5. The non-contact eddy current displacement gage was

used to measure the movement of the SBPA pendulum mass. The specific impulse delivered by the flyer impact was calculated from the pendulum displacement. Finally, the inferred flyer velocity was calculated from specific impulse using equation (6.8).

6.7. Impact Pressure

On selected flyer/target assemblies, a thin film carbon pressure gage [8, 32, 33] was applied to the target surface to measure impact pressure from the flyer. The carbon gage is similar in appearance to a strain gage, and is made up of two layers of Kapton® sandwiching a carbon slurry. The total gage thickness, prior to epoxy application to the target surface, is between 0.010 cm (0.004") and 0.018 cm (0.007") thick. The gage is piezoresistive and when configured in a whetstone bridge circuit, changes resistance as a function of the applied pressure to the 0.127 cm (0.050") square active element. A pulse power supply, with a timing window of 100 μs, is required to apply power to the gage circuit. Precise timing and triggering is therefore necessary to record the impact pressure.

Application of the carbon gage to the target surface required a multi-step process to achieve optimal results. This procedure included target surface preparation, the mixing and evacuating specialized epoxy and clamping procedures. The leads of each gage were wrapped around the target structure and epoxied to the rear surface. An instrumentation cable was soldered to each gage, and the connection covered with 5-minute epoxy for strain protection. At this point, the offset spacer and flyer assembly could be attached to the target plate, suspending the flyer above the carbon gage.

The use of the carbon gage requires special attention to the reported gage output for the reason that in this application, the presence of the gage can return a pressure amplitude somewhat different than that produced by the actual flyer impact. This pressure difference is the result of material impedance mismatches between the flyer, the

gage, and the target material. This effect can be simulated and quantified by hydrocode analysis to determine the correct pressure profile had the impact occurred without the gage in place.

7. DEVELOPMENT OF THE TWO-DIMENSIONAL FLYER

The LIHE driven flyer must be expanded beyond the one-dimensional case to be truly useful to the impulse community. In the previous chapter, the design of the one-dimensional flyer experiments was developed for a uniform load over a flat surface. These theories and experimental results can be used to expand the LIHE driven flyer to more complex shapes and impulse load profiles.

The objective of the present chapter is to expand the LIHE flyer theory to a cylindrical surface with a cosine varying impulse load over that surface. In particular, this two-dimensional study will investigate the ability of the LIHE-driven flyer to excite the structural response of a ring structure, while satisfying the constraints of a high fidelity impulse test. This will require that the flyer impact the target surface near simultaneously over half of the circumference with an impact velocity profile that results in the proper cosine impulse distribution.

Much like the one-dimensional experiments, there are multiple aspects of the two-dimensional flyer experiment that must be addressed to achieve a successful test. These include the characterization of the desired loading in both amplitude and distribution over the target surface, determination of the varying flyer standoff distance, the proper deposition of SASN explosive on the flyer, physical setup and handling, as well as the recording of experiment instrumentation. It will be seen in the following sections that the two-dimensional flyer experiments are of significantly increased complexity to the one-dimensional flyer tests in design, physical setup, handling, and analysis.

The design of these experiments must accommodate a number of constraints imposed by the ongoing LIHE test and spray activities external to this study. These

include spray pattern, remote handling, available space, and initiation location. The result is that these flyer experiments are designed with an externally specified explosive deposition in mind. The basic assumptions in the design of the flyer and target assembly are as follows:

1. Explosive deposition at the 0º location on the target ring surface will be approximately 31.12 mg/cm^2.
2. The explosive deposition will vary in a cosine distribution over the flyer surface.
3. A 20.32 cm (8.0") outer diameter target ring is required.
4. Remote handling of all test hardware is required.
5. Explosive initiation will take place by the large bank light array in the LIHE facility test cell.

7.1. Experimental Design Overview

The process for designing a two-dimensional ring/flyer experiment utilizes the same flyer velocity equations (5.11 and 5.12) used to design the one-dimensional flyer experiments, but is significantly more difficult to implement. The design of the ring/flyer experiment requires varying flyer velocities, varying offset gap distances, and the requirement that the flyer simultaneously impact the entire target surface. The following overview lists the steps, discussed in further detail in the sections below, that are employed in the experimental design.

First, the experimental requirements and objectives must be defined. These include the required maximum impulse at each theta location, impact simultaneity constraints, as well as the desired pressure pulse shape and amplitude. This first step will facilitate the design of a flyer configuration (material and thickness) that incorporates each of the test objectives and requirements.

With the test objectives defined and an initial estimate of required flyer material and thickness chosen, the iterative design process is started at the 0º maximum impulse location. Typically, the impulse required at this position will be given as a design constraint. An initial estimate of flyer velocity is calculated to achieve the desired impact pressure. Next, an offset gap is chosen that reflects the approximate distance to full flyer velocity at impact. With these initial estimates of flyer material, thickness, and terminal velocity, as well as offset gap thickness, the rebound factor for the current position is calculated by hydrocode analysis.

Iteration on the design begins at this point. With an updated estimate of rebound, the flyer velocity is recalculated to achieve the desired local load. The rebound is again computed by hydrocode analysis and compared with the previous calculation. This process continues until the flyer velocity, rebound, and desired impulse match within acceptable constraints. After these parameters have been chosen, the approximate flyer transit time through the offset gap is computed. The result to this point is the initial "flyer design" for the 0º theta location. While not set in stone, it will provide the basis for the remaining flyer design over the target surface.

The design process then moves to the next theta position where flyer velocity, offset gap, and rebound are calculated. For a cosine load, the velocity and offset gap will decrease, and the corresponding rebound factor will generally increase. The additional design constraint at this location is to match the transit time to that of the previous position. This process is repeated through 90º of the ring surface due to the symmetry of the desired load over the ring surface. With the cosine load distribution, the 0º location receives the maximum design load, and the 90º location receives no direct load.

With the velocity profile calculated, an explosive deposition is computed. This involves the flyer velocity equations (5.11 and 5.12) to determine the specific areal density required at each theta position over the flyer surface. The final step is to review the entire flyer/offset gap/explosive deposition design for consistency and implementation. Figure 7.1 presents a basic flowchart for these steps.

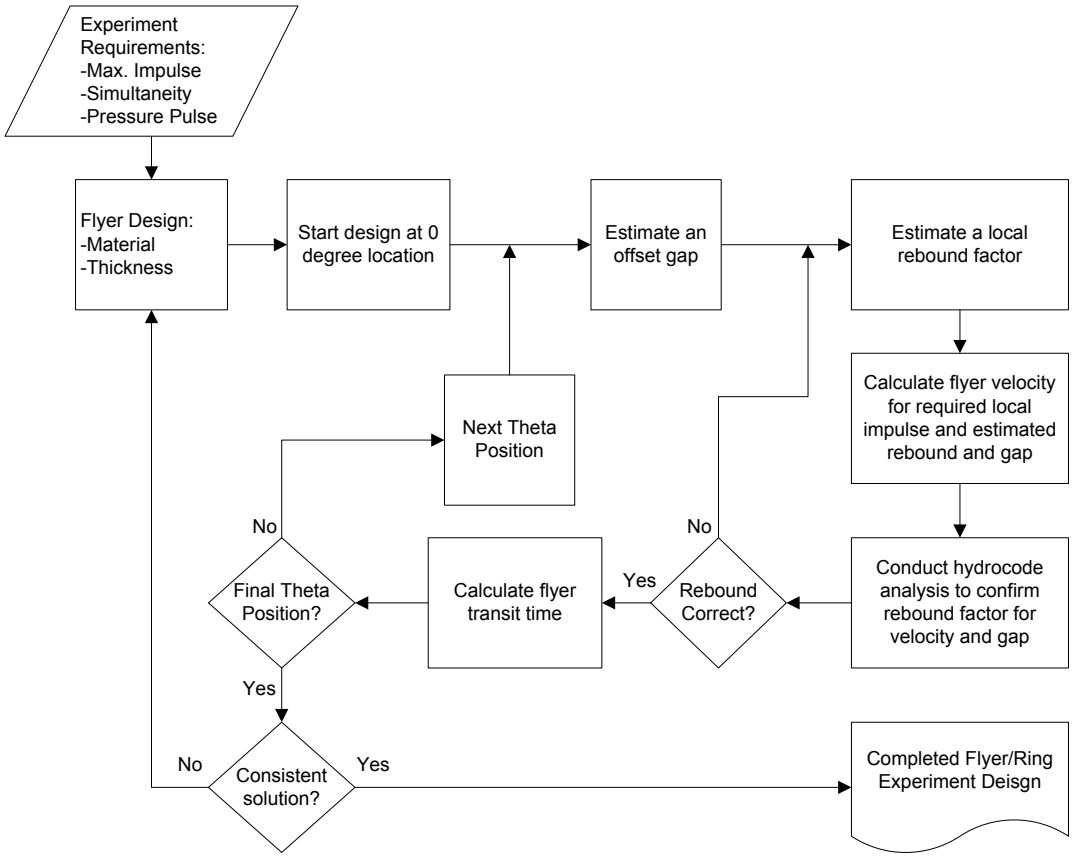

Figure 7.1: Two Dimensional Flyer Design Flowchart

7.2. Flyer/Target Assembly Overview

A ring test assembly was developed to accommodate the objectives of the two-dimensional portion of this study. Specific design characteristics will be discussed in the following sections, but a brief overview is given here to aid the reader through the chapter.

The ring test assembly is made up of the target ring, an aluminum flyer, a thin foil flyer support layer, two guard rings, and two bridge support pieces. An instrumented 20.32 cm (8.0") diameter ring structure is chosen as the target to accommodate space and handling constraints. The two 20.32 cm (8.0") diameter guard rings and variable thickness bridge supports hold the flyer in place and maintain the theta specific offset gap during spray and handling operations. The bridge supports form a maximum gap at the 0º location which tapers to zero at the ±90º locations. The assembly is held together using spray and contact adhesives, as well as brittle dental cement to attach the guard rings to the target ring.

The explosive is spray deposited on the flyer surface in a nearly cosine distribution, which results in the required variable flyer velocity. When the explosive is initiated, the flyer support layer shears at the edges of the bridge supports, allowing the flyer to accelerate towards the target unimpeded. At impact, the brittle dental cement is fractured allowing the target ring to respond to the impulse load independent of the support and handling hardware. Figure 7.2 shows an exploded view of the ring test assembly.

Each target ring was instrumented with three strain gages located on the inner surface of the ring to measure strain response. In addition, thin film carbon pressure gages were utilized to verify impact pressures, which relate directly to flyer impact velocity, as well as flyer impact simultaneity. Cabling for the instrumentation was run from the inner surface of the ring to the instrumentation system at the LIHE facility.

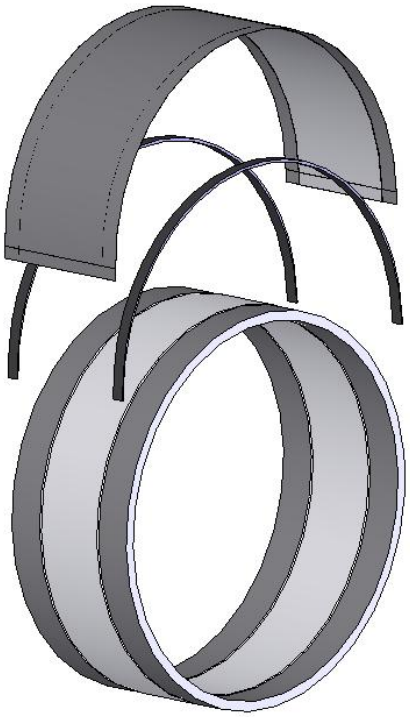

Figure 7.2: Exploded Two-Dimensional Flyer/Ring Test Configuration

7.3. Flyer Material and Design

The process for choosing the flyer material is nearly the same as that for the one-dimensional flyer, described in section 6.3. A strong material with well characterized shock properties to produce a representative pulse shape and delivered impulse is required. Neither pressure pulse shape nor required impulse was specified for this investigation. Instead, experimental design was based on an expected cosine distributed explosive deposition. Due to its favorable physical characteristics and shock properties, 1100 aluminum was again chosen as the flyer material.

Like the flyer assembly used in the one-dimensional case, the two-dimensional flyer utilized a two-layer flyer design. The majority of the thickness of the flyer was made up of a 0.030 cm (0.012") thick 1100 aluminum foil, which directly impacts the target surface. The remainder of the flyer thickness consisted of a 0.0025 cm (0.001")

thick layer of household heavy duty aluminum foil, likely 8111 aluminum [69]. The two layers were joined by a thin layer of 3M™ spray adhesive and is considered homogenous through the thickness. The purpose of the thinner layer of aluminum foil was to provide a structure strong enough to hold the flyer assembly away from the target ring during spraying and handling operations, as well as a shear location to allow the flyer to accelerate freely after explosive detonation. The flyer and support layer assembly is shown in Figure 7.3.

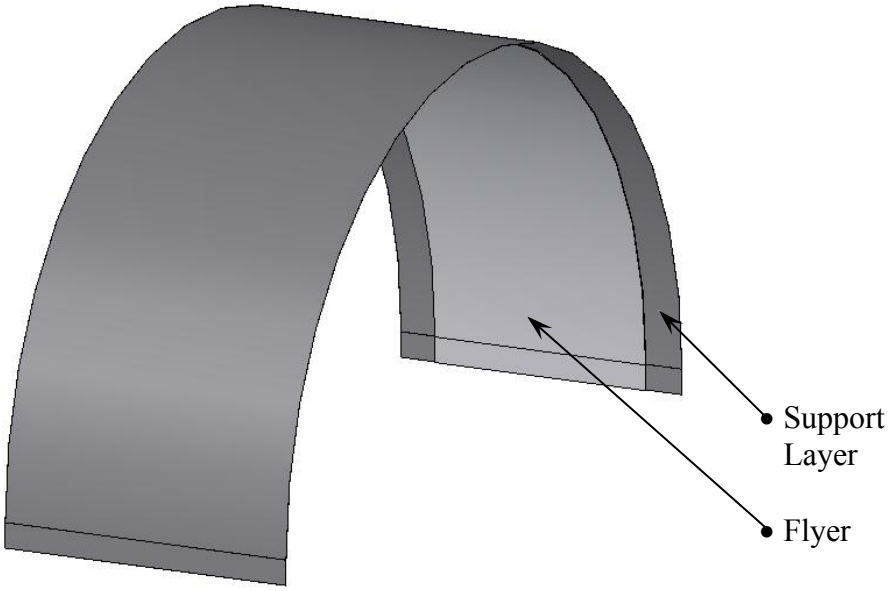

Figure 7.3: Two-Dimensional Flyer and Support Layer Assembly

7.4. Flyer Offset

A cosine varying impulse load, assuming a constant thickness flyer, requires that the flyer impact the target at different velocities depending on the load required at any given point on the surface. A logical start to a design would be to use a constant gap spacing between the flyer and the target with a varying explosive load deposited on the flyer for a varying flyer velocity. A constant offset gap is not feasible due to the

requirement that the flyer impact the entire surface within a given simultaneity tolerance (within the ¼ cycle time of the highest response frequency of interest at minimum). With the constant gap configuration, at the lower explosive loads the flyer velocity will be a fraction of the velocity at the maximum load, translating into longer transit times, and violating the simultaneity requirement. In addition, it is known that the air cushion effect, as most manifested in the flyer rebound, is greater for lower velocities and larger gap thicknesses. For these reasons, a varying gap as a function of angular location and impulse is required.

Again, the design of the offset gap assumed an expected maximum explosive deposition of approximately 31.12 mg/cm^2. This deposition corresponds to a flyer velocity of approximately 17,500 cm/s (6950 in/s), leading to a maximum impulse loading of approximately 2279 taps. For the purposes of this discussion, an impulse of 2279 taps was considered to be the desired loading for the experimental design.

7.4.1. Determination of the Flyer Offset Profile

A cylindrical coordinate system is necessary to describe the impulse and gap required at any point on the ring surface. The coordinate system is simplified in that the impulse is applied at the constant radius surface of the ring, and a constant impulse is applied along the axis of the ring. Therefore, only the theta position is varied in this calculation of impulse and gap. In addition, the load is symmetric about the 0º location spanning the surface between ±90º, thus requiring calculations for only one quadrant of the target ring.

At the 0º location, the specific impulse will be at a maximum (I_{max}) and will vary in a cosine fashion along the surface to zero at ±90º, as described by

$$I_{sp}(\theta) = I_{\max} \cdot \cos(\theta) \tag{7.1}$$

Starting with the maximum impulse at the 0º location, a gap was chosen that would satisfy the desire that the flyer be at or near full velocity at impact. It was observed in section 6.2 that for a general SASN driving pressure pulse, a 0.10 cm (0.039") gap is necessary to reach ~99% of terminal velocity. For this reason, a gap of 0.102 cm (0.040") was chosen for the 0º location for this analysis.

The next step was to make an educated approximation of the rebound factor at the present location. It is known that the rebound must be greater than 1.0 (which would indicate that the flyer impacted the target and stuck to the surface). Also known is that the rebound must be less than 2.0 since the outbound velocity of the flyer cannot be greater than the incoming velocity. A logical first approximation for the rebound factor might be 1.5. With the desired impulse (I_{sp}), flyer density (ρ_f), flyer thickness(t_f), and approximated rebound factor (R_f) for the given offset gap, a flyer velocity (V_f) is calculated by

$$V_f = \frac{I_{sp}}{\rho_f t_f R_f} \tag{7.2}$$

But, this is the velocity required for an *assumed* rebound factor, which may or may not be correct. At this point, the rebound must be confirmed by hydrocode analysis.

KOWIN provided the means to iterate the design constraints to determine the correct velocity and rebound for the desired impulse. The one-dimensional hydrocode modeling of the chosen geometry and flyer velocity provided indication to the validity of the rebound assumptions. If the rebound factor calculated by KOWIN differed from the assumed rebound factor, the flyer velocity and/or offset gap was changed and re-run until a consistent set of flyer parameters existed.

With the flyer velocity and gap determined, the approximate transit time required for the flyer to reach the target surface was calculated. As discussed in section 6.2, the

flyer undergoes an acceleration from rest to terminal velocity based on the explosively applied pressure pulse. But since the precise driving pulse, and thus acceleration profile, is not known at every areal density, the transit time was approximated by the time required for the flyer to transit the gap distance at the constant impact velocity. At this point, an initial, consistent, set of flyer parameters were defined for the 0º position, each of which are listed in Table 7.1.

Table 7.1: Zero Degree Flyer Parameters

Position	Impulse (taps)	Assumed Gap (cm)	Assumed Rebound	Flyer Velocity (cm/s)	Rebound Velocity (cm/s)	Calculated Rebound Factor
0º	2279	0.102	1.35	17518	6300	1.354

With the flyer velocity and offset gap calculated at the 0º location, the process was repeated at the next angular location. For a 20.32 cm (8.0”) diameter ring, 15º increments were sufficient resolution for determination of the offset gap. This spacing provided six offset gap steps over 90º corresponding to 2.66 cm (1.05”) of circumference per step to calculate and make consistent.

The calculation starting points for the next theta location are a known impulse requirement and flyer transit time, which again leads to an iteration of velocity and rebound factor. In general, the rebound factor increases with lowered initial flyer velocity. Much like the set of calculations for the 0º location, an assumption of rebound and offset gap was necessary to generate the flyer velocity required for the desired impulse at that point. But unlike the 0º calculation where a starting gap distance was somewhat arbitrary, this calculation required a gap which would result in a transit time consistent with the 0º position.

The entire process was repeated though each theta location, each time checking for consistency with the previous location's calculated flyer parameters. If an acceptable and consistent solution could not be found, another set of iterative calculations, starting with the 0º location, were required to correct the inconsistencies. For this investigation, it was not necessary to change flyer material, flyer thickness, or offset gaps, in order to maintain the pressure pulse characteristics, to achieve the proper impulse distribution. This process was repeated until a consistent set of impulse requirements, flyer parameters, offset gap parameters, and transit times existed. Table 7.2 gives the consistent set of flyer and offset parameters used for the 2279 tap cosine loading scenario.

Table 7.2: Flyer Velocity/Gap Design for a 2279 tap Cosine Loading

Theta	Impulse (taps)	Assumed Gap (cm)	Assumed Rebound	Flyer Velocity (cm/s)	Rebound Velocity (cm/s)	Rebound Factor	Transit (μs)
0º	2279	0.102	1.35	17518	6300	1.354	5.80
±15º	2201	0.100	1.44	15863	6260	1.373	6.08
±30º	1974	0.090	1.45	14125	6310	1.402	6.29
±45º	1611	0.070	1.49	11223	6160	1.460	5.79
±60º	1140	0.050	1.58	7484	5900	1.662	6.01
±75º	590	0.022	1.71	3579	3060	1.880	6.15

7.4.2. Flyer Offset Implementation

The implementation of the flyer offset was accomplished by two bridge support pieces, each affixed to a guard ring on either side of the target ring. As shown in section 7.3, the main thickness of the flyer was supported by the flyer support layer below the outer edge of the bridge support. Therefore, to assure the proper gap, the offset spacer consisted of the thickness of the desired gap at each location plus the thickness of the flyer.

Two guard rings, one on either side of the target ring, were required to support the offset bridge supports. Each 20.32 cm (8.0”) diameter, 1.91 cm (0.75”) wide, guard ring was fabricated from 6061-T651 aluminum tubing. The wall thickness was turned down to 0.51 cm (0.2”) to match the target ring. Each guard ring was fixed to the target ring by means of a brittle dental cement, taking special care to match the outer diameter surfaces as close as reasonably possible.

For this investigation, the bridge support was fabricated from layers of 0.013 cm (0.005”) thick aluminum tape. The proper gap thickness and circumferential distribution was built up on a flat surface then applied to the curved surface of the guard ring. To assure that a proper gap was achieved at each theta location, a depth micrometer was used to measure the actual gap at multiple locations. At any point where the gap was less than desired, additional layers of aluminum tape were applied to locally build the gap to the correct depth.

7.5. Target Material and Design

Two target ring designs were utilized for this study. The first was a simple aluminum ring comparable to that used extensively for similar impulse experiments in the past [17, 71]. The structural response of the simple ring is predicted by the Humphrys-Winter analytical solution, making the comparison of experimental to the analytical solution relatively straightforward. No attempt was made with this ring design to ascertain material response of the impacted surface material.

As a combined structural response and material response experiment, a 20.32 cm (8.0”) diameter composite ring structure was also used. This sample was composed of an outer layer of polycarbonate, an inner layer of 6061-T651 aluminum, concentrically bonded together with a thin layer of silicone rubber. The original purpose of this test was

to attempt to measure structural response as well as observe any gross qualitative interaction between layers.

Detail drawings for both the aluminum and composite rings can be found in the appendix.

7.5.1. Aluminum Target Ring

The objective of the flyer/ring experiments was to generate a predictable and measurable structural response in the ring target. It was seen in the Humphrys-Winter discussion in section 2.2.1 that the primary parameters for the analytical ring response solution are material density, modulus of elasticity, ring radius, and ring thickness. Aluminum 6061-T651, with a density of 2.71 g/cc (0.0975 lb/in^3) and a modulus of elasticity of 68.9 GPa (10 x 10^6 psi) [56], is extensively used as a structural aluminum alloy, is well characterized, and is readily available. Per spraying and handling constraints, a 20.32 cm (8.0") diameter target ring was employed. Each target ring was 3.81 cm (1.5") wide with a constant wall thickness of 0.51 cm (0.2"). The response of this aluminum ring structure was expected to be fully elastic, resulting in no permanent damage to the structure from the flyer impact. The simple aluminum target ring was not dissected for any material response analysis in this study. An illustration of the aluminum ring target is given in Figure 7.4.

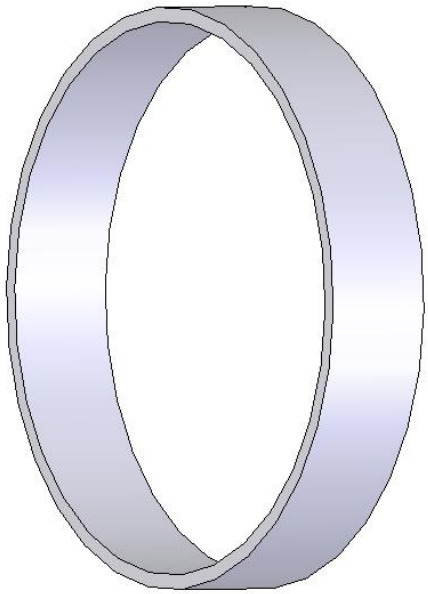

Figure 7.4: Aluminum Ring Target Structure

7.5.2. Composite Target Ring

The purpose of a secondary composite ring structure experiment was to attempt to observe a combined structural and material response in the target ring. Like the simple aluminum ring structure, the outer diameter of the composite ring was 20.32 cm (8.0”), but was made up of a polycarbonate outer shell and a 6061-T651 inner shell, bonded together with a layer of silicone rubber. The thickness of the polycarbonate was 0.635 cm (0.250”) and the aluminum 0.127 cm (0.050”). The approximate thickness of the silicone rubber was 0.127 cm (0.050”), resulting in a total wall thickness of 0.889 cm (0.350”). An illustration of the composite target ring is given in Figure 7.5 below.

Work was done in the mid-1970s by Sagarts and Forrestal [79] into an analytical solution to the cosine impulse loading of a composite ring structure. The published results claim an analytical solution which is, at best, difficult to implement, though impressive in its mathematical approach. The solution is presented as a set of complicated functions

which are given partially in the time domain, and partially in the Laplace ("s") domain. It is not known if their solution has ever been simplified or extensively used.

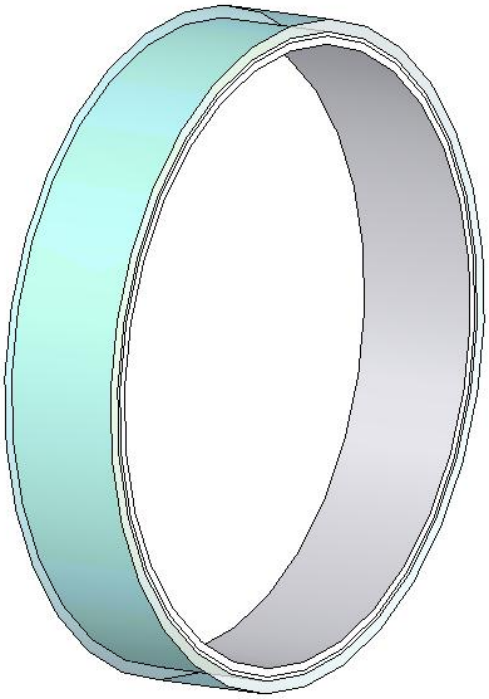

Figure 7.5: Composite Target Ring Structure

For the reason that the comparison of experimental data to an analytical solution for the composite ring is not easily done, the primary purpose of adding the composite ring to the test matrix was to observe any reaction between the polycarbonate layer and the aluminum sub-structure.

7.6. Explosive Deposition

While the explosive deposition distribution was externally specified for this investigation, this section details the process necessary to design an explosive profile to generate flyer velocities for a cosine distributed impulse load. The explosive deposition contour required to drive the flyer must be calculated before an explosive spray design

can be accomplished. Using equations (5.11), and (5.12), the explosive areal density is iterated at each theta location until the driven flyer velocity matches the required flyer velocity from the impulse design presented earlier in the chapter. An iterative process is necessary because the areal density is not easily isolated from the right hand side of the extended Gurney velocity equations. Table 7.3 lists the required deposition and flyer parameters for each theta location for the 2279 tap flyer/ring experiment.

Table 7.3. Explosive Deposition For Required Flyer Velocity

Theta	Impulse (taps)	Gap (cm)	Rebound Factor	Flyer Velocity (cm/s)	Explosive Deposition (mg/cm^2)	Velocity from Deposition	Updated Transit (μs)
0º	2279	0.102	1.354	17518	31.30	17467	5.82
±15º	2201	0.100	1.373	15863	30.21	16804	5.74
±30º	1974	0.090	1.402	14125	28.34	15652	5.68
±45º	1611	0.070	1.460	11223	24.77	13404	4.85
±60º	1140	0.050	1.662	7484	17.96	8917	5.05
±75º	590	0.022	1.880	3579	10.24	3477	6.33

The physical addition of the gap and flyer to the target ring was a relatively small difference from the cylindrical surface of the target ring itself. At the maximum gap distance, the spray surface was effectively a 20.46 cm (8.055") diameter ring. From the standpoint of the spray gun and robot motion, the flyer surface was essentially the same cylindrical surface as that of the 20.32 cm (8.0") diameter test ring. The real challenge in applying explosive to the flyer was the nearly cosine distribution required to drive the flyer to the proper velocities at the proper theta locations.

The LIHE conical explosive deposition design code [82] was employed for the explosive deposition design task. To start, spray target physical parameters, desired loading, and spray assumptions were entered into the two-dimensional design code. Virtual spray passes were added to the spray target surface at 10º angular locations until

the proper deposition distribution was achieved. This became the basis for the explosive spray operations. Figure 7.6 shows the graphical user interface (GUI) of the LIHE Conical Design program for the spray design used for these two-dimensional experiments.

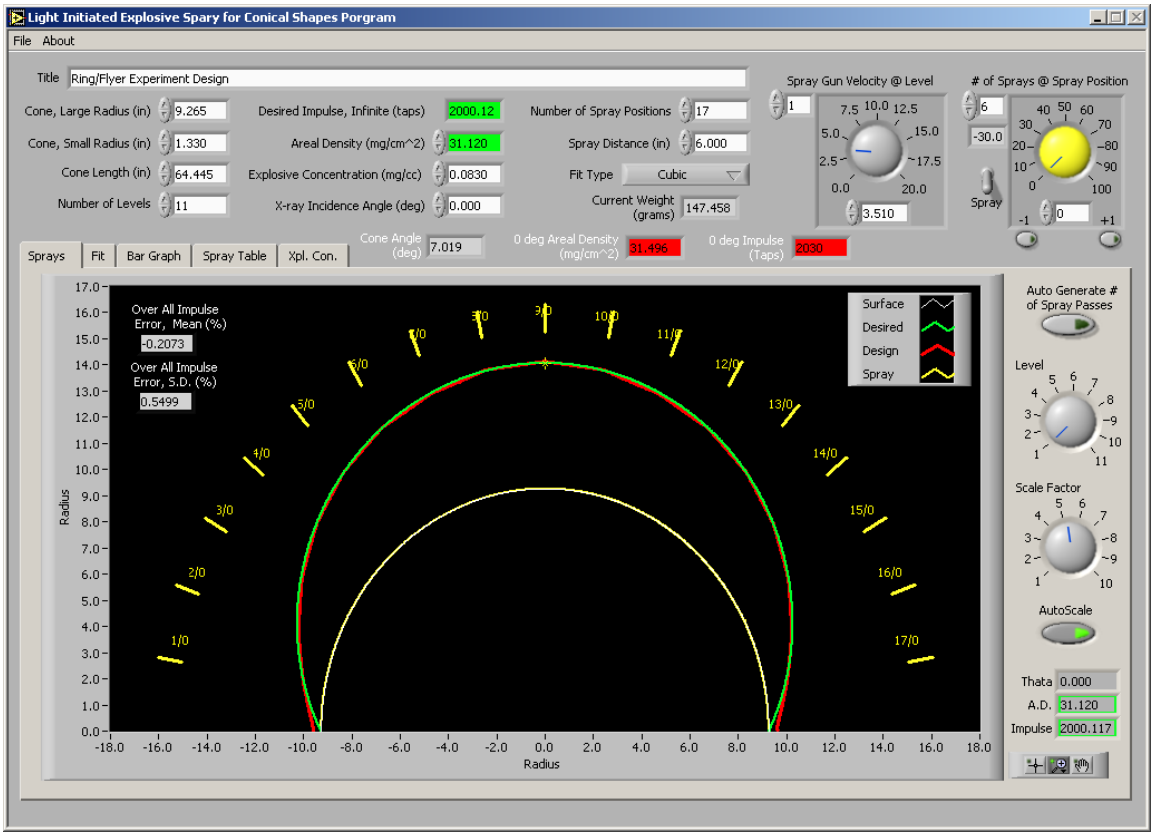

Figure 7.6: Conical Design Program GUI

To accomplish the explosive deposition in the proper distribution, the explosive spray gun was setup on the robot arm to deliver spray passes in a single column. Several ring test assemblies were stacked into a cylindrical column making up the spray surface. The cylinder was rotated about its axis by a computer controlled turntable located below the assembly. After each pass was made, the cylinder was rotated to the next spray

position for the next pass. This process was repeated numerous times until the proper distribution of explosive had been deposited on the flyer surface.

7.7. Instrumentation and Analysis

Three diagnostic methods were utilized to measure aspects of the flyer/target ring experiments. Flash x-ray radiography analysis was used to determine the rigid body motion of the ring structure after flyer impact. Structural response was measured by strain gages located on the inner surface of the target rings. Thin film carbon pressure gages were utilized to measure flyer impact pressure and impact simultaneity. Each diagnostic was used to calculate the total impulse delivered to the ring structure by the flyer impact.

7.7.1. Rigid Body Motion Measurement

Upon flyer impact, the entire ring structure horizontally translated away from the impact location. Assuming minimal external forces acting on the body, this rigid body motion of the structure provided a good indication of the total impulse delivered by the flyer impact.

A number of methods can be used to capture the rigid body motion of the ring after impact. String displacement gages have been used in the past for rigid body measurement of large test items, but due to the relatively light weight of the ring, a non-contact displacement measurement method was preferred. Photographic methods have also been used, but the flash of the light array and the ensuing fireball from the explosive detonation generally obscured the details of the ring movement in the desired timeframe.

The image capture method preferred in this application was the use of a flash x-ray system. This system utilized three 150 kV x-ray heads to take three snapshots of the ring position on a single piece of “x-ray film”. The system at the LIHE facility uses a type of digital film that does not require the use of chemical development generally

associated with this type of analysis. Three x-ray discharge times of interest, within a few milliseconds of each other—one for each head, were input to the system to generate the three snapshots in time. After each ring experiment, the film pack was digitally "scanned" to electronically produce the composite image of the three ring positions taken at three given times. Special attention was paid to the locations of the x-ray heads in relation to the test ring in relation to the film pack. The distances and angles created a parallax effect which distorted the image locations on the film, adding complexity to the analysis. Relative ring position was measured on the developed image to determine the rigid body velocity of the ring due to the flyer impact.

Rigid body velocity of the ring structure was calculated by the basic equation

$$V_{ring} = \frac{\Delta x}{\Delta t} \tag{7.3}$$

Analysis of the three exposures resulted in three calculations of rigid body velocity. The spatial and temporal difference between the first and second, the first and third, and the second and third exposures were used. An average rigid body velocity was calculated from the three individual velocity calculations.

The total impulse delivered to the target ring was calculated assuming an ideal cosine distributed impulse. Starting with the definition of specific impulse combined with the geometry of the cosine distributed impulse on ½ of the ring surface, the total impulse is defined as

$$\Delta(mV) = I_{sp} \cdot A = 2w \cdot \int_0^{\pi/2} I_{\max} \cdot r \cdot \cos^2(\theta) d\theta \tag{7.4}$$

Here, w is the width of the ring, r is the radius, m is the total mass of the ring structure (including instrumentation and shielding), and V_{ring} is the rigid body velocity of the total

ring structure immediately after the impulse is applied. Solving the integral on the right side of equation (7.4), the velocity of the ring structure becomes

$$V_{ring} = \frac{w \cdot I_{\max} \cdot r \cdot \pi}{2 \cdot m} \tag{7.5}$$

Rearranging equation (7.5) yields the relation for the maximum delivered impulse as a function of the measured ring initial velocity

$$I_{\max} = \frac{2 \cdot m \cdot V_{ring}}{w \cdot r \cdot \pi} \tag{7.6}$$

7.7.2. Strain Response Measurement

Strain gages were placed on the inner surface of each test ring at the 90º, 180º, and 270º locations to measure structural response in terms of strain. Due to the large EMP environment generated by the light array, each of the strain gage lead wires was configured with copper shielding to properly isolate the strain response signal from extraneous electrical noise.

The structural response of a metallic ring to a cosine distributed impulse load over half of the circumference is well characterized by the Humphrys-Winter analytical solution to this problem. Equations (2.5), (2.6), and (2.7), presented in section 2.2.1, describe the expected structural response in terms of the impulse amplitude, target ring dimensions, and material. The applied load was determined by comparison of the measured strain response to the calculated H-W solution. Each of the physical parameters of the ring structure were fixed for this investigation, so only the maximum impulse was varied to match the measured strain response.

7.7.3. Impact Pressure Measurement

Impact pressure and simultaneity were measured using thin film carbon pressure gages applied to the outer surface of several of the target ring structures. These were

located between the target surface and flyer at the 0º and ±30º locations, with the leads being run around to the inner surface of the ring. Again, copper tape was used to shield the instrumentation leads from the EMP environment. Data recording was accomplished on digitizers within the LIHE instrumentation room. As discussed throughout this report, care was taken to understand that the presence of the relatively soft carbon gage at the impact surface affected the pressure measured by the gage. In general, the gage read a slightly lower pressure than the impact of the aluminum flyer on the target surface. Hydrocode analysis was useful in understanding this effect. The specific impulse at the gage location was calculated by integrating the pressure-time output from the carbon gage.

8. EXPERIMENTAL DETAILS

Two major test series have been completed to investigate the LIHE driven flyer theory developed in the previous chapters. The first of these was an extensive flyer performance and material response series working with small one-dimensional test samples in various configurations of target geometry and material. The second, with fewer tests of increased complexity, was a series of structural response ring experiments. In all, forty tests were conducted, including thirty-five one-dimensional tests, four aluminum ring tests, and one composite ring test. Eight spray operations were required to complete both series, of which six were required for the one-dimensional tests, and two for the ring tests.

As has been discussed throughout this report, this investigation was riding on other testing conducted at the SNL LIHE facility. For this reason, the nomenclature used to describe each experiment corresponds to the LIHE facility's spray and sample identification numbering, and is not changed for presentation purposes. This identification scheme was maintained in this document to eliminate as much confusion as possible between the testing, analysis, and reporting.

8.1. Safety

The processes required for safely working with silver acetylide-silver nitrate explosive are established and well documented. It cannot be overemphasized that SASN is an extremely sensitive primary explosive. Safe conduct of operations requires special training, on-the-job experience, and often times remote handling. The safety requirements specific to this investigation were no different. To conduct the LIHE driven flyer experimentation phase of this study, multiple operating procedure (OP) and safe working procedure (SWP) documents were required. These include specialized procedures for

spraying SASN [26], operation of the large and small capacitor banks [76, 75], operation of the robotic arm [25], specific handling of flyer test specimens [63, 77] and the operation of the 150 kV flash x-ray system [47].

The explosive output of the SASN is considered to be relatively low, and the amounts deposited on the flyer test samples were considered to be relatively small. But, whenever human exposure to the explosive was required, generally during handling operations, special personal protective equipment (PPE) was needed. This PPE included a leather welding jacket, safety glasses, a face shield, and hearing protection at a minimum. In addition, it was required that the explosive handler wear cotton clothing to avoid the generation of static which could initiate the explosive with a static discharge. During firing operations within the SBPA blast enclosure, safety glasses and hearing protection was required.

8.2. One-Dimensional Flyer Testing

In total, thirty-five one-dimensional flyer (flat plate) tests were conducted over the six spray operations, TP-2004-06, -07, -08, -09, -10, and -12. Explosive depositions ranged from a low of 35.0 mg/cm^2 to a high of 53.7 mg/cm^2. While each test sample had a specific purpose in the investigation, all of the tests had many common aspects in design and implementation. Once sprayed and conditioned, each was moved to the SBPA for testing.

The pendulum mass of the SBPA was outfitted with a target assembly holder to rigidly secure the test sample to the pendulum mass. The holder allowed sufficient room behind the back surface of the target for instrumentation cabling. In addition, a free surface boundary condition at this location was important to allow for material spall analysis in un-instrumented target assemblies. Quantitative measurement of the pendulum

mass rigid body motion, as well as qualitative flyer and material response conditions were recorded for each test. Post-test analysis for some samples included visual evaluation for the presence of spall in the plastic materials, as well as dissection, hardness testing, and metallography analysis for the metallic target samples.

Table 8.1 below lists each of the thirty-six one-dimensional experiments attempted. Test sample #4 was considered a no-test due to the flyer assembly falling from the target plate during spray operations. In each experiment a primary test objective was to measure the delivered impulse from the flyer impact, in order to infer flyer velocity. The flyer parameters (material, thickness, area, and assembly technique) were maintained constant throughout the one-dimensional testing. In each experiment, the flyer material was considered to be a homogenous thickness of 0.033 cm (0.013") 1100 aluminum foil (temper 0) with an area of 14.52 cm^2 (2.25 in^2).

8.2.1. Target Preparation

Eight material types were used in the one-dimensional portion of this investigation. These included two plastics, two types of aluminum, copper, nickel, and two stainless steels. Figure 8.1 shows some of the different target plates prior to assembly of the flyer plate and offset spacer. Each one-dimensional target required some level of preparation before assembly and testing. This included cleaning, annealing the metallic targets, and installation of carbon gages on the impact surface of selected target plates.

Table 8.1: LIHE Driven Flyer One-Dimensional Test Matrix

Spray ID	Test ID	Sample ID	Target Material	Primary Experiment Purpose
TP-2004-06	1	A	6061 Al	Direct Spray Detonation Pressure
	2	B	LEXAN®	Direct Spray Detonation Pressure
	3	C	PMMA	Direct Spray Detonation Pressure
	4*	D	6061 Al	Impulse Delivery/Handling
	5	E	LEXAN®	Material Response/Impulse Delivery
	6	F	PMMA	Material Response/Impulse Delivery
TP-2004-07	7	A	6061 Al	Impact Pressure
	8	B	LEXAN®	Impact Pressure
	9	C	PMMA	Impact Pressure
	10	D	6061 Al	Impulse Delivery/Handling
	11	E	LEXAN®	Material Response/Impulse Delivery
	12	F	PMMA	Material Response/Impulse Delivery
TP-2004-08	13	A	6061 Al	Impact Pressure
	14	B	LEXAN®	Impact Pressure
	15	C	PMMA	Impact Pressure
	16	D	LEXAN®	Material Response/Impulse Delivery
TP-2004-09	17	A	304 SS	Impact Pressure
	18	B	316 SS	Impact Pressure
	19	C	Ni 200	Impact Pressure
	20	D	304 SS	Material Response/Impulse Delivery
	21	E	316 SS	Material Response/Impulse Delivery
	22	F	Ni 200	Material Response/Impulse Delivery
TP-2004-10	23	A	304 SS	Material Response (Dissected)
	24	B	316 SS	Material Response (Dissected)
	25	C	Ni 200	Material Response (Dissected)
	26	D	304 SS	Material Response (Dissected)
	27	E	316 SS	Material Response (Dissected)
	28	F	Ni 200	Material Response (Dissected)
TP-2004-12	29	A	C110 Cu	Material Response (Dissected)
	30	B	C110 Cu	Impact Pressure
	31	C	C110 Cu	Material Response (Dissected)
	32	D	1100 Al	Material Response (Dissected)
	33	E	1100 Al	Impact Pressure
	34	F	1100 Al	Material Response (Dissected)
	35	G	PMMA	Impact Pressure
	36	H	6061 Al	Impact Simultaneity

* No-test due to assembly failure during spray operations

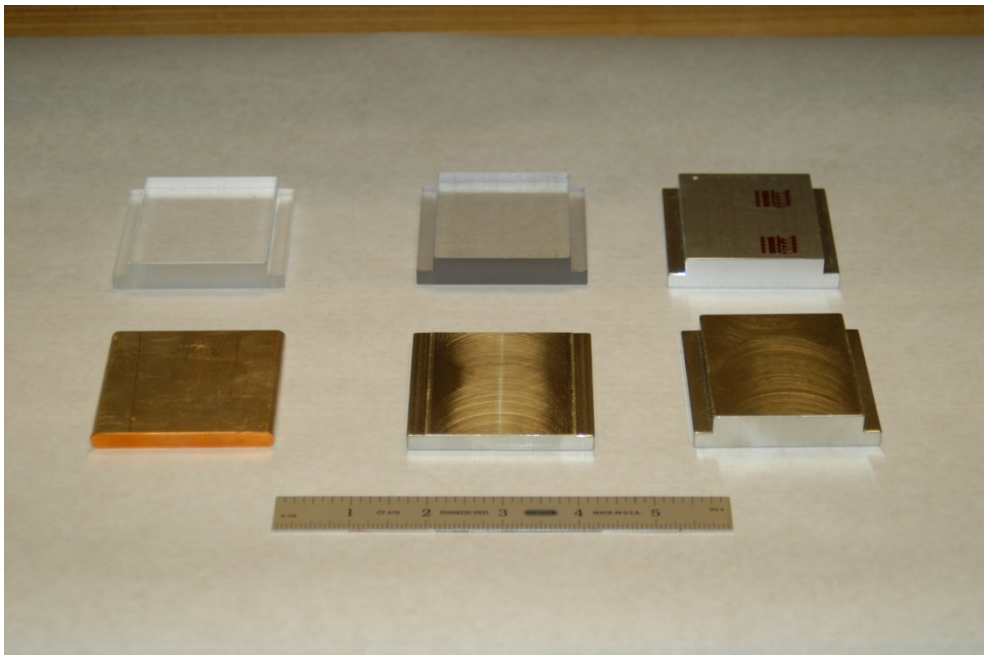

Figure 8.1: One-Dimensional Targets

Annealing is the restoration of a cold-worked or heat-treated metal or alloy to its original properties [48]. This process can increase ductility, reduce hardness and strength, modify the microstructure, or can be used to relieve residual stresses in a manufactured part [22]. The annealing process requires that the sample be heated to a specific temperature, high enough to effect the desired change in material properties. The sample is held or "soaked" at the annealing temperature for a specified time to allow for any necessary transformation reactions to occur. Finally, the sample is cooled to room temperature. This process was necessary for the present investigation because the material history prior to testing was unknown. The annealing step was taken to provide reasonable assurance of a known material starting condition prior to testing.

Thin-film carbon gages (Dynasen Inc. type FC300-50-EKRTE [33]) were installed on sixteen of the target samples to determine the pressure pulse shape and amplitude induced by the flyer impact. The established process of applying a carbon gage

to a surface 1 is similar to that of applying a strain gage to a surface, and was used extensively for this study. The surface of the target was prepared by lapping with 400 grit sand paper and cleaning with alcohol. The gage mounting surface was "roughed-up" with 600 grit sand paper to better grip the adhesive epoxy. A two-part epoxy (HYSOL® RE2038 resin and HD3475 hardener) was mixed and vacuum evacuated to remove any air entrained within the epoxy. The epoxy was then transferred to the mounting surface of the target, as well as the Kapton® backing material of the gage, which was then pressed into place. Pressure was applied to the mounted gage using a vice apparatus, maintaining, as close as possible, the surface planarity (or curvature for a target ring). The epoxy was then cured for a minimum of 12 hours. Finally, an instrumentation cable was soldered to the exposed leads of the carbon gage and the connection covered with a quick setting epoxy for strain relief and protection. The presence of the gage leads and strain relief epoxy voided the free surface boundary condition for these instrumented samples. The final gage package thickness (including epoxy) was approximately 0.13 cm (0.005") to 0.18 cm (0.007").

8.2.2. Flyer Plate Assembly

Four basic steps were required to fabricate each one-dimensional flyer/target assembly. These included fabricating the individual parts (flyer, flyer support, offset spacer, and target plate), building of the flyer subassembly, flyer attachment to the offset spacer, and attachment to the target plate.

The aluminum flyer and flyer support layers were cut to the proper dimensions using a paper shear. Flyer dimensions of 3.81 cm by 3.81 cm (1.5" by 1.5") were carefully measured to maintain a constant flyer area from test to test. Precise initial dimensions of the flyer support layer were not required because the thin foil was trimmed

after assembly to the offset spacer. The offset spacer was manufactured using a wire EDM process, and the target plate was milled to the proper dimensions.

After each of the individual parts were manufactured, the next step was to fabricate the flyer/flyer support subassembly. The 0.0018 cm (0.0007") thick foil flyer support was placed on a clean flat surface and smoothed to eliminate any wrinkles or foreign debris from the surface. Next, 3M™ brand transfer adhesive was applied to one side of the flyer layer, taking special care to avoid air bubbles and wrinkles in the adhesive. The flyer layer was then centered onto the flyer support. Finger pressure was applied to achieve a good bond between the two aluminum layers. Figure 8.2 (a) shows the 14.52 cm^2 (2.25 in^2) flyer layer and Figure 8.2 (b) the assembled composite flyer/flyer support subassembly.

(a) 0.030 cm (0.012") Flyer Layer **(b)** 0.033 cm (0.013") Composite Flyer Assembly

Figure 8.2: Flyer/Flyer Support Subassembly

At this point, the flyer/flyer support subassembly was ready to be fixed to the offset spacer. The offset spacer was placed in a well-ventilated area and one side sprayed with a thin layer of 3M™ Super 77 brand spray adhesive. With the flyer/flyer support

subassembly placed on a clean flat surface, the spacer, adhesive side down, was pressed in place onto the exposed flyer support layer. Care was taken to center, as close as possible, the flyer plate within the offset spacer window. At this point, the excess flyer support foil around the outside of the offset spacer was trimmed. The offset spacer and flyer assembly is shown in Figure 8.3 (a) and the assembled flyer/offset spacer subassembly in Figure 8.3 (b).

(a) Al Flyer Subassembly and Offset Spacer **(b)** Flyer/Offset Spacer Assembly

Figure 8.3: Flyer/Offset Spacer Subassembly

The final step in the assembly process was to couple the flyer/offset subassembly to the target plate. At this point, the flyer was quite fragile due to the very thin foil used for the flyer support, and extreme care was taken not to damage the flyer or support layers. 3M™ transfer adhesive was applied to the target side of the offset spacer. The flyer/offset subassembly was centered on the target surface and carefully press fit into place. Finally, aluminum tape was used to secure the offset spacer to the target plate. The purpose of this tape was to assure that the flyer/offset spacer remain attached to the target during spray and handling operations. The necessity of this step became apparent during the first spray operation, where in the absence of this precaution, the offset spacer for sample #4 separated from the target during the spray, falling to the spray booth floor.

While nothing detrimental happened as a result of this event (other than losing the experiment) the possibility existed that the falling explosive covered piece could have detonated on impact, potentially causing greater damage to the facility or other experiments in the spray booth. Figure 8.4 (a) shows the assembled flyer/offset/target assembly prior to application of the aluminum tape, and Figure 8.4 (b) with the tape precaution in place.

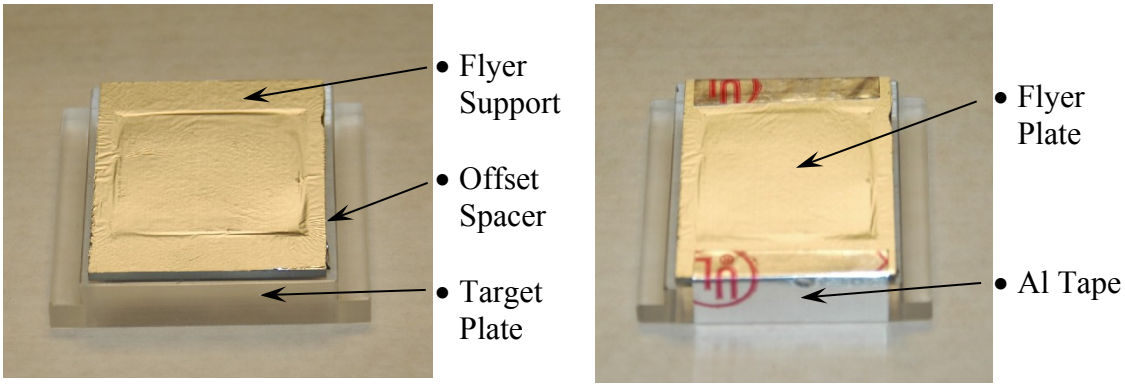

(a) Flyer Assembly to Target **(b)** Complete Flyer/Target Assembly

Figure 8.4: One-Dimensional Flyer/Offset/Target Assembly

8.2.3. Explosive Spray

Ideally, an explosive deposition would be calculated to produce the desired flyer velocity profile, which would in turn produce the desired impulse loading profile. Instead, for this study the achieved deposition was used to predict the flyer velocity, impact pressures, and delivered impulse—given the chosen flyer material and thickness.

Explosive deposition was measured using the coupon technique described in section 3.5. Coupons were placed on the aluminum masking between target assemblies to ascertain an average deposition on the flyer surface. These coupons were weighed at the end of spray operations to determine the final deposition. Additionally, most target assemblies were weighed independently of the coupons to determine an approximation of

explosive accumulation. In general, the two deposition measurements were comparable. The exceptions to this step were the heavier stainless steel samples (~375 grams), where explosive deposition (~0.73 grams) was a small fraction (~0.2%) of the total weight of the target assembly.

Regardless of deposition magnitude, it was desired that the explosive only be sprayed over the 14.52 cm^2 (2.25 in^2) area of the flyer. In order to deposit explosive on the desired area, masks were employed during the spray process to shield the areas where explosive was not wanted. These masks were generally made of aluminum sheet and attached to the spray surface using magnets. After the proper amount of explosive had been applied to the spray surface, the deposition was halted. At this point, the masking was removed leaving the explosive on the flyer surface, with minimal overspray. Removal of an aluminum mask is shown in Figure 8.5.

Figure 8.5: Aluminum Mask Removal

Spraying, explosive deposition measurement, masking, and remote handling operations for the one-dimensional testing were completed successfully, showing only minor issues in a few cases. Table 8.2 below lists the explosive deposition for each target sample and its expected flyer performance. Tests #1, #2, and #3 were direct spray experiments (no flyer plate) to determine the detonation pressure of the SASN against a target material, as well as the impulse delivered from just the explosive layer.

8.2.4. Handling

Each of the one-dimensional flyer experiments required handling within close proximity by the author (a qualified explosive operator). For safety reasons, and due to the relatively small explosive capacity of the SBPA, each sample could have no more than 1.0 grams (0.002 lb) of total explosive deposition. In addition, the target assemblies had to be small enough to be handled by the master/slave manipulator arms for weighing and removal from the spray booth.

After spray operations were complete, each sample was removed from the spray backboard, where it was held in place by magnets, using the master/slave manipulators. This operation is shown in Figure 8.6. The sample was then placed on the spray booth digital scale for weighing. Each sample was then removed from the spray booth to a grounded, explosive rated metal case for transfer to the SBPA location. The closed case was hand carried ~6.1 m (~20') to the SBPA room and re-grounded at that location. The samples were removed from the case in a small polycarbonate tray to the sun-tanning array location beneath the SPBA. Placement of the individual test assemblies on the pendulum mass was aided by a metal "spatula" to keep the explosive operator's hands out of direct contact with the explosive and target assembly.

Table 8.2: One-Dimensional Explosive Deposition and Expected Performance

Spray ID	Test ID	Sample ID	Target Material	ρ_A (mg/cm^2)	Expected V_f (cm/s)	Expected I_{sp} (taps)
TP-2004-06	1	A	6061-T651 Al	46.47	N/A	3247
	2	B	LEXAN®	45.48	N/A	3166
	3	C	PMMA	43.87	N/A	3033
	4	D	6061-T651 Al	No Test		
	5	E	LEXAN®	45.82	27326	3006
	6	F	PMMA	42.78	25577	2900
TP-2004-07	7	A	6061-T651 Al	50.70	30053	3618
	8	B	LEXAN®	50.70	30053	3241
	9	C	PMMA	50.70	30053	3322
	10	D	6061-T651 Al	41.50	24829	3134
	11	E	LEXAN®	44.35	26485	2946
	12	F	PMMA	41.05	24564	2802
TP-2004-08	13	A	6061-T651 Al	50.80	30108	3625
	14	B	LEXAN®	53.70	31683	3450
	15	C	PMMA	50.75	30081	3324
	16	D	LEXAN®	50.24	29800	3208
TP-2004-09	17	A	304 SS	54.65	32192	4419
	18	B	316 SS	54.65	32192	4419
	19	C	Ni 200	54.65	32192	4527
	20	D	304 SS	45.85	27343	3845
	21	E	316 SS	45.85	27343	3196
	22	F	Ni 200	45.85	27343	3935
TP-2004-10	23	A	304 SS	53.35	31495	4339
	24	B	316 SS	53.35	31495	4339
	25	C	Ni 200	53.35	31495	4447
	26	D	304 SS	44.45	26543	3755
	27	E	316 SS	44.45	26543	3755
	28	F	Ni 200	44.45	26543	3836
TP-2004-12	29	A	C110 Cu	35.30	21094	3086
	30	B	C110 Cu	35.30	21094	3086
	31	C	C110 Cu	35.30	21094	3086
	32	D	1100 Al	35.00	20908	2763
	33	E	1100 Al	35.00	20908	2763
	34	F	1100 Al	35.00	20908	2763
	35	G	PMMA	35.30	21094	2503
	36	H	6061-T651 Al	35.30	21094	2782

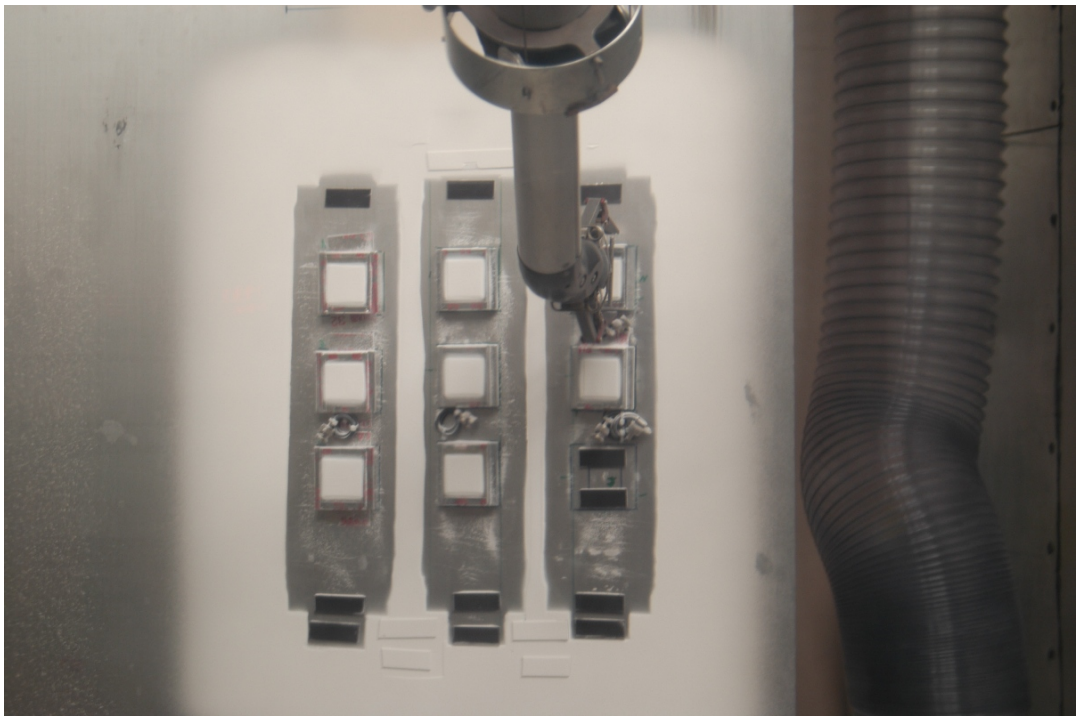

Figure 8.6: Master/Slave Manipulator Handling of a Target Assembly

Safe operating procedures were explicitly followed with each handling step in the investigation. At no point were there any handling issues or problems that were not anticipated and planned for.

8.2.5. Explosive Test Apparatus

The small bank pendulum apparatus, described in section 5.3.2, was utilized to fire each of the one-dimensional flyer experiments. The SBPA was capable of accommodating a single flyer experiment per capacitor discharge, measuring rigid body motion of the pendulum mass to determine the delivered total impulse by the flyer impact. As discussed, a holder was fabricated to hold the target in place on the pendulum face, as well as provide a 0.635 cm (0.25") gap behind the target to allow for spall if applicable. Each of the material target assemblies were designed to be fired by the 10kV, two-wire, light array of the SBPA. The light array's small size required that the explosive deposition area be no greater than the 14.52 cm^2 (2.25 in^2) of the flyer design. Figure 8.7

shows the SBPA in the flyer experiment configuration. In the picture, a braided shorting strap is in place across the leads of the light array for safety purposes. This strap is removed prior to capacitor bank discharge for explosive test operations.

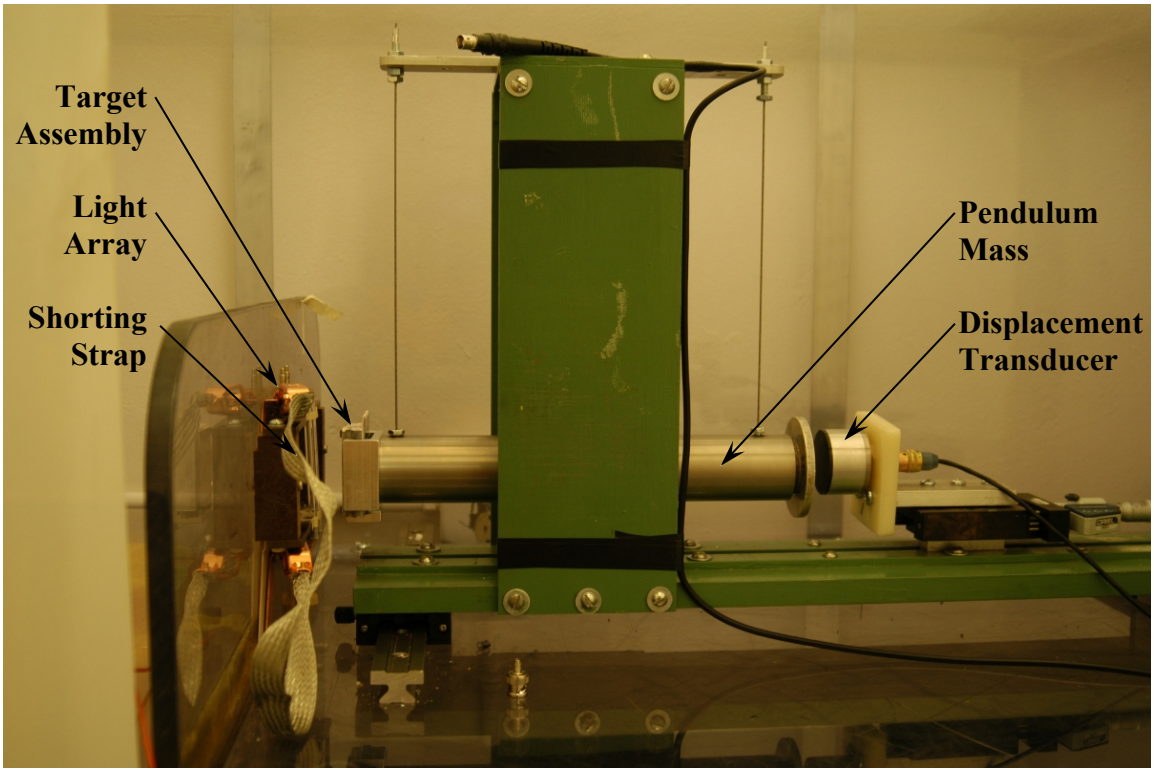

Figure 8.7: Small Bank Pendulum Apparatus for Flyer/Target Assembly Firing

The process for firing the flyer/target assembly on the SBPA was similar to firing a coupon. After sample movement to the SBPA room, the explosive was sun-tanned by a small bank of UV lights for five minutes. Next, the target assembly was picked up with a steel spatula by means of the magnets which held the assembly to the backboard for spraying. Excess explosive overspray was carefully cleaned from the non-flyer surfaces with a wet cotton swab. The flyer/target assembly was then carefully positioned in the target holder on the 5.085 kg (11.2 lb) pendulum mass, shown in Figure 8.8 detached from the SBPA. If carbon pressure gages had been installed on the target, the cabling was

connected to the data recording system in the SBPA instrumentation rack. At this point, the explosive operator closed the LEXAN® enclosure, exited the SBPA room, armed the instrumentation system, charged the capacitor bank, and conducted the test.

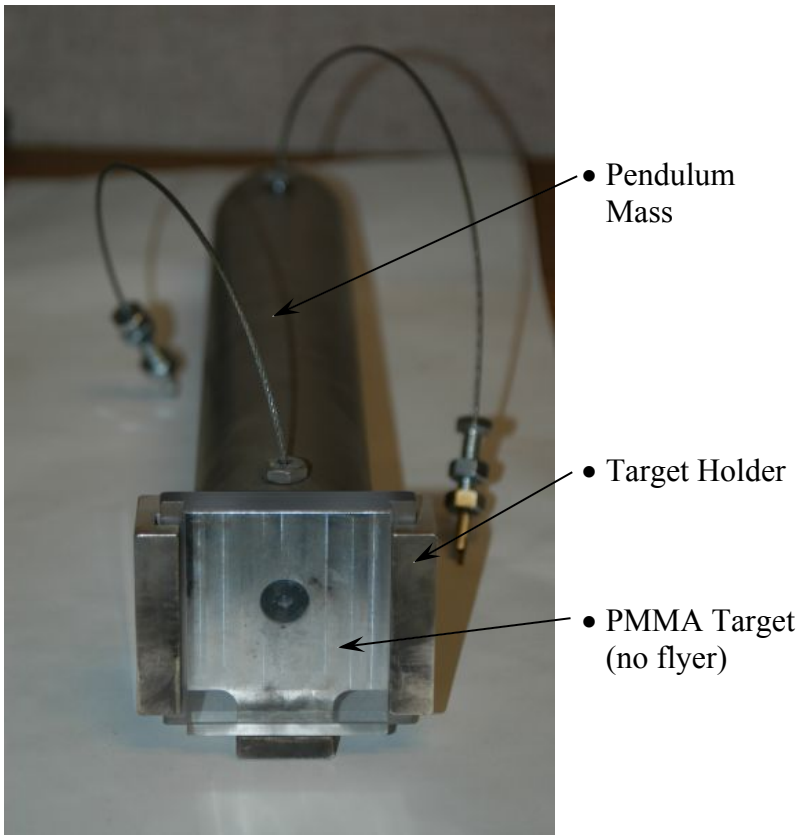

Figure 8.8: 5.085 kg (11.2 lb) Ballistic Pendulum Mass and Target Holder

8.2.6. One-Dimensional Problems and Errors

Three notable issues were found during the one-dimensional flyer tests. First, it was found during the investigation that a high degree of precision in the placement of the explosive masking was required. On the TP-2004-08 spray, target masking for test samples A, B, and C was slightly skewed, resulting in a non-symmetric explosive deposition on the flyer. This skewed deposition possibly resulted in errors in the determination of the impact area and the total delivered impulse by the flyer. As will be

seen in Chapter 9, these three samples measured a significantly higher than expected delivered impulse, and corresponding flyer velocity.

Second, pressure data from a number of tests was incorrectly recorded or not collected at all due to partial instrumentation failures. Specifically, triggering issues caused the pulse power supply, required for the carbon gage instrumentation circuit, to not power the gage at the proper time. The result appeared to be a trigger failure of the recording digitizer, but further investigation yielded an improper cable connection as the culprit. Despite losing the pressure data, the majority of these unsuccessful tests yielded other useful information, such as total delivered impulse.

8.3. Two-Dimensional Flyer Testing

Five LIHE flyer impulse tests were conducted with ring structure targets over two spray operations. The purpose of these tests was to employ the LIHE driven flyer technique to induce a cosine distributed impulse load over half of the ring surface. Impulse load diagnostics included x-ray analysis as well as comparison of the measured ring strain response with the H-W analytical solution. Data was successfully collected on all five of the tests, though two are considered no-tests due to a malfunction of the large bank light array. Table 8.3 lists the five tests conducted.

Table 8.3: LIHE Driven Flyer Research Two-Dimensional Ring Test Matrix

Spray ID	Test #	Sample ID	Target Material	Purpose
TP-2005-14	37	Ring 1	6061-T651 Al	Strain Response
	38	Ring 2	LEXAN®/Al	Material Response
TP-2005-15	39	Ring 3	6061-T651 Al	Strain Response
	40	Ring 4	6061-T651 Al	Strain Response
	41	Ring 5	6061-T651 Al	Strain Response

8.3.1. Target Ring Preparation

As discussed in Chapter 7, two 20.32 cm (8.0”) diameter target ring configurations were used for the two-dimensional testing. Both configurations were

instrumented with three strain gages located on the inner surface of the ring at the 90º, 180º, and 270º positions. Three of the four simple aluminum ring structures were instrumented with carbon pressure gages on the impact surface at the -30º, 0º, and 30º positions. Carbon gages were not used on the composite ring structure.

Each of the aluminum ring structures was fabricated from stock 6061-T651 seamless tubing. The seamless condition was important to avoid stress wave reflections in the ring membrane response, making comparison to the H-W difficult or impossible. The individual components of the composite ring were machined from stock materials. The aluminum substrate was turned from 6061-T651 aluminum tubing, and the polycarbonate outer layer was machined from 3.81 cm (1.5") thick LEXAN® sheet. The two layers were assembled with an adhesive layer of silicone rubber, maintaining concentricity between the aluminum and polycarbonate layers. Instrumentation was applied to the ring structures in a similar method to that described in section 8.2.1. Figure 8.9 shows an instrumented aluminum ring (ready for flyer assembly).

8.3.2. Flyer/Target Ring Assembly

The flyer/target ring assembly began with the fully instrumented target ring. The two guard rings, used to support the flyer during spraying and handling operations, were secured to the target ring using a two-part dental cement. Four dabs at the inner surface, at the 45º, 135º, 225º, and 315º locations, were sufficient to secure the guard rings to the target ring. Care was taken to maintain a constant outer diameter surface between the guard rings and the target ring. In addition, an approximately 0.13 cm (0.05") gap was left between the target ring and each guard ring to allow the carbon gage leads to snake from the outer ring surface to their solder point on the inner surface.

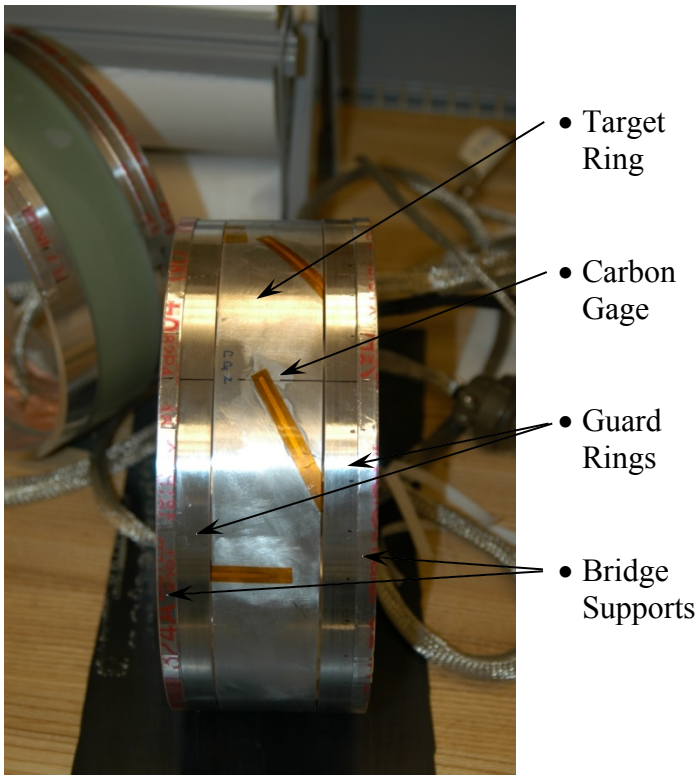

Figure 8.9: Target Ring with Instrumentation (and Guard Rings) Applied

The next step was to assemble the bridge support pieces. The bridge supports form the variable gap required to achieve a simultaneous flyer impact at the target surface. The bridges were fabricated as a buildup of 0.127 cm (0.005") thick layers of 6.35 cm (2.5") wide aluminum tape. Given the required gap calculated in Chapter 7 and adding the thickness of the flyer, the gap was broken into segments equating to the nearest 0.127 cm (0.005") of required offset gap distance. Each segment corresponded to a linear length around the circumference of the ring. Layers were built up until the desired offset bridge profile was achieved. Once the layers of the bridge support were assembled, the lay up was cut into a width of approximately 0.63 cm (0.25") using a paper shear, prior to placement on the guard rings. The bridge pieces were assembled to each guard ring by means of the tape's own lower-most adhesive layer, taking special care to maintain alignment of the 0º location on the test ring to that of the bridge support

pieces. Figure 8.10 shows the profile of the bridge support pieces as fixed to the guard ring surfaces. These photographs emphasize the relatively small maximum gap of slightly over 0.10 cm (0.039”), as compared to the size of the ring structures and flyer assemblies.

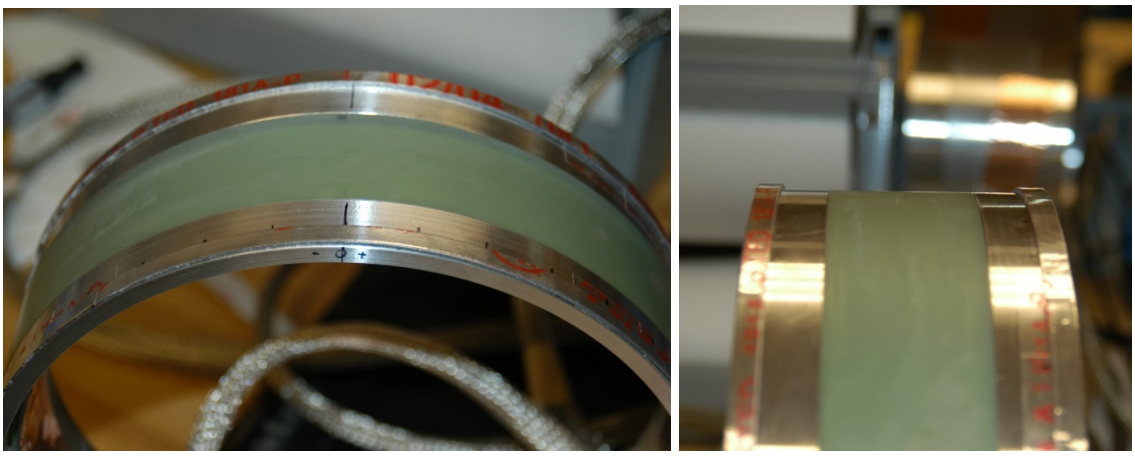

Figure 8.10: Bridge Support Assembled to Guard Rings

At this point, a depth gage was employed to measure the precise gap at increments of 10º around the target impact surface. Any deviations from the desired gap were corrected with additional layers of aluminum tape. This gap measurement and correction process was repeated until the desired gap was achieved. Figure 8.11 plots the measured gap achieved for the ring tests 3, 4, and 5.

With the target and guard rings assembled, and the bridge supports in place, the assembly was ready for the flyer itself. The flyer size was dictated by the size of the ring that was being impacted. As discussed earlier, the ring size chosen for this testing is 20.32 cm (8.0”) in diameter and 3.81 cm (1.5”) wide. Requirements for the flyer size was that it must fully cover half of the ring circumference [31.92 cm (12.57”)] and at least the full width of the ring. To satisfy these constraints, a flyer size of 33.0 cm (13.0”) by 5.72 cm (2.25”) was chosen. The chosen flyer width impacted the full width of the ring, along with a portion of both guard rings, and aided in the fracture of the dental cement

connecting the flyer and guard rings. The thin foil aluminum flyer support layer was cut to a minimum width of 7.62 cm (3.0") to fully engage the bridge supports on both guard rings, and cut to a length slightly longer than half of the circumference of the ring.

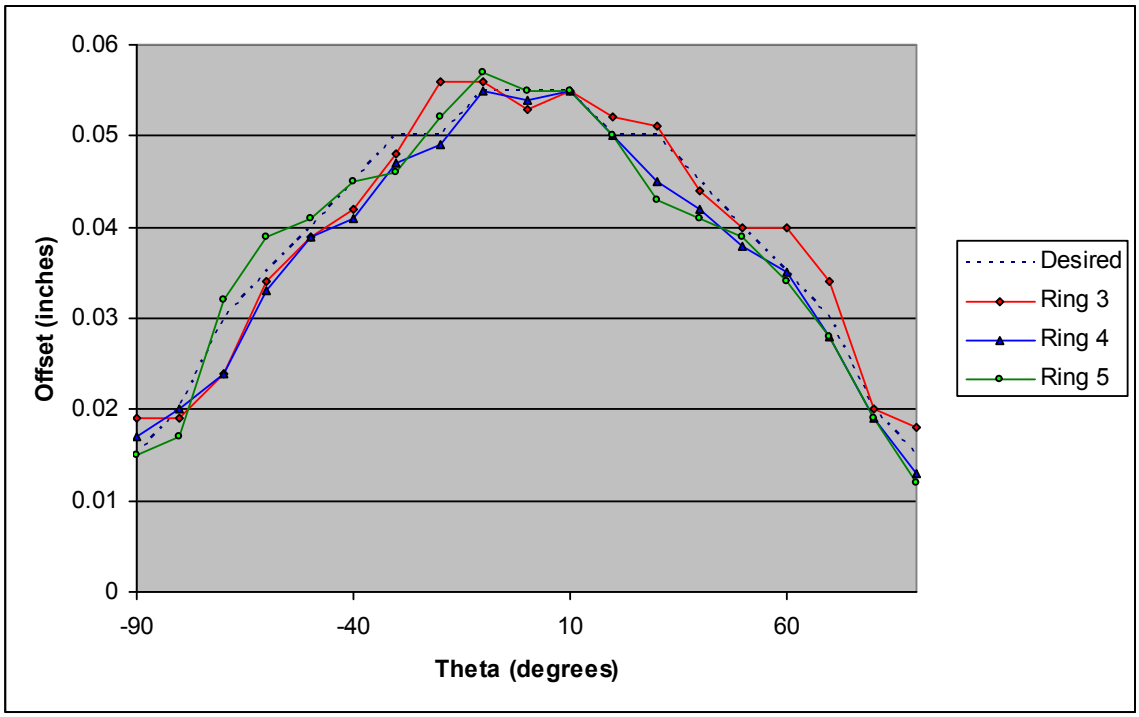

Figure 8.11: Achieved Offset Gap Profile for Rings 3, 4, and 5

The flyer support layer was placed on a clean, flat surface and smoothed to remove any wrinkles or debris. In a well-ventilated area, 3M™ Super 77 brand adhesive was sprayed onto the flyer layer. The flyer was then centered and press-assembled onto the flyer support foil. The flyer/flyer support assembly, shown in Figure 8.12, was fixed to the bridge supports using 3M™ brand transfer adhesive. This adhesive was placed on the bridge support surface and trimmed to the width of the bridge support. Working with two other facility personnel, the 0º location on the ring assembly was placed in contact with the 0º location on the still flat, exposed flyer support portion of the flyer/flyer support assembly. The ring was then rolled onto one side of the flyer, making sure that

the flyer layer didn't touch the bridge support at any point. A small piece of masking tape, shown in the fully assembled flyer/target ring assembly in Figure 8.13, was used to secure the end of the flyer to the guard rings using the flyer support extension beyond the 90º location. This prevented the flyer from lifting away from the bridge supports during spray and handling. Finally, the other half of the flyer was applied to the bridge supports and secured. At this point, the flyer/target ring assembly was ready for spray.

Figure 8.12: Flyer/Flyer Support Assembly

Figure 8.13: Assembled Flyer/Target Ring Assembly

8.3.3. Explosive Spray

Two spray operations, TP-2005-14 and TP-2005-15, were required to spray the five different ring test samples. In both sprays, the expected maximum explosive deposition at the 0º location was 31.12 mg/cm^2. After spraying, each flyer/ring test assembly had approximately 2.0 grams of total explosive deposition, in an achieved cosine distribution of ~31.1 mg/cm^2 at the 0º location varying to a zero deposition at the ±90º locations.

For spray operations, multiple ring structures were stacked on their sides, forming a cylindrical spray surface. The spray was accomplished by making multiple passes along a single vertical trajectory at 15º increments, where the stacked rings were rotated between passes by means of a computer controlled turntable located beneath the cylindrical structure. Coupons were placed at various locations between test rings to determine explosive deposition and distribution. Figure 8.14 shows coupon weighing activities during the spray operation, where two flyer experiments are positioned in the lower two ring positions and direct spray rings located in the upper three ring positions.

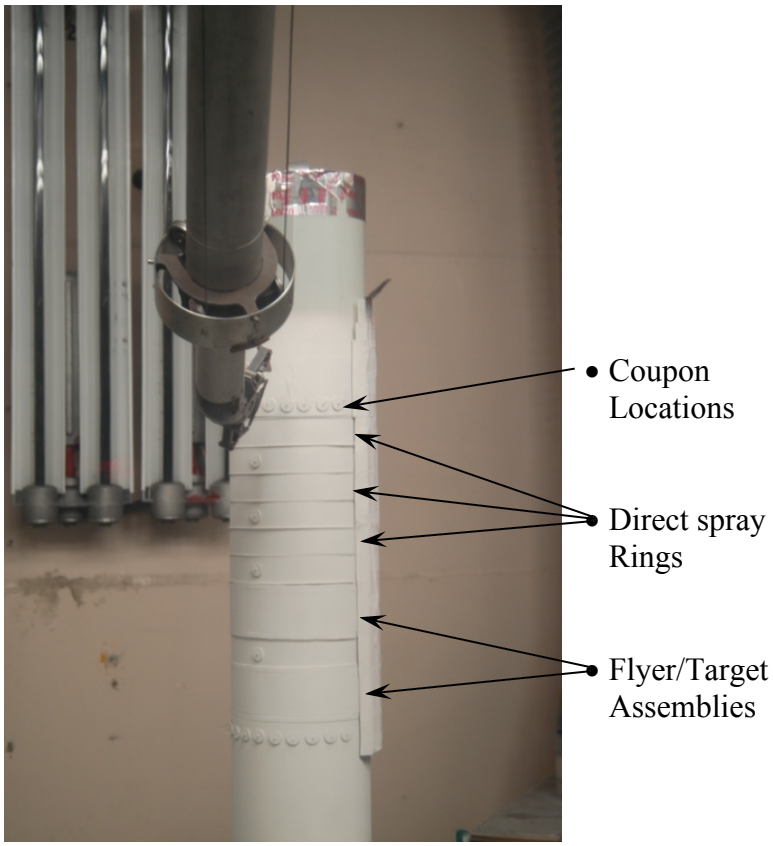

Figure 8.14: Stacked Ring Structures for Explosive Spray

The explosive deposition achieved in TP-2005-14 and TP-2005-15 accounted for approximately 99.3% and 100.5%, respectively, of the expected loading with the proper cosine loading in both sprays. The achieved explosive deposition on the spray target for both spray operations, as measured by coupons placed near the flyer surfaces is given in Figure 8.15. Again, the design deposition for these spray operations was cosine distributed to achieve a cosine distributed impulse load on several direct spray rings that were not part of this investigation. (The results of these direct spray tests are not reported here.) But, it should be noted that the difference in spray deposition, calculated in Chapter 7, required for a flyer delivered cosine distributed impulse and a direct spray cosine loading is small. The primary difference in the two methods is that the flyer will deliver a greater impulse, and higher peak pressure, for the same explosive load.

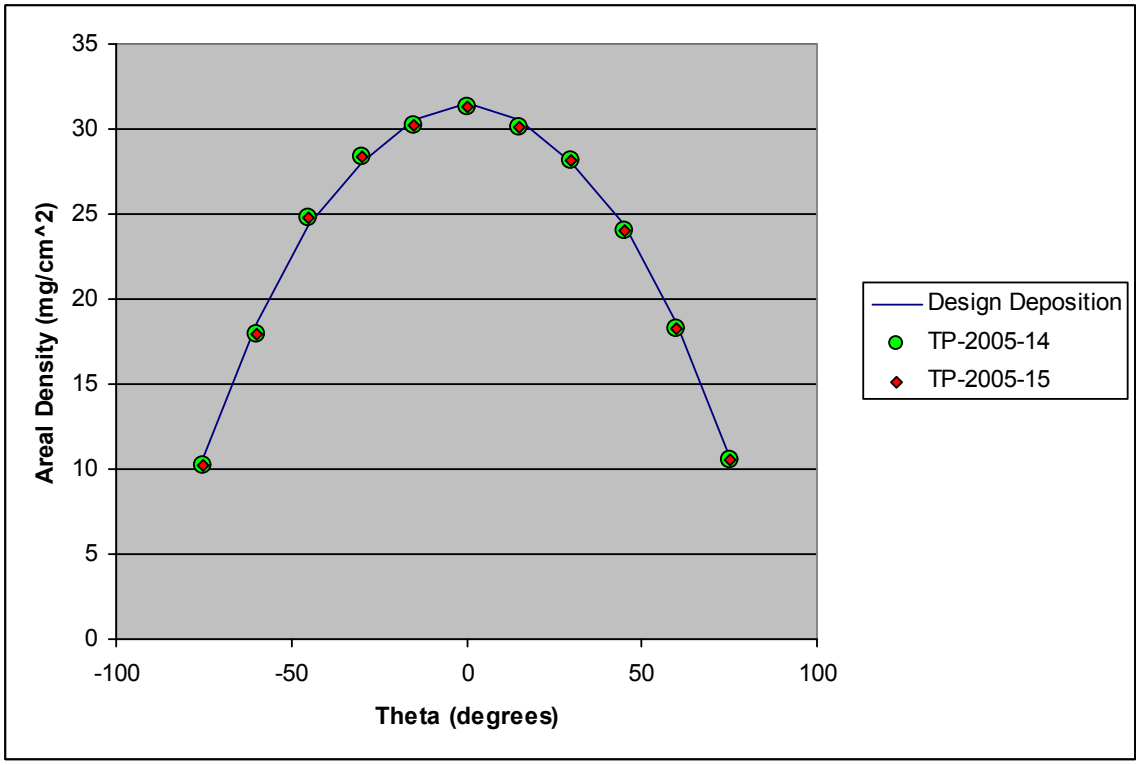

Figure 8.15: Ring Test Achieved Cosine Distributed Explosive Deposition.

Five coupons were test fired on the SBPA from each explosive formulation and spray. The explosive performance for the two spray operations is given in Figure 8.16. While both sets of the coupon firing results indicate reasonable explosive performance, with all of the coupon data points falling within the expected tolerance bounds, the average performance of the TP-2005-14 explosive was on average 7.8% below the expected performance. The explosive formulation for TP-2005-15 was on average, exactly predicted by the explosive calibration curve. From this data, it was predicted that the flyer performance, as a function of areal density, would follow equations 5.11 and 5.12 with the caveat that the impulse as a function of areal density portion of the equations be lowered by 7.8% for the TP-2005-14 experiments. Therefore, the performance expectation for the flyer plate impact was a reasonably cosine distributed impulse load, of nearly the design amplitude, for each of the ring structures.

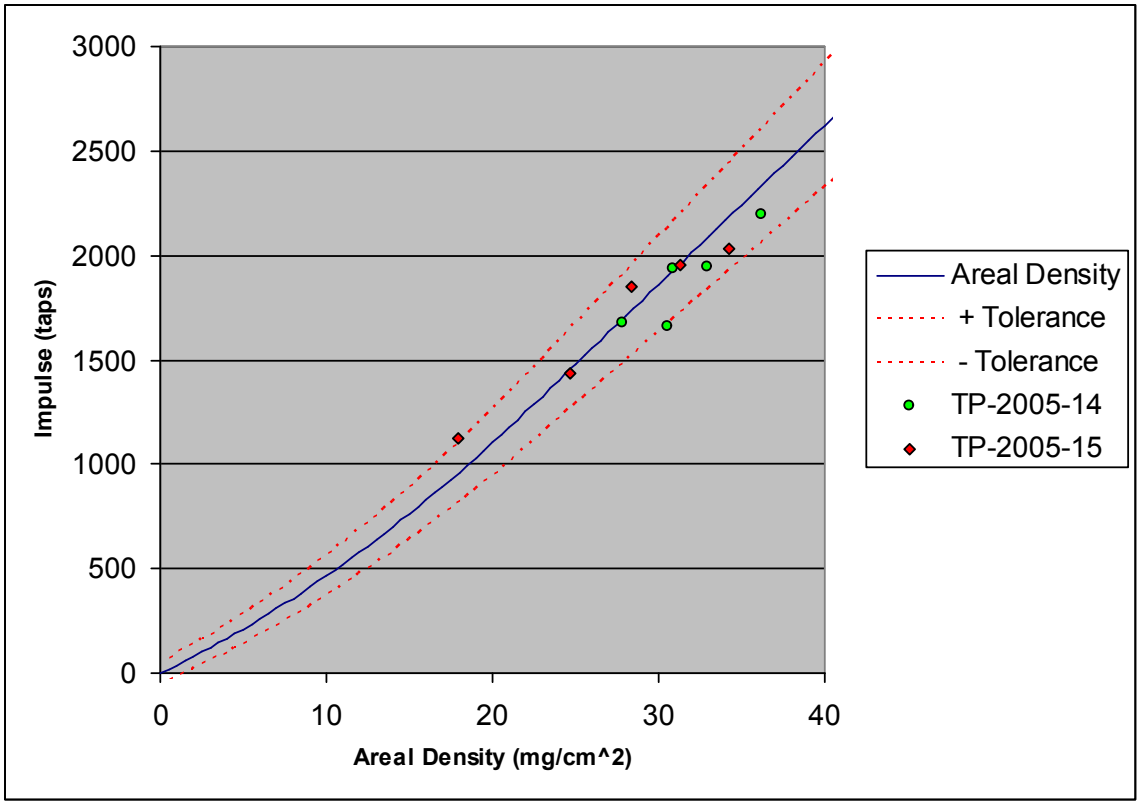

Figure 8.16: Ring Test Explosive Performance

The achieved explosive deposition and explosive performance predicts the flyer performance presented in Table 8.4. As discussed, the predicted flyer velocity and impulse vary from the design velocity and impulse based on the actual explosive deposition achieved during the spray.

Table 8.4: Predicted Flyer Performance for Achieved Explosive Deposition

		TP-2005-14		TP-2005-15	
	Diagnostic	**Value**	**Predicted load (Taps)**	**Value**	**Predicted load (Taps)**
Design Load		**31.12**	**2320**	**31.12**	**2320**
Explosive Deposition	Coupon Weight	30.91	2298	31.3	2331
Explosive Performance	Coupon Firing	92.2%	2169	100%	2331

8.3.4. Handling

After spray operations and explosive conditioning operations were completed, handling of the flyer/target ring assemblies was accomplished remotely using the master/slave manipulators. Each test ring assembly was carefully picked up by the non-explosive side of the ring and hung, by an attached loop of waxed string, on an aluminum hook hanging from the monorail trolley. Next, the instrumentation cabling, which was placed interior to the stacked rings for the spray, was removed and placed on another hook attached to the trolley. Figure 8.17 (a) shows the composite flyer/target ring assembly being lifted from its spray location, and Figure 8.17 (b) shows the assembly being placed on the trolley hook.

(a) Master/Slave Handling of Ring **(b)** Placement of Ring on Trolley Hook

Figure 8.17: Flyer/Ring Test Assembly Handling

The ring was then moved forward towards a bank of UV lights on the spray booth doors to sun-tan the explosive surface for 5 minutes. During this movement, the monorail trolley advanced very slowly to avoid jostling the test ring assembly, which could have resulted in explosive falling off of the spray surface. After tanning was completed, the spray booth doors to the test cell were opened, and the ring continued its trek to the large bank light array in the test cell. Once at the light array, the ring assembly was positioned at approximately 10.2 cm (4.0”) from the closest element, and the trolley locked in place. The spray booth doors were then closed to shield the remaining explosive in the booth from the light and shock of the explosive test.

After the test ring assembly was in place, a qualified explosive operator entered the test cell to hook-up the ring instrumentation to the facility data recording system. All safety precautions and procedures were followed for this operation. The operator wore the proper PPE, and was grounded to prevent any static discharge to the instrumentation cable or ring assembly.

8.3.5. Explosive Test Apparatus

The large bank light array, introduced in section 3.7, was utilized to fire each of the two-dimensional flyer experiments. Two (of the available six) capacitor bank modules were used to initiate the explosive deposited on the flyer surface. Each module was charged to 40 kV and powered six elements (tungsten wires strung in quartz tubes). Prior to movement of the flyer/target ring assembly, paper and aluminum foil reflectors were positioned around the light array to enhance the energy transfer from the array to the explosive. Figure 8.18 shows the setup of the array with a simple aluminum ring (without guard rings, flyer, or instrumentation cabling) at the test location.

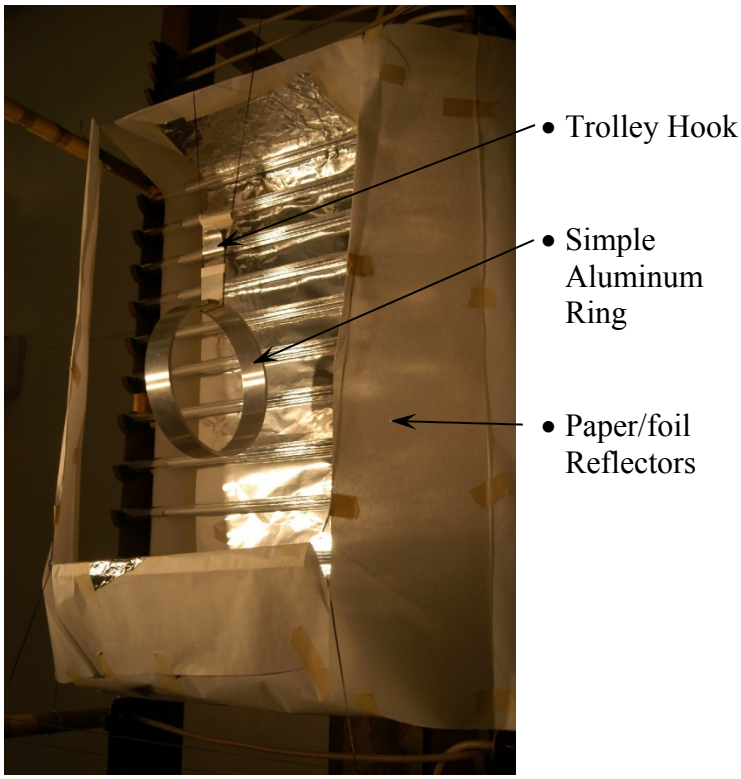

Figure 8.18: Simple Aluminum Ring in Front of Light Array

While the large bank light array can accommodate a test item of significantly larger size than was being used with the current flyer experiments, only one ring experiment per capacitor discharge was tested. Measurement of the rigid body motion of the target ring was accomplished by the flash x-ray system, giving three positions of the ring at known times. The LIHE facility instrumentation system recorded the strain response of the ring, and if present, the impact pressure from the carbon gages.

The process for firing the flyer/target ring assembly on the large bank light array was somewhat more complicated than firing a sample on the SBPA. In this case, preparation of the entire facility was involved. Personnel were accounted for in specified areas, blast doors were interlocked to prevent entry to hazardous areas, such as the test cell or capacitor bank room, and the fenced area around the facility was monitored to prevent unauthorized personnel from encountering a hazardous situation. With personnel

accounted for, the capacitor bank operator charged each module to 40 kV. This operation took several minutes, and required the presence of two personnel to assure that each step in the process was properly done in the correct order. During this charging period, camera lighting was energized, final checks with the instrumentation room personnel were made, and final checks of capacitor bank instrumentation were conducted. Finally, the operator triggered a sequencer which in turn initiated a series of events within the capacitor bank system, culminating in the discharge of the bank through the light array and initiation of the explosive.

8.3.6. Two-Dimensional Problems and Errors

One serious problem occurred during the second set of two-dimensional flyer/ring tests. The first two experiments from spray TP-2005-15 resulted in no-tests due to a partial failure of the light array. It was found that a reflector configuration involving aluminized Mylar® tape and the aluminum foil behind the quartz tubing resulted in a favorable electrical path exterior to the quartz tube. The result was that the electrical energy bypassed the tubing and did not initiate the explosive on the flyer surface as designed. Instead, a portion of the explosive was initiated by a part of the light array that was working correctly, causing a sweeping detonation wave across the surface of the flyer. The result was a load that was not simultaneous over the surface and likely not impulsive to the structure. After an intense investigation, the problem was found and corrected prior to the final ring test.

9. ONE-DIMENSIONAL EXPERIMENTAL RESULTS AND DISCUSSION

Thirty-six flyer experiments to investigate and validate LIHE driven flyer impulse generation technique were planned. Of these planned tests, thirty-five were successfully conducted with a high rate of data recovery. In all cases tested, the impulse delivered by the flyer to the target plate was recorded by the SBPA instrumentation system. Data recovery for the tests where impact pressure was measured by thin film carbon gages was less successful, with partial failures occurring in three of thirteen tests. Material response data was collected for each of the target materials, as well as comparison data from unshocked standards for each of the metallic materials.

The test matrix evolved during the experimental phase to adapt to unexpected events, such as instrumentation failures, with each experiment having one or more functions towards the overall goals of the investigation. The final matrix consisted of three direct spray experiments, two tests for scoping purposes, thirteen pressure measurement experiments, and eighteen material response experiments. Each experiment in the test matrix is summarized below in Table 9.1.

Six spray operations (TP-2004-06, -07, -08, -09, -10, and -12) were required to complete the thirty-five successful tests. Sprays TP-2004-06, -07, and -08 primarily involved scoping experiments to work out feasibility and handling issues. Impact and detonation pressures, impulse delivery, and material response data were collected with 6061 aluminum, LEXAN®, and PMMA targets. Sprays TP-2004-09, -10, and -12 again utilized the developed one-dimensional flyer configuration. Lessons learned in the earlier sprays were implemented to conduct material response and impact pressure experiments with stainless steel, nickel, copper, and 1100 aluminum targets. Target samples dissected

for changes in grain structure and hardness were generated from this latter group. The final test in this series measured flyer impact simultaneity at the target surface.

Table 9.1: One-Dimensional Test Matrix

Spray ID	Test ID	Sample ID	Target Material	Primary Experiment Purpose
TP-2004-06	1	A	6061 Al	Direct Spray Detonation Pressure
	2	B	LEXAN®	Direct Spray Detonation Pressure
	3	C	PMMA	Direct Spray Detonation Pressure
	4	D	6061 Al	Impulse Delivery/Handling
	5	E	LEXAN®	Material Response/Impulse Delivery
	6	F	PMMA	Material Response/Impulse Delivery
TP-2004-07	7	A	6061 Al	Impact Pressure
	8	B	LEXAN®	Impact Pressure
	9	C	PMMA	Impact Pressure
	10	D	6061 Al	Impulse Delivery/Handling
	11	E	LEXAN®	Material Response/Impulse Delivery
	12	F	PMMA	Material Response/Impulse Delivery
TP-2004-08	13	A	6061 Al	Impact Pressure
	14	B	LEXAN®	Impact Pressure
	15	C	PMMA	Impact Pressure
	16	D	LEXAN®	Material Response/Impulse Delivery
TP-2004-09	17	A	304 SS	Impact Pressure
	18	B	316 SS	Impact Pressure
	19	C	Ni 200	Impact Pressure
	20	D	304 SS	Material Response/Impulse Delivery
	21	E	316 SS	Material Response/Impulse Delivery
	22	F	Ni 200	Material Response/Impulse Delivery
TP-2004-10	23	A	304 SS	Material Response (Dissected)
	24	B	316 SS	Material Response (Dissected)
	25	C	Ni 200	Material Response (Dissected)
	26	D	304 SS	Material Response (Dissected)
	27	E	316 SS	Material Response (Dissected)
	28	F	Ni 200	Material Response (Dissected)
TP-2004-12	29	A	C110 Cu	Material Response (Dissected)
	30	B	C110 Cu	Impact Pressure
	31	C	C110 Cu	Material Response (Dissected)
	32	D	1100 Al	Material Response (Dissected)
	33	E	1100 Al	Impact Pressure
	34	F	1100 Al	Material Response (Dissected)
	35	G	PMMA	Impact Pressure
	36	H	6061 Al	Impact Simultaneity

9.1. Post-Test Hardware Inspection

Post-test inspection of the flyer plates showed minimal explosive-caused damage to the flyer surfaces. In no case was the flyer thickness breached or significantly damaged by the explosive detonation. Many of the flyers indicated post-test impacts with the light array and SBPA enclosure [Figure 9.1 (a)], occurring after rebound from the target. These secondary impacts did not affect the results of the flyer-delivered impulse or target response. In all cases, the flyer surface showed evidence of good detonation patterns [Figure 9.1 (b)], indicating a nearly simultaneous explosive detonation over the surface of the flyer. The explosive side of the flyer surface showed slight damage to the 0.0018 cm (0.0007") thick flyer support aluminum foil layer in the form of localized pitting and scarring.

(a) Post-Test Flyer Inspection (b) Detonation Pattern

Figure 9.1: Post-Test Flyer Inspection

Nearly all of the one-dimensional flyer experiments exhibited a width of approximately 0.38 cm (0.15") around the edges of the flyer where the flyer material was uniformly curled away from the target impact. Inspection of the target surfaces indicated that a full 3.81 cm (1.5") square area was impacted by the 3.81 cm (1.5") square flyer, though a reduced area, of approximately 3.43 cm (1.35") square, showed a slightly more

pronounced impact marking. It is unknown if this edge deformation occurred as a result of the explosive detonation, the flyer motion, or the impact. Regardless of the cause, an ideal flyer impact over the entire flyer area may not have occurred.

In three cases, two in spray TP-2004-09 [samples 21 and 22 (shown in Figure 9.2)] and one in spray TP-2004-10 (sample 24), a portion of the flyer was explosively welded to the target surface along one edge. In the case of sample 24, the flyer was torn, leaving only a 1.65 cm (0.65") long portion of the flyer attached. The conditions to explosively weld two dissimilar metals are well documented [24, 27, 28, 29, 46, 66] and were not expected in this investigation. In essence, the formation of an explosive weld requires a sweeping high velocity impact between two metal plates at an oblique angle [24, 66]. While there was no indication of a sweeping detonation pattern in these tests, an angled impact at these locations may have occurred as a result of a deformed flyer edge prior to impact.

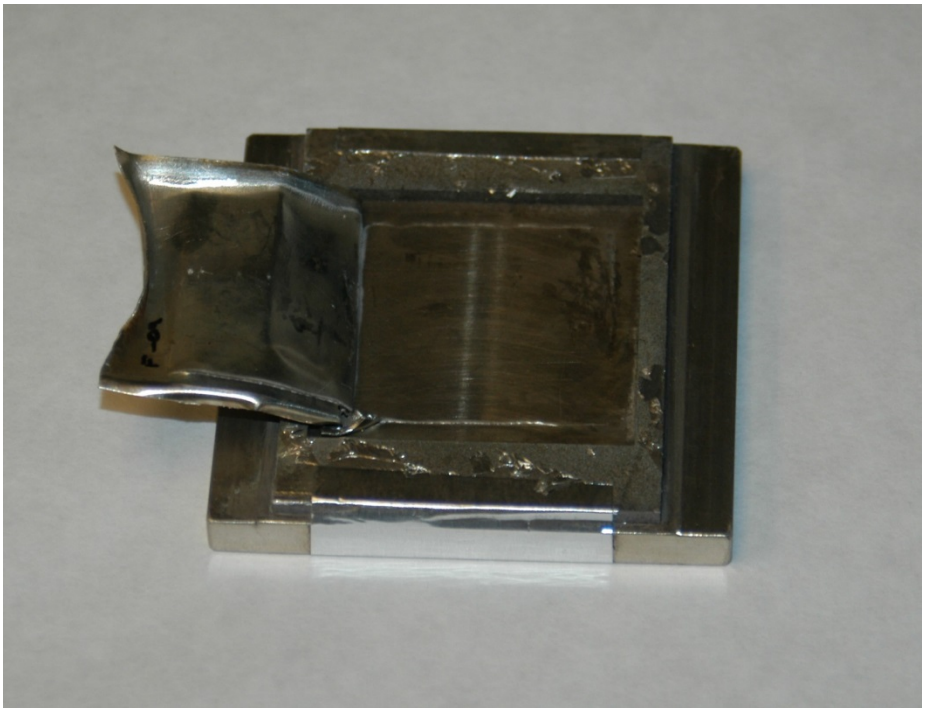

Figure 9.2: Flyer Welded to Target (Sample 22)

The lack of a weld at the target/flyer interface does not eliminate the possibility of a sweeping flyer impact at the flyer edges. The range of conditions to generate an explosive weld are very narrow, and without proper design can be difficult to achieve. A sweeping impact may have occurred without a weld being generated. In addition, due to the very short time frame in which this potential non-simultaneous impact may have occurred (~4 μs), the impact would still be considered impulsive to the pendulum mass. Therefore, any sweeping effect over this small area may not have been detected by post-test data reduction and analysis. In contrast, the three experiments with welded flyers showed a significant decrease in delivered impulse, indicating at least a problem with the flyer impact. This result will be discussed further in section 9.3.

The condition of the target impact surface generally varied as a function of target material. Each of the targets showed irregular, superficial blast marks around the impact area due to the hot product gases of the explosive detonation. The plastic targets showed a slight outline of the flyer impact area, with no noticeable compressive damage. Each of the plastic samples showed a small spall area from the back of the target or encased within the target thickness. The metallic targets also showed indication of the flyer impact area with either a marring or a very slight dent at the target surface. The dented surface was detectable by touch, but the depth was virtually indistinguishable from the un-impacted surface using a stainless steel straight edge. It appeared that the dented area, approximately 81% of the full area of the flyer, corresponded to the smaller non-curled portion of the flyer samples. None of the metallic targets showed a spall as a result of the flyer impact. The flyer/target impact surface is shown in Figure 9.3 (a) for the LEXAN® target sample 16 and Figure 9.3 (b) for the aluminum target sample 34.

(a) Plastic Target Impact Surface **(b) Metallic Target Impact Surface**

Figure 9.3: Post-Test Target Inspection

In those targets with carbon gages installed, the lead portion of the gage on the rear surface of the target was generally de-bonded from the target plate as a result of interaction with the traveling shock pulse. This occurred after the pressure pulse had been measured, and the test was essentially over. At this surface, the instrumentation leads were soldered to the gage leads, and covered with epoxy for protection during handling. This conglomeration of low impedance and non-homogeneous materials effectively acted as a momentum trap, preventing a tensile pulse from returning back though the target. For this reason, along with the pressure perturbation at the impact surface due to the presence of the gage material, none of the pressure test samples were used for material analysis. Figure 9.4 (a) shows a post-test target impact surface with the carbon gage still attached. Figure 9.4 (b) shows the back surface of the same target, with minimal damage to the instrumentation cable and gage leads (covered with epoxy and Kapton® tape). Figure 9.4 (c) shows the reduced spall damage at the rear surface of a PMMA target (as compared to the samples with no gage), as well as the de-bonded gage leads. Figure 9.4 (d) shows the gage indentation in the impact surface of the flyer.

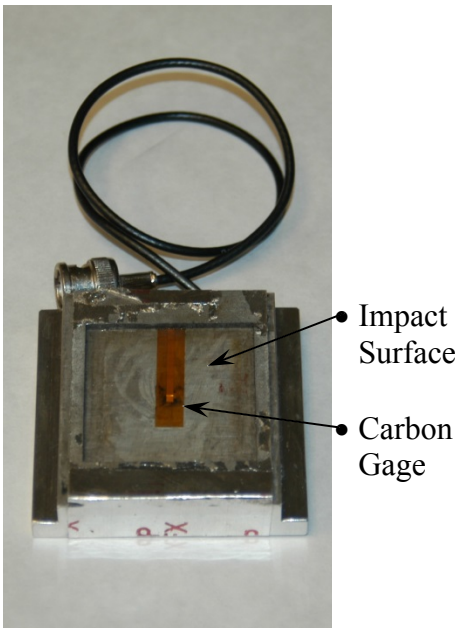

(a) Impact Surface (Aluminum) with Carbon Gage

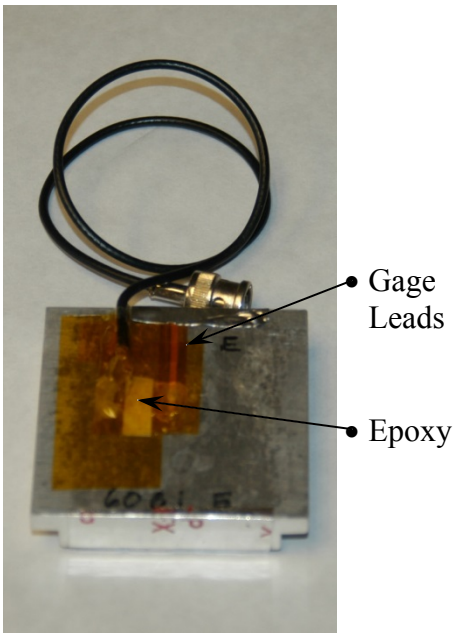

(b) Rear Surface (Aluminum) with instrumentation

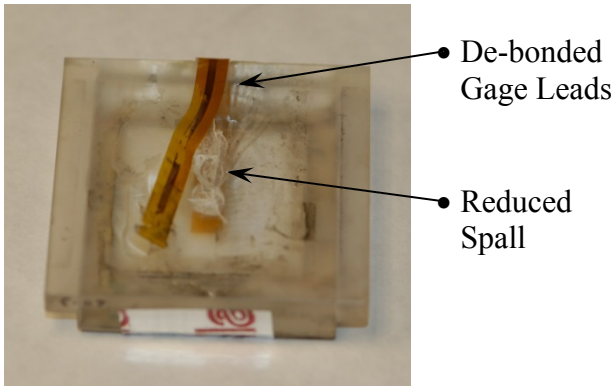

(c) Rear Surface (PMMA) with Carbon Gage

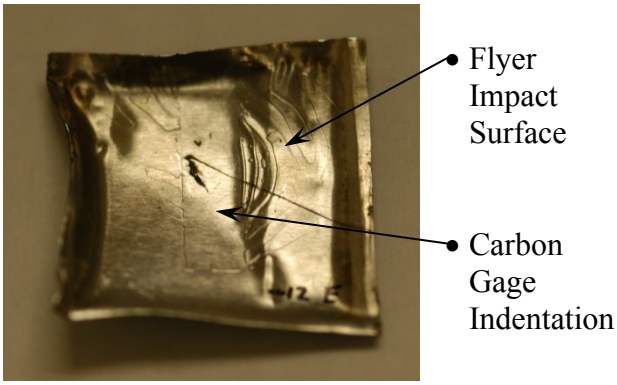

(d) Impact Surface of Aluminum Flyer with Carbon Gage Indentation

Figure 9.4: Post-Test Target/Flyer with Carbon Gage Instrumentation

9.2. Direct Spray Detonation Pressure and Impulse Delivery

The first three one-dimensional experiments were used to "ring-out" the target handling, firing, and data collection procedures and processes, as well as measure detonation induced pressure in the direct spray configuration. These experiments sought to validate the process, without the added complexity of an impulse generated by flyer impact. The process for measuring impulse delivered from a directly sprayed layer of explosive on a target structure is similar to that described in the explosive calibration in Chapter 5. But instead of explosive deposited and fired on a Kovar® coupon, the explosive was directly sprayed onto the material target surface and then fired on the SBPA. Three different target materials were used to measure the detonation pressure as it interacted with different impedance materials; aluminum, polycarbonate (LEXAN®), and PMMA. As the Hugoniot relations predicted, and the measured results confirmed, the incident pressure at the target surface decreased with decreasing material shock impedance.

Overall, the results of the direct spray experiments were somewhat mixed. Peak pressure was measured and pendulum rigid body motion was recorded in each of the three tests. But the measured impulse on the target from the explosive layer was significantly lower than the predicted impulse in two of the three experiments. The delivered impulse is a function of the sprayed areal density and the sprayed area, and should be predicted by the explosive calibration. The measured impulse for Test #1 was 85% of predicted, 88% for Test #2, and 97% for Test #3. This result was unexpected and could be the result of lower than expected local explosive deposition, greater than expected edge effects, or instrumentation error.

To further complicate the results, the calculated impulse from the measured pressure data (area under the pressure time curve) indicated impulse levels approximately two times higher than either predicted or measured. It was found that this calculated impulse was incorrect, the reasons for which are discussed in the following paragraphs. The predicted and measured impulse, as well as measured peak pressure, from each experiment are listed in Table 9.2 for the direct spray experiments.

Table 9.2: Direct Spray Impulse Delivery and Pressure

Test ID	Sample ID	Target Material	ρ_A (mg/cm^2)	Predicted I_{sp} (taps)	Measured		
					I_{sp} (taps)	P (kbar)	$I_{sp} = \int P(t)dt$
1	A	6061-T651 Al	46.47	3247	2756	6.83	6001
2	B	LEXAN®	45.48	3166	2773	3.85	5865
3	C	PMMA	43.87	3033	2943	3.57	7766

As discussed throughout this report, the pressure pulse measured by the thin film carbon gage differs from the actual pressure at the explosive/target interface due to the presence of the gage itself. Unlike the flyer impact experiments, hydrocode modeling for these direct spray experiments was not possible due the lack of a sufficient equation of state for the SASN explosive in KOWIN. Hydrocode modeling with low-density PETN, conducted for scoping purposes, was useful in predicting pressure pulse characteristics, but was not able to accurately predict the measured peak pressure with SASN.

The detonation pressure pulse was successfully recorded in each of the three direct spray experiments. Unfortunately, the measured pulse shape was not representative of the actual pulse. The thin film carbon pressure gage is a piezoresistive transducer, placed in a whetstone bridge circuit, which decreases in resistance as the applied pressure increases. In addition to applied pressure, the resistance will decrease as a function of a rise in temperature. In the case of the direct spray experiments, the explosive detonation

(and subsequent expanding detonation product gases) heat the gage and surrounding mounting surface. The result is that the measured pressure pulse remains artificially positive as the actual pressure pulse returns to zero. It is believed that the peak pressure was measured correctly because the gage cannot thermally respond in the rise time (~10s of nanoseconds) of the initial shock. Figure 9.5 shows the measured pressure pulse, with the artificially elongated tail, on the aluminum target plate. As can be seen, the pulse abruptly ends at 14.6 μs (5.5 μs after first pressure) where the gage or gage leads break. Also of interest is a short bump in amplitude at 0.5 μs after first pressure. KOWIN hydrocode analysis predicts this bump as a shock reflection within the carbon gage thickness. PMMA and polycarbonate targets showed similar results with lower peak pressures.

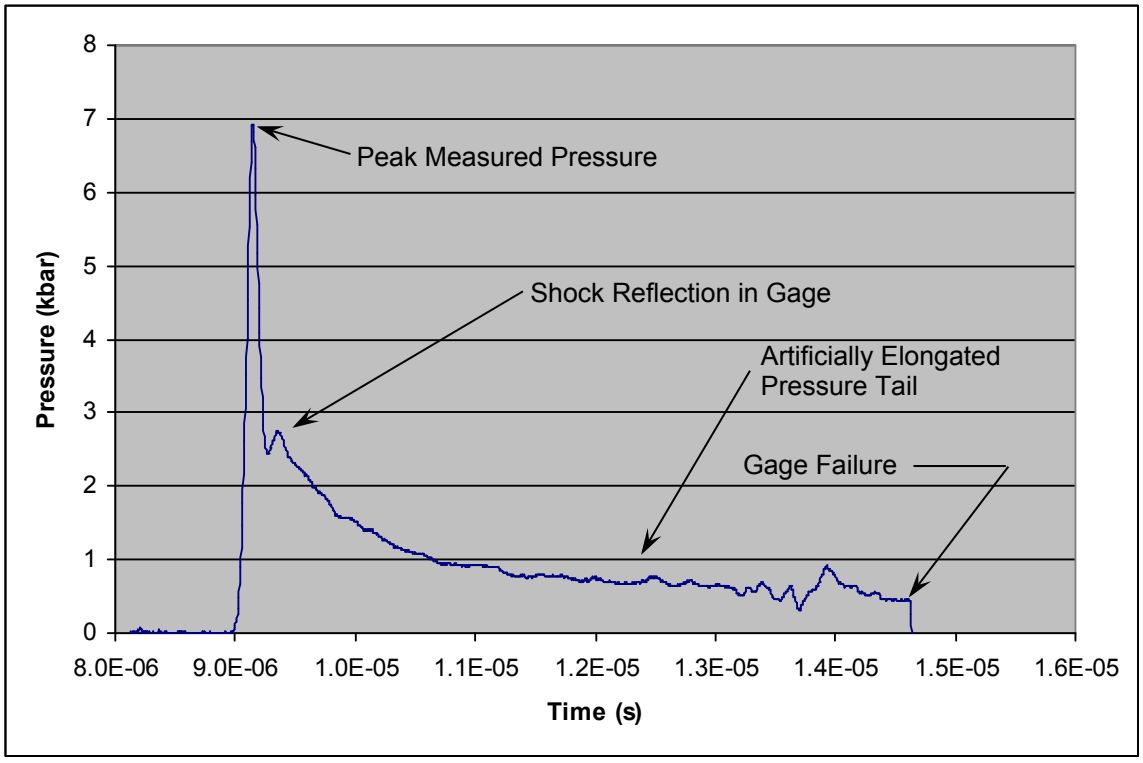

Figure 9.5: Measured Direct Spray Explosive Detonation Pressure (Aluminum)

A note about timing: the instrumentation system was triggered from the first application of electrical current to the SBPA light array. From this zero time, it took approximately 9.0 μs for the light array to fully energize, transfer its thermal energy to the explosive, and the explosive to achieve a full detonation. This explosive response time is consistent in both the direct spray experiments and in the flyer tests, where flyer transit times were approximately 6 μs, resulting in a first pressure at approximately 15 μs after current has been applied to the light array.

The measured pressure on the aluminum target material was of particular interest because the flyer material chosen for this study was aluminum. The transfer function between the measured detonation pressure on the relatively thick aluminum target and the thin aluminum flyer is not known, and is not directly measurable by conventional means. What is postulated by the theory developed in Chapters 4 and 5 is that a larger explosive loading (deposition) results in a higher flyer velocity. The higher deposition creates a higher peak pressure at the explosive/aluminum interface, with approximately the same pulse duration as lower explosive depositions. The area under the pressure-time curve determines the impulse on the flyer, and ultimately the velocity to which the flyer is driven. Because the duration of the pressure pulse remains relatively constant, the time to achieve terminal flyer velocity also remains relatively constant, independent of explosive areal density. Therefore, the explosive deposition is the primary metric in designing and determining the flyer velocity, while the time to terminal velocity is held relatively constant for this formulation of SASN explosive.

The one-dimensional direct spray experiments provided good experience in the challenges of handling and firing the small target samples, though the exact cause of the

impulse measurement inconsistencies was not determined. This discrepancy was not further investigated because it was felt that the deposition conditions were not adequately recorded to challenge the measured impulse delivered to the direct spray target. It was determined that better quantification of the explosive deposition and area was required. Regardless, a greater understanding of the carbon gage performance was achieved. Each of the parameters measured in this phase, while not necessarily required for understanding of the flyer theory, were used to make parameter predictions and set windows for data collection in the later experiments.

9.3. Flyer Velocity and Delivered Impulse

A total of thirty-one successful one-dimensional flyer plate tests were conducted. In each experiment, the rigid body motion of the pendulum mass of the SBPA was measured to determine specific impulse and flyer impact velocity. On average, the calculated (from measurement) flyer velocity was 97.3% of that predicted by the flyer performance equations (5.11) and (5.12). Table 9.3 (below) presents the predicted and measured impulse and velocity data from each of the thirty-two samples sprayed. Test #4 was considered a no-test because the flyer assembly fell off the target during spray operations.

The flyer velocity for each of the one-dimensional tests was calculated from the measured total impulse applied to the target structure. As described and developed in Chapters 4 and 5, the flyer impact imparted an impulsive load to the target. The generated impulse then drove, through the target mounting structure, the pendulum mass to an initial velocity, translating to a sinusoidal pendulum motion. The displacement of the pendulum mass was measured, and through a set of conversion steps, the total delivered and specific impulse was calculated. From this result, combined with gathered

information about the flyer impact area and explosive deposition, equations (5.11) and (5.12) were used to calculate the flyer velocity. Throughout this chapter, the calculated flyer velocity is considered a "measured" quantity, and for clarity is referred to as such.

Table 9.3: Predicted and Measured Flyer Velocity and Impulse

Test ID	Sample ID	Target Material	ρ_A (mg/cm^2)	Predicted		Measured	
				V_f (cm/s)	I_{sp} (taps)	I_{sp} (taps)	V_f (cm/s)
4	D	6061-T651 Al	No Test				
5	E	LEXAN®	45.82	27,326	3006	2943	26,753
6	F	PMMA	42.78	25,577	2900	2679	23,625
7	A	6061-T651 Al	50.70	30,053	3618	3617	30,042
8	B	LEXAN®	50.70	30,053	3241	3251	30,140
9	C	PMMA	50.70	30,053	3322	2988	27,035
10	D	6061-T651 Al	41.50	24,829	3134	3439	27,243
11	E	LEXAN®	44.35	26,485	2946	2894	26,022
12	F	PMMA	41.05	24,564	2802	2780	24,367
13	A	6061-T651 Al	50.80	30,108	3625	3076	25,550
14	B	LEXAN®	53.70	31,683	3450	4163	38,229
15	C	PMMA	50.75	30,081	3324	3927	35,535
16	D	LEXAN®	50.24	29,800	3208	3210	29,821
17	A	304 SS	54.65	32,192	4419	4045	29,465
18	B	316 SS	54.65	32,192	4419	4281	31,184
19	C	200 Ni	54.65	32,192	4527	4496	31,973
20	D	304 SS	45.85	27,343	3845	3447	24,513
21	E	316 SS	45.85	27,343	3196	2857	20,317
22	F	Ni 200	45.85	27,343	3935	2753	19,132
23	A	304 SS	53.35	31,495	4339	4145	30,088
24	B	316 SS	53.35	31,495	4339	3823	27,750
25	C	Ni 200	53.35	31,495	4447	4116	29,154
26	D	304 SS	44.45	26,543	3755	3550	25,090
27	E	316 SS	44.45	26,543	3755	3105	21,945
28	F	Ni 200	44.45	26,543	3836	3332	23,053
29	A	C110 Cu	35.30	21,094	3086	3059	20,907
30	B	C110 Cu	35.30	21,094	3086	3128	21,380
31	C	C110 Cu	35.30	21,094	3086	2972	20,311
32	D	1100 Al	35.00	20,908	2763	2798	21,170
33	E	1100 Al	35.00	20,908	2763	2645	20,008
34	F	1100 Al	35.00	20,908	2763	2363	17,880
35	G	PMMA	35.30	21,094	2503	2662	22,436
36	H	6061-T651 Al	35.30	21,094	2782	2700	20,468

Figure 9.6 plots the "measured" flyer velocity as a function of areal density in comparison with the predicted flyer velocity from the developed theory. As can be seen, the "measured" flyer velocity data loosely follows the predicted impact velocity. Statistical analysis of the residuals, using Microsoft Excel [63], shows that the data were reasonably normally distributed about the predicted velocity with an average residual of -707 cm/s (-278 in/sec), with a standard deviation of 2190 cm/s (862 in/sec).

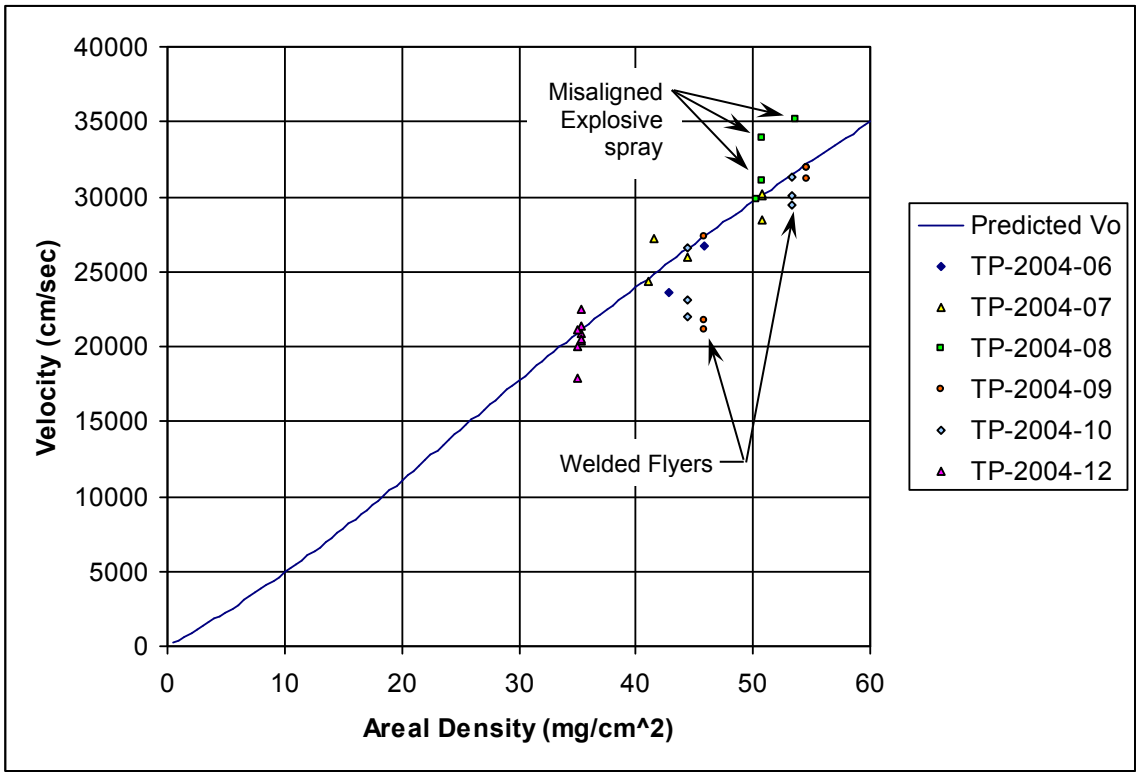

Figure 9.6: "Measured" Flyer Velocity as a Function of Areal Density

Three crucial pieces of data were used in the calculation of flyer velocity from impulse measurement. The first was the areal density of the explosive deposited on the flyer. Explosive deposition was measured using coupons placed near the flyer surfaces during spray operations. This is a common measurement at the facility, and was assumed to be adequate to determine the deposition on the sprayed flyer surface. Where possible,

(i.e., when the flyer/target assembly was within the measurement range of the spray booth scale) the explosive deposition on the flyer was weighed directly.

The second important piece of data was the impact area of the flyer on the target surface. This was especially significant for these very small one-dimensional tests, where the potential for edge effects to introduce error into the total delivered impulse measurement was high. As discussed above in Section 9.1, inspection of the target surfaces indicated that the flyer impact area was approximately the full 14.52 cm^2 (2.25 in^2) of the flyer, with some uncertainty based on the effect of the curled edges of the flyer.

The third important piece of data was the quality of the explosive deposition on the flyer. This qualitative observation focused on the ability of the masking to allow a constant deposition solely on the flyer surface, and not on surrounding portions of the target assembly. In three cases from spray TP-2004-08, the explosive layer covered portions of the flyer as well as the offset spacer as a result of poor alignment of the masking. The resulting impulse was higher than expected, which led to a "measured" flyer velocity that was correspondingly high. These three data points, two of which resulted in the largest deviation above the predicted flyer velocity curve, are highlighted in Figure 9.6.

The curled edges of the flyers presented a dilemma in the understanding of the impact area. Because it was not known when, or by what mechanism, the curling occurred, its effect on the total delivered impulse is not precisely known. Based on the three samples where explosively generated welds were observed, it could be assumed that the flyer impact within these edge regions was not precisely planar. But, as discussed

above, the total time to impact the target, including the curved edges, was still impulsive to the pendulum, therefore making it difficult to detect a non-ideal impact. For these reasons, it was assumed that the edge deformation effect to the measured total impulse was small, if measured at all.

Of interest was the low "measured" velocity for samples E and F of TP-2004-09, as well as for sample B of TP-2004-10, where the flyer was explosively welded to the target along one edge. The "measured" flyer velocities for the two '09 experiments were 77.3% and 79.3%, respectively, of the predicted velocity based on the measured delivered impulse. The flyer velocity for sample B of spray -10 was 93.7% of expected. The lower "measured" velocities were the result of a lower than expected measured rigid body motion of the pendulum mass. The effect of the weld was that the flyer rebound from the target surface was impeded, affecting the momentum transfer, and therefore reducing the motion of the pendulum mass. The calculated impulse to the target was correspondingly reduced. With a lower calculated impulse, a lower than expected flyer velocity was calculated, though the actual incoming flyer velocity of the flyer was likely close to that predicted by the developed theory.

As discussed, six data points from the thirty-one experiments experienced known deviations from the designed test conditions. Three of these resulted in "measured" velocities higher than predicted, and three lower than predicted. Excluding these six points from the data set, the average flyer velocity was 97.5% of that predicted.

9.4. Flyer Induced Shock Loading

Both the Hugoniot and shock physics analysis indicated that the flyer impact was sufficient to create a prompt, high-frequency, shock pressure pulse into the target structure. The pulse shape, duration, and amplitude are functions of the target and flyer

material interaction, as discussed in Chapter 4. For the plastic targets, the pulse shape was triangular, and for the metallic targets, the pulse was somewhat haversine-shaped. The smoothed and rounded shape differed from the ideal square or stepped pulse due to the trapped air between the flyer and target.

Two analysis techniques were applied to understand the time varying shock state of the target plate. The first was one-dimensional hydrocode modeling, used to analyze the effect of the flyer impact on the target structure. The second was direct pressure measurement using thin film carbon gages. Because the shock impedance for 6061 aluminum is nearly identical to 1100 aluminum and has a better equation of state in KOWIN, 6061 was used to model and measure the representative pressure for the aluminum target samples.

9.4.1. Hydrocode Modeling

As discussed in previous chapters, the hydrocode KOWIN has been used extensively to design, predict, and analyze the LIHE driven flyer experimental results. While this tool has been extremely useful, it is not without its limitations. Specifically, some of the material equations of state (EOS) do not support tensile loads. Therefore, it was necessary to use the hydrocode model output with additional diligence. In addition, it was known that the "one-dimensional" flyer experiments were not purely one-dimensional. After impact, rarefaction waves moved inward from the edges of the impact zone towards the center of the target as the shock pulse moved through the target thickness. But for the designed experiments, the thickness of the target—in relation to the impact area—ensured that an area of at least 1.3 cm by 1.3 cm (0.5" by 0.5") experienced a nearly one-dimensional loading. For this area, the hydrocode should have adequately predicted the shock history.

Numerous flyer/target configurations were modeled in KOWIN over the course of this investigation. Two post-test representative one-dimensional flyer/target configurations are reported here. The flyer was modeled as a 0.033 cm (0.013") thick 1100 aluminum plate with an initial velocity of 26,134 cm/s (10,289 in/s). For modeling purposes, the flyer was given an initial velocity based on the expected terminal velocity for an explosive deposition of 43.7 mg/cm^2. Again, this was necessary because an adequate EOS for SASN to effectively model the explosively driven flyer was not available. This velocity was chosen to correspond to an average of the "measured" impact velocities on the PMMA targets. An initial offset gap of 0.20 cm (0.079") between the flyer and target was used. The target was modeled as either a PMMA or 6061 aluminum plate, 1.0 cm (0.39") in thickness. Pressure, particle velocity, and particle displacement were recorded at locations within the flyer and target materials, the results are given in Table 9.4.

Table 9.4: Hydrocode Predicted Flyer Performance

Target Material	ρ_A* (mg/cm^2)	Gap (cm)	V_f (cm/s)	Hugoniot Pressure (kbar)	Peak Pressure (kbar)	Rebound Factor	Pressure w/ Gage (kbar)
PMMA	43.7	0.2	26,134	7.19	4.96	1.26	7.88
6061 Al	43.7	0.2	26,134	19.51	18.8	1.39	12.9

*Effective areal density to achieve V_f = 26,134 cm/s

Modeled flyer velocity histories for the PMMA and aluminum target models are given in Figure 9.7. The plot shows the nearly constant incoming velocity of 26,134 cm/s (10,289 in/s), and the impact where the velocity quickly drops to zero, then rebounds in the opposite direction where the flyer velocity is reported in the negative direction. The modeled flyer displacement histories are given in Figure 9.8. Both models show a constant flyer displacement rate until impact, where the flyer reverses direction away

from the target. Of interest is the difference in flyer rebound velocity, and corresponding displacement, between the PMMA and aluminum targets. The higher rebound velocity (in the negative direction) observed with the aluminum target is due to the higher impedance of the aluminum target versus the PMMA target. Also, the aluminum target material results in a change in flyer velocity that is much sharper than with the PMMA target. This observation is consistent with the modeled pressure pulse, where the duration of the aluminum target pulse is approximately half that of the PMMA target pulse.

The equation of state in KOWIN for PMMA supports both compressive and tensile loading. With the hydrocode configured to not allow spall, an expected tensile pulse from the rear surface of the target was modeled. The impact pressure pulse attenuation through the target thickness is shown in Figure 9.9. For the modeled conditions, with a PMMA target, the 4.96 kbar (496 MPa, 71,900 psi) peak impact pressure attenuates by ~40% to approximately 3.0 kbar (300 MPa, 43,500 psi) near the rear surface. The left-going return tensile pulse amplitude is slightly over 2 kbar (200 MPa, 29,000 psi), which is significantly greater than the reported ultimate tensile strength range of 62.1-75.8 MPa (9000-12000 psi) [55], and is more than sufficient to create a spall at the rear surface.

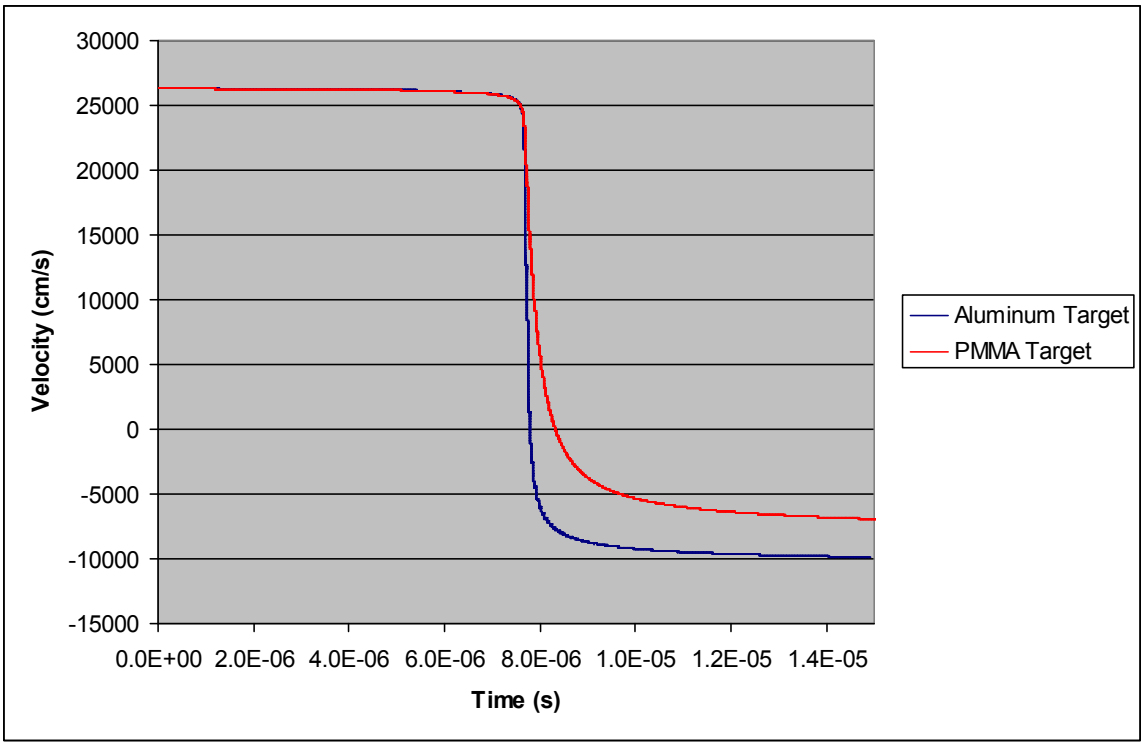

Figure 9.7: Flyer Velocity with an Aluminum and PMMA Target

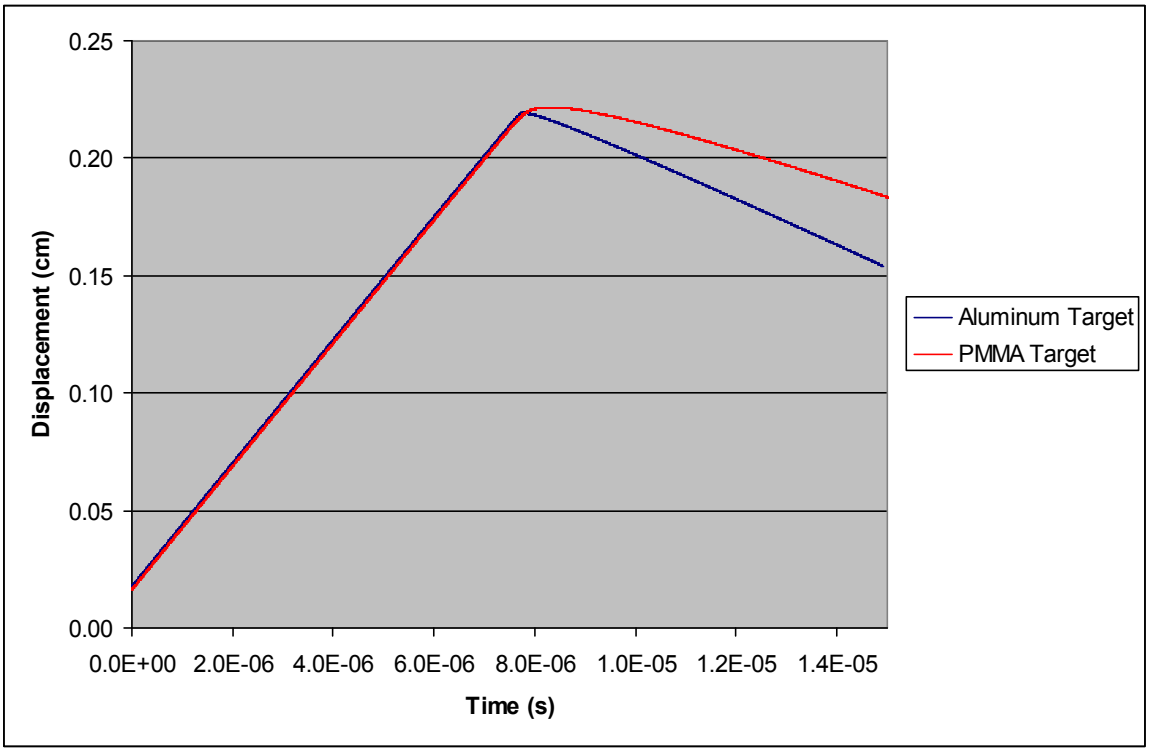

Figure 9.8: Flyer Displacement with an Aluminum and PMMA Target

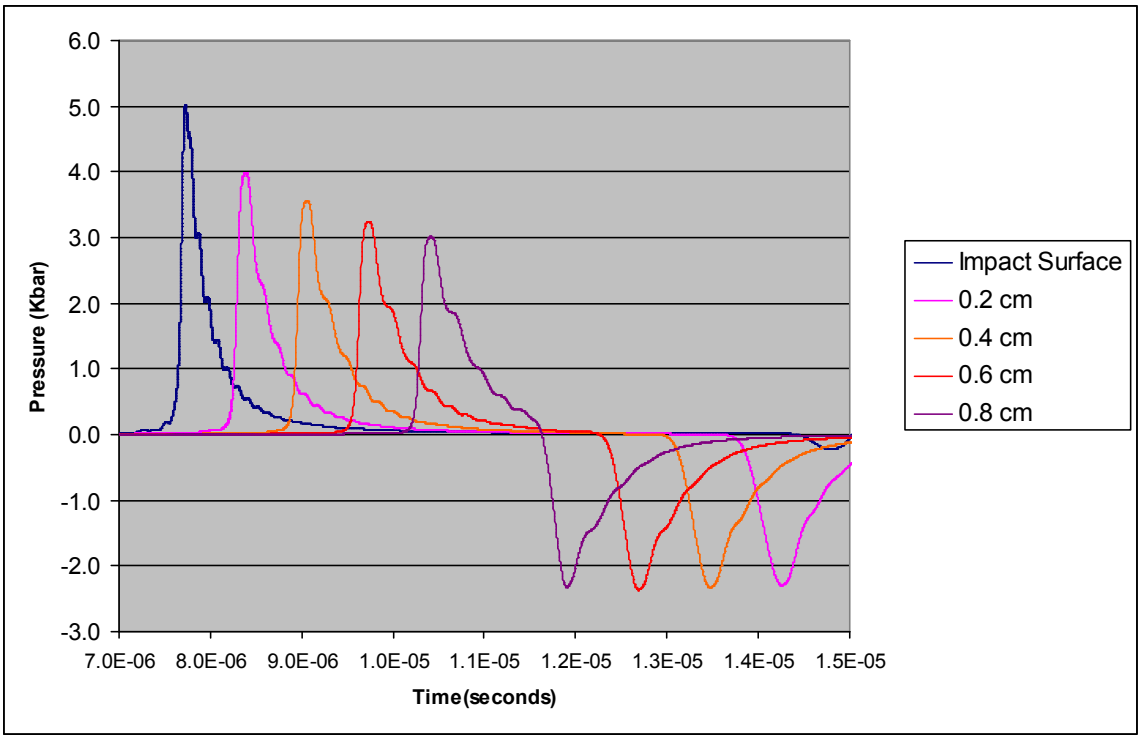

Figure 9.9: Pressure Pulse Degradation in PMMA

The compressive shock through the target thickness, due to a flyer impact, was successfully modeled for the 6061 aluminum target. The predicted impact pressure for the given set of conditions was 18.8 kbar (1880 MPa, 272,700 psi) attenuating by approximately 26% to 14.1 kbar (1410 MPa, 204,500 psi) through the target thickness. In contrast to the PMMA equation of state, the KOWIN 6061 aluminum EOS does not support tensile forces. The result being that the model was unable to predict the tensile pulse from the rear surface, and therefore unable to predict a spall condition if one were to occur. Figure 9.10 shows the pressure attenuation through the thickness of the aluminum target. The model predicts the compressive impact pressure to be over than an order of magnitude than the reported yield strength of 6061 aluminum {145 MPa (21,000 psi) [22]}.

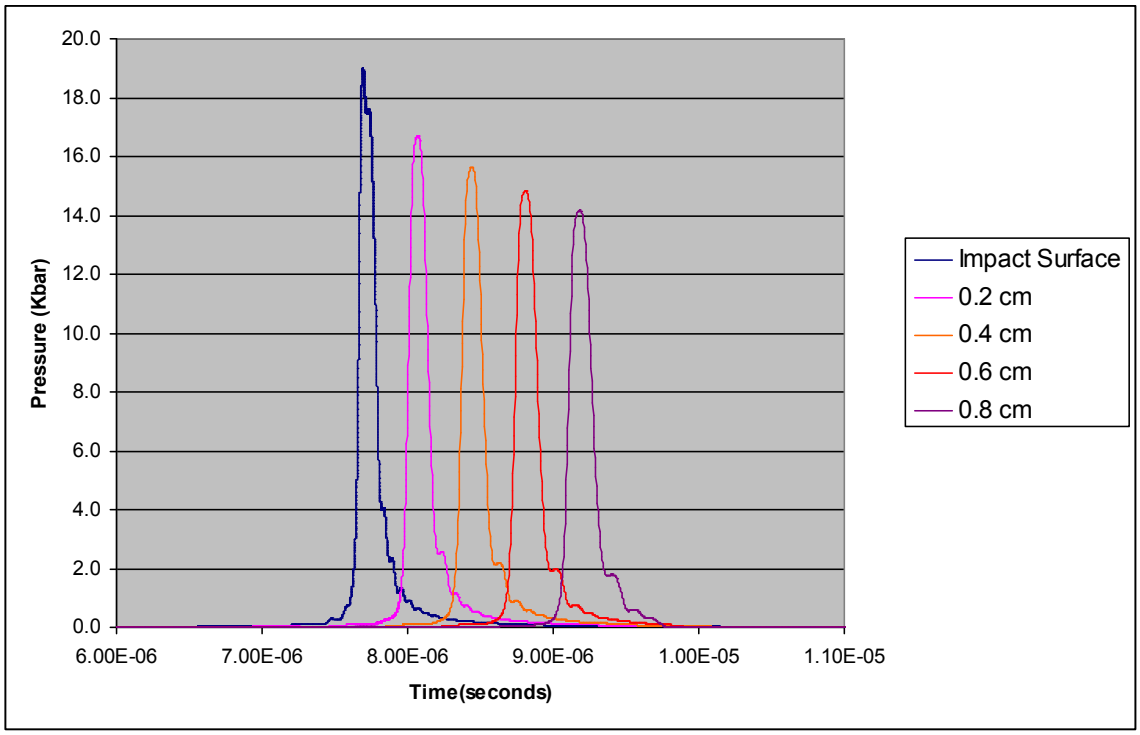

Figure 9.10: Pressure Pulse Attenuation in 6061-T6 Aluminum

A second set of models were run to predict the effect of the carbon gage on the measured pressure. The gage was modeled as a 0.0165 cm (0.0065") layer of Kapton® on the surface of the target layer. Impact pressure was recorded half-way through the Kapton® material to simulate the gage output pressure. In the case of the PMMA target, the Kapton® material was of a higher impedance than the PMMA target. This resulted in a higher predicted pressure by ~59% within the Kapton® layer than if the flyer were to impact the PMMA itself. In contrast, the Kapton® layer is of much lower impedance than the 6061 aluminum target. This impedance mismatch, with the gage material in place, resulted in a predicted pressure lower in amplitude by ~30%. Figure 9.11 shows the two predicted pressure pulse shapes for an aluminum flyer impact on an aluminum target with, and without, the simulated gage in place. Because the delivered impulse is independent of target material, but is directly a function of the flyer velocity, material

density, and thickness, the area under the pressure-time curve (impulse) is equal for both pressure pulses.

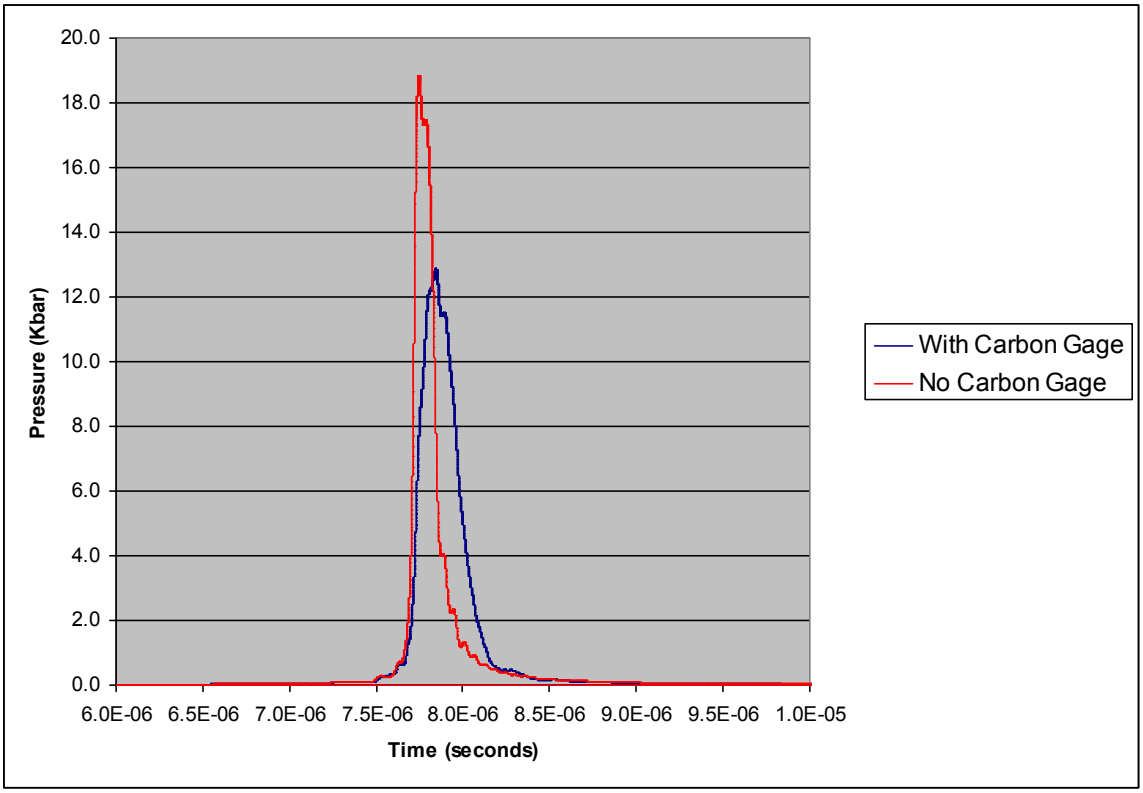

Figure 9.11: Impact Pressure With and Without Carbon Gage

9.4.2. Measured Impact Pressure

Direct measurement of the flyer impact pressure was accomplished using thin film carbon gages mounted to the impact surface. Attempts were made to measure the impact pressure on each of the target materials used in this study. Unfortunately, the results were less successful than expected. Thirteen pressure experiments were attempted, with three full, and three partial, instrumentation failures occurring. Table 9.5 provides a summary of each of the one-dimensional impact pressure experiments, including the predicted impact pressure from Hugoniot analysis (no trapped air) and KOWIN hydrocode analysis, as well as the uncorrected (for the presence of the gage) measured pressure.

Table 9.5: Predicted and Measured Flyer Impact Pressure

Test ID	Sample ID	Target Material	ρ_A (mg/cm^2)	V_f (cm/s)	Predicted		Measured
					Hugoniot	KOWIN	Carbon
7	TP-2004-07	6061 Al	50.70	30,042	22.55	22.2	27.95
8	TP-2004-07	LEXAN®	50.70	30,140	7.78	7.5	8.89
9	TP-2004-07	PMMA	50.70	28,468	8.40	6.0	10.28
13	TP-2004-08	6061 Al	50.80	31,096	22.57	22.3	NR
14	TP-2004-08	LEXAN®	53.70	35,123	7.78	7.5	NR
15	TP-2004-08	PMMA	50.75	33,961	8.41	7.03	10.70
17	TP-2004-09	304 SS	54.65	31,900	34.90	31.6	35
18	TP-2004-09	316 SS	54.65	31,184	34.90	31.6	36.7
19	TP-2004-09	Nickel	54.65	31,973	36.10	33.0	38.5
30	TP-2004-12	Copper	35.30	21,380	22.34	20.1	22.6
31	TP-2004-12	6061 Al	35.00	20,008	15.51	13.6	14.6
32	TP-2004-12	PMMA	35.30	22,436	5.69	3.5	NR
33	TP-2004-12	6061 Al	35.30	20,468	15.65	13.9	16.1

* NR=Not Recorded

The thin film carbon gage, from Dynasen, Inc., was designed to be used essentially from zero pressure up to 100 kbar [33]. But the calibration curve, plotting percent change in resistance vs. applied pressure, above 25 kbar becomes less accurate due to the non-linear characteristics of the curve [32]. Dynasen suggests using a manganin piezoresistive pressure gage above the 25 kbar mark. The author has extensive experience with the manganin gage between 30 kbar and 125 kbar, having a high degree of confidence in their performance. Unfortunately, the manganin gage is constructed such that its metallic element, etched on a Kapton® substrate, would be electrically shorted upon impact by the aluminum flyer. For this reason, the carbon gage is used with the understood potential error at higher pressures.

As discussed in the previous section, the carbon gage may report a different pressure than actual due to shock impedance mismatches between the flyer, the gage, and the target surface. Under the conditions where a thin layer of low impedance material is sandwiched between a relatively thick flyer and a target of higher shock impedance

materials, the pressure in the low impedance material will "shock-up" to the pressure encountered if the flyer impacts the target directly [24]. The time required for the pressure rise to occur in the low impedance layer is dependent on the number of shock transits through the thin material before achieving the final pressure. A contrasting result occurs when the gage Kapton® layer is of higher impedance than the target material. In this scenario, the gage will initially read a higher pressure, then ring down, by successive wave transits through the Kapton® layer, to the pressure between the flyer and target materials. The phenomenon in either case is generally very quick. The number of transits can be predicted by Hugoniot relations in the ideal case with no trapped air, but requires a significantly more complicated analysis to account for the trapped air between the flyer and target. The analysis was further complicated, for these experiments, by the fact that the thickness of the flyer was of the same order as the gage material. Under this circumstance, the carbon gage may not achieve the final pressure as if a semi-infinite flyer impacted the target.

Impact pressure was successfully recorded on ten of thirteen experiments. Of those ten recorded pressure pulses, three were somewhat corrupted by electrical noise being recorded on the pulse shape. As expected, the peak pressure and pulse duration varied as a function of target impedance. Figure 9.12 shows the measured pressure pulse (without correction to account for the presence of the gage, and shifted in time for representation purposes) on each of the target materials.

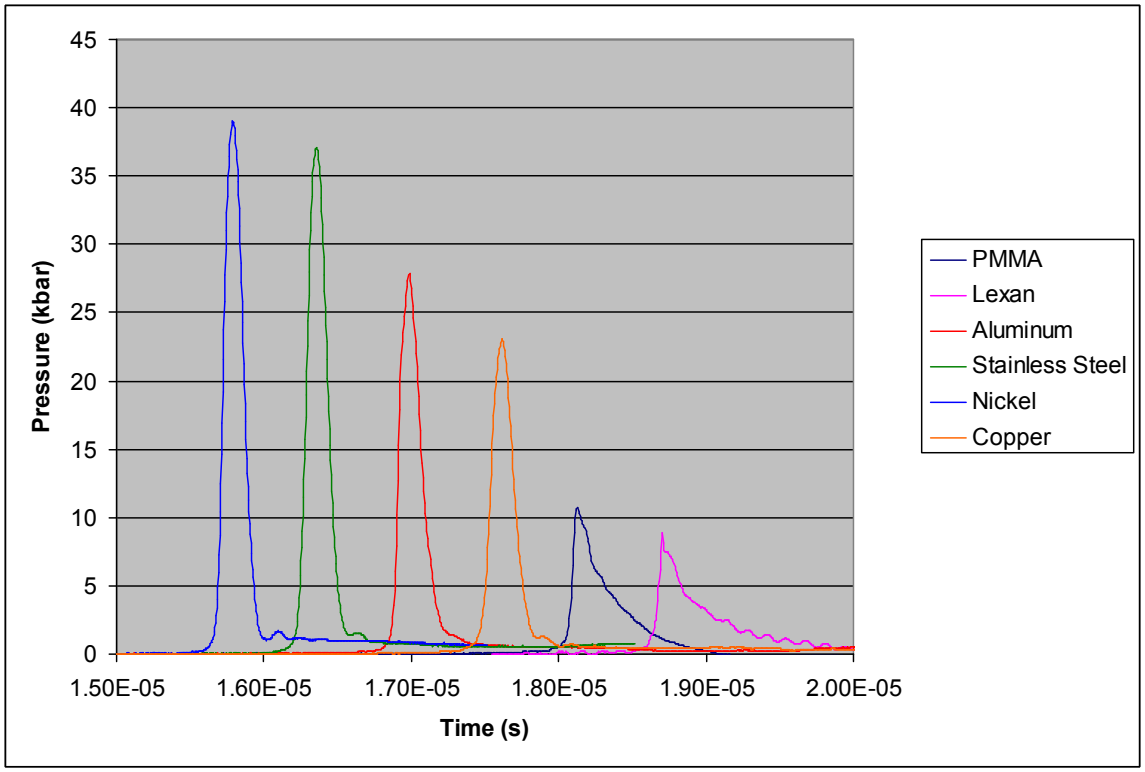

* Measured pressure pulses shifted in time for presentation only.

Figure 9.12: Measured Pressure on Each Target Material*

It was immediately observed that the measured pressure (without correction) in nearly all of the pressure experiments was greater than the predicted Hugoniot pressures by an average of 9.8%, and greater than the KOWIN calculated pressures by an average of 24.7%. The higher than expected measured pressures on PMMA and LEXAN® were likely reasonable given that the Kapton® layer is of a higher impedance than these target materials. Conversely, the Kapton® layer of the gage was of a lower impedance than the metallic targets, requiring that the gage shock-up to the proper pressure at impact. While the relative magnitudes of the measured and predicted pressures in the metallic samples were similar, it is known for these cases that the actual pressure cannot exceed the Hugoniot for a given velocity. This inconsistency suggests that the impact velocity may have been greater than predicted for a given explosive deposition. This may also lend

support to a smaller impact area with a higher impact velocity, resulting in a coincidentally similar delivered total impulse. This hypothesis cannot be easily evaluated with the present study because the flyer velocity is inferred from the displacement of the SBPA pendulum mass.

As discussed above in Section 9.1, observation of the explosive side of the flyer surface showed an expected detonation pattern in the flyer support foil layer. It appeared that this very thin layer was somewhat disturbed by the detonation process, possibly leading to a driving of a 0.030 cm (0.012") thick flyer instead of the 0.033 cm (0.013") used in the predictions and calculations. Based on KOWIN models, this difference may account for up to approximately 8% difference in flyer velocity from that originally predicted.

A number of gage errors and failures were encountered during the impact pressure measurement experiments. Each resulted in these impact pressure measurements being compromised in some way. The errors included instrumentation failures as well as less serious high-frequency electrical noise pickup problems. It should be noted that the pendulum displacement instrumentation system was isolated from the carbon gage instrumentation system, and in no case was a common failure experienced where pendulum motion was corrupted or not recorded.

Three of the thirteen experiments encountered issues where the carbon gage instrumentation either was triggered late, or not at all. In these cases, no impact pressure was recorded. In several other tests, high-frequency electrical noise, caused by a faulty Rogowski loop, was picked up and reported by the carbon gage in addition to the measured impact pressure. The Rogowski loop is a passive transducer used to measure

current in high voltage applications, and is used in this application to trigger the SBPA instrumentation system. In these noise pickup cases, it was attempted to filter the high-frequency rider on the pulse shape with a Sandia developed data reduction software package called PlotData [85]. Unfortunately, in most cases, the noise was not completely eliminated, and due to the relatively high frequency of the pulse itself, the peak pressure may have been somewhat degraded by this operation. For these reasons, selected local filtering was accomplished to maintain the peak pressure under the assumption that the local noise at the peak was a minimal effect. Figure 9.13 shows one measured pressure pulse, from a flyer impact on a PMMA target, where local filtering was done on the data after ~1.0 μs of pressure data. As can be seen, the noise was not totally eliminated by the procedure, but the general pulse shape was maintained.

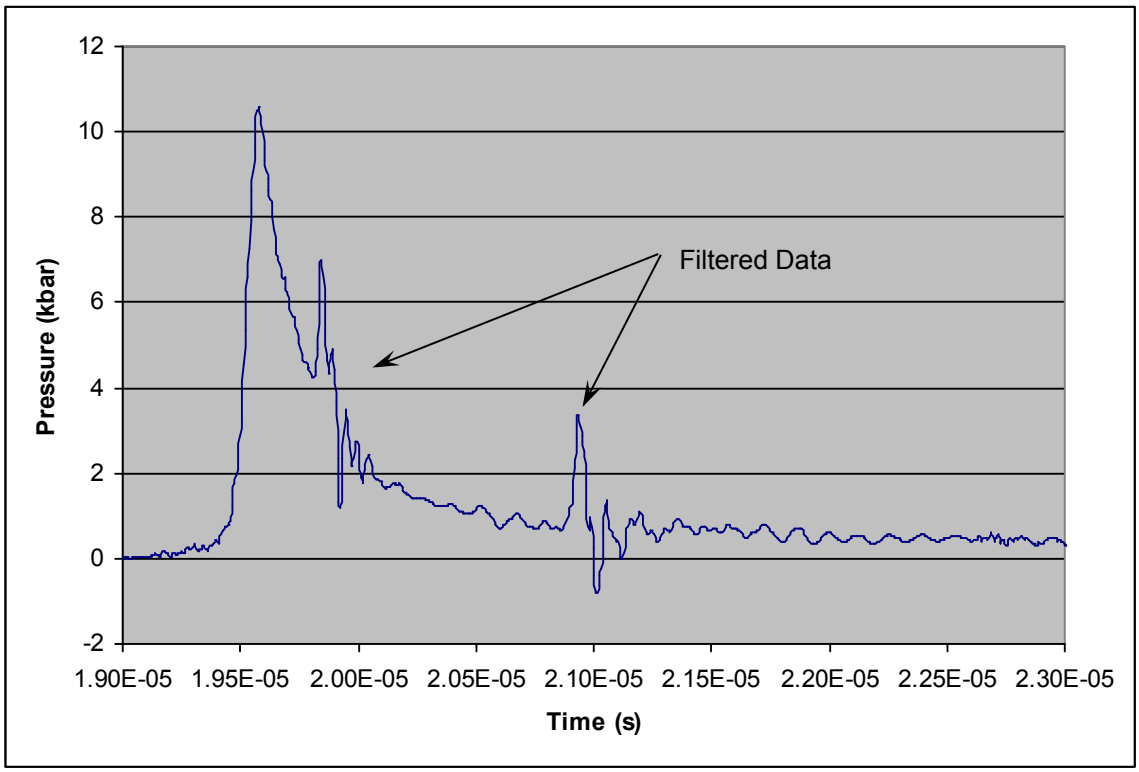

Figure 9.13: Measured Pressure with Partially Filtered Electrical Noise

9.5. Flyer Impact Simultaneity

One additional experiment was conducted to measure both impact pressure and impact simultaneity over a portion of the impact surface. This was accomplished by applying two carbon gages to the impact surface 2.16 cm (0.85") apart, shown in Figure 9.14. The measured pressure pulses from the two gages is given in Figure 9.15. The impact simultaneity over this distance was 0.50 μs, which was still considered impulsive to the target. Assuming a flyer velocity, based on an areal density of 35.3 mg/cm^2, of 20,468 cm/s (8058 in/s) the impact angle over the distance between gages was 0.27 degrees. Of interest was that the second impacted gage indicated a lower peak pressure than the first gage. This may indicate that the flyer impact velocity at the second gage was lower than that of the first gage. It is postulated that the lower velocity, and thus lower pressure and later time impact, may have been the result of a slightly lower explosive deposition on the flyer at that location. Post-test inspection of the flyer surface showed no difference in detonation pattern between the two locations, ruling out a sweeping detonation across the flyer.

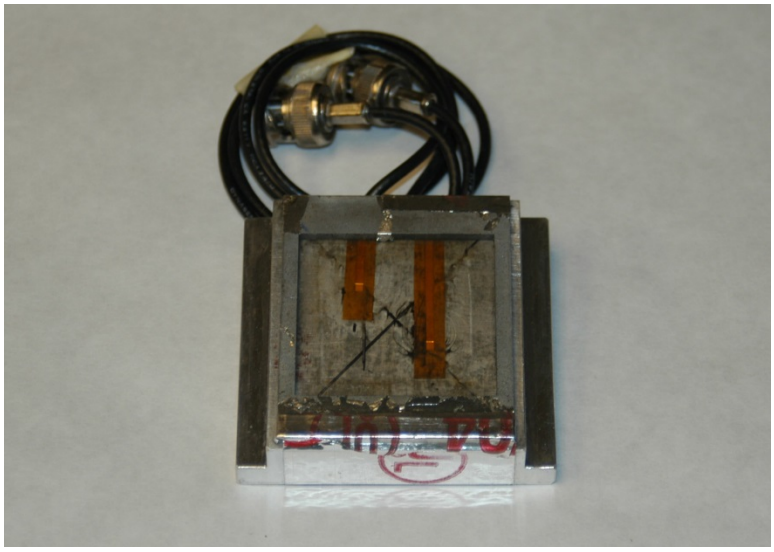

Figure 9.14: Dual Carbon Gage Experimental Setup

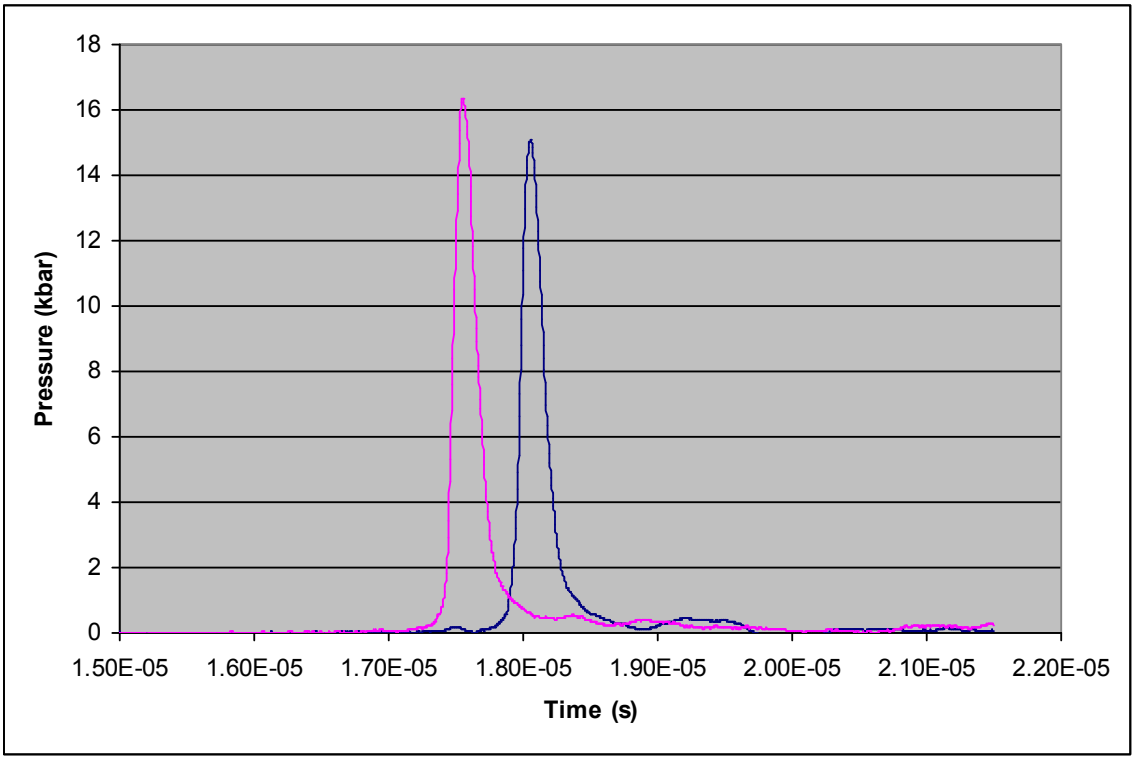

Figure 9.15: Impact Simultaneity Experiment

9.6. Target Material Response

A primary goal of this investigation has been to induce a material response in a target sample using the developed LIHE driven flyer technique. Because very little public information was available on material response due to thin flyer impact, it was unknown which materials might exhibit the best material response for study. For this reason, a range of target materials and material characteristics were chosen for testing. These included both plastic and metallic targets, each chosen with the goal of inducing some response such as spall or an increase in material hardness from the flyer impact.

A predictable shock can be induced into a material specimen by means of a gas gun experiment, direct interaction with various explosives, or by other methods of controlled mechanical impact. The shock level produced by the LIHE driven flyer impact is generally considered to be in the weak shock regime as compared to other impact and

shock loading scenarios. As discussed, the impact pressure produced by these LIHE driven flyer experiments ranged from approximately 5 to 50 kbar (500 to 5000 MPa, $72.5x10^4$ to $72.5x10^5$ psi), which in comparison is orders of magnitude lower than the strong shock regime, between 10,000 and 100,000 MPa. In the weak shock regime, Graham [41] predicts spall in PMMA as well as yield in copper and aluminum.

Eighteen material response experiments were conducted. Qualitative response of each of the plastic targets was accomplished by post-test inspection. Both qualitative and quantitative material response was ascertained for the metallic targets by post-test inspection, sectioning, micrographing, and hardness testing. Under the constraints of budget, the sectioning and analysis process was completed for one unshocked standard and two flyer impacted targets for each of the five metallic target materials. Table 9.6 lists each of the eighteen material response experiments with the shaded cells indicating those targets that were dissected and further analyzed.

Overall, a definitive material response was generated in each of the one-dimensional experiments. Spall was successfully induced in the PMMA and polycarbonate (LEXAN®) targets, and each of the metallic targets showed a measured increase in macrohardness at the target surface, due to the flyer impact. Dissection and analysis of these metallic targets showed that in no case did the microstructure at or near the impact surface change from the annealed state, as compared to the unshocked standard. Hardness analysis of the metallic samples through the thickness of the targets was generally inconclusive in measuring a gradient in hardness in the thickness direction. Unlike the plastic targets, spall was not induced in any of the metallic targets.

Table 9.6: Target Material Strengths and Summary Response

Test ID	Sample ID	Target Material	Tensile Yield (MPa)	Ultimate Strength (MPa)	Impact Pressure* [MPa (kbar)]	Summary Material Response
5	E	LEXAN®	62	86	656 (6.56)	Spall Induced
6	F	PMMA	60	62.1-75.8	480 (4.80)	Spall Induced
11	E	LEXAN®	62	86	656 (6.28)	Spall Induced
12	F	PMMA	60	62.1-75.8	451 (4.51)	Spall Induced
16	D	LEXAN®	62	86	740 (7.40)	Spall Induced
20	D	304 SS	205	515	2710 (27.1)	No Visual Change
21	E	316 SS	170	485	2710 (27.1)	No Visual Change
22	F	200 Ni	148	462	2710 (27.1)	No Visual Change
23	A	304 SS	205	515	3190 (31.9)	Increased Hardness
24	B	316 SS	170	485	3190 (31.9)	Increased Hardness
25	C	200 Ni	148	462	3220 (32.2)	Increased Hardness
26	D	304 SS	205	515	2590 (25.9)	Increased Hardness
27	E	316 SS	170	485	2590 (25.9)	Increased Hardness
28	F	200 Ni	148	462	2580 (25.8)	Increased Hardness
29	A	C110 Cu	69	220	2010 (20.1)	Increased Hardness
31	C	C110 Cu	69	220	2010 (20.1)	Increased Hardness
32	D	1100 Al	35	90	1370 (13.7)	Increased Hardness
34	F	1100 Al	35	90	1360 (13.6)	Increased Hardness

* Based on hydrocode calculation for the predicted (from areal density) flyer velocity.
** Shaded cells indicate dissected targets.

9.6.1. Plastic Target Response

Two of the seven target materials were common structural plastics: PMMA and polycarbonate. The purpose for introducing these materials into the test matrix, in addition to evaluation of the experimental process with relatively light target assemblies, was to provide material response data for softer and weaker target materials. The primary response expected in these experiments was a spall condition at the rear surface of the target. The transparency of these materials allowed for immediate visual analysis without further dissection.

PMMA (polymethyl methacrylate) is a light weight thermoplastic, often referred to as acrylic or by the trade names Plexiglas or Lucite. The PMMA material used for this study was manufactured by Polycast Technology Corporation under the trade name

POLY II® UVT. Extensive gas gun experimentation [18, 55] has been done to characterize this particular brand and formulation of PMMA in the 19 to 69 kbar range. Matthews [55] lists a PMMA tensile strength of 62.1-75.8 MPa (9000-11,000 psi) with a density of 1.19 g/cm^3 (0.043 lb/in^3).

Immediately, it was observed that the flyer impact on each of the PMMA targets induced a material spall at approximately 0.112 cm (0.044") from the back of the target. The area of the spall was somewhat oval-shaped with the approximate dimensions of 2.54 cm (1.0") by 1.14 cm (0.45") where the material was partially removed from the target plate, leaving a rough and fractured surface. Cracks emanated away from the spalled area toward the edges of the target. No other visual material damage was evident in either of the samples, other than superficial burn marks from the blast. Post-test photographs of the PMMA target sample 12 are given in Figure 9.16.

(a) Post-Test PMMA Target Impact Side (b) Post-Test PMMA Target Rear Surface

Figure 9.16: Post-Test Photographs of PMMA Target

It was expected from hydrocode analysis that the flyer impact onto the PMMA would create a spall at the rear surface of the target. Given that PMMA is a relatively brittle material, the separation of the spalled material from the target, by tensile fracture,

was also predicted. While spall was expected, the reduced size of the spall area was not. Post-test analysis, depicted in Figure 9.17, indicated that the shock pulse entered the target at the impact surface and immediately started to attenuate as it traversed through the target thickness. Rarefaction waves moved towards the center of the target from the sides of the flyer impact zone, decreasing through the thickness the shock loaded area of the target. As the compressive shock reached the rear surface of the target, the shock reversed direction and became a tensile shock moving back towards the impact surface. After a short transverse from the rear surface, the tensile stresses were sufficiently high in the target material to create a spall plane [40, 61]. At the point of the spall, the tensile pulse was effectively terminated in the target material.

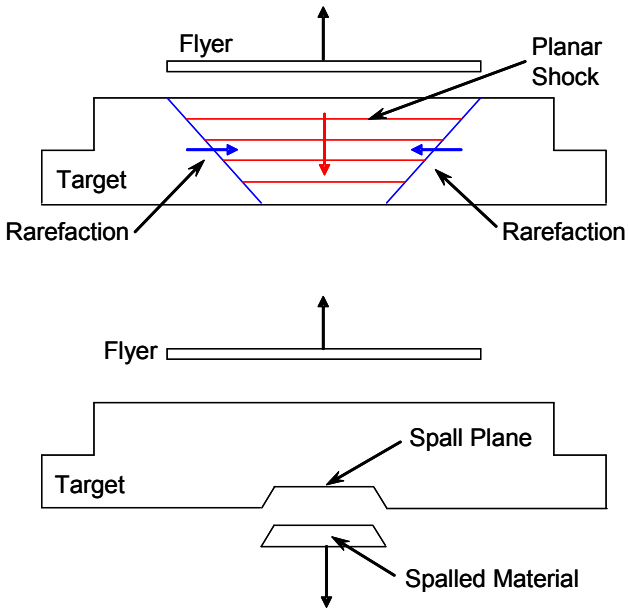

Figure 9.17: PMMA Spall Process

The polycarbonate sheet used for this study was manufactured by GE Plastics under the trade name LEXAN® 9034. GE characterizes LEXAN® as an amorphous engineering thermoplastic with high levels of mechanical, optical, electrical, and thermal performance [37]. LEXAN®, as well as other brands of polycarbonate sheet, are widely

used in large numbers of structural and product applications due to its strength and durability. In addition, polycarbonate sheet is used extensively in the explosives and ballistics community where its impact and shatter resistant properties are required. For these reasons, LEXAN® was chosen for this study as a plastic material with similar strength properties to PMMA, but with a superior impact resistance to acrylic sheet [37]. The reported tensile strength for the LEXAN® used was 62.1 MPa (9000 psi) with a density of 1.20 g/cm^3 (0.043 lb/in^3) [56].

Hydrocode modeling of the flyer impact onto the LEXAN® target was unable to predict spall because the KOWIN EOS for polycarbonate did not support tensile loading, thus making the magnitude of the return tensile pressure pulse difficult to predict. In addition, the less brittle polycarbonate material was known to withstand a high level of ballistic impact without shatter [37]. The reported impact strength (Izod Milled Notch test) of PMMA is 0.35-0.40 ft-lb/in [69], and 12-16 ft-lb/in for LEXAN® 9034 [56], but given the relatively similar tensile strengths of polycarbonate and PMMA, spall in the LEXAN sheet was expected. The response of the polycarbonate was predicted to result in less catastrophic spall damage than the PMMA due to its superior energy absorption properties.

Post-test inspection of the LEXAN® targets showed a spall area similar to that observed in the PMMA target experiments. But unlike the PMMA, the spall in the polycarbonate was completely encased within the target, only observable through the transparent material. The depth of the spall was estimated to be 0.25 cm (0.10”) from the rear surface. The area of the spalled region was an irregular oval-shape with dimensions of ~2.41 cm by ~1.40 cm (~0.95” by ~0.55”). The texture of the spalled area appeared to

be smoother than the PMMA targets with indication of a crack from the spall area to the rear surface in one of the three LEXAN® experiments. Damage in the other two targets was limited to the spall plane with no indication of cracks beyond the spall. Post-test photographs of the sample 11 LEXAN® target are given in Figure 9.18.

(a) LEXAN® Target Impact Surface (b) LEXAN® Target Rear Surface

Figure 9.18: Post-Test Photographs of LEXAN® Target

The plastic target material response results indicated that the explosively driven thin aluminum flyer impact was sufficient to create a shock to overcome the tensile strength of the thermoplastic materials at the rear surface of the target. Comparison of the PMMA to the LEXAN® response shows that despite the similar tensile strength, shock impedance, and density, the polycarbonate material had a greater ability to dissipate energy and contain the spall damage within the target. The PMMA target reacted as expected, failing in brittle tensile fracture. No compressive damage was evident in either material.

9.6.2. Metallic Target Response

Five metallic target materials were selected for material response analysis: 1100 aluminum, 304 stainless steel, 316 stainless steel, C110 copper, and nickel 200. This

range of materials was chosen in an attempt to achieve a different material response in harder and stronger materials than the plastics discussed in the previous section. Each was chosen as a material that may exhibit changes in microstructure and/or hardness, as a function of cold work being done by the impact of the flyer. Material changes from similarly prepared unshocked samples were the primary metallic material response investigated in this study. As will be seen in the following results, mixed material responses were observed in the dissected metallic materials, where increases in impact surface hardness were measured in each of the target samples, with no appreciable changes in microstructure observed in any of the target samples.

Both strength and hardness are indicators of a metal's resistance to plastic deformation, and are generally thought of as being linearly proportional [22, 48]. The mechanism by which cold work increases hardness and strength is that a deformation in the metal causes the entanglement of dislocations with grain boundaries, resulting in a material exhibiting higher strength [48]. It was predicted that surface deformation due to the flyer impact would be sufficient to measurably increase the surface hardness of the target.

As discussed above in section 9.4, the predicted and measured peak impact pressures were significantly higher than the reported tensile yield strength in each of the target materials. For this reason, it was expected that the targets would show some deformation at the impact surface, which would result in cold work being done to the target material to some depth. The expected result was a layer near the impact surface with flattened and elongated grain structure with an increased hardness in the affected area.

Each of the samples and standards were prepared by soaking the specimens at an elevated temperature (annealing) to standardize a microstructure and hardness to a known state prior to testing. For the actual flyer plate testing, the explosive detonation and subsequent air compression between the flyer and target was insufficient to significantly raise the target temperature above room temperature. In addition, the time at which the target surface would be exposed to any increased temperature would be very short in comparison to the minimum time required for the annealing process. Because the metallic target surface did not experience conditions necessary for recrystallization during flyer impact, any change in target material characteristics was considered the result of mechanical cold work due to the impact of the flyer.

The KOWIN equations of state for the five metallic target materials were generally insufficient to predict spall as a result of the flyer impact. Regardless, it was understood that the metallic targets were significantly stronger and tougher than the plastic targets used in the initial phase of the experiments. For these reasons, spall was not expected in these metallic target samples as a result of the flyer impact.

Three samples for each metallic material were dissected and analyzed: a single material "standard" with the purpose of having a basis of comparison for the material response of the flyer impacted targets, and two flyer impacted target samples. In the case of the 1100 aluminum and 304 and 316 stainless steels, the standard sample was taken from unused targets, which were annealed at the same time as their corresponding material targets. The C110 copper and nickel 200 standards were of the identical material stock as their corresponding flyer impacted targets, but due to a shortage of available finished parts, the standards were annealed in a second operation.

Each target to be dissected was taken to the Sandia Optical Metallography Lab for sectioning and analysis after the flyer impact portion of the testing was completed. The samples were first sectioned by a Struers Secotom-10 sectioning saw and placed in Allied cold mount cups using Struers EPORS two-part epoxy, as shown in Figure 9.19. After the holder epoxy was sufficiently cured, each sample was polished using a Rotopol 31 automated polisher at 150 RPM, using diamond suspension from 9 micron to 1 micron and varying cloths for each different material. Each sample was finished using a vibratory polisher using 0.5 and 0.04 micron oxide polish for 15 min to 2 hours, depending on the material. Next, the samples were etched, using the acid mixtures listed in Table 9.7, to expose the grain structure for micrographing.

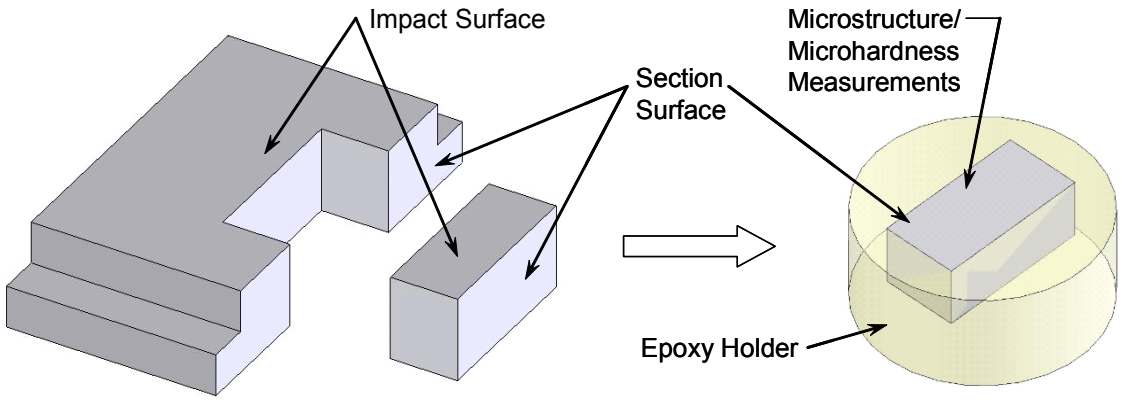

Figure 9.19: Sectioning and Mounting of Target Sample

Each sample was micrographed using a LEICA MEF4A Metallograph microscope and camera. Two digital micrographs were taken for each sample, one at 25x and one at 100x. Visual comparison was made between the impacted target samples and the standard sample for changes in microstructure. The results of this comparison are presented below for each of the five metallic target materials.

Table 9.7: Etching Chemicals and Processes

Material	Acid
1100 Aluminum	2.5 ml HNO_3, 1.5ml HCI, 1.0 ml HF, 95ml H_2O or 100 ml DI H_2O, 0.5 ml 49% HF swab etch for 0.5 – 1.0 minute
304 Stainless Steel	Oxalic Acid, 6 volts 15 seconds (electrolytic etch)
316L Stainless Steel	Oxalic Acid, 6 volts 15 seconds (electrolytic etch)
C110 Copper	Ammonium Hydroxide, Hydrogen Peroxide, and H_2O, in even amounts
Nickel 200	50ml HNO_3, 50ml Acetic Acid

After micrographing, each sectioned sample was once again polished in preparation for Vickers microhardness testing. This analysis was conducted with a Shimadzu hardness tester, using a load of 100 g (0.22 lb) for 15 seconds. The test hardware was calibrated at the beginning and at the end of each of two test days to assure quality measurements. Microhardness was recorded for each sample at multiple locations near the impact surface. Figure 9.19 shows the general location of the microhardness measurement area. Unfortunately, the microhardness results were inconclusive to determine either an increase in hardness due to cold work, or a potential hardness gradient through the thickness. It is believed that the microhardness measurements were compromised by issues associated with the sample surface preparation, such as the insufficient removal of material from the sectioned surface.

Macrohardness measurements were made at the impact surface using an Instron Wilson-Rockwell Series 2000 hardness tester. Due to the varying relative hardnesses of the five materials, three different Rockwell hardness scales were required: HRB for the stainless steel and nickel samples, HRE for the aluminum samples, and HRF for the copper samples. First, Rockwell hardness measurements were made on the standard unshocked sample for use as a basis for comparison. Next, hardness measurements were taken at the impact surface for each dissected target, with additional measurements made

in unshocked material exterior to the impacted area of the target. In all cases, the impact surface showed an increased hardness in both the unshocked standard and the un-impacted surface of the target. Figure 9.20 shows the locations of the Rockwell hardness measurement areas on the dissected target sample. For subsequent comparison and discussion, each of the measured Rockwell hardness values was converted to a common Brinell hardness scale. Table 9.8 lists the averaged Rockwell and Brinell (in parenthesis) macrohardness results for each of the five target materials.

Table 9.8: Macrohardness Measurement Results

Material	Scale	Standard	Sample 1		Sample 2	
		Unshocked	Shocked	Unshocked	Shocked	Unshocked
1100 Al	HRE (BHN)	31.8 (~30)	37.1 (~37)	33.3 (~33)	37.3 (~37)	33.9 (~34)
304 SS	HRB (BHN)	78.7 (146.0)	86.3 (169.8)	77.76 (143.3)	83.5 (160.4)	78.2 (144.6)
316 SS	HRB (BHN)	77.0 (141.0)	82.2 (156.6))	77.4 (142.1)	81.4 (154.3)	76.4 (139.7)
C110 Cu	HRF (BHN)	33.9 (~40)	54.7 (~53.5)	32.9 (~40)	54.3 (~53.5)	29.5 (~40)
Ni 200	HRB (BHN)	49.1 (82.1)	61.2 (96.3)	47.3 (80.3)	60.2 (95.2)	46.4 (79.4)

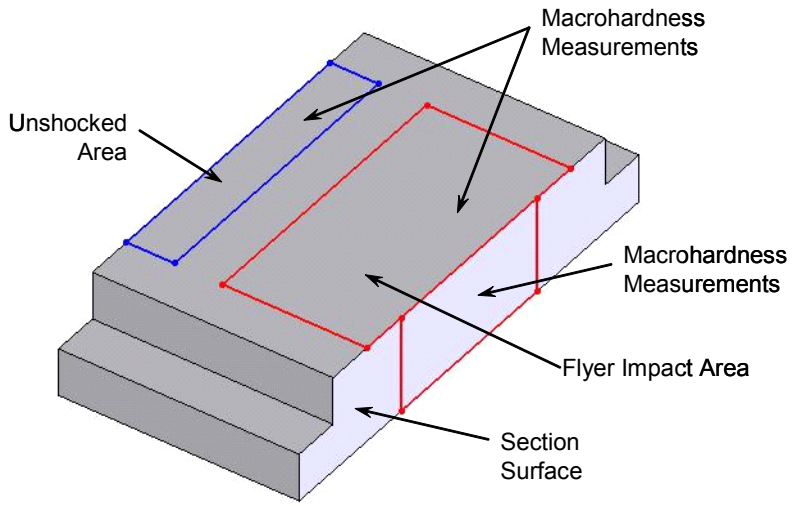

Figure 9.20: Dissected Target Sample Hardness Measurement Locations

Multiple macrohardness measurements were also taken through the thickness of each dissected sample. In contrast to the microhardness measurements, the macrohardness measurements were taken on the opposite side of the sectioned surface, in

the still intact portion of the target. Again, these through the thickness measurements were inconclusive in determining a consistent hardness gradient from the impact surface to the rear surface. In the thicker stainless steel targets, at the mid-point thickness, the hardness in both impacted samples was the same as the surface measurements of the standard. In the thinner copper and nickel samples, including the standard, the through the thickness measurements were lower in hardness than the surface measurements of the standard. In addition, the through the thickness indentions created by the Rockwell tester in these thin samples showed a greater than expected deformation. This unexpected and unexplained result brought the through the thickness measurements into question. The measurement error was possibly due to the geometry of the target sample on the Instron hardness tester. The end result, much like the microhardness results, was that the macrohardness testing at this location proved to be inconclusive.

9.6.2.1 1100 Aluminum

1100 Aluminum is a nearly pure aluminum alloy with only trace amounts of impurities such as copper [22, 56]. In the annealed state, the yield strength of 1100 Al is reported as 35 MPa (5000 psi) with an ultimate tensile strength of 90 MPa (13,000 psi) [22]. The impact pressures for the aluminum targets were approximately 13.7 kbar (1370 MPa, 1.99×10^5 psi). The impact resulted in a pressure at the target surface ~39 times greater than yield. As will be discussed below, there is a high likelihood that the material tested was not fully annealed, but was 1100 aluminum in the half hard condition. The reported tensile strength for half-hard 1100 aluminum is approximately 117 MPa (17,000 psi). In this case, the impact pressures were still over eleven times greater than yield. Visual observation of the target surfaces indicated a very slight indention at the edges of

the flyer impact area. As expected, dissection of the target materials showed no spall generation in either impacted sample.

Comparison of the standard sample and the shocked samples indicated that neither of the targets showed any appreciable difference in grain structure at the impact surface. In all three samples, the grain size throughout the depth was nearly equal, with no indication of deformation from the flyer impact. Figure 9.21 shows each of the micrographs from the 1100 aluminum samples. Pitting, in the form of black specks in the micrographs, are the result of the etching process where impurities in the metal were highlighted. The micrographs of the standard are given in Figure 9.21 pictures (a) and (b), test sample 32 in pictures (c) and (d), and test sample 34 in pictures (e) and (f).

A precise conversion to Brinell hardness was not accomplished because measured Rockwell hardness was relatively low, and the ASTM E140 conversion charts [3] did not report values in this range. The result was estimated values of BHN reported below. Macrohardness results, given in Table 9.9, indicate that the flyer impact resulted in a nominal increase in hardness of 17.0% over the standard and 10.7% over the un-impacted area of the target in relation to Rockwell E hardness. The area of the target surface not impacted by the flyer nominally showed a higher hardness of 5.7% (HRE) over the unshocked standard, possibly due to the traveling stress waves in the target after impact.

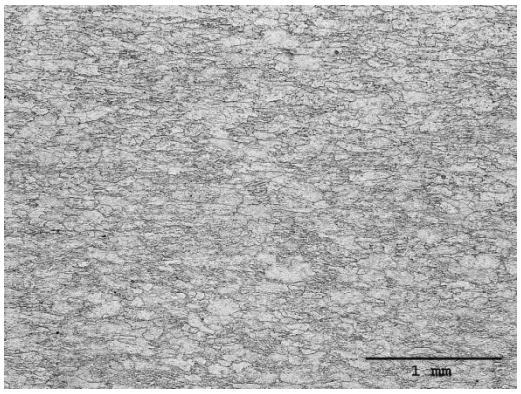

(a) Un-shocked Sample (25X)

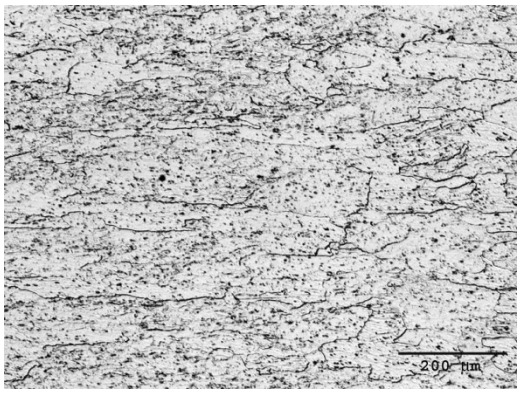

(b) Un-shocked Sample (100X)

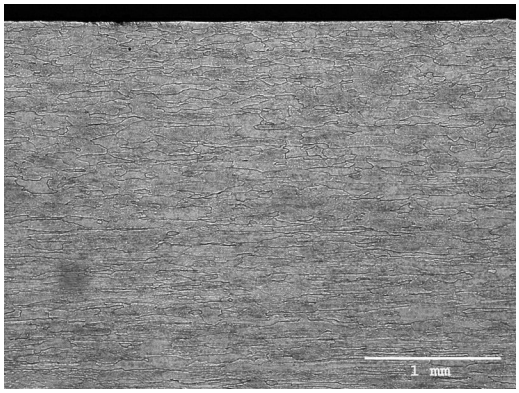

(c) 1100 Aluminum Sample 32 (25X)

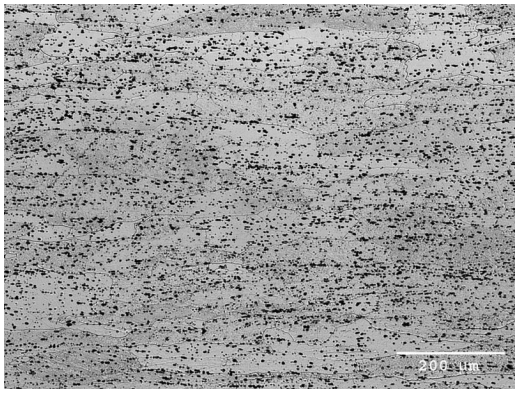

(d) 1100 Aluminum Sample 32 (100X)

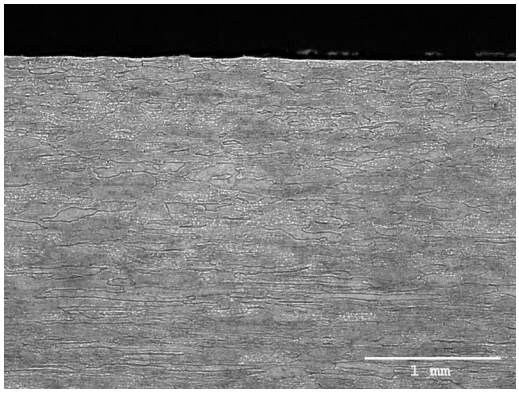

(e) 1100 Aluminum Sample 34 (25X)

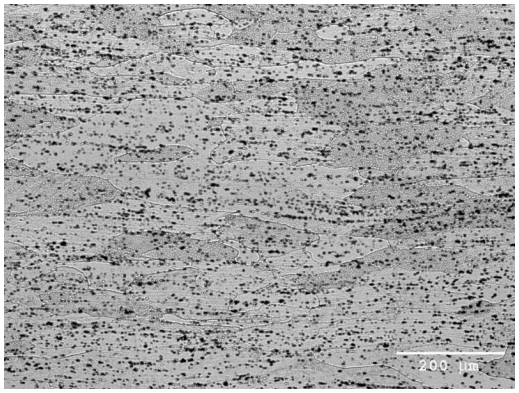

(f) 1100 Aluminum Sample 34 (100X)

Figure 9.21: 1100 Aluminum Standard and Target Micrographs

Table 9.9: 1100 Aluminum Macrohardness Results

Sample	Unshocked [HRE (BHN)]	Flyer Impacted [HRE (BHN)]	% of Standard	% of Unshocked
Standard	31.83 (~31)	-	-	-
Sample 32 (D)	33.32 (~33)	37.11 (~37)	116.6 (119)	111.4 (112)
Sample 34 (F)	33.94 (~34)	37.32 (~37)	117.3 (119)	110.0 (109)

Macrohardness results for the aluminum samples possibly indicate that the material used for the targets was not fully annealed 1100 aluminum. The measured hardness of ~33 BHN is closer to a half-hard 1100 aluminum (cold rolled ~35%) [43, 34], than to fully annealed 1100 (~23 BHN). In addition, the microstructure of both the target samples as well as the standard showed an elongated grain structure, which is consistent with a cold worked material. This error could have been made in that the raw stock was received with a material certification indicating 1100 aluminum, but with no indication of cold work condition. It is reported that fully hard (cold rolled ~75%) 1100 aluminum is completely recrystallized in ~10 minutes at 340ºC [43]. It is also known that recrystallization temperature increases with decreasing amount of prior cold work, or if the working is done at temperatures significantly above room temperature [34]. Given this scenario, the annealing process undertaken was likely insufficient to recrystallize the target samples to the fully annealed state.

9.6.2.2 304 and 316 Stainless Steel

Two types of stainless steel were utilized for material targets: 304 and 316. Austenitic stainless steels were chosen for this study because of the possibility that the cold work caused by the flyer impact would be sufficient to induce a change in the surface material of the target. In the annealed state, the yield strength of 304 stainless is 205 MPa (30,000 psi) and the ultimate strength is 515 MPa (75,000 psi) [22]. For 316 stainless, the yield strength is 170 MPa (25,000 psi) with an ultimate strength of 485 MPa (70,000 psi) [22].

The impact pressure range for the 304 targets was approximately 25.9 to 31.9 kbar (2590-3190 MPa, 3.76×10^5-4.63×10^5 psi). The impact resulted in a pressure at the target surface over 12 times greater than yield. Visual observation of the target surfaces

indicated only blast markings from the explosive detonation gases. As predicted, dissection of the target materials showed no spall generation in either impacted sample.

Dissection of the 304 stainless steel targets, shown in Figure 9.22, indicated that no microstructural changes were evident as compared to the unshocked samples of either of the impacted targets. The annealed and unshocked sample showed a slightly larger grain structure near the surface, which was equally evident in the micrographs of each of the impacted targets. This increased grain size at the target surface is likely the result of machining at this surface, as well as an unconstrained interface during annealing [78]. The micrographs of the 304 standard are given in Figure 9.22 pictures (a) and (b), test sample 23 in pictures (c) and (d), and test sample 26 in pictures (e) and (f).

Macrohardness results for the 304 stainless steel samples, given in Table 9.10, indicate that the flyer impact resulted in an increase in hardness in both targets in comparison to the standard. Sample 23, which experienced an ~31.9 kbar (3190 MPa, 4.63×10^5 psi) impact, showed an increase (BHN) of 16.3% over the standard, and a 9.8% increase with an ~25.9 kbar (2590 MPa, 3.76×10^5 psi) impact for sample 26. The area of the target surface not impacted by the flyer showed a nominal hardness nearly equal to that of the unshocked standard.

Table 9.10: 304 Stainless Steel Macrohardness Results

Sample	Unshocked [HRB (BHN)]	Flyer Impacted [HRB (BHN)]	% of Standard	% of Unshocked
Standard	78.67 (146.0)	-	-	-
Sample 23 (A)	77.76 (143.3)	86.27 (168.8)	109.7 (116.3)	110.9 (118.5)
Sample 26 (D)	78.21 (144.6)	83.48 (160.4)	106.1 (109.8)	106.7 (111.0)

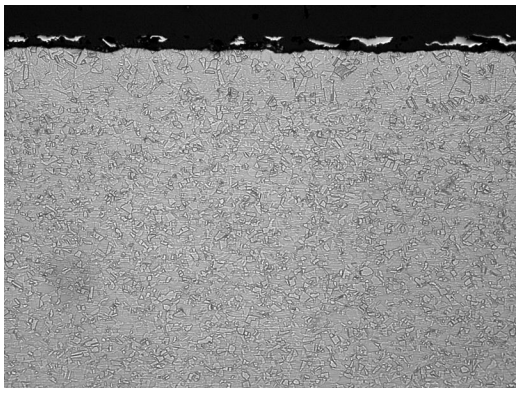

(a) 304 SS Un-Shocked Sample (25X)

(b) 304 SS Un-Shocked Sample (100X)

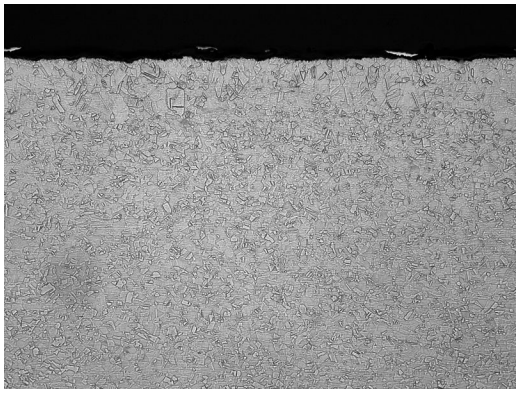

(c) 304 SS Sample 23 (25X)

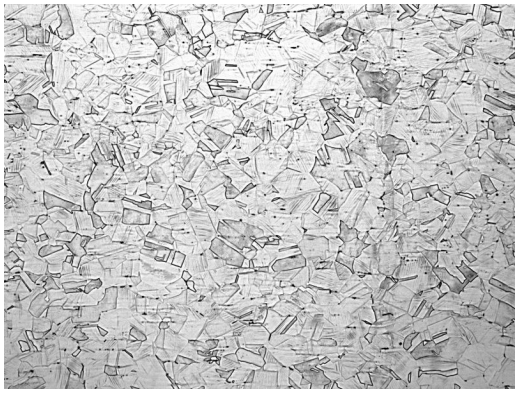

(d) 304 SS Sample 23 (100X)

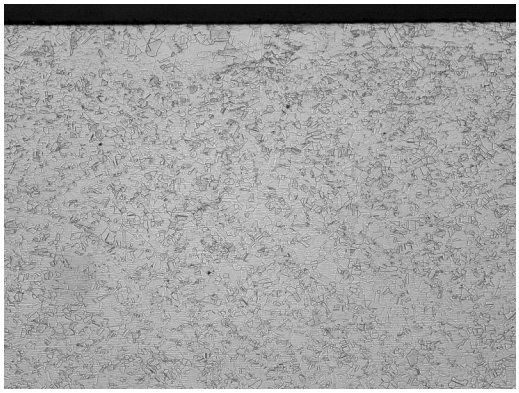

(e) 304 SS Sample 26 (25X)

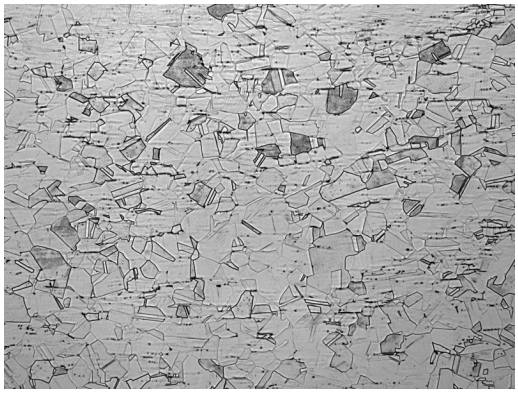

(f) 304 SS Sample 26 (100X)

Figure 9.22: 304 Stainless Steel Standard and Target Micrographs

The microstructural results for the 316 stainless steel were similar to those of the 304 samples. The microstructure was enlarged near the surface of both impacted samples as well as the standard, with no noticeable changes from the standard to the impacted targets observed. The micrographs of the 316 standard are given in Figure 9.23 pictures

(a) and (b), test sample 24 in pictures (c) and (d), and test sample 27 in pictures (e) and (f).

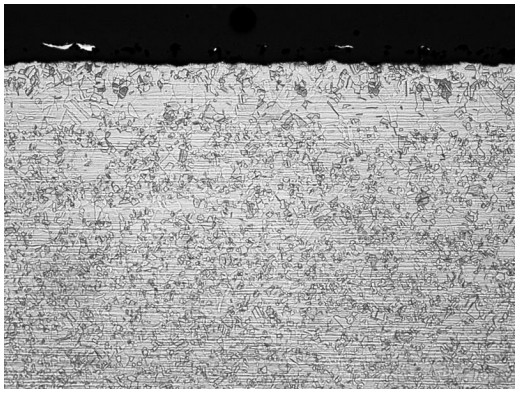

(a) 316 SS Un-Shocked Sample (25X)

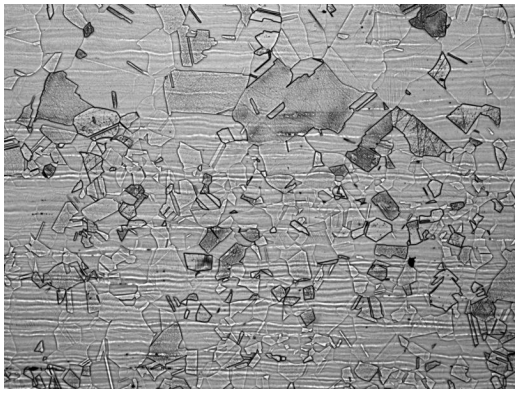

(b) 316 SS Un-Shocked Sample (100X)

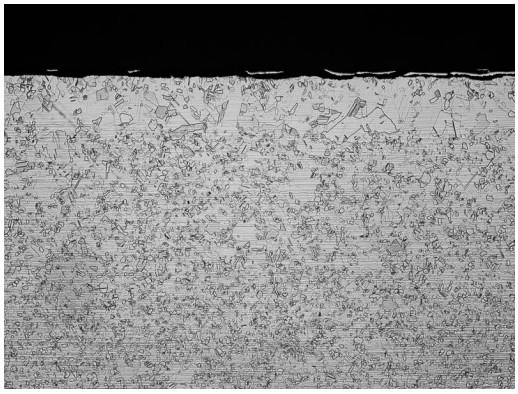

(c) 316 SS Sample 24 (25X)

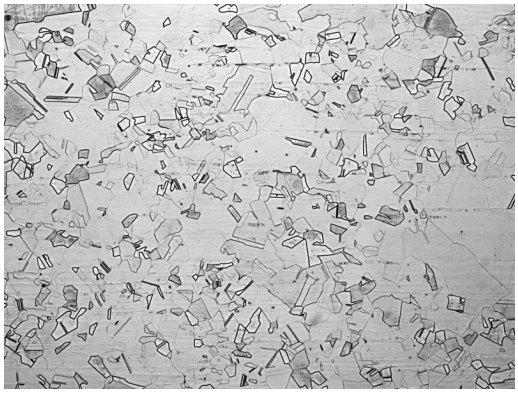

(d) 316 SS Sample 24 (100X)

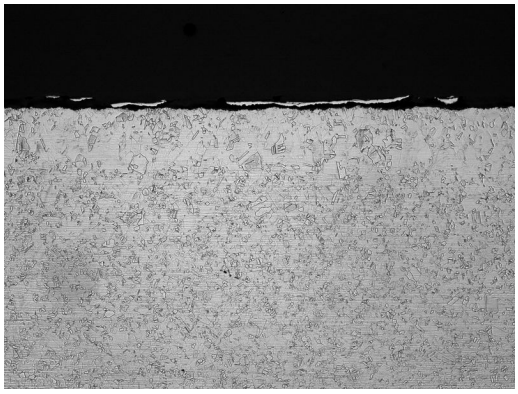

(e) 316 SS Sample 27 (25X)

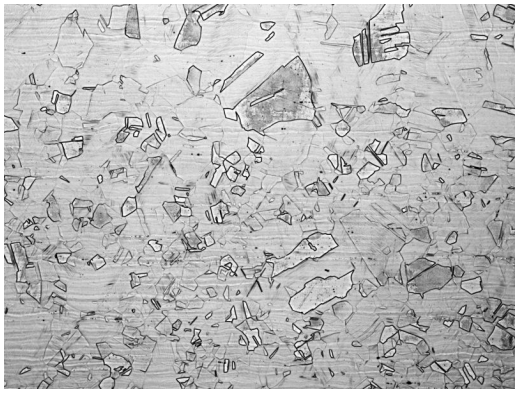

(f) 316 SS Sample 27 (100X)

Figure 9.23: 316 Stainless Steel Standard and Target Micrographs

Macrohardness results for the 316 stainless steel samples, given in Table 9.11, indicate that the flyer impact again resulted in an increase in hardness in both targets in

comparison to the standard. Sample 24, which experienced a 31.9 kbar (3190 MPa, 4.63×10^5 psi) impact, shows an increase (BHN) of 11.0% over the standard, and Sample 27 a 9.4% increase (BHN) with a 25.9 kbar (2590 MPa, 3.76×10^5 psi) impact. The area of the target surface not impacted by the flyer showed a nominal hardness nearly equal to that of the unshocked standard.

Table 9.11: 316 Stainless Steel Macrohardness Results

Sample	Unshocked [HRB (BHN)]	Flyer Impacted [HRB (BHN)]	% of Standard	% of Unshocked
Standard	76.98 (141.0)	-	-	-
Sample 24 (B)	77.36 (142.1)	82.19 (156.6)	106.8 (111.0)	106.3 (110.2)
Sample 27 (E)	76.35 (139.7)	81.42 (154.3)	105.8 (109.4)	106.7 (110.4)

9.6.2.3 C110 Copper

Commercially available, nearly pure, C110 copper bar was utilized for the copper targets in this study. Target samples were used in the stock condition with a very thin layer of silver plating to avoid any contact of the SASN explosive with the copper. Conversations with previous LIHE personnel [20] indicated that this precaution was necessary to avoid the formulation of the explosive cupric-azide, which is not characterized for any interaction within this study. In the annealed state, C110 copper has a tensile yield strength of 69 MPa (10,000 psi) and an ultimate tensile strength of 220 MPa (32,000 psi) [22].

The impact pressure for the C110 copper targets was approximately 20.1 kbar (2010 MPa, 2.92×10^5 psi). The impact resulted in a pressure at the target surface over 29 times greater than yield. The micrographs of the C110 copper standard are given below in Figure 9.24 (a) and (b), test sample 29 in pictures (c) and (d), and test sample 31 in pictures (e) and (f).

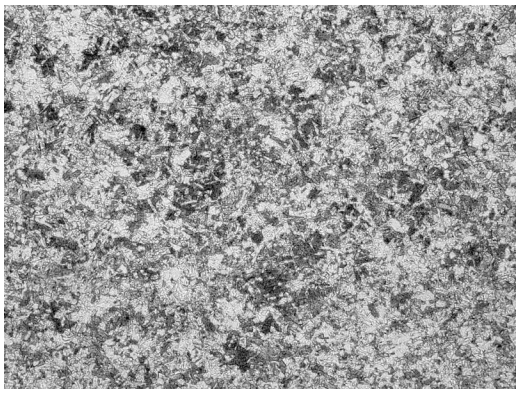

(a) C110 Cu Un-Shocked Sample (25X)

(b) C110 Cu Un-Shocked Sample (100X)

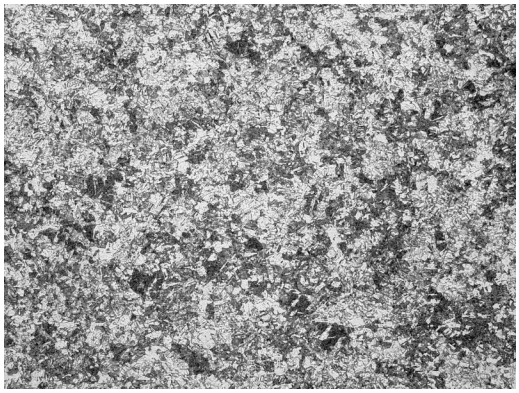

(c) C110 Copper Sample 29 (25X)

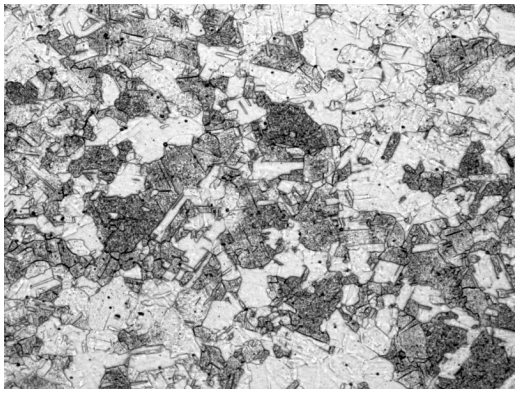

(d) C110 Copper Sample 29 (100X)

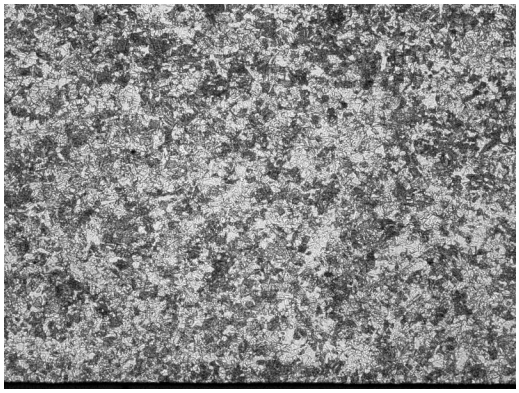

(e) C110 Copper Sample 31 (25X)

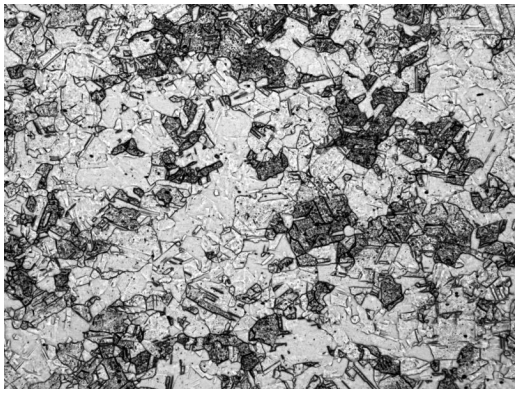

(f) C110 Copper Sample 31 (100X)

Figure 9.24: C110 Copper Standard and Target Micrographs

Macrohardness results for the C110 copper samples, given in Table 9.12, indicate that the flyer impact again resulted in an increase in hardness in both targets in comparison to both the standard as well as the unshocked portion of the target. A precise conversion to Brinell hardness was not accomplished because measured Rockwell

hardness was relatively low, and the ASTM E140 conversion charts [3] did not report values in this range. The result was estimated values of BHN reported below. For the copper experiments, the area of the target surface not impacted by the flyer nominally showed an ~13% decrease in hardness as compared to the unshocked standard. Considering that the standard was annealed at a different time as the target samples, this may indicate that the standard underwent a slightly different heat treatment. In reference to the measured Rockwell B hardness, sample 24 showed an increase of 61.7% over the standard and 83.9% over the unshocked area. Sample 27 showed an increase (HRB) of 60.5% over the standard and 84.3% over the unshocked area of the target.

Table 9.12: C110 Copper Macrohardness Results

Sample	Unshocked [HRB (BHN)]	Flyer Impacted [HRB (BHN)]	% of Standard	% of Unshocked
Standard	33.85 (~40)	-	-	-
Sample 24 (B)	32.91 (~40)	54.72 (~53.5)	161.7 (N/A)	183.9 (N/A)
Sample 27 (E)	29.49 (~40)	54.34 (~53.5)	160.5 (N/A)	184.3 (N/A)

9.6.2.4 Nickel 200

Nickel 200 is a nearly pure alloy with a composition of 99.5% nickel with trace amounts of carbon, manganese, and silicon [51]. Much like each of the metallic materials, nickel was chosen for this study due to the possibility that the cold work caused by the flyer impact would induce a change in the surface material hardness of the target. In the annealed state, nickel 200 has a tensile yield strength of 148 MPa (21,500 psi) and an ultimate tensile strength of 462 MPa (67,000 psi) [51].

The impact pressure range for the nickel targets was approximately 25.8 to 32.2 kbar (2580-3220 MPa, 3.74×10^5-4.67×10^5 psi). The impact resulted in a pressure at the target surface over 17 times greater than yield. Dissection of the target samples showed no spall generation in either impacted sample. Similar to the other metallic samples in the

study, little to no change in microstructure was observed between the unshocked standard and the impacted targets. Increased grain size near the surface was observed in each of the impacted specimens, as well as the standard. The micrographs of the nickel 200 standard are given in Figure 9.25, pictures (a) and (b), test sample 25 in pictures (c) and (d), and test sample 28 in pictures (e) and (f).

Macrohardness results for the nickel 200 samples, given in Table 9.13, indicate that the flyer impact once again resulted in an increase in hardness in both targets in comparison to both the standard as well as the unshocked portion of the target. Target 25 experienced an ~25.8 kbar (2580 MPa, 3.74×10^5 psi) impact pressure and an ~32.2 kbar (3220 MPa, 4.67×10^5 psi) impact pressure for target 28. The area of the target surface not impacted by the flyer showed a nominal 2.2% decrease in hardness (BHN) as compared to the unshocked standard. Again, the standard was annealed at a different time as the target samples, possibly indicating that the standard underwent a different heat treat. Sample 25, showed an increase (BHN) of 17.3% over the standard and 20.0% over the unshocked area. Sample 28 showed an increase (BHN) of 15.9% over the standard and 19.9% over the unshocked area of the target.

Table 9.13: 200 Nickel Macrohardness Results

Sample	Unshocked [HRB (BHN)]	Flyer Impacted [HRB (BHN)]	% of Standard	% of Unshocked
Standard	49.06 (82.1)	-	-	-
Sample 25 (C)	47.26 (80.3)	61.17 (96.3)	124.7 (117.3)	129.4 (120.0)
Sample 28 (F)	46.40 (79.4)	60.19 (95.2)	122.7 (115.9)	129.7 (119.9)

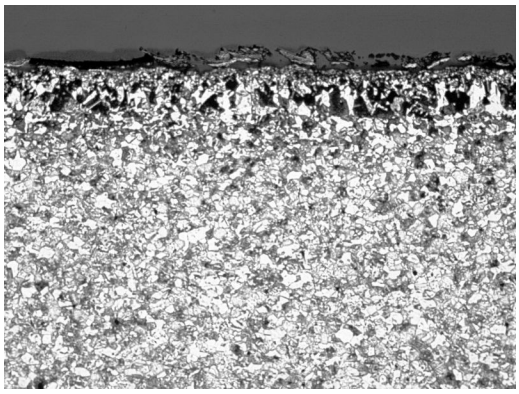

(a) Nickel 200 Un-Shocked Sample (25X)

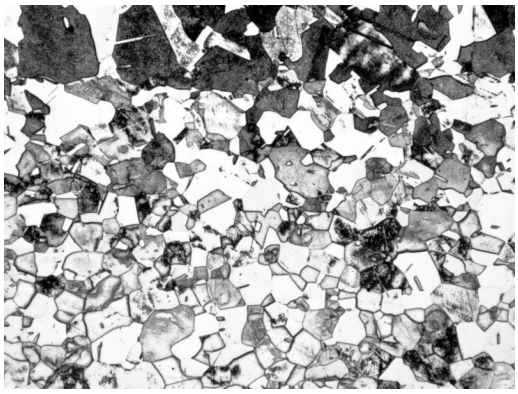

(b) Nickel 200 Un-Shocked Sample (100X)

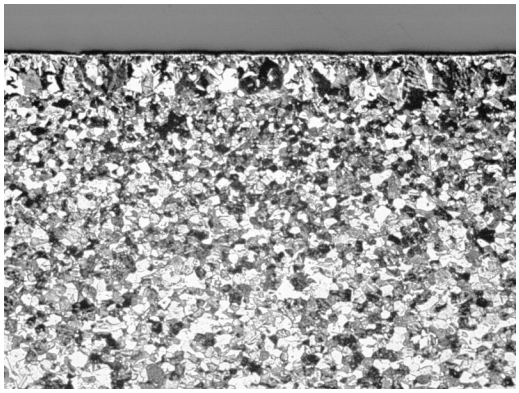

(c) Nickel 200 Sample 25 (25X)

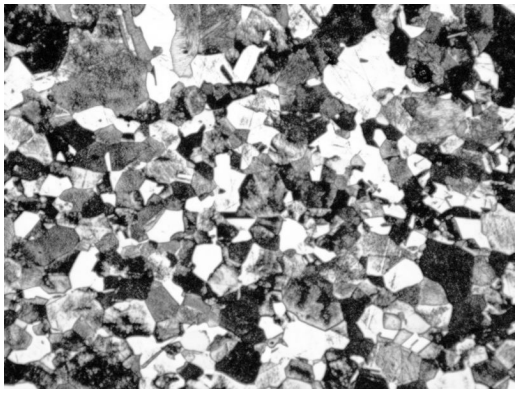

(d) Nickel 200 Sample 25 (100X)

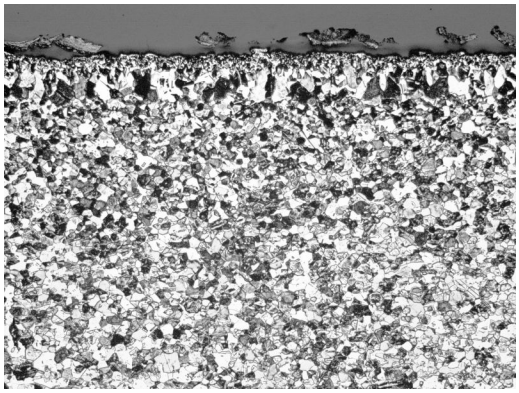

(e) Nickel 200 Sample 28 (25X)

(f) Nickel 200 Sample 28 (100X)

Figure 9.25: Nickel 200 Standard and Target Micrographs

9.7. Discussion of One-Dimensional Results

The one-dimensional results for the LIHE driven flyer show a great deal of promise towards describing the developed LIHE driven flyer theory. It was observed that the detonation of a measured SASN explosive deposition could accelerate a thin metallic flyer plate to impact a target with a reasonably predictable flyer motion, impact pressure

pulse, and delivered impulse. On average, from the fully successful experiments, the "measured" flyer velocity from measured impulse, indicated a velocity 2.5% lower than predicted; however, the one-dimensional results showed a larger than expected variation from the predicted performance. The standard deviation of the residuals from all of the flyer experiments was approximately 7% of the maximum velocity tested, indicating a fair amount of normally distributed scatter in the data.

The impulse delivery from the flyer impact and rebound appears to be prompt and efficient, driving the pendulum mass of the SBPA in a predictable fashion. The measured pressure pulses indicated sharp rise times, and pulse widths similar to those calculated by hydrocode analysis. In contrast, in some cases the measured pressures were slightly higher than predicted. Given the large number of factors influencing the flyer performance, these measured impact pressures are in the realm of possibility for a flyer velocity slightly higher than expected. This could have been the case due to an effectively thinner flyer, higher than inferred explosive deposition, or a combination of the two.

A possible source of "measured" flyer velocity deviation from the predicted velocity was an inaccurate quantification of the explosive deposition on the flyer. As discussed earlier, the explosive deposition is measured by means of coupons placed near the flyer surface. In the case of this testing, there were small differences in sprayed geometry from the flyer surface location and the coupon locations. The coupons were placed on the spray masking, while the flyer surfaces were slightly below the mask opening. A potential deposition difference scenario may have occurred where the deposition on the flyer surface was different than that measured on the coupon due to the

surrounding geometry. Unfortunately, direct measurement of the explosive deposition and distribution was not available to this investigation.

Another potential source of performance variation from predicted was the curled edges of the small flyer samples. The effect of the curled edges has not been entirely ascertained. As discussed earlier, the effect on delivered total impulse should have been minimal, though an exact quantification was not possible. It is believed that variations in flyer performance were the result of uncharacterized boundary conditions magnified by the small scale of these one-dimensional experiments. This potentially introduced error into the test design and diagnostics, which may account for some of the random error in the measured impulse and therefore calculated flyer velocity.

A qualitative material response was measured in each of the plastic targets impacted by the thin aluminum flyer. The spall generated in the plastic targets was anticipated, and indicated that the flyer impact was able to produce a transient pressure pulse sufficient to overcome the tensile strength of the relatively weak materials. These observations agree with basic shock physics principles and confirm that the induced shock into the target was of a high frequency and amplitude.

Quantifiable increases in hardness were measured in each of the metallic target samples, although no observable changes in microstructure between the shocked target material and the unshocked standards were found. Visual inspection of the impact surfaces showed very little damage, other than discoloring due to blast, and in some cases a very slight dent. As expected, none of the metallic targets indicated any degree of spall due to the flyer impact.

The degree of hardness increase at the impact surface can be generally tied to the material strain hardening exponent, n, of the true-stress – true-strain curve approximation

$$\sigma = K\varepsilon^n \tag{9.1}$$

where σ is the true-stress, K is the strength coefficient, and ε is the true-strain [48]. Table 9.14 lists the strain hardening information for each of the five metallic target materials used. Again, for comparison of hardness data between target materials, the Rockwell hardness measurements were converted to the Brinell scale (BHN) using ASTM conversion tables [3, 34].

Table 9.14: Measured Initial Hardness and Comparison With Handbook Data

Material	Condition	Expected Hardness (BHN)	Measured Hardness (BHN)	Expected YS [MPa (ksi)]	Expected Strain Hardening Exponent
1100 Al	Annealed	23	31	35 (5)	0.24 (a)
1100 Al	Half-hard	32	31	117 (17)	0.12 (b)
C110 Cu	Annealed	43	40	69 (10)	0.35 (b)
Ni 200	Annealed	75-125	94	148 (21.5)	0.38 (b)
304 SS	Annealed	149	149	205 (30)	0.425 (b)
316 SS	Annealed	149	144	170 (25)	0.41 (b)

a) Measured from plastic portion of true stress-true strain curve [43]
b) Estimated from strain at peak load or tensile elongation

In all cases, the impact pressure was well over a magnitude greater than the yield strengths of the target materials, and ranged from 11x in the aluminum samples to 29x in the nickel samples. Despite this fact, the observed target material response was limited to a hardness increase at the target surface. Although, the material preparation for metallography and analysis may have impeded the measurement of damage deeper through the target thickness. Calculating the hardness increase from the unshocked material to the shocked material, and plotting against the strain hardening exponent, a loose liner relationship can be observed for aluminum (warm worked and partially

annealed), copper, and nickel materials. The hardness increase in the stainless steel samples deviated somewhat from this linear relationship, but trended in the expected direction. Table 9.15 lists the hardness increases (in BHN), and are given graphically in Figure 9.26.

Table 9.15: Measured Hardness And Estimated Strain Hardening Exponents*

Material	Condition	Unshocked Hardness (BHN)	Estimated Strain Hardening Exponent	Shock-Induced Hardness Increase (BHN)	Shock Pressure / Yield Strength
1100 Al	Warm worked and partially annealed	31	.12	3.5	12
C110 Cu	Annealed	40	.35	13.5	29
Ni 200	Annealed	94	.38	15	17
316 SS	Annealed	144	.41	15	12
304 SS	Annealed	149	.425	21	12

* Tensile properties estimated based on hardness and tabulated values from several sources, including: [1, 60, 68]

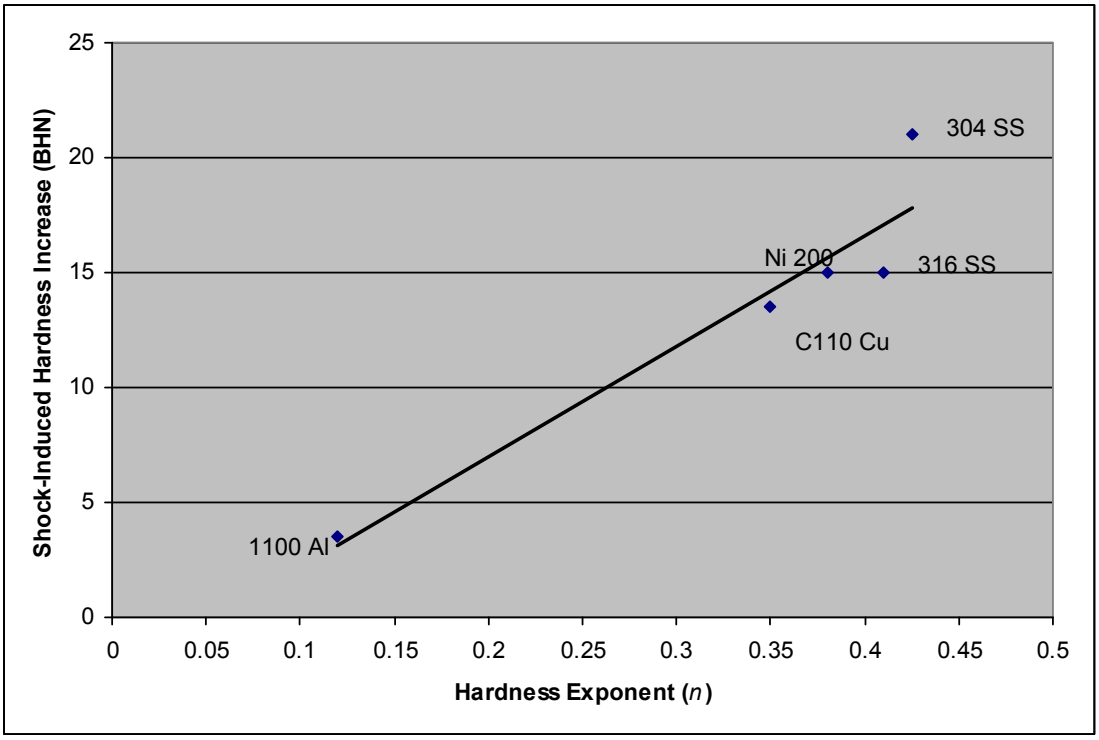

Figure 9.26: Correlation Between Hardness Exponent and Hardness Increase

While the one-dimensional results were not as definitive as had been hoped, they do provide a great deal of information towards the validity of the developed LIHE driven flyer theory. The flyer velocity, "measured" for each of the thirty-five experiments conducted, showed reasonable adherence to the predicted flyer velocity based on the coupon measured explosive deposition. Uncertain boundary conditions at the flyer edge are believed to be the cause of the relatively large variance in flyer performance. Given the multiple measurements required to calculate the flyer performance and the errors associated with each, the correlation between predicted and inferred is believed to be quite good.

Although the presented one-dimensional results are encouraging, there exists the need to better quantify the flyer motion to fully validate the theory. Additional experiments will be proposed in Chapter 11 that may add confidence to the theory's validity. In short, these will include direct measurement of the flyer velocity, better controlled impact pressure measurement, and larger flyer and target samples to minimize edge effects. Fortunately, enough confidence was gained in the one-dimensional experiments to proceed to the more complex two-dimensional loading scenario. The following chapter builds on the one-dimensional understanding of the flyer theory to load a ring structure with a cosine distributed impulse load.

The results of the one-dimensional tests complete a fundamental step towards the validation of the developed LIHE driven flyer theory. While relatively thick explosively driven flyer plates are not new to the explosives community, and high-energy driven flyers for impulse work have been used since the 1960s, the presented work extends the understanding of the explosively driven thin flyer technique and forms the basis for a new

impulsive loading method available to the community. These one-dimensional experiments potentially provide the first steps for confidence within the impulse generation community that LIHE driven flyer plates can be used predictably and reliably to simulate the exo-atmospheric cold x-ray deposition environment.

10. TWO-DIMENSIONAL FLYER EXPERIMENTS

Five two-dimensional flyer ring tests were conducted over two spray operations. The primary goal of each experiment in the series was to load the target ring structure with a nearly cosine distributed impulse by the LIHE driven flyer. Of the five rings tested, four were simple 20.32 cm (8.0") diameter 6061-T651 aluminum rings, and one was a 20.32 cm (8.0") diameter layered composite ring of 6061-T651 aluminum, polycarbonate, and silicone rubber. In each case, the rings were instrumented with three strain gages located on the inner surface to measure structural strain response. On the four aluminum ring structures, thin film carbon gages were placed on the outer target surface to measure flyer impact pressure and simultaneity.

The explosive deposition for sprays TP-2005-14 and TP-2005-15 both showed a nearly perfect distribution to load a ring with a cosine distributed impulse using the direct spray technique. The 0º explosive deposition on each of the flyer samples was measured to be within ±1% of the design deposition. As will be discussed throughout this chapter, this was not the optimum deposition to drive a flyer to similarly load a ring with a precise cosine impulse, but for this investigation, the loading differences were minor and the resulting structural response was little affected.

The overall test configuration and results for the two-dimensional experiments are given in Table 10.1. Detailed results from each of these tests are discussed in the following sections. All relevant data recorded from each ring experiment are included in Appendix C – Two-Dimensional Ring Tests.

Table 10.1: Two-Dimensional Summary Results

Ring ID	Spray ID	Target Configuration	Target Material	Expected Impulse	Achieved Impulse
1	TP-2005-14	Simple Ring	6061 Al	2267 taps	2175 taps
2	TP-2005-14	Composite Ring	LEXAN®/Al	2267 taps	2012 taps
3	TP-2005-15	Simple Ring	6061 Al	2331 taps	No Test
4	TP-2005-15	Simple Ring	6061 Al	2331 taps	No Test
5	TP-2005-15	Simple Ring	6061 Al	2331 taps	2331 taps

10.1. Simple Aluminum Ring Experiments

Of the four two-dimensional simple aluminum ring tests conducted, only two were considered good tests, where two were considered no-tests due to electrical breakdown failures of the large bank light array. In both of these cases, the explosive initiation was not simultaneous over the flyer surface. Instead, a discrete area was initiated by the light array, resulting in a sweeping detonation wave across the flyer surface. The result was the explosive not driving the flyer towards the target as designed. In both of these cases, the measured load was lower than expected and likely not impulsive to the ring structure. These light array and initiation problems were non-normal to the LIHE process, and were unexpected. The issues causing the large bank light array failure were investigated and solved for the remainder of the investigation.

A still frame from the high-speed video coverage, showing the rebounding flyer, is given in Figure 10.1. The picture is taken approximately 3.3 ms after explosive initiation. At this point, the light array has been energized, the explosive initiated, and the flyer has impacted and rebounded away from the target ring. A residual fireball can still be seen in this timeframe, as well as remnants of the electrical arcs emanating from the ends of the quartz tubes. Digital photography in the time frame of explosive detonation is difficult due to the extremely bright light from the light array and very short exposure

times, as well as the large EMP from the discharging capacitor bank interfering with the camera electronics.

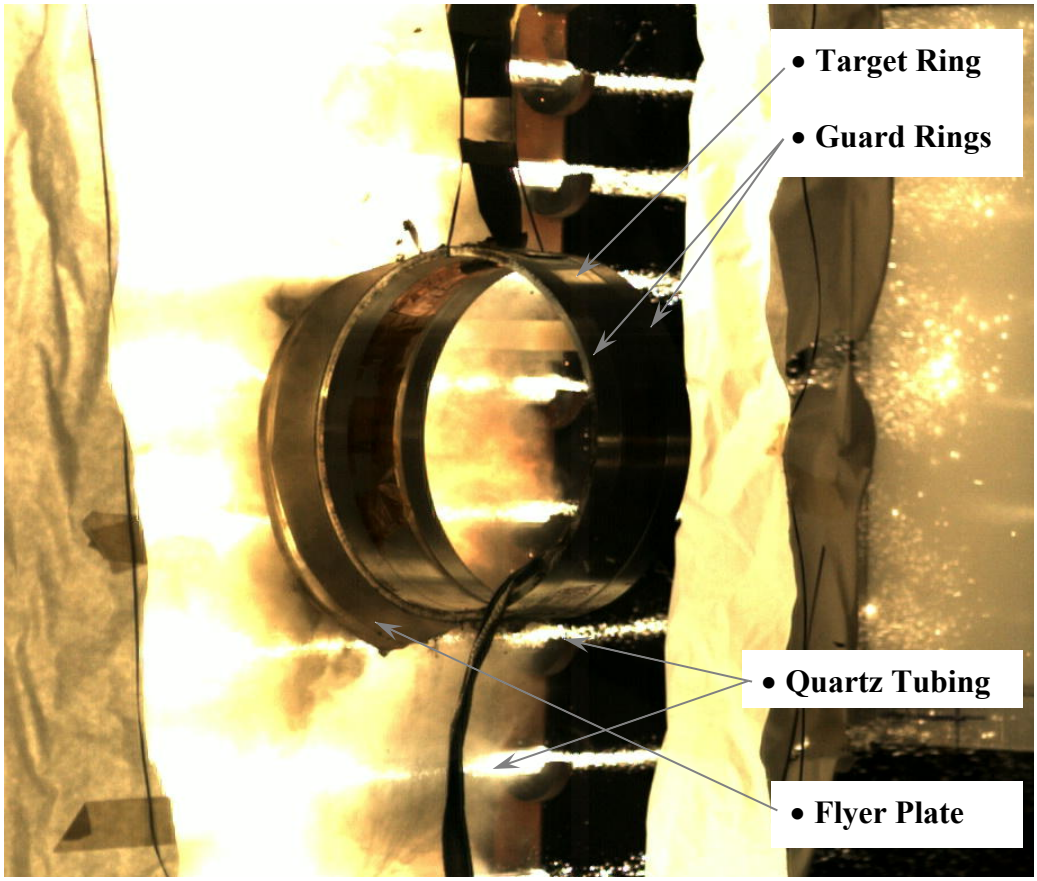

Figure 10.1: High-Speed Video Frame From a Simple Aluminum Ring Test

10.1.1. Aluminum Ring Experiment #1

Ring experiment #1 was configured as a simple aluminum ring with strain gages, carbon pressure gages, and flash x-ray instrumentation. The achieved 0º explosive deposition was 30.91 mg/cm^2, corresponding to a flyer velocity at this location of ~17,230 cm/s (6,783 in/s). The predicted impulse from this deposition, given a 0.035 cm (0.014") thick 1100 aluminum flyer, was 2267 taps. The test was conducted with no handling or explosive initiation issues. Recording of high-speed digital video and strain data was successful with no problems encountered. Unfortunately, the second and third

heads of the flash x-ray system fired simultaneously, resulting in the recording of only two ring positions corresponding to the first and second x-ray times. In addition, the instrumentation trigger to the carbon gage pulse power supply was incorrectly sent (late), causing the impact pressure at the gage locations to not be recorded.

While the results based on the maximum deposition at the 0º location were promising, the actual deposition to achieve a precise cosine load at the target surface was not achieved. The LIHE facility purpose for this spray operation was to achieve a cosine impulse load on a ring structure using the direct spray technique. Based on the theory developed in Chapters 4 and 5, to achieve a specific impulse loading using a 0.036 cm (0.014") thick LIHE driven flyer, a slightly lower explosive deposition than was required for the direct spray was necessary. For the achieved spray, the explosive deposition was slightly greater than required around the circumference of the flyer. The result was an impulse load which approximates a cosine, but does not precisely match it. Had the deposition been designed to achieve the proper explosive loading on the flyer, a better matching cosine load could have been achieved. This information was known prior to the spray, and the resulting explosive deposition was expected.

Five coupons were fired on the SBPA to ascertain the specific performance of the explosive formulation prior to conducting the TP-2005-14 ring experiments. The average explosive performance for this formulation was 92.2% of the nominal performance used in the experimental design. The difference was accounted for by reducing the explosive performance curve, experimentally determined in Chapter 5, by 7.8% in the post-test analysis of the flyer velocity calculations. In reality, this adjustment is an engineering approximation due to the small number of coupons tested over only a portion of the areal

densities achieved on the flyer surface. Given this data, the predicted maximum loading of the ring structure became 2169 taps. The difference between the desired and achieved cosine loading, based on the maximum deposition at the 0º location and the reduced explosive performance, is given in Figure 10.2.

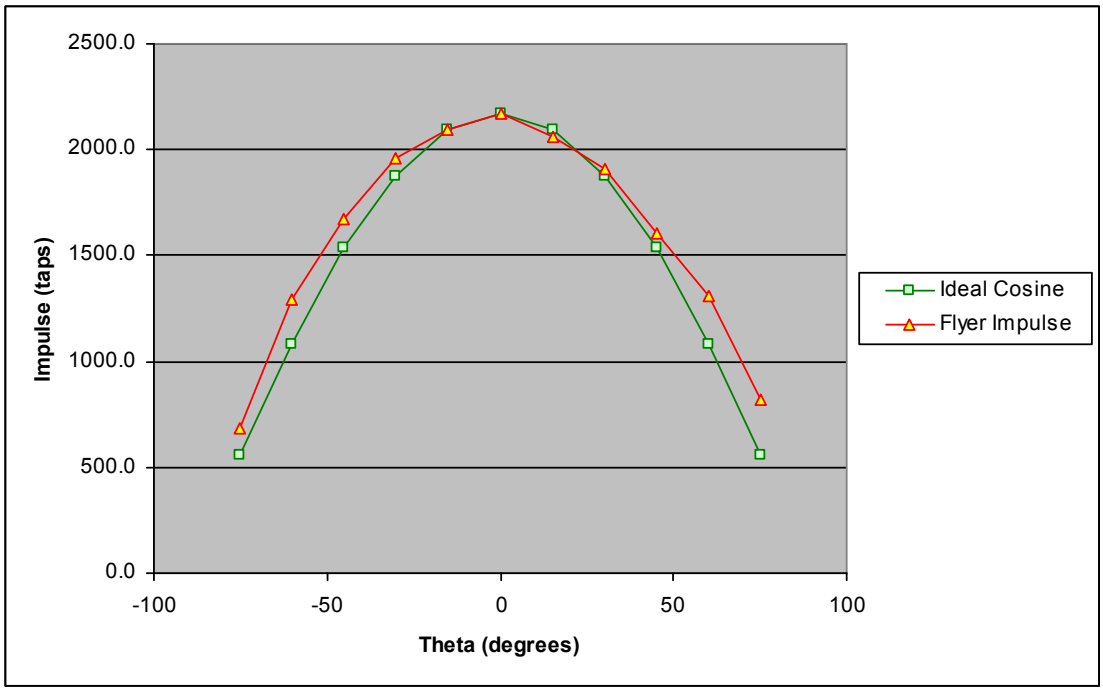

Figure 10.2: TP-2005-14 Flyer Generated Impulse Profile (Rings #1 & #2)

Post-test observation of the experiment hardware indicated a good detonation pattern on the flyer surface. As expected, the 1100 aluminum flyer yielded into the shape of the target ring. In addition, the impression of the three carbon gages on the ring surface were left in the flyer impact surface as a result of the impact pressure. The target ring showed no damage due to material yield or post-test secondary impact. Figure 10.3 (a) shows the pre-test ring structure with the flyer in place and instrumentation cabling, and Figure 10.3 (b) the post-test flyer and ring hardware. Though the guard rings are posed next to the target ring in the photograph, both successfully separated from the test ring

during the test. The four dents on the edge surfaces of the flyer were the result of a secondary impact with the light array long after impact with target ring.

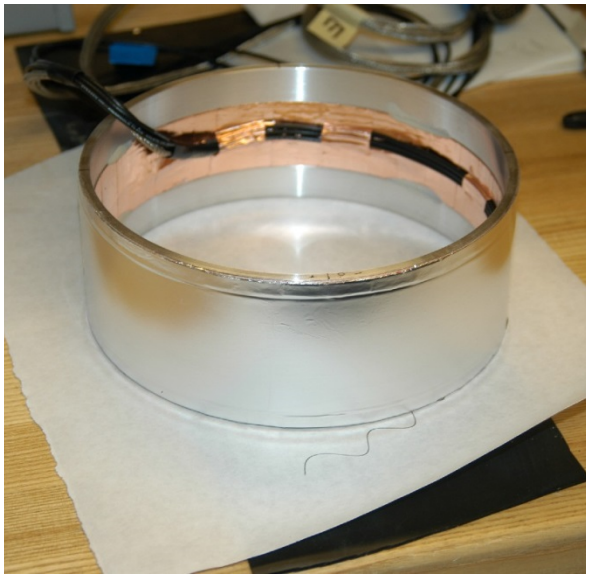

(a) Pre-Test Flyer/Ring Assembly

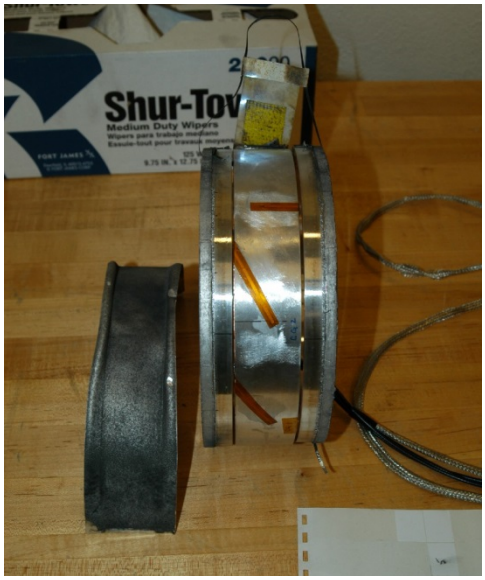

(b) Post-Test Ring Test Hardware

Figure 10.3: Ring #1 Pre-Test and Post-Test Photographs

As mentioned above, the flash x-ray system partially failed during the test. Of the three ring positions desired for analysis, only the first and second were recorded due to a pre-trigger in the third head of the x-ray system. Despite the glitch, the system did provide an indication to the initial rigid body velocity of the ring as a result of the flyer impact. Figure 10.4 shows the x-ray image of the horizontal translation of the ring at position 1, taken 0.0006 seconds from capacitor bank trigger, and a double image at position 2, taken 0.012 seconds from trigger. In the figure, the rings appear to translate both in the horizontal and vertical directions. The horizontal movement is correctly depicted, but the vertical movement is a result of a parallax effect (the apparent displacement of an object caused by a change in the position from which it is viewed) due to the vertically stacked configuration of the x-ray heads. The purple image color is an artifact of the software used to "develop" the digital image on the x-ray "film."

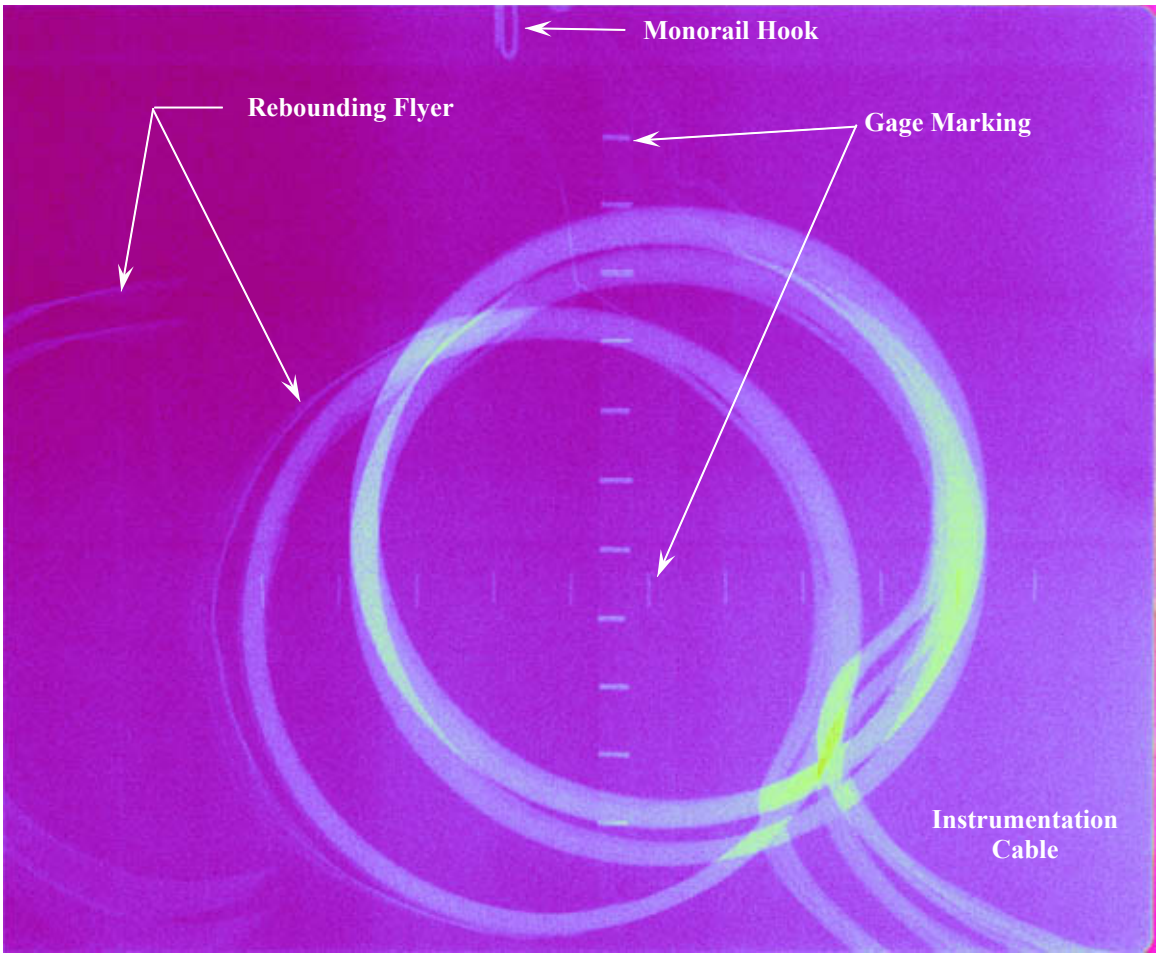

Figure 10.4: Ring #1 X-Ray Data

The flash x-ray rigid body motion data indicated an initial ring velocity of approximately 378.8 cm/s (149.1 in/s), corresponding to a total delivered impulse of 2180 taps. In the first exposure, the flyer can be seen rebounding from the target ring surface in a reasonably symmetric fashion, likely indicating a symmetric and simultaneous impact. High-speed digital video showed no abnormalities with the functioning of the light array or explosive initiation.

Vertical and horizontal 2.54 cm (1.0”) gage marks were positioned on the film prior to testing to aid in the x-ray analysis. These marks provided an indication of the parallax magnification effect as a result of the geometry of the test setup. The horizontal

marks were made prior to the test by firing one head of the x-ray with the spatial gage in the expected position of the ring. The vertical marks were made by placing the gage at the film surface during the test. Initial rigid-body velocity was calculated by equation (7.5) using the measured horizontal distance traveled between x-ray exposures. The delivered impulse is similarly calculated by equation (7.6).

Other information of note in the x-ray image is the instrumentation cabling and monorail attachment. The instrumentation cables can be seen trailing the ring to the lower right of the image. The aluminum hook from the monorail trolley is seen at the upper portion of the picture.

The comparison of the early-time strain response to the H-W solution showed good agreement for a cosine distributed load of 2170 taps. At these early times, the response was nearly all membrane strain, which mostly damped out within 0.010 seconds of impact. The membrane strain response matched the major structures of the H-W solution indicating proper excitation of the predicted modal frequencies. The first four membrane frequencies predicted by the H-W solution for the aluminum ring geometry were 8.11, 11.47, 18.14, and 33.45 kHz. Figure 10.5 shows the early time strain response and H-W solution for a load of 2170 taps at the 180º location. Figure 10.6 shows the early time strain response at the 90º and 270º degree locations with the corresponding H-W solution. Of interest is that under a proper cosine loading, these opposite gages behave nearly the same. Typically good agreement between the first few peaks at any angular position on the ring is indicative of a symmetric load applied in the proper cosine distribution.

The late time (up to 0.030 sec) strain response also closely matched the H-W solution. At the later time frames, the response was dominated by bending strain of significantly lower frequency than the membrane response. The major bending frequencies predicted by the H-W solution were 314.3 Hz, and 16.82 kHz. Figure 10.7 and Figure 10.8 show the 180º and 90º/270º strain responses respectively as well as their H-W comparison for the total recording time. As can be seen, there is excellent agreement between theoretical analysis and the measured strain response at each of these locations.

A test summary of Ring Test #1 is presented in Table 10.2. The final reported load for this experiment, calculated as an average of the x-ray analysis and H-W analysis was 2175 taps. This equated to 91.6% of the design load, and 100.3% of the "as-sprayed" load. As discussed above, the carbon pressure gage data was not recorded for this experiment. It was found after the test that a 0.5 second delay was present in the trigger circuit to the carbon gage pulse power supply. This effectively triggered the gage circuit after the test was concluded, resulting in no data being recorded for pressure or impact simultaneity.

Table 10.2: Ring #1 Data Results Summary

	Diagnostic	**Value**	**Indicated Load**
Design Load at 0º	Design Code	31.12 mg/cm^2	2279 taps
Explosive Deposition	Coupon Weight	30.91 mg/cm^2	2267 taps
Explosive Performance	Coupon Firing	92.2%	2169 taps
Initial Velocity	X-Ray Analysis	378.8 cm/s	2180 taps
Impact Pressure	Carbon Gage	N/A	N/A
Analytical Comparison	H-W solution		2170 taps
		Final Reported Load	**2175 taps**

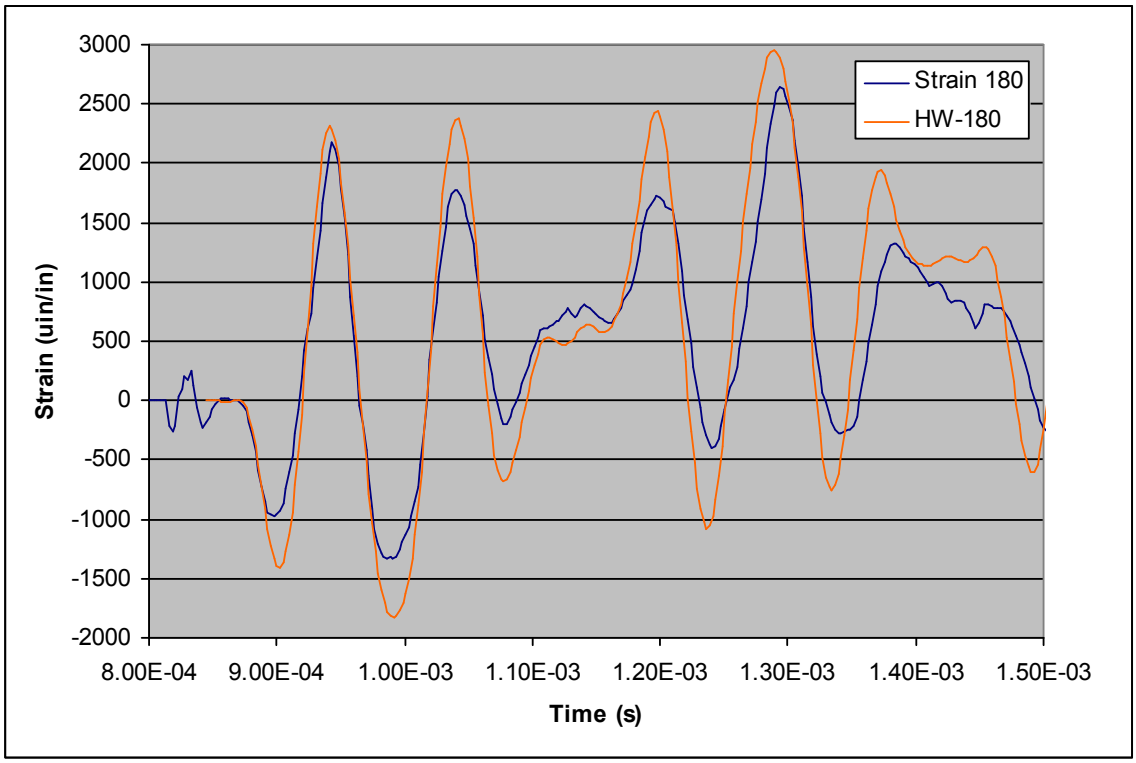

Figure 10.5: Ring #1 Strain Response at 180º (1.5 ms)

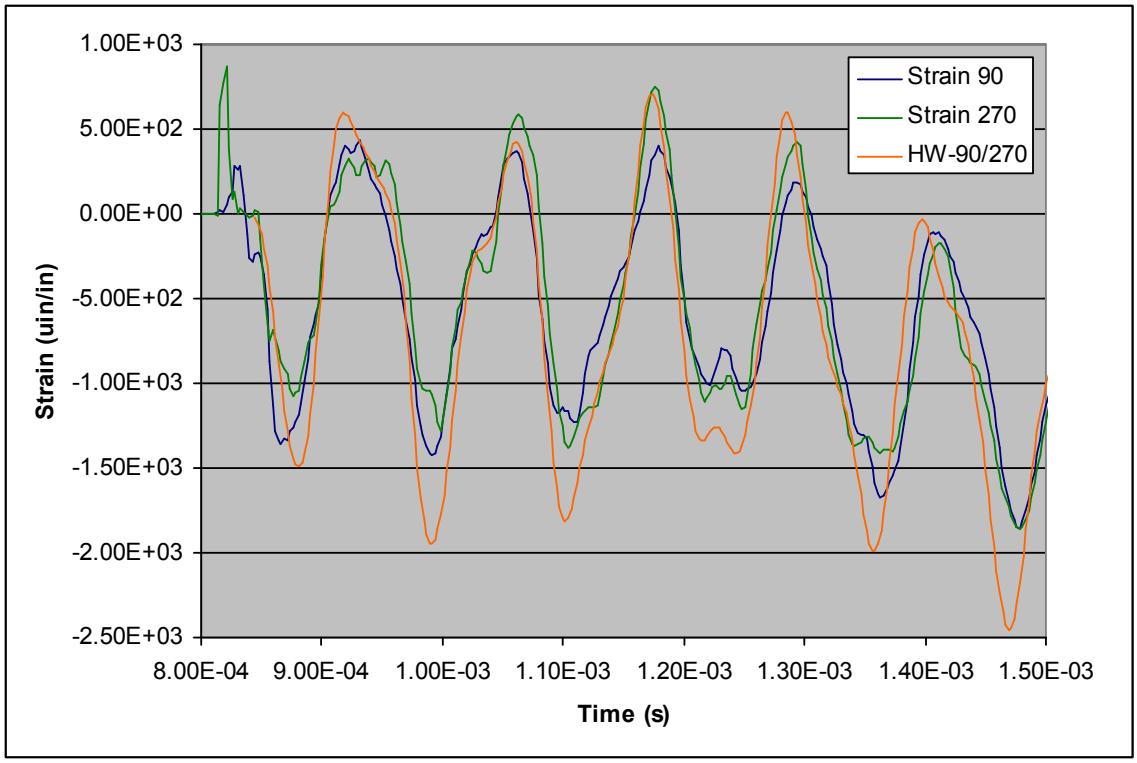

Figure 10.6: Ring #1 Strain Response at 90º/270º (1.5 ms)

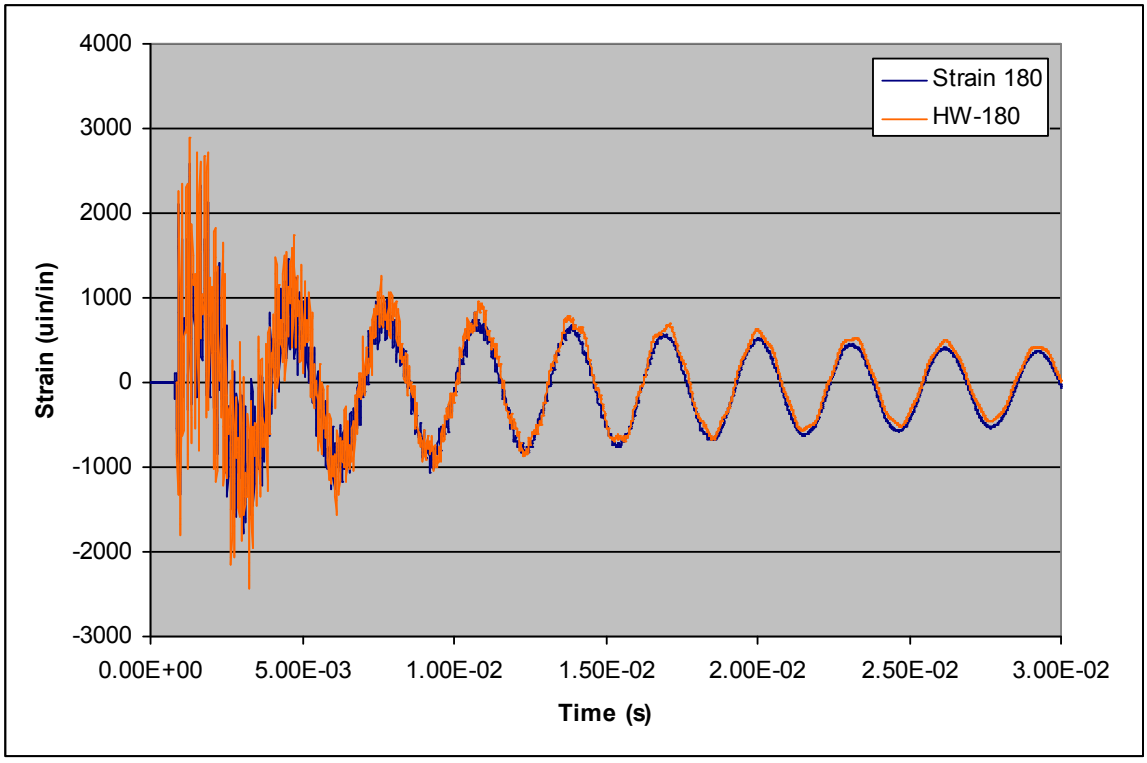

Figure 10.7: Ring #1 Strain Response at 180º (30 ms)

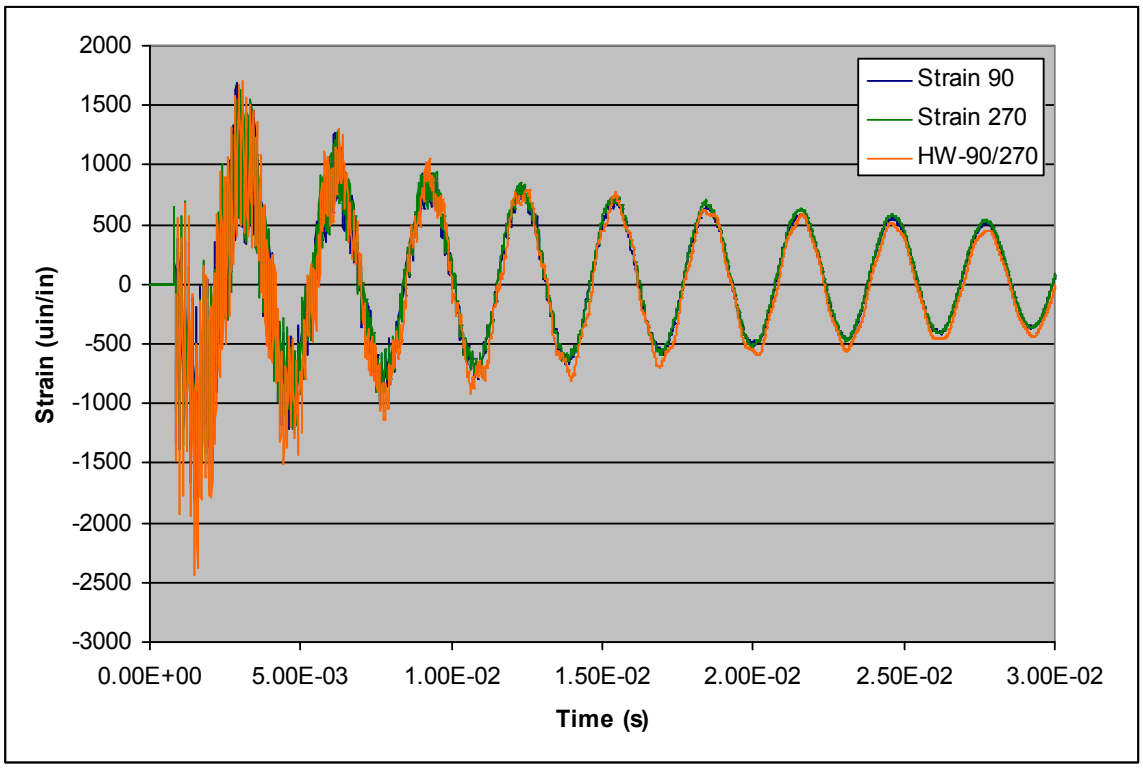

Figure 10.8: Ring #1 Strain Response at 90º/270º (30 ms)

10.1.2. Aluminum Ring Experiments #3 and #4

Ring tests #3 and #4, along with Ring #5, were successfully sprayed in the TP-2005-15 spray operation. The details for this spray are given in the following section in conjunction with the results for ring test #5. While the explosive deposition was deemed acceptable, an unexpected series of light array failures resulted in tests #3 and #4 being considered "no-tests." In both of these experiments, it was observed that the light array did not function as designed, causing the explosive to be initiated incorrectly.

The explosive initiation patterns on the surface of the flyers, shown in Figure 10.9, indicate that the explosive was not initiated simultaneously over the flyer surface. It appeared that discrete areas of the explosive were initiated by the light array, causing a sweeping detonation wave over portions of the flyer. This sweeping detonation, moving at approximately 120,000 cm/s (47,200 in/s), was insufficient to drive the flyer to a symmetric impact. The result was that a simultaneous flyer impact was not achieved.

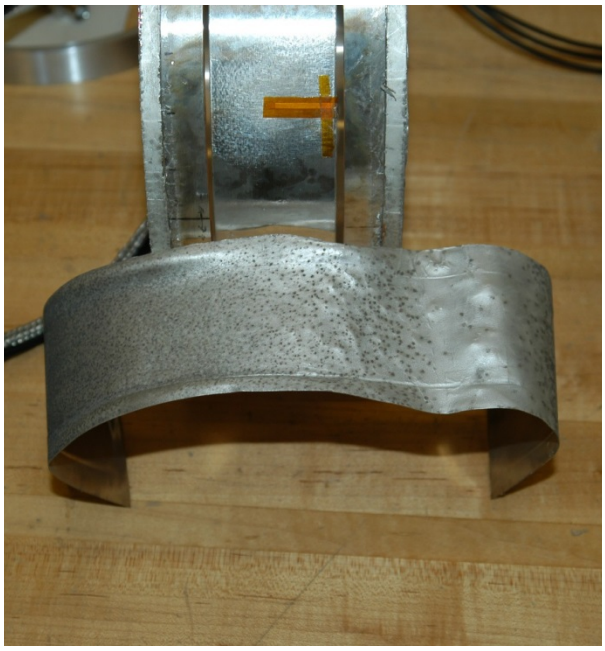

(a) Ring #3 Ring Test Hardware

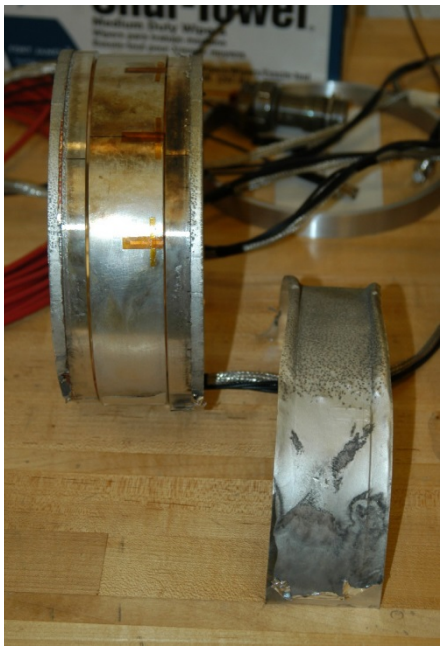

(b) Ring #4 and Flyer

Figure 10.9: Sweeping Wave Detonation Pattern on Flyer Surface

An investigation into the anomalous behavior discovered a systematic malfunction in the light array setup. A faulty configuration allowed the current from the capacitor bank to be diverted from the tungsten wire elements to a series of aluminized Mylar® and aluminum foil reflectors behind the light array. This deviation from the designed current path resulted in a significantly lower than expected energy output from the affected tubes.

The sweeping detonation on the sprayed surface in this situation is not unexpected, but is certainly considered an abnormal occurrence. The LIHE detonation process involves initiating the SASN explosive at a large number of "hot-spots" or initiation points on the surface that start the detonation of the surrounding explosive. A detonation front will sweep along the surface until the wave encounters another wave front or an end to the sprayed explosive layer. The greater the density of detonation points, the quicker the full detonation over the sprayed area will occur. Typically, there are hundreds of detonation points per square centimeter, effectively detonating the entire surface nearly simultaneously. But in these no-test cases, there was not enough energy from several discrete elements of the light array to create initiation points over the full surface. The result was a sweeping wave around circumference of a large portion of the flyer.

This type of issue is not uncommon when dealing with the very large voltages (typically 40 kV) and extremely high currents (300 kAmps). At these energy levels, electrical arcs can jump across a 2.8 cm (1.1 inch) air gap at unexpected locations. The problem was solved for subsequent testing by moving the conductive reflectors further away from the ends of the quartz tubing to prevent arcing.

Analysis of the ring test data indicated that the results from these two tests could not be used in the overall flyer analysis. The x-ray analysis, shown for ring #4 in Figure 10.10, showed an unsymmetrical flyer rebound, further bringing into question the simultaneity of the flyer impact on the surface. The measured rigid body motion of 356 cm/s (140 in/s) diminished the expected impulse by approximately 12%.

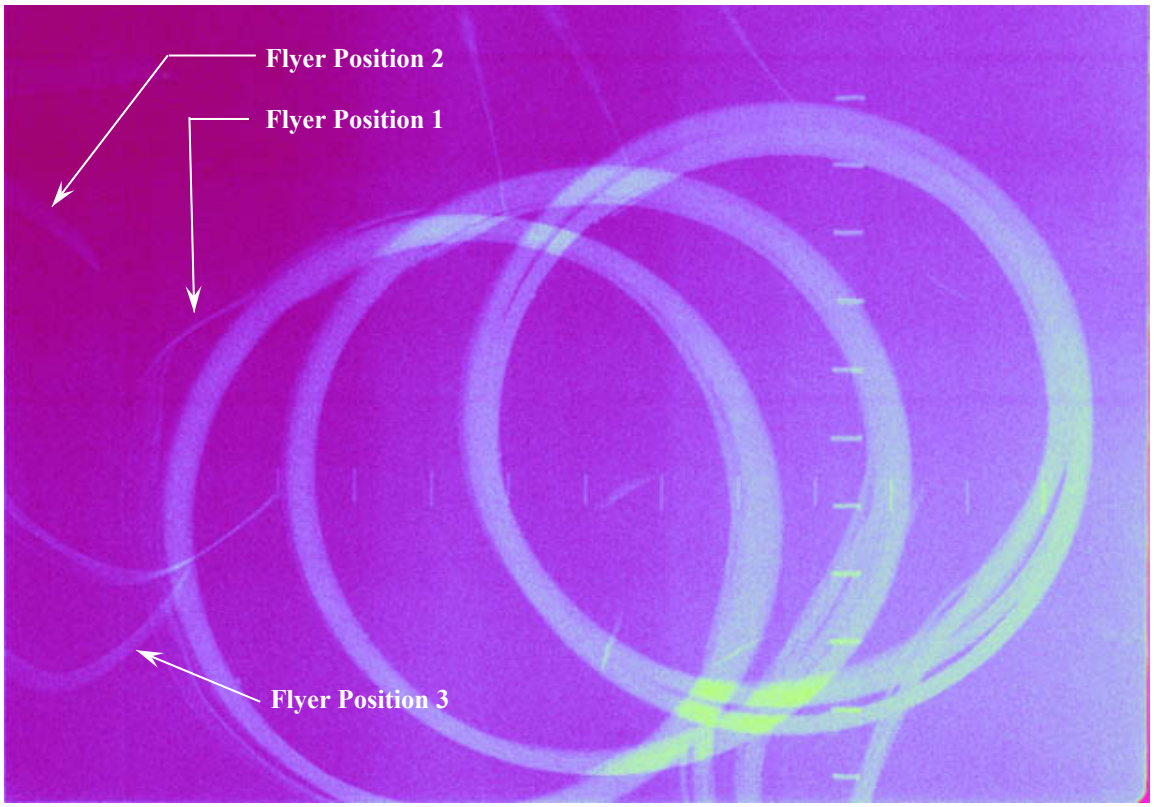

Figure 10.10: Ring #4 X-Ray Data

In addition to the post test x-ray analysis, the measured strain response showed significant disagreement with the expected response for the achieved explosive deposition. Figure 10.11 shows the early-time strain response at the 180º location. It can be seen that while the waveform structure was similar to the H-W prediction for the desired loading, additional higher frequencies were also present in the response. The

disagreement was great enough to invalidate the assumption of a simultaneously applied, cosine-distributed impulse load. These experiments were therefore not included in the validation of the flyer theory. A summary of the results from these failed experiments is given in Table 10.3.

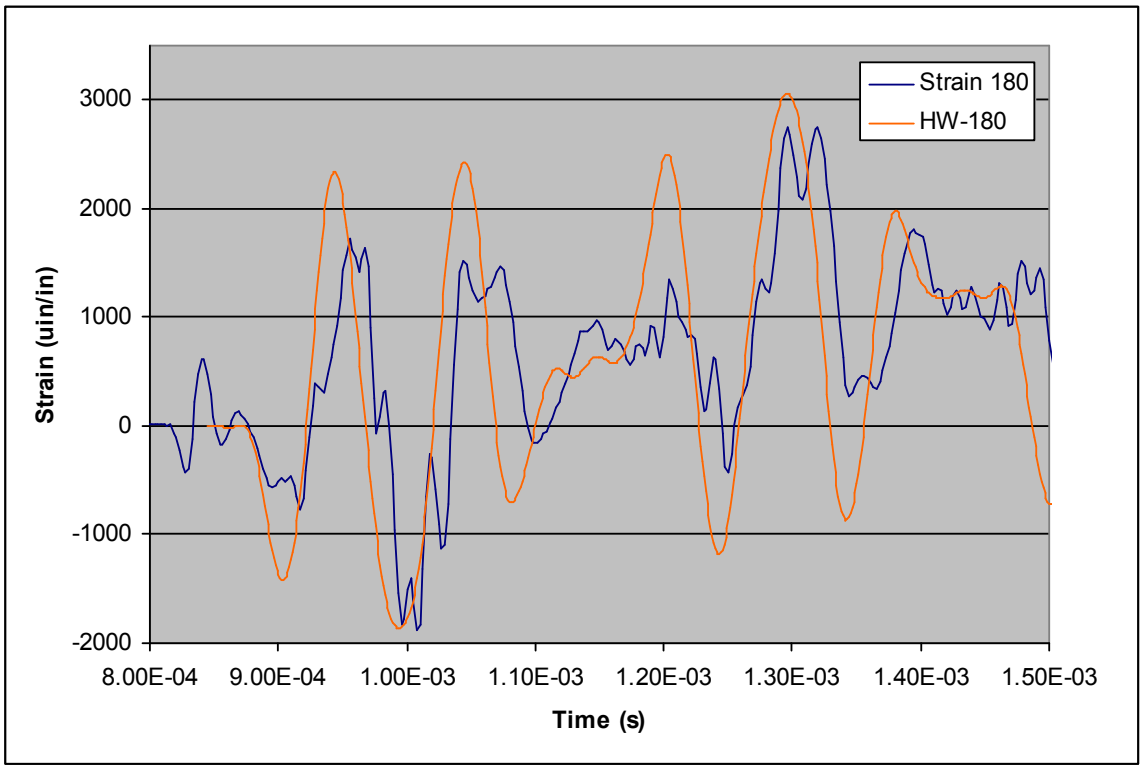

Figure 10.11: Ring #4 180° Strain Response (1.5 ms)

Table 10.3: Ring Tests #3 & #4 Data Summary

	Diagnostic	Value	Ring #2 Load	Ring #3 Load
Design Load	Design Code	31.12 mg/cm^2	2279 taps	2279 taps
Explosive Deposition	Coupon Weight	31.3 mg/cm^2	2331 taps	2331 taps
Explosive Performance	Coupon Firing	100%	2331 taps	2331 taps
Initial Velocity (cm/s)	X-Ray Analysis	356.4 / 357.6	2051 taps	2058 taps
Impact Pressure	Carbon Gage		N/A	N/A
Analytical Comparison	H-W solution		N/A	N/A
		Final Reported Load	**2051 taps**	**2058 taps**

10.1.3. Aluminum Ring Experiment #5

Aluminum Ring Test #5 achieved an explosive deposition of 31.3 mg/cm^2 at the 0º location, corresponding to a flyer velocity at this location of ~17,467 cm/s (6,876 in/s). The predicted impulse from this deposition, again given for a 0.035 cm (0.014") thick 1100 aluminum flyer, was 2331 taps. The test was conducted with no handling or explosive initiation issues. Recording of flash x-ray, high-speed digital video, strain, and impact pressure data was successful.

Five coupons were fired on the SBPA to determine the explosive performance prior to conducting the TP-2005-15 ring experiments. The average explosive performance for this formulation was 100% of nominal. With this result, the predicted maximum loading of the ring structure remained 2331 taps. The difference between the desired and achieved cosine loading, based on the maximum deposition at the 0º location and the nominal explosive performance, is given in Figure 10.12.

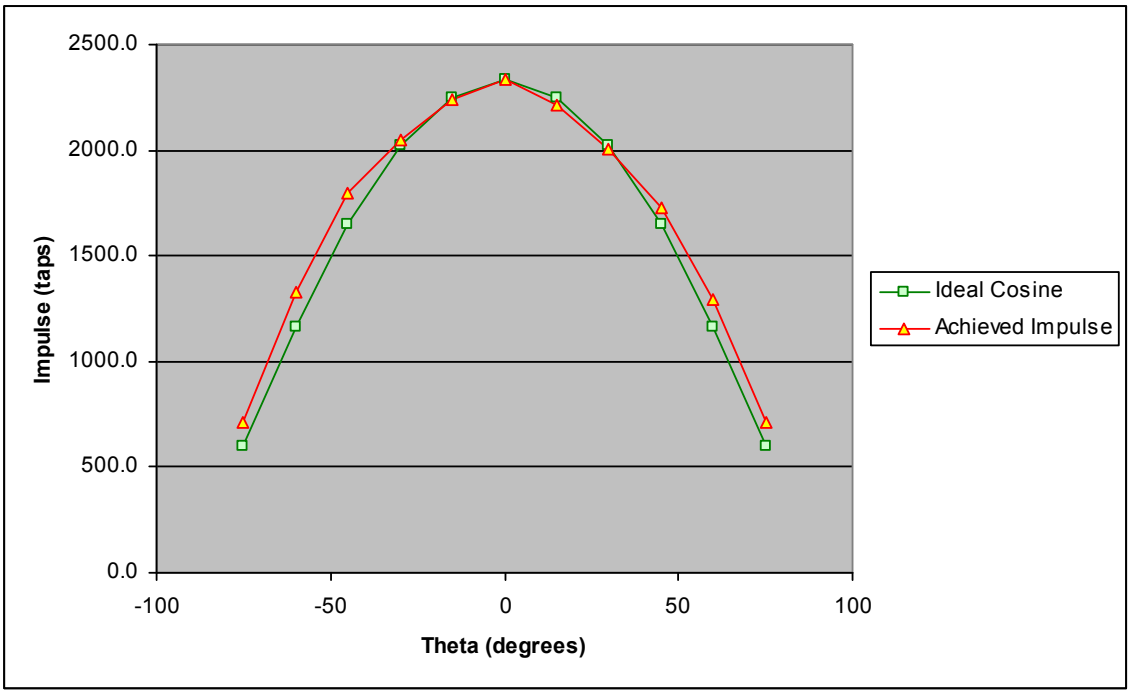

Figure 10.12: TP-2005-15 Flyer Generated Impulse Profile (Rings #3, #4, & #5)

The flash x-ray rigid body motion data (Figure 10.13) indicated an initial ring velocity of approximately 378.8 cm/s (149.1 in/s), corresponding to a cosine distributed delivered impulse of 2274 taps. Incoming flyer motion was not recorded, but the rebounding flyer shape appeared to indicate a reasonably symmetric impact and rebound. Inspection of the flyer hardware, shown in Figure 10.14, indicated a good initiation pattern with no abnormalities. Dents on the flyer edges are the result of secondary impacts with the light array after rebound from the target. The ring structure itself was undamaged by the flyer impact.

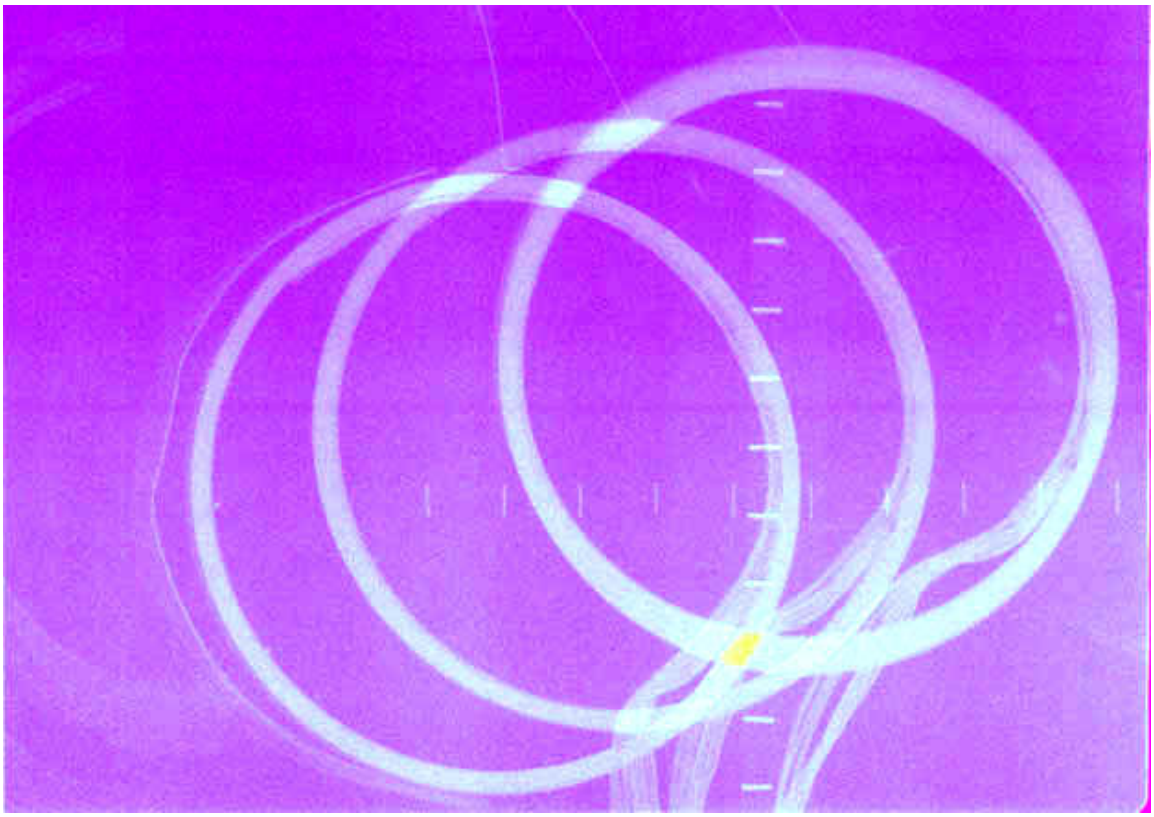

Figure 10.13: Ring #5 X-Ray Data

Structural strain response of the ring was measured with strain gages located on the inner surface of the ring. Each gage measured a strain that closely corresponds to the H-W solution calculated for a loading of 2330 taps. Figure 10.15 and Figure 10.16 show

this excellent correlation for early and late time strain response at the 180º location. Figure 10.17 shows the early-time, and Figure 10.18 the late-time, responses for the 90º and 270º strain gages compared to the H-W solution, again at the 2330 tap load. Due to the symmetry of the experiment, the 90º and 270º gages record nearly the same strain.

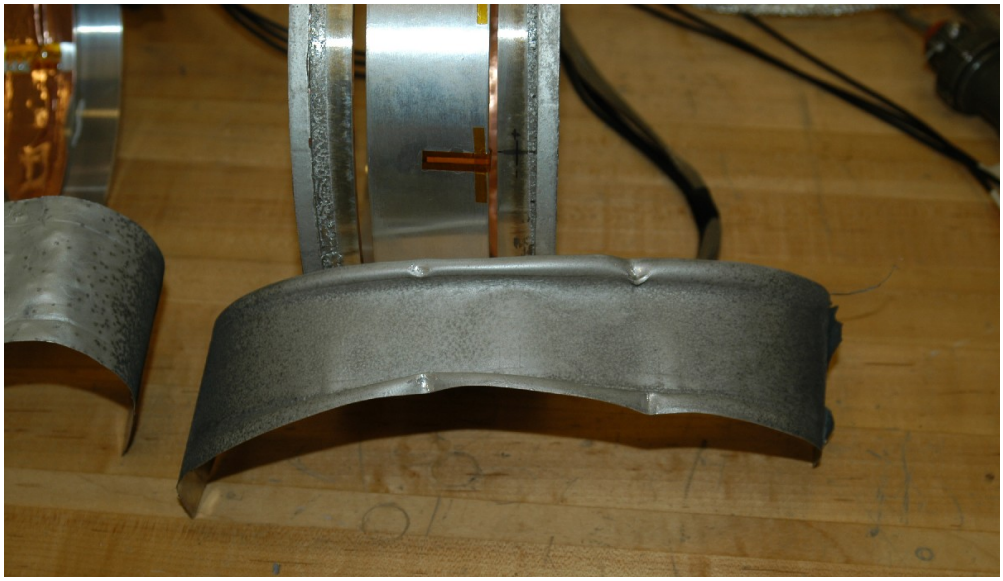

Figure 10.14: Post-Test Flyer and Target Ring #5

Analysis of the ring #5 pressure gage data showed a measured impact pressure of 7.60 kbar at the -30º location, 8.58 kbar at the 0º location, and 7.13 kbar at the +30º location. The pressure pulse shape, shown in Figure 10.19, was haversine in nature with a rounded peak due to the trapped air between flyer and target, consistent with previous work [8]. The impact simultaneity for the three impact points was 2.1 μs with the +30º gage being impacted first, then the 0º gage 1.15 μs later, and finally the +30º gage 0.95 μs after the 0º gage. The magnitudes of these measured impact pressures were inconsistent with those predicted for an aluminum flyer impact with an aluminum target at a velocity of 17,467 cm/s (6,876 in/s). Hugoniot calculations (no trapped air) predicted an impact pressure of 13.07 kbar and KOWIN hydrocode analysis predicted 12.8 kbar.

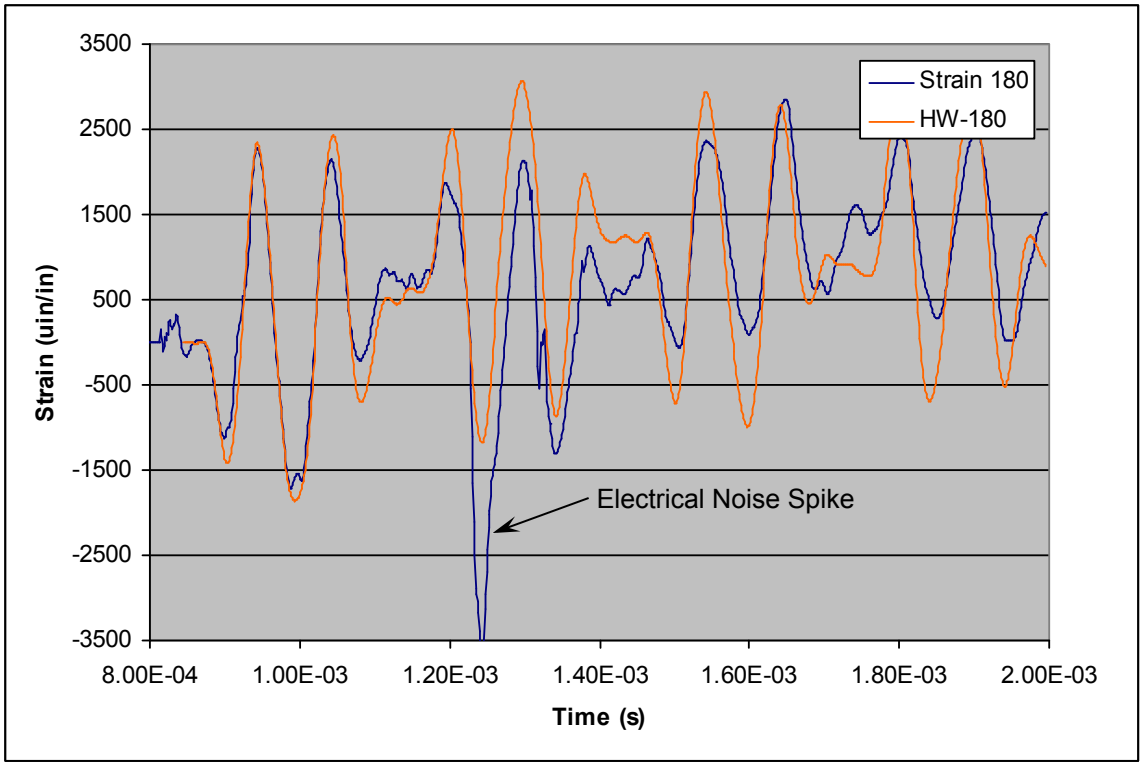

Figure 10.15: Ring #5 Early Time Strain Response at 180º (2.0 ms)

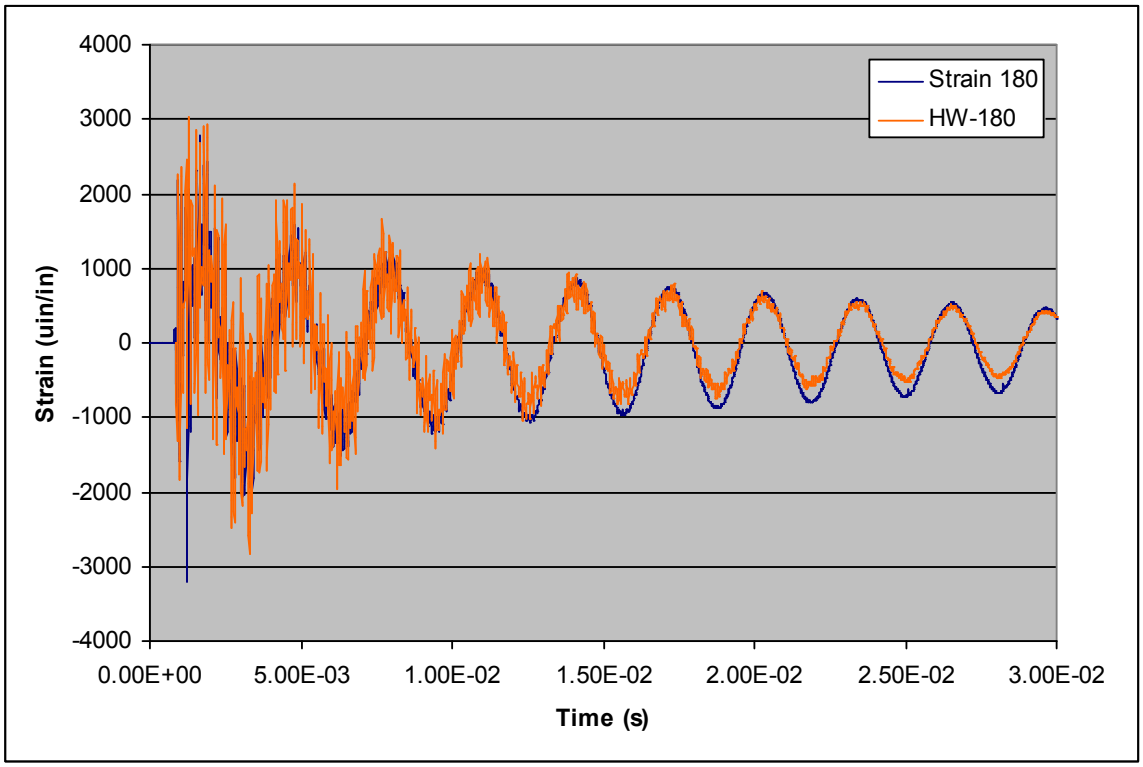

Figure 10.16: Ring #5 Late Time Strain Response at 180º (30 ms)

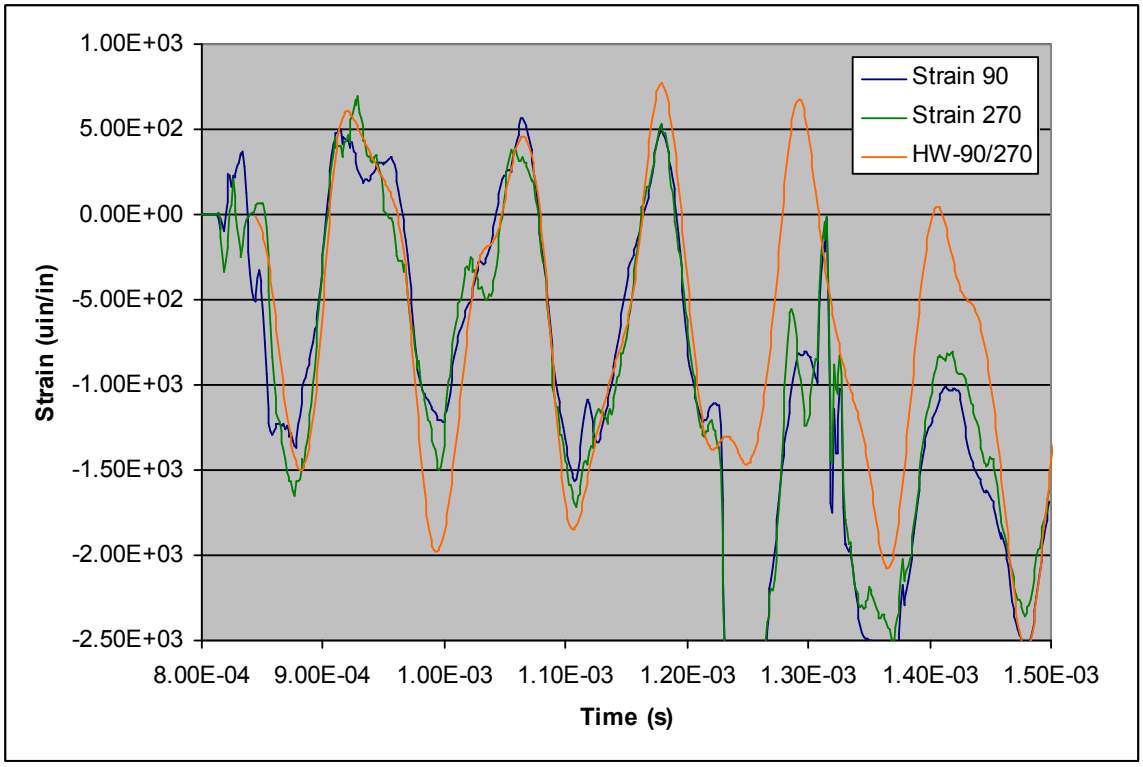

Figure 10.17: Ring #5 Early Strain Response at 90º/270º Locations (1.5 ms)

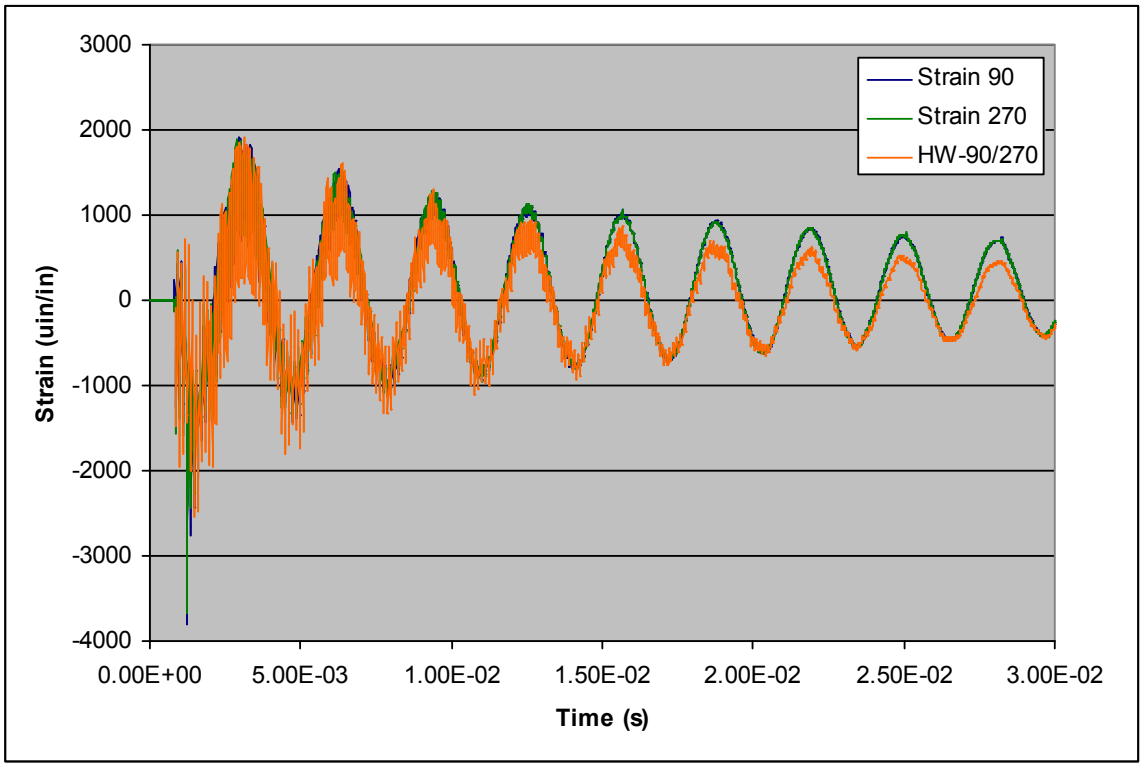

Figure 10.18: Ring #5 Late Strain Response at 90º/270º Locations (30 ms)

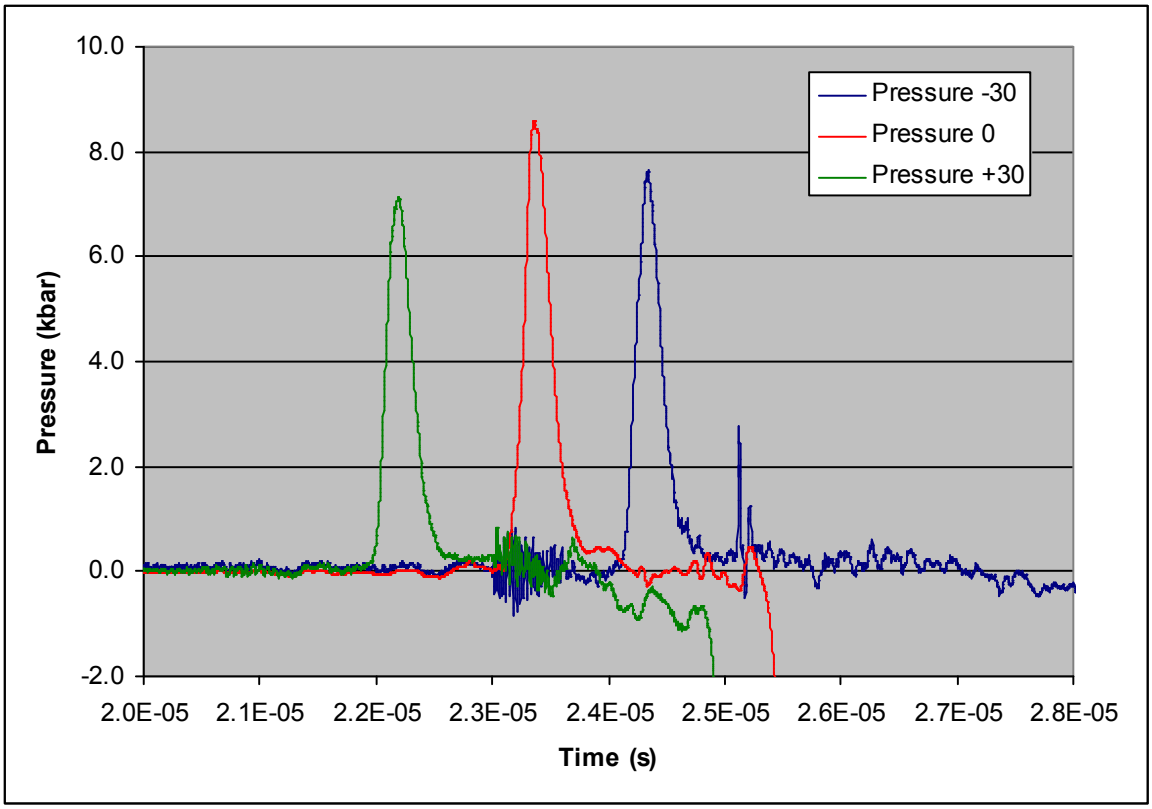

Figure 10.19: Impact Pressure from Flyer Impact on Aluminum Ring

Once again, in this application, the presence of the thin film carbon gage unavoidably affected the pressure value that it was trying to measure. The carbon gage consists of a graphite/epoxy layer sandwiched by two thin layers of Kapton®, and has a significantly lower shock impedance than either the aluminum flyer plate or aluminum target. The approximate thickness of the gage package applied to the ring, including the glue layer, was 0.0165 cm (0.0065”). The result was that the gage read a pressure that was lower than the actual pressure observed between the flyer and the ring.

Hydrocode analysis of the flyer/gage/target geometry has been useful in understanding the effect of the gage package at the impact surface. By including the gage material and thickness in a one-dimensional model of the flyer impact, it was observed that a flyer velocity of 17,300 cm/s (6811 in/s) was required to achieve a pressure of 8.58

kbar within the virtual gage material. The model was then run again, without the gage material in place with the same initial flyer velocity. The result was a calculated impact pressure of 12.8 kbar. This result is much more consistent with the predicted pressure of an aluminum flyer impacting an aluminum target at the given impact velocity.

The data throughout this experiment was fully consistent with the flyer theory developed in Chapter 4. The pressure measured by the carbon gages indicated a flyer velocity within 1.0% of that predicted for the achieved areal density. In addition, the impulse delivered was consistent with the inferred flyer velocity as well as being reasonably cosine distributed as suggested by the excellent correlation with the H-W analytical solution. Table 10.4 lists the summary results from the ring #5 experiment.

Table 10.4: Ring #5 Data Results Summary

	Diagnostic	Value	Indicated load
Design Load	Design Code	31.12 mg/cm^2	2279 taps
Explosive Deposition	Coupon Weight	31.3 mg/cm^2	2331 taps
Explosive Performance	Coupon Firing	100%	2331 taps
Initial Velocity	X-Ray Analysis	378.8 cm/s	2274 taps
Impact Pressure	Carbon Gage	8.58 kbar	2390 taps
Analytical Comparison	H-W solution		2330 taps
		Final Reported Load	**2331 taps**

10.2. Composite Ring Testing

Ring test #2 utilized a composite target ring structure to perform a crossover experiment in an attempt to observe both structural response as well as material response. Unfortunately, a closed form analytical solution to the layered ring problem was not found during the literature search phase of the project. As a result, the purpose of the composite ring experiment changed to qualitatively report the material damage to the ring, if any, as well as record the structural response for future analysis.

The ring #2 experiment was sprayed in conjunction with test TP-2005-14. The achieved deposition predicted a nearly cosine distributed impulse load with a maximum at the 0º location of 2298 taps. As discussed earlier, the explosive performance was diminished by 7.8%, resulting in a predicted load of 2169 taps. Figure 10.2, in section 10.1.1, compares the ideal cosine load with that predicted by the achieved spray deposition and explosive performance.

By all indications, Ring Test #2 was conducted successfully. A measured total impulse load of 2012 taps was achieved, which is an additional 7% lower than predicted. The x-ray, high speed video, and strain data were all recorded successfully. There were no carbon gages placed on the target ring for impact pressure measurement.

Post-test visual analysis of the target ring indicated a separation of the composite ring layers between the -50º and +50º stations. The load between these locations was a minimum of 1500 taps. This separation manifested itself in the form of a slight change of color under the polycarbonate layer. No physical damage was evident in any individual layer of the ring structure. Figure 10.20 presents the pre- and post-test photographs of the composite ring structure.

Analysis of the x-ray data indicated that the flyer impact was reasonably symmetric and simultaneous. The measured rigid body initial velocity was 401.0 cm/s (157.9 in/s), corresponding to a delivered total impulse of 2012 taps. Figure 10.21 shows the x-ray data for the composite ring test.

(a) Pre-Test Target Ring Assembly

(b) Post-Test Ring #2 (Flyer Not Pictured)

Figure 10.20: Composite Ring Pre and Post-Test

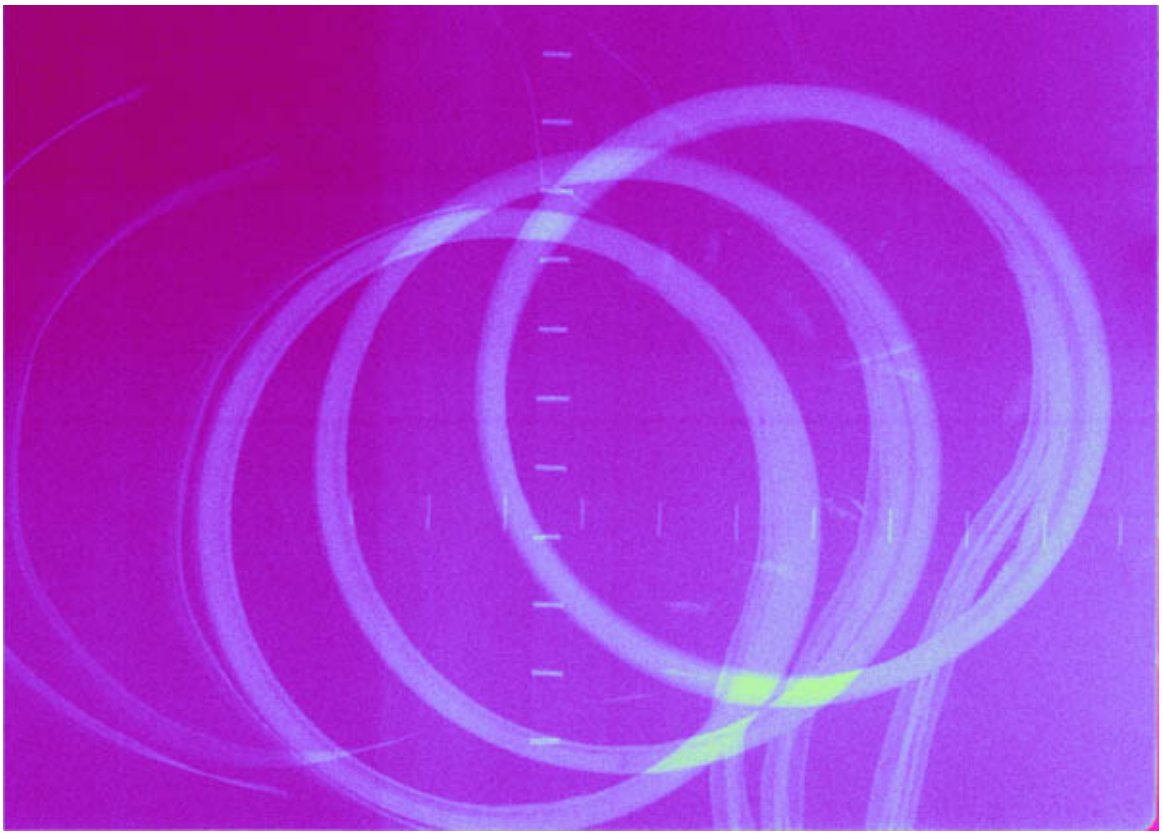

Figure 10.21: Composite Ring (#2) X-Ray Data

Analysis of the measured strain was limited to qualitative observation. The early-time strain from any of the three gages was inconsistent, as expected, with the H-W

solution used for the aluminum target rings. The membrane response of the composite structure seemed to attenuate within the first 1.6 ms, leaving only bending response. The strain measurement showed that the aluminum substrate did not yield, at least at the locations being monitored. Figure 10.22 shows the first 2.5 ms of the strain response at the 180º location. The 90º and 270º strain gage responses (not presented) show similar characteristics.

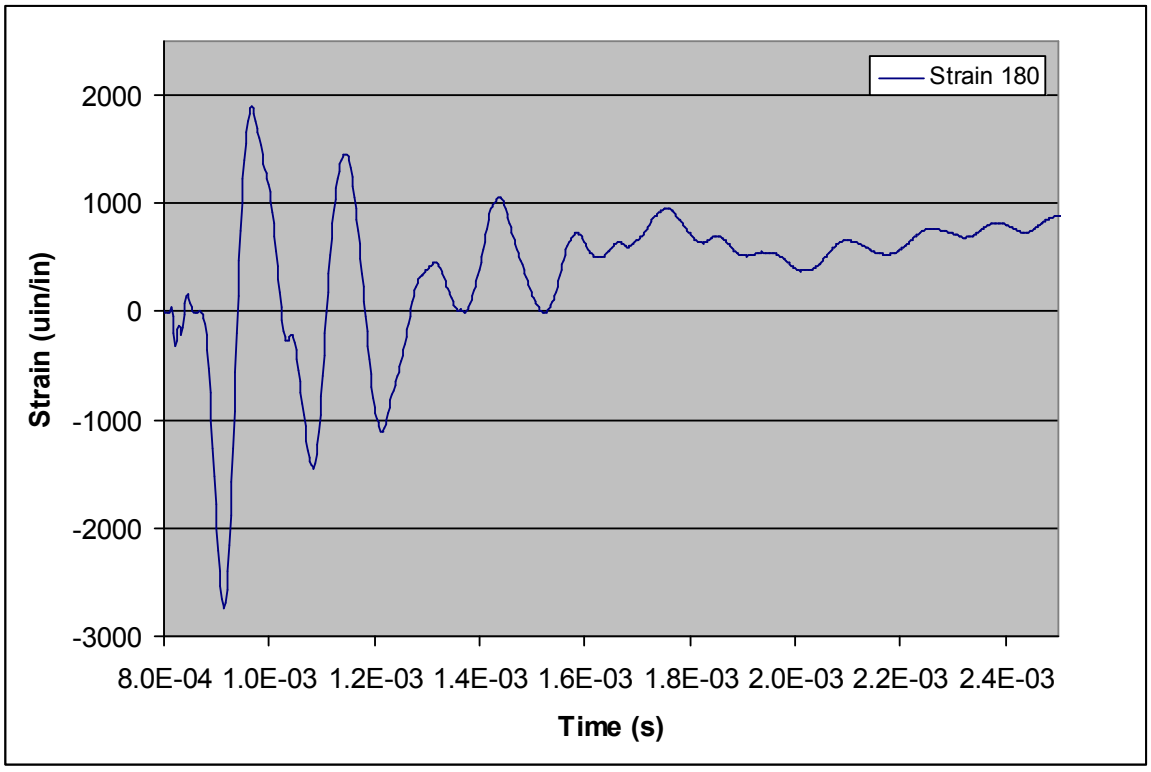

Figure 10.22: Composite Ring 180º Strain Response (1.5 ms)

The late time response of the ring was dominated by low-frequency bending stresses, as compared to the simple aluminum ring response. Of considerable interest was the first 5 ms of the recorded response. It appears that the composite ring structure underwent some sort of structural property change between 1.5 ms and 2.0 ms, where the bending response seemed to take over. This may be a result of the onset of the

delamination between the polycarbonate and silicone rubber layers. Also of note is the symmetry of response measured by the 90º and 270º degree strain gages. Both locations showed nearly identical strain response, likely indicating that any structural changes due to the flyer impact were symmetric with respect to the 0º location.

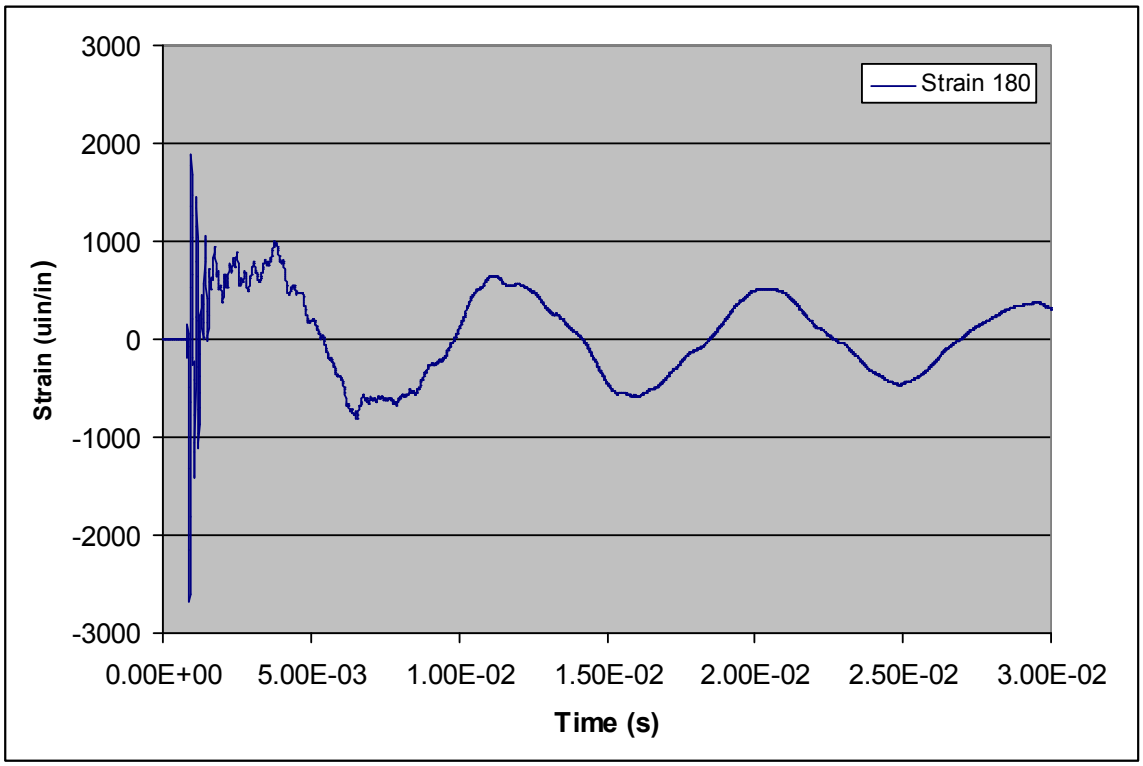

Figure 10.23: Composite Ring 180º Strain Response (30 ms)

The 7% difference between the measured impulse by the x-ray analysis and the predicted loading is not accounted for. With the measurement tolerance of the x-ray diagnostic, the predicted loading may have been achieved, but cannot be proven with the information recorded. Table 10.5 lists the results from the composite ring test.

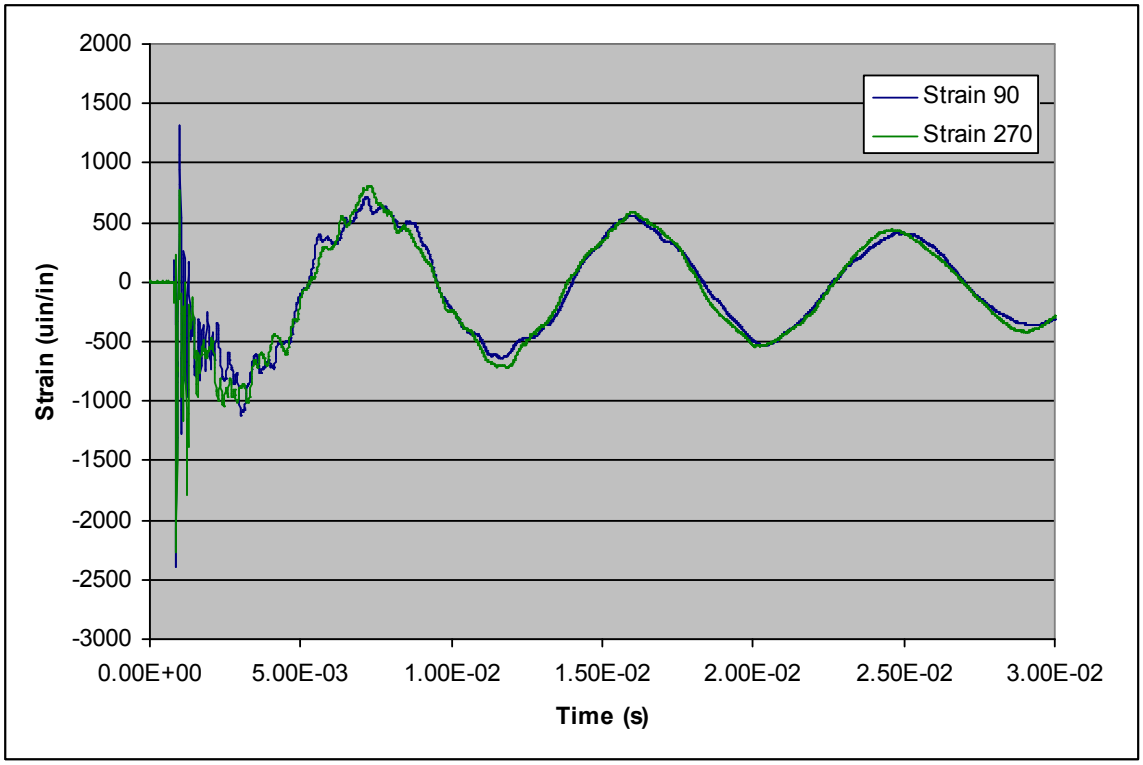

Figure 10.24: Composite Ring 90º/270º Strain Response (30 ms)

Table 10.5: Composite Ring (#2) Data Results Summary

	Diagnostic	Value	Indicated load
Design Load	Design Code	31.12 mg/cm^2	2279 taps
Explosive Deposition	Coupon Weight	30.91 mg/cm^2	2267 taps
Explosive Performance	Coupon Firing	92.2%	2169 taps
Initial Velocity	X-Ray Analysis	401.0 cm/s	2012 taps
Impact Pressure	Carbon Gage		N/A
Analytical Comparison	H-W solution		N/A
		Final Reported Load	**2012 taps**

10.3. Two-Dimensional Discussion of Results

The results of the two-dimensional tests have been extremely promising. Even though all five sprayed ring experiments were not successful, and the composite ring test turned out to provide more qualitative information than quantitative, the ring experiment series has provided excellent validation to the flyer theory. Each of the test failures and

shortcomings were the result of issues external to the flyer development, and while disappointing, take nothing from the theory. Each of these tests have been integral to the understanding of the LIHE driven flyer technique and will prove to be useful in future work.

As seen in Figure 10.2 and Figure 10.12, the achieved explosive deposition resulted in a flyer delivered impulse that varied from the desired precise cosine distribution. While the deviation was small, the measured total impulse and inferred cosine distribution indicated a nearly perfect cosine loading. Sebrill and Lobitz [80] discuss that precise cosine loading is not required to excite the structural response, as long as the impulse is delivered in a near-cosine distribution. This theory can certainly be applied here. As has been shown, when loaded with an impulse which nearly approximates a cosine, the differences in load distribution were not significant enough to affect the structural response of the ring structures.

The results from ring tests #3 and #4 have been instrumental in understanding the importance of properly coupling energy from the light array to the SASN explosive for a successful nearly simultaneous detonation. The light array has been designed to "over-drive" the explosive initiation, so that small differences in current and voltage do not affect the test. But in the no-test failures, the array was unable to transfer enough energy to the explosive surface for initiation. Post-test analysis of the light array output, in the form of current measurement and physical inspection, was vital in understanding the bank output performance. The implication here is that a fully functioning light array is necessary to conduct a successful test in any configuration.

Overall, the two-dimensional test series was a resounding success. The results for ring tests #1 and #5 yielded measured loads at 100% of the predicted load for the achieved spray. While the interim tests were not as successful for the reasons discussed, the two good aluminum ring tests achieved each of the objectives. The successful two-dimensional impulsive cosine loading of a ring structure was an important step in the development and validation of the LIHE driven flyer theory. This work has shown that the developed theory can be implemented to drive a flyer to a desired impact velocity, with a spatially varying impulse load, and can be simultaneously applied to a simple two-dimensional surface. These steps have been vital in establishing to the impulse community that the LIHE driven flyer technique is fully capable of being a high-fidelity impulse test method.

11. CONCLUSIONS AND RECOMMENDATIONS

11.1. Conclusions

A significant series of steps have been completed in the development of the LIHE driven flyer technique to simulate the exo-atmospheric cold x-ray deposition environment for material and structural response. With the given problem definition, an analytical derivation for flyer velocity as a function of SASN deposition, flyer thickness, and flyer material density, has been developed. An explosive impulse calibration was completed to verify the explosive performance as a function of explosive deposition. Both one- and two-dimensional flyer delivered impulse experiments were designed and built. Thirty-five one-dimensional experiments were conducted to ascertain impulse delivery, impact pressure at the target surface, and material response of seven common materials. Finally, five two-dimensional ring experiments were conducted, where an aluminum or composite ring was subjected to a flyer delivered, cosine distributed, impulsive loading.

The results of the experimental phase of the investigation show good agreement with the developed theory. An inferred flyer velocity was calculated from the measurements of explosive deposition on the flyer and delivered impulse to the one-dimensional target structure. This calculated flyer velocity was on average 97.5% of the predicted velocity for the measured explosive deposition on the flyer. The pressure pulse shape, in each material case, closely corresponded to the predicted waveform shape, and indicated that the impact pressure was prompt, high-frequency, and of a high-amplitude, representative of a cold x-ray deposition environment. A definitive material response was generated in each of the one-dimensional target structures. Post-test analysis of the aluminum ring strain response indicated excellent agreement with the analytical strain solution, where the applied load was impulsive and cosine distributed.

This research has taken multiple steps to bridge the gap in impulse test techniques between the structural response generated by the conventional direct spray LIHE technique, and the combined response generated by a flyer impact. With the completion of this investigation, the theory and methods developed can be utilized to load one- and two-dimensional items of interest with spatially varying impulse levels. This research extends the basic explosively driven thin-flyer theory beyond the inception phase, to yield a unique above-ground simulation to a complex impulse loading scenario. This impulse test technique, once completely validated, has the capability to dominate the above-ground simulation of exo-atmospheric cold x-ray blow-off on relatively large and complex test items.

11.2. Recommendations For Further Experimentation

The one- and two-dimensional experiments were significant in the validation process of the developed theory of the LIHE driven thin flyer for impulse loading. But there is additional work that can be done to further reinforce the current results and lend confidence to the theory. It is believed that the small size of the one-dimensional flyer experiments introduced a fair amount of scatter into the measured impulse, and therefore the calculated flyer velocity. In addition, it was necessary to infer the flyer velocity from impulse measurement, rather than measure it directly. For these reasons, it is recommended that future research and experiments be completed to directly measure flyer velocity as a function of explosive deposition and flyer properties, as well as characterize and/or minimize the error due to edge effects.

Ideally, velocity measurement would include quantification of the flyer motion from explosive initiation, to impact, to rebound. This would be best accomplished by a direct, non-contact, optical measurement. In addition, increasing the impact area by at

least an order of magnitude, may significantly decrease the edge effects on the measurement of delivered impulse. Both of these suggestions would require redesign of the one-dimensional experiments to accommodate instrumentation fixtures and handling constraints. Edge-on x-ray analysis of the flyer motion would be instrumental to quantify the flyer condition during flight, focusing on the degree of edge deformation prior to impact, as well as flyer impact simultaneity.

A second level of investigation would be to vary the flyer and target properties. Because the flyer delivered impulse to the target is a direct function of explosive deposition, flyer material, flyer thickness, and target material, varying these parameters in conjunction with the above suggested testing, would provide additional information towards the validation of the theory. Finally, as the technique is expanded to increasingly complex test items, hydrocode modeling of the entire test process will be desirable. This step will require a better implementation of a SASN equation of state into a two- or three-dimensional shock physics hydrocode.

12. BIBLIOGRAPHY

1. Aerospace Structural Metals Handbook, AFML-TR-68-115, Vol. 3, Air Force Materials Laboratory, Belfour Stulen, Inc., 1975.

2. H. Anderson, Personal Communication, Sandia National Laboratories, 2004-2005.

3. ASTM E140, "Standard Hardness Conversion Tables for Metals", Annual Book of ASTM Standards 2000, Section Three, "Metals Test Methods and Analytical Procedures", Volume 03.01, ASTM, Conshohocken, PA, 2000.

4. W.E. Baker, F.O. Hoese, S. Silverman, "Development of Capabilities of a Light-Initiated, Sprayed Explosive", Technical Report IR Project No. 02-9008-01, Southwest Research Institute, San Antonio, TX, September 1969.

5. W.E. Baker, W.G. Martin, E.W. Spacek, "The Use of Light-Initiated, Sprayed Explosive to Accelerate Flyer Plates", Technical Report AFWL-TR-70-114, Air Force Weapons Laboratory, March 1971.

6. L.M. Barker, R.E. Hollenbach, "Laser interferometer for measuring high velocities of any reflecting surface", J. Appl. Phys., Vol 43, No. 11, November 1972.

7. F.A. Baum, K. Stanyukoich, B.I. Shekhter, *Physics of an Explosion*, English translation, Federal Clearinghouse AD400151, pp505-507, 1959.

8. B.C. Bedeaux, J.F Gilbride, et al., "Carbon Stress Gauge Results from Impulse Test Conducted for the Joint Test Program", SAND2005-3900, Sandia National Laboratories, November 2005.

9. R.A. Benham, F.H. Mathews, "X-Ray Simulation with Light-Initiated Explosive," The Shock and Vibration Bulletin, Bulletin 45, June 1975, pp 87-91.

10. R.A. Benham, "Light Initiated Explosive Formulation and Impulse Calibration Procedures", Memorandum of Record, Sandia National Laboratories, April 7, 1977.

11. R.A. Benham, F.H. Mathews, P.B. Higgins, "Application of Light Initiated Explosive for Simulating X-Ray Blowoff Impulse Effects on a Full Scale Reentry Vehicle", The Shock and Vibration Bulletin, Bulletin 47, September 1977, pp 9-16.

12. R.A. Benham, “Terminal Velocity and Rotation Rate of a Flyer Plate Propelled by a Tube-Confined Explosive Charge”, Shock and Vibration Bulletin 49, 1979, pp 193-201.

13. R.A. Benham, “Preliminary Experiments Using Light – Initiated High Explosive for Driving Thin Flyer Plates”, SAND79-1847, Sandia National Laboratories, Albuquerque, NM, February 1980.

14. R.A. Benham, “An Initiation and Gas Expansion Model for the Light-Initiated Explosive Silver Acetylide-Silver Nitrate”, SAND79-1829, Sandia National Laboratories, Albuquerque, NM, February 1980.

15. R.A. Benham, “Predicting the Motion of Flyer Plates Driven by Light-Initiated Explosive for Impulse Loading Experiments”, The Shock and Vibration Bulletin, Bulletin 50, September 1980, pp191-198.

16. R.A. Benham, “Combined Response Impulse Testing Using Light Initiated High Explosives”, SAND87-1297, Sandia National Laboratories, Albuquerque, NM, November 1987.

17. R.A. Benham, T.D. Goolsby, “Light Initiated High Explosively Driven Flyer Plates for Impulse Testing with Pressure Control”, SAND90-2516, Sandia National Laboratories, Albuquerque, NM, February 1991.

18. R.A. Benham, L.J. Weirick, L.M. Lee, “Calibration of Thin-Foil Manganin Gauge in ALOX Material”, SAND95-1890C, Sandia National Laboratories, Albuquerque, NM, 1995.

19. R.A. Benham, W.G. Rivera, T.M. Skaggs, T.D. Goolsby, “Explosively and Magnetically Accelerated Flyer Plates for Generating Surface Impulse Loads: A Technical Comparison”, SAND2003-0343, Sandia National Laboratories, Albuquerque, NM, March 3003.

20. R.A. Benham, personal communication, Sandia National Laboratories (Retired), 2002-2005.

21. M. Bhardwaj, K. Pierson, et al., "Salinas: A Scalable Software for High-Performance Structural and Solid Mechanics Simulations", Gordon Bell winner. Supercomputing 2002. Baltimore, MD. November 2002.

22. W. Callister, Materials *Science and Engineering An Introduction*, 6th Edition, John Wiley & Sons, New York, 2003.

23. K. Carpenter, “KOWIN v 1.3.4 User’s Manual”, Created by K. Carpenter for R. Lee of Lawrence Livermore National Laboratories, 2002.

24. P.W. Cooper, *Explosives Engineering*, 2nd Edition, Wiley-VCH: New York, 1996.

25. T. Covert, "Operating Procedures for Operation of Robotic Arms at the LIHE Facility/Bldg 6715", Sandia National Laboratories Operating Procedure, OP-905-0320, Issue A, February 2004.

26. T. Covert, "Spraying Silver Acetylide-Silver Nitrate Explosive at the Light Initiated High Explosive Facility (LIHE)", Sandia National Laboratories Operating Procedure, OP-905-0318, Issue C, August 2004.

27. B. Crossland, J.D. Williams, "Explosive Welding". Metallurgical Review, Review 144, 1970, pp. 79-100.

28. B. Crossland, "The development of explosive welding and its application in engineering" Metals and Materials, December 1971, pp.401-413.

29. B. Crossland, *Explosive Welding of Metals and its Application*. Oxford: Clarendon Press, 1982, pp. 84-208.

30. D.R. Curran, L. Seaman, D.A. Shockey, "Dynamic Failure of Solids", Physics Reports (Review Section of Physics Letters) 147, Nos. 5 & 6, 1987, pp253-388.

31. D.R. Curran, L. Seaman, R.E. Tokheim, H.E. Lindberg, "Tutorial Handbook on X-Ray Effects on Materials and Structures", SRI International Publication, September 1985, pp. 10-145 to 10-195.

32. Dynasen Incorporated, "Hands On Course (HOC17) on Stress Wave Measurements Using Thin Film Stress Gauges", Course Handouts, May 2000, pp. 4.

33. Dynasen Incorporated, "Introduction to Dynasen's Stress Gauges", Homepage, http://www.dynasen.com/html/stressgaugeintro.html, Accessed 9/18/2005.

34. K. Eckelmeyer, Personal Communication, Sandia National Laboratories (Retired), 2005-2006.

35. J. Z. Farber, G.W Seman, T. Ciolkosz, "Magnetic Flyer Combined Response Testing of Composite Specimens", Technical Report No. AFWL-TR-69-18, Air Force Weapons Laboratory, December 1969.

36. M.J. Forrestal, M.J. Sagarts, H.C. Walling, "Comment on "Dynamic Response of a Cylinder to a Side Pressure Pulse"", AIAA Journal, September 1973, p. 1355.

37. General Electric, "GE Structured Products", Homepage, LEXAN® 9034 Sheet, Product Overview, http://www.gestructuredproducts.com/sp1/gesp_amer/industry/product.jsp?gradeCLID=2291, Accessed 8/16/2005.

38. T.D. Goolsby, R.A. Benham, “Test Report for LIHE Samples Test Done on 7/12/91”, Memo to F.H. Mathews, Sandia National Laboratories, August 12, 1991.

39. T.D. Goolsby, R.A. Benham, “Comparison of Pressure Pulse & Impulse for an Aluminum Flyer into an Aluminum Target with and without Carbon Gages on the Target Surface”, Memo of Record, Sandia National Laboratories, January 10, 1991.

40. D.E. Grady, “The Spall Strength of Condensed Matter”, J. Mech. Phys. Solids, Vol. 36, No. 3, pp. 353-384, 1988.

41. R.A. Graham, *Solids Under High-Pressure Shock Compression – Mechanics, Physics, and Chemistry*, Springer-Verlag, New York, 1993.

42. R.W. Gurney, The Initial Velocities of Fragments from Bombs, Shells, and Grenades, Army Ballistic Research Laboratory, Report BRL405, 1943.

43. J.E. Hatch, ed., “Aluminum Properties and Physical Metallurgy”, ASM International, 1984, pp.110-111.

44. P.B. Higgins, “An Arc Source for Initiating Light-Sensitive Explosives,” The Shock and Vibration Bulletin, Bulletin 46, June 1976, pp 191-195.

45. J.S. Humphreys, R. Winter, “Dynamic Response of a Cylinder to a Side Pressure Pulse”, AIAA Fifth Annual Structures and Materials Conference, Palm Springs, CA, April 1964, pp 27-32.

46. T.O. Inal, C.A. Zimmerly. “Processing of materials with explosives”, 9th International Metallurgy and Materials Congress, Istanbul, Turkey, 1997. p. 751 – 764.

47. A. Jimenez, “Flash X-Ray Operations”, Sandia National Laboratories Operating Procedure, OP-905-0005, Issue G, June 2004.

48. S. Kalpakjian, S. Schmid, *Manufacturing Processes for Engineering Materials*, Fourth Edition, Prentice Hall, Pearson Education Inc, Upper Saddle River, NJ, 2003.

49. J.E. Kennedy, “The Gurney Model for Explosive Output For Driving Metal”, Chapter 7, *Explosive Effects and Applications*, J.A. Zukas, W.P. Walters, Eds., Springer-Verlag: New York, 1998, pp 221-258.

50. M.E. Kipp, R.J. Lawrence, “WONDY V – A One-Dimensional Finite-Difference Wave Propagation Code”, Sandia National Laboratories Report, SAND81-0930, June 1982.

51. W.L. Mankins, S. Lamb, “Nickel and Nickel Alloys”, ASM Handbook (formally Tenth Edition, Metals Handbook), Volume 2, Properties and Selection: Nonferrous Alloys and Special-Purpose Materials, ASM International, 1993, pp 429-445.

52. F. H. Mathews, “A Theory for the Calculation of Explosive Deposition Profiles from the Spray Painting of Light Initiated Explosive”, The Shock and Vibration Bulletin, Bulletin 51, May 1981, pp 189-204.

53. F. H. Mathews, “A Computational Model Describing the Initiation of Silver Acetylide-Silver Nitrate Explosive by and Intense Light Source”, The Shock and Vibration Bulletin, Bulletin 49, September 1979, pp 177-191.

54. F.H. Mathews, “Estimate of the Influence of Edge Relief for Impulse Calibration of SASN”, Memorandum of Record, Sandia National Laboratories, May 10, 1973.

55. F.H. Mathews, L.J. Weirick, “A Hugoniot Study on PMMA Manufactured by Polycast Technology Corporation”, SAND90-2402, Sandia National Laboratories, February 1991.

56. MatWeb.com, “The Online Materials Information Resource”, Homepage, http://www.matweb.com, Accessed 9/18/2005.

57. J.M. McGlaun, S.L. Thompson, and M.G. Elrick, "CTH: A Three-Dimensional Shock Wave Physics Code," International Journal of Impact Engineering, Vol. 10, pp 281-294.

58. T.F.V Meagher, D.C. Williams, “The Theory and Capabilities of Magnetically Driven Flyers”, DASA Technical Report Number KN-770-70-35, Defense atomic Support Agency, Washington DC, June 1970.

59. T.F.V Meagher, “Graybeard Guide for Surface Loading Simulators”, DTRA Technical Report Number POR7654, Defense Threat Reduction Agency, Ft. Belvior VA, July 2004, pp. 1-41.

60. Metals Handbook (formally Tenth Edition, Metals Handbook), Volume 1, Properties and Selection: Irons, Steels, and High Performance Alloys, ASM International, 1990.

61. M.A. Meyers, C.T. Aimone, “Dynamic Fracture (Spalling) of Metals”, Progress in Materials Science, Vol. 28, 1983, pp. 1-96.

62. Microgroup, “Tubing Materials, Services and Products, Materials Reference”, Homepage, http://www.microgroup.com/materials_reference.cfm, Accessed 12/1/2005.

63. Microsoft Excel 2002, Service Pack 3, Microsoft Corporation.

64. E. Mulligan, “Entry into the Test Cell to Attach Instrumentation Cables to a LIHE Sprayed Test Unit”, Sandia National Laboratories Safe Working Procedure, SWP-905-0318-02, January 2005.

65. E. Oberg, F.D. Jones, H.L. Horton, H.H. Ryffel, *Machinery’s Handbook*, 26th Edition, Industrial Press Inc., New York, 2000.

66. R.A. Patterson, “Fundamentals of Explosion Welding”, ASM Handbook, Vol. 6, “Welding, Brazing, and Soldering”, ASM International, Materials Park, OH, 1993, pp. 160-164.

67. K.L. Pendleton, “Robotic Application of Light-Initiated Explosive to Conical Reentry Vehicles”, SAND87-1900, Sandia National Laboratories, Albuquerque, NM, December 1987.

68. Penton, Materials Engineering, Metals Selector, December 1986.

69. Regal Piedmont Plastics, llc, Homepage, http://www.regalpiedmontplastics.com/, Accessed 2006.

70. Reynolds Kitchen, “Reynolds Wrap Foil FAQ – reyonldskitchens.com”, Homepage, http://www.reynoldskitchens.com/reynoldskitchens/kitchenconnection/products/reynolds_wrap/faq.asp, Accessed 9/21/2005.

71. W.G. Rivera, R.A. Benham, B. Duggins, T. Simmermacher “Explosive Technique for Impulse Loading of Space Structures”, 70th Shock and Vibration Symposium, Albuquerque, NM, November 1999.

72. W.G. Rivera, “Light Initiated High Explosive Driven Flyer Plate Design, Implementation, and Performance”, 75th SAVIAC Shock and Vibration Symposium, Virginia Beach, VA, October 2004.

73. W.G. Rivera, “Light Initiated High Explosive Impulse Load Calibration”, 75th SAVIAC Shock and Vibration Symposium, Virginia Beach, VA, October 2004.

74. W.G. Rivera, R.A. Benham, D. Smallwood, “Shock Machine for Inducing High Frequency Shock into MEMS Devices”, 72nd Shock and Vibration Symposium, Destin FL, November 2001, pp 120-127.

75. W.G. Rivera, “Operating Procedures for Firing Explosive Samples on the 300J Capacitor Bank at the LIHE Facility/Building 6715”, Sandia National Laboratories Operating Procedure, OP-905-0322, Issue B, June 2004.

76. W.G. Rivera, “Operating Procedures for Capacitor Bank Arming and Firing at the LIHE Facility/Building 6715”, Sandia National Laboratories Operating Procedure, OP-905-0321, Issue A, January 2004.

77. W.G. Rivera, “Use of the Small Bank to Fire Flyer Experiments for Data Collection”, Sandia National Laboratories Safe Working Procedure, SWP-905-0322-02, June 2004.

78. C. Robino, Personal communication, Sandia National Laboratories, November, 2005.

79. M.J. Sagartz, M.J. Forrestal, “Membrane Response of a Two-Layered Circular Shell Including The Effects of an Interlayer Bond”, SC-R-68-1807, Sandia National Laboratories, September 1968.

80. S.C. Schmidt, W.C. Tao, *Shock Compression of Condensed Matter – 1995*, Proceedings of the Conference of the American Physical Society Topical Group on Shock Compression of Condenses Matter, Seattle, WA, American Institute of Physics, 1996.

81. W.A. Sebrell, D. Lobitz, “Membrane Response in Rings and Simulation Testing”, SC-TM-71 0069, Sandia National Laboratories, May 1971.

82. D.L. Shirey, “Metal Hardening Test (100 Kilobar)”, Memo to D.J. Mottern, Sandia National Laboratories, January, 1972.

83. R.S. Thurston, W.L. Mudd, “Spallation Criteria for Numerical Computations”, LA-4013, Los Alamos Scientific Laboratory, September 1968.

84. D. Wackerbarth, "Software Documentation for the Light Initiated High Explosive (LIHE) Spray Program for Conical/Cylinder Structures", Sandia National Laboratories Report, SAND2002-1537, May 2002

85. D. Wackerbarth, “PlotData Graph Plot Software User Manual: Version 2”, SAND2003-3747P, Sandia National Laboratories, October 2003.

86. H.C. Walling, “Impulse Loading of Single-Layered Rings with Magnetically-Driven Flyer Plates”, SC-TM-69-538, Sandia National Laboratories, May 1970.

87. A.B. Wenzel, W.E. Baker, “The use of Light-Initiated Explosives for the Impulsive Loading of Structures”, 16th Proceedings, IES, April 1970, pp 142-149.

13. APPENDIX A – EXPERIMENTAL HARDWARE

The following pages provide detail drawings of the test hardware.

- One-dimensional target
- One-dimensional flyer offset spacer
- One-dimensional flyer plate
- One-dimensional target plate holder
- Two-dimensional simple ring
- Two-dimensional composite ring (inner layer)
- Two-dimensional composite ring (outer layer)
- Two-dimensional composite ring (assembly)

One Dimensional Target

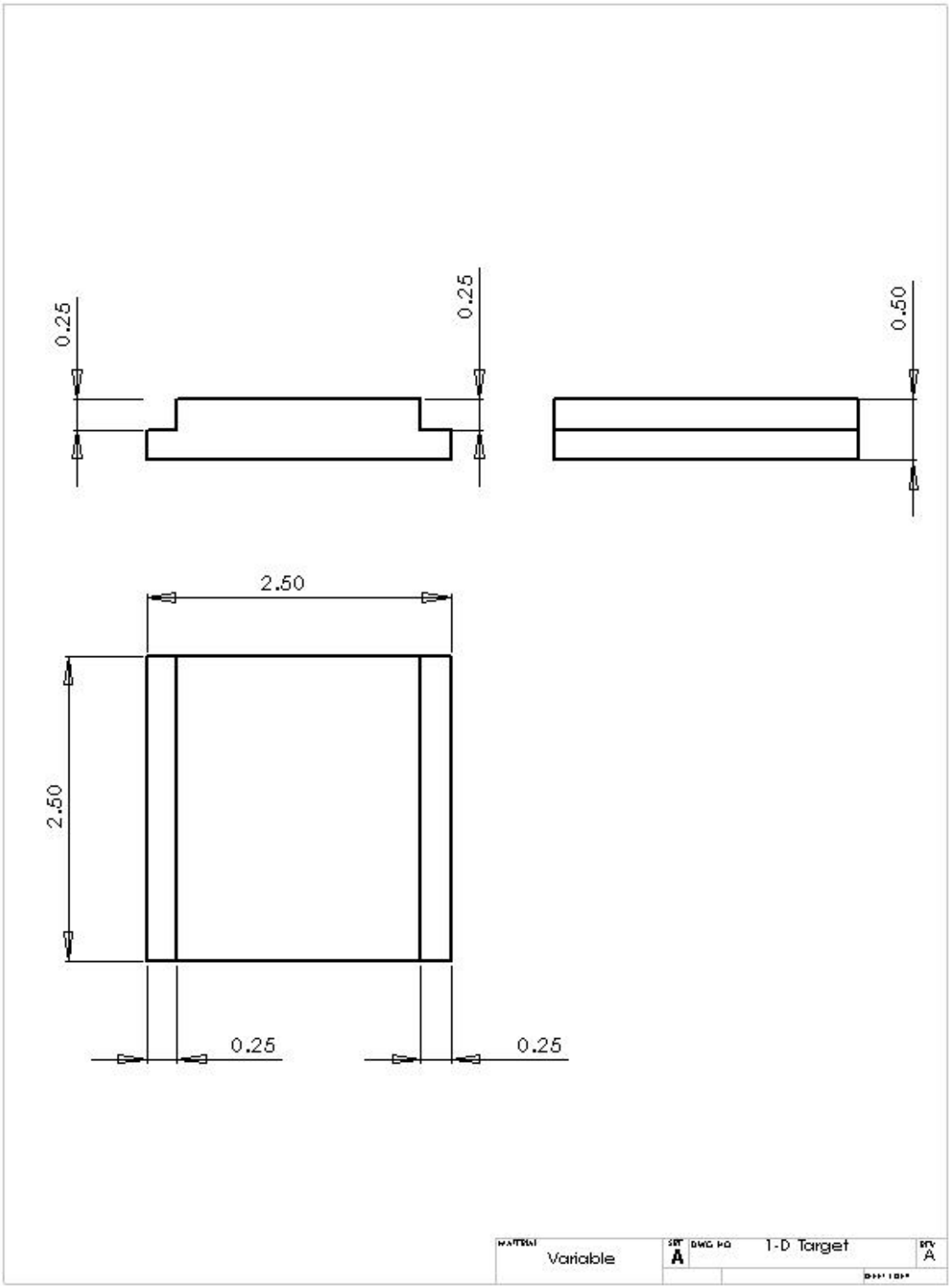

One-Dimensional Flyer Offset Spacer

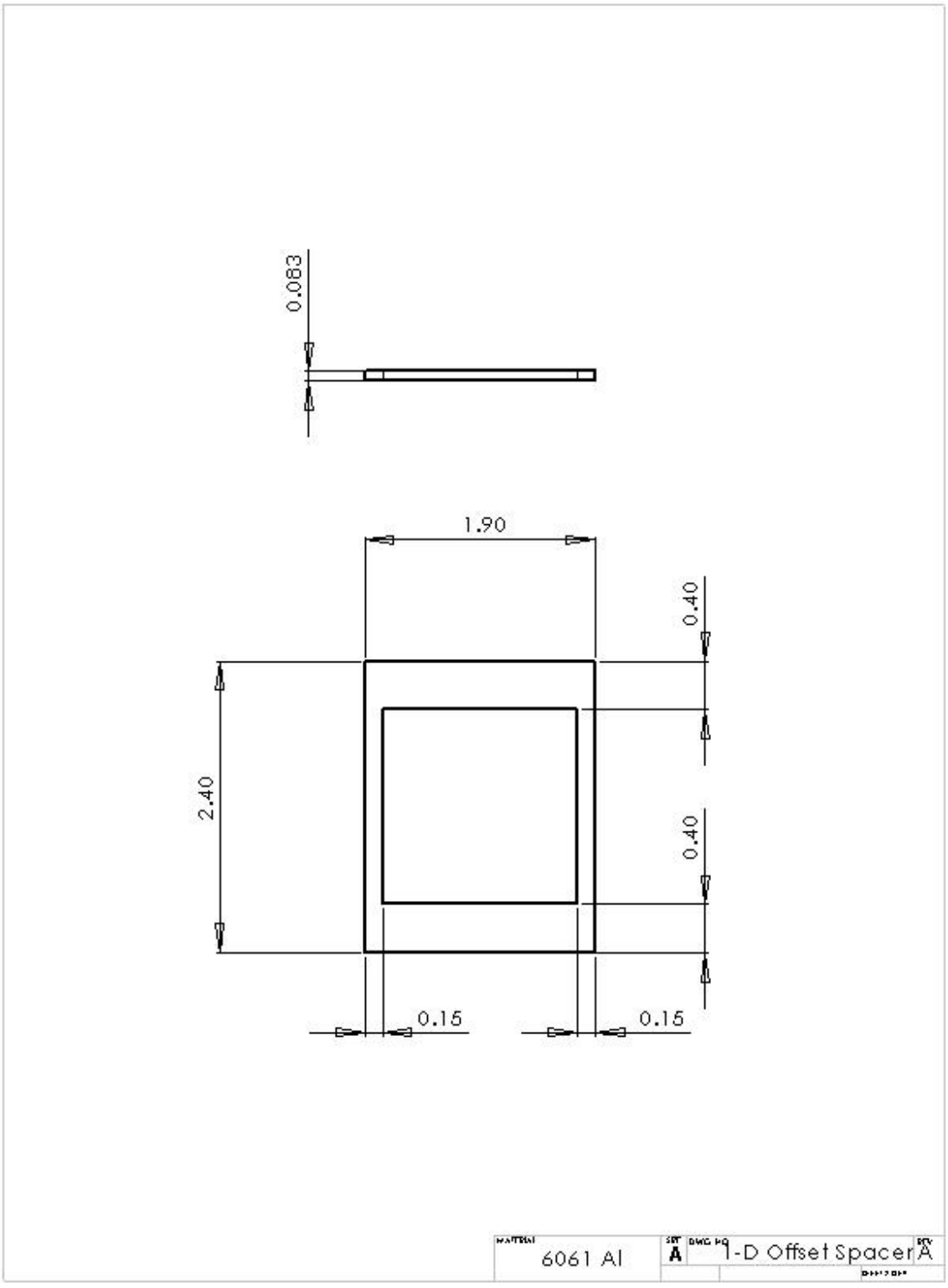

One-Dimensional Flyer Plate

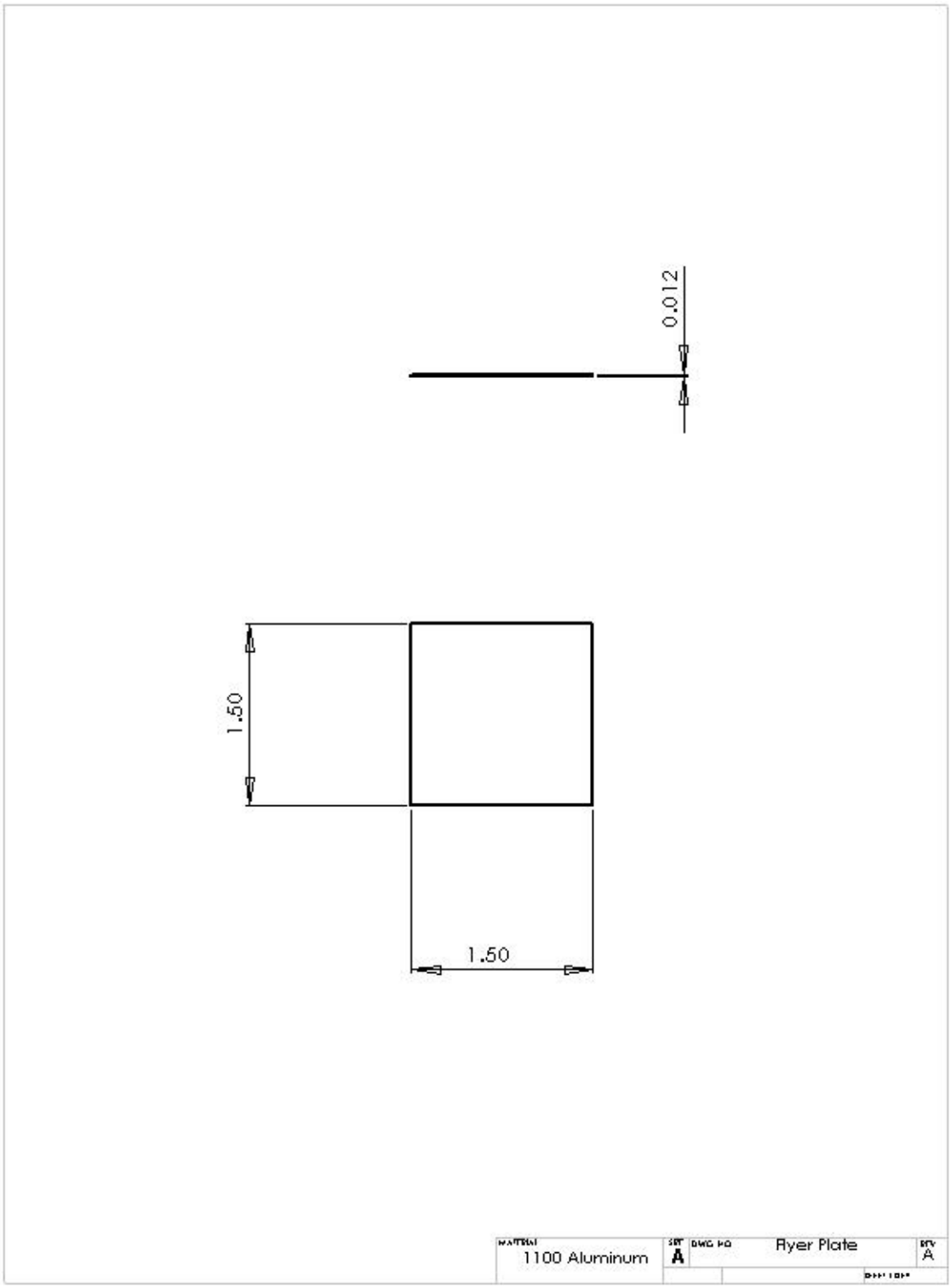

One-Dimensional Target Plate Holder

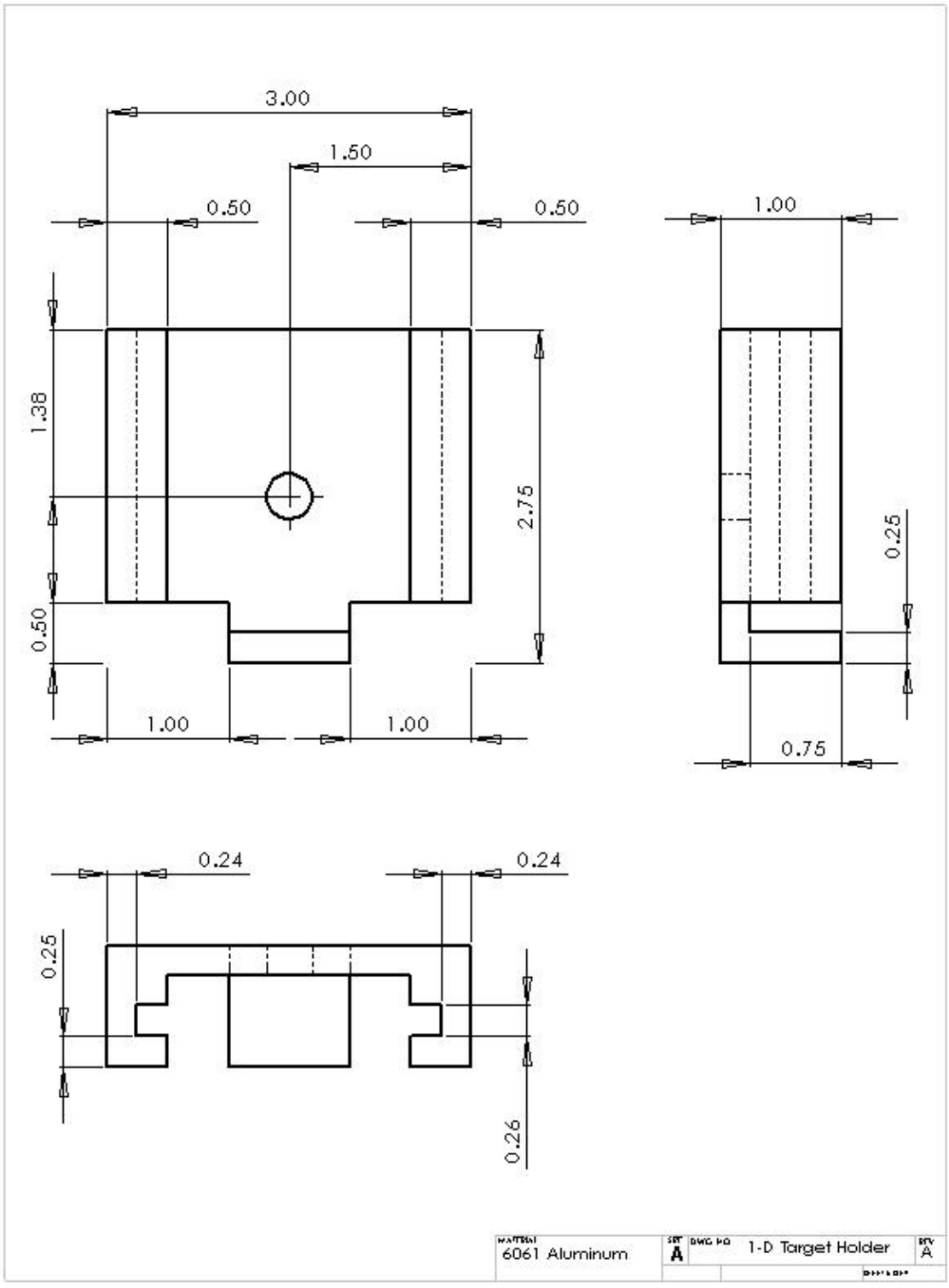

Two-Dimensional Simple Test Ring

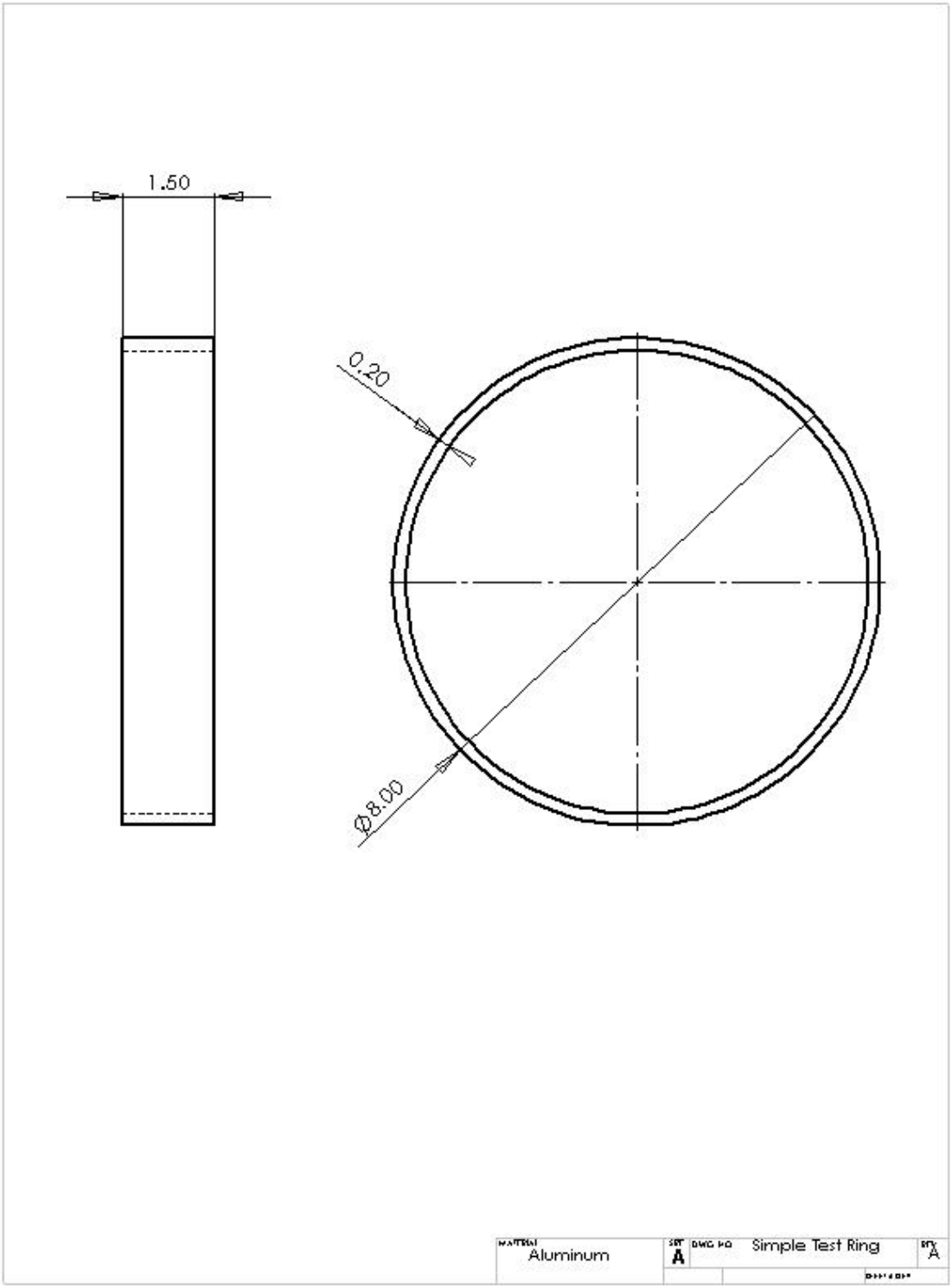

Two-Dimensional Composite Ring (Inner Aluminum Layer)

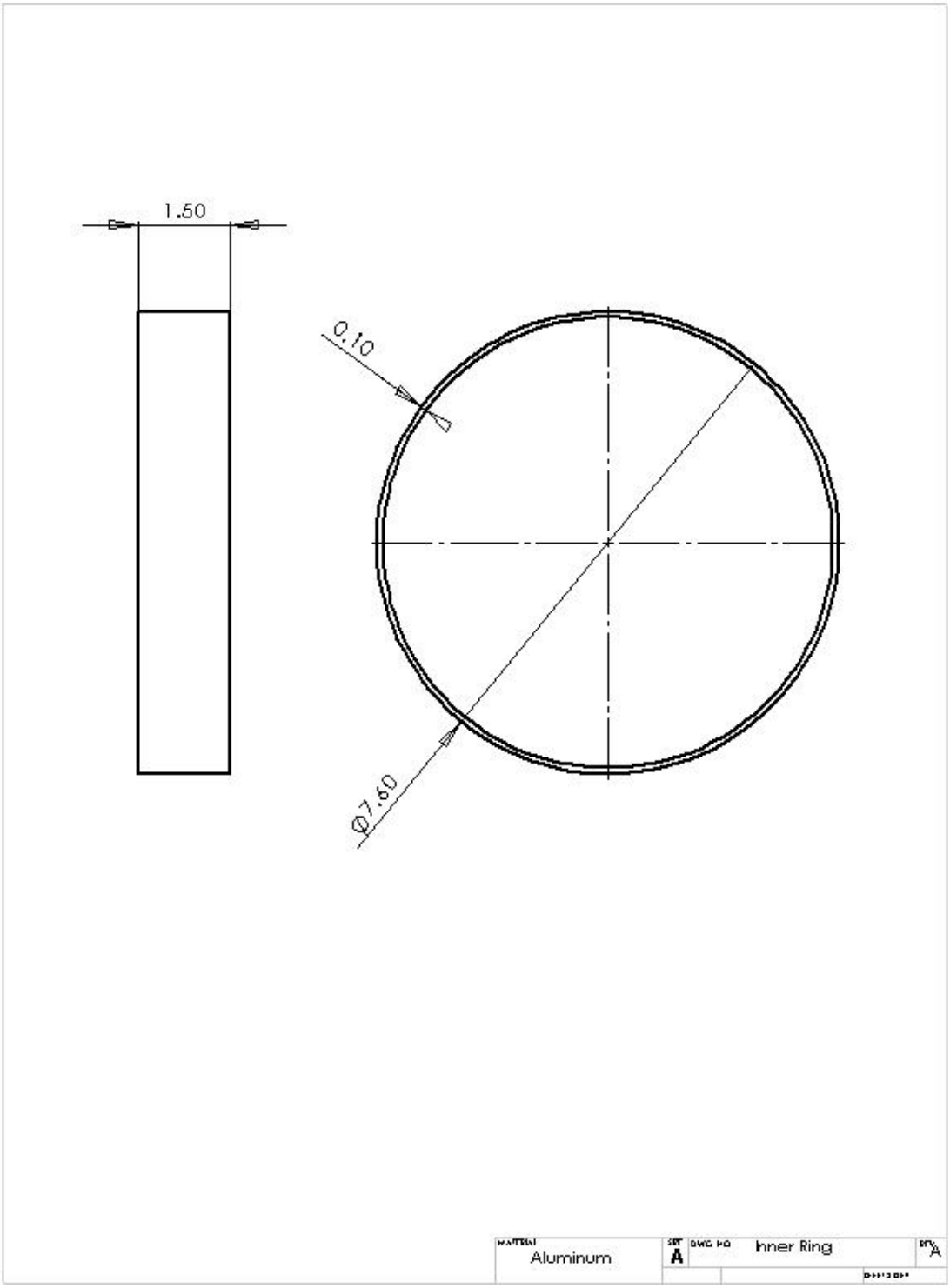

Two-Dimensional Composite Ring (Polycarbonate Outer Layer)

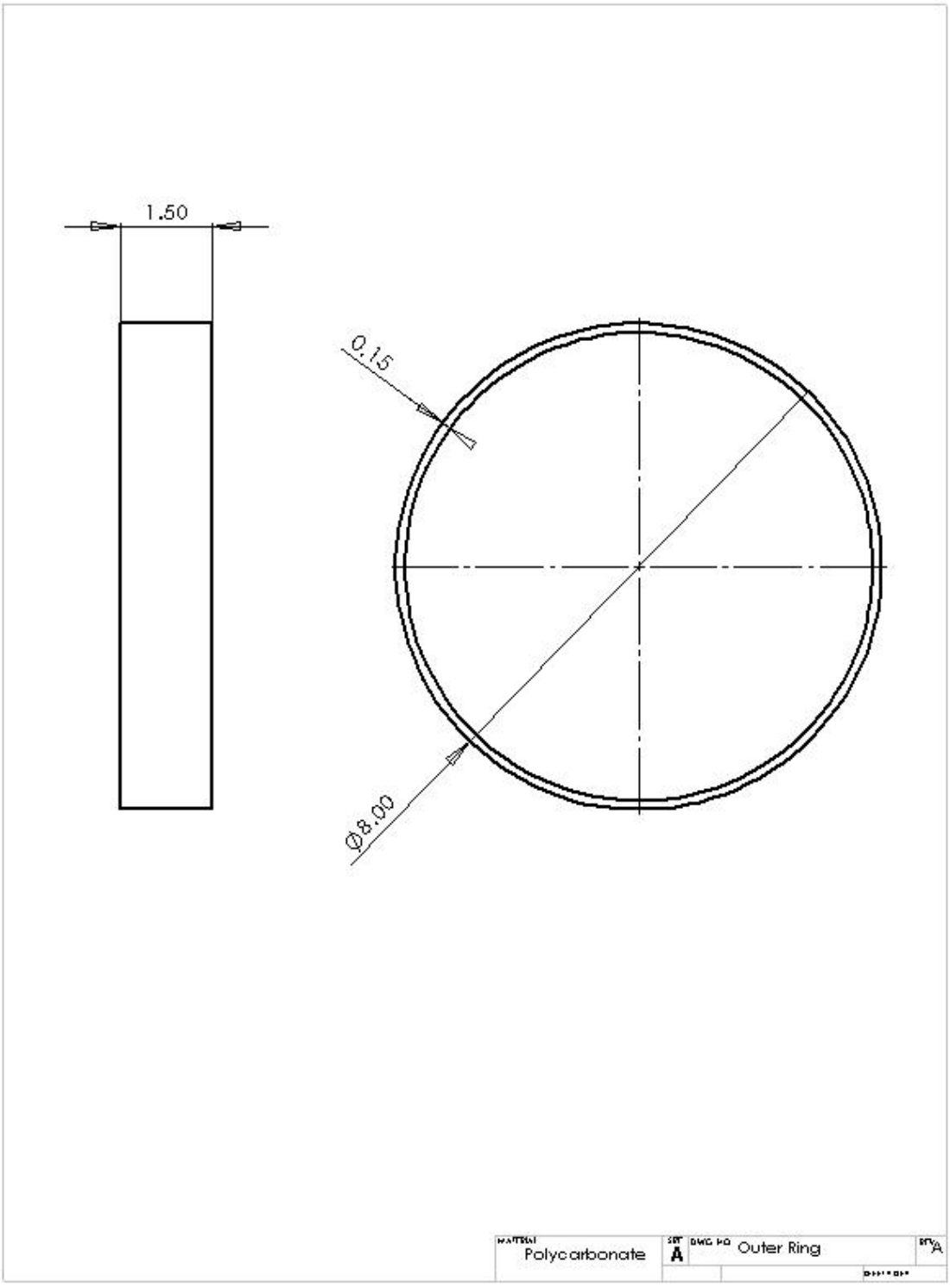

Two-Dimensional Composite Ring (Assembly)

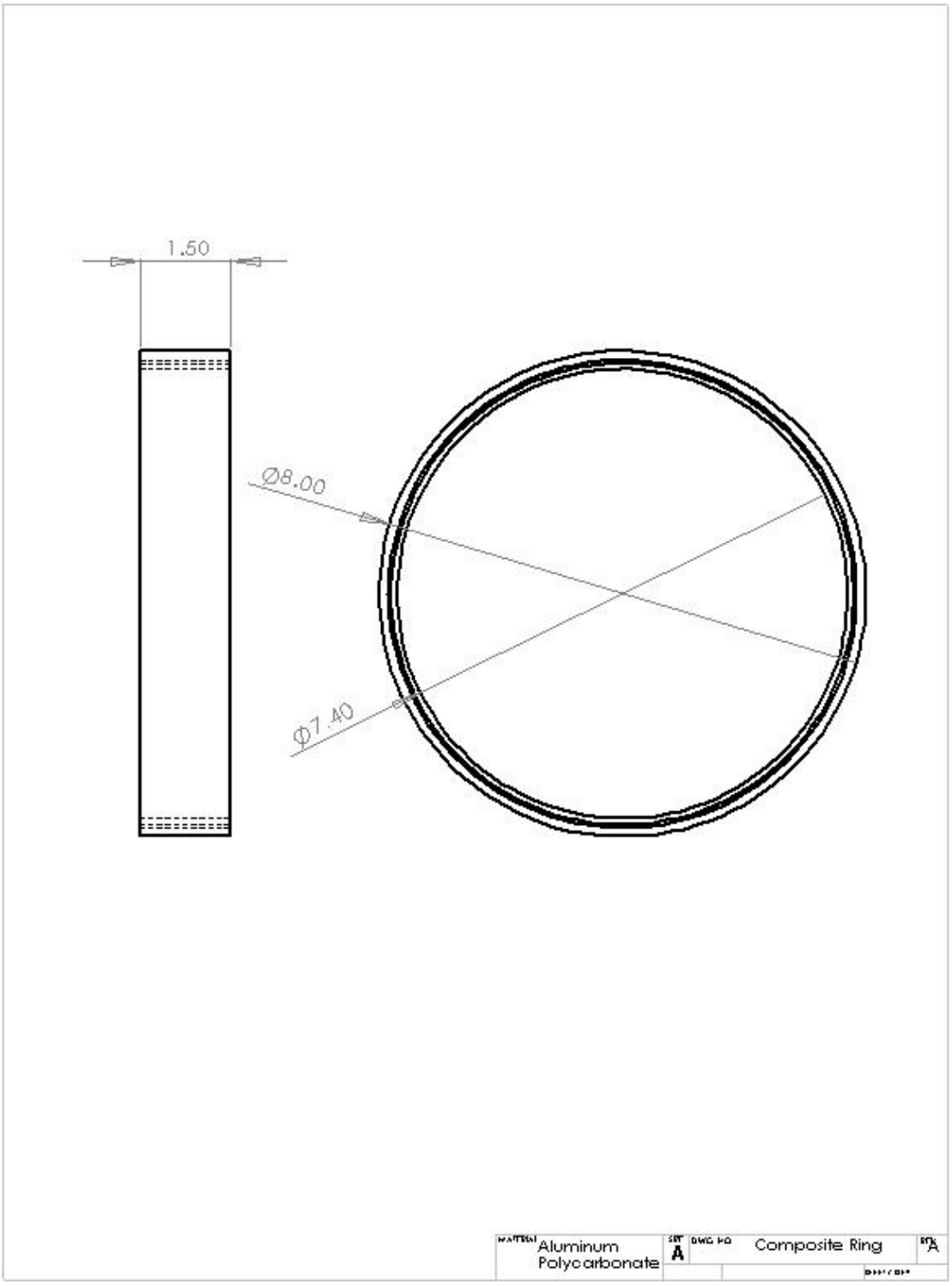

14. APPENDIX B – ONE-DIMENSIONAL FLYER EXPERIMENTS

Spray ID	Test ID	Sample ID	Target Material	Primary Experiment Purpose
TP-2004-06	1	A	6061 Al	Direct Spray Detonation Pressure
	2	B	LEXAN®	Direct Spray Detonation Pressure
	3	C	PMMA	Direct Spray Detonation Pressure
	4	D	6061 Al	Impulse Delivery/Handling
	5	E	LEXAN®	Material Response/Impulse Delivery
	6	F	PMMA	Material Response/Impulse Delivery
TP-2004-07	7	A	6061 Al	Impact Pressure
	8	B	LEXAN®	Impact Pressure
	9	C	PMMA	Impact Pressure
	10	D	6061 Al	Impulse Delivery/Handling
	11	E	LEXAN®	Material Response/Impulse Delivery
	12	F	PMMA	Material Response/Impulse Delivery
TP-2004-08	13	A	6061 Al	Impact Pressure
	14	B	LEXAN®	Impact Pressure
	15	C	PMMA	Impact Pressure
	16	D	LEXAN®	Material Response/Impulse Delivery
TP-2004-09	17	A	304 SS	Impact Pressure
	18	B	316 SS	Impact Pressure
	19	C	Ni 200	Impact Pressure
	20	D	304 SS	Material Response/Impulse Delivery
	21	E	316 SS	Material Response/Impulse Delivery
	22	F	Ni 200	Material Response/Impulse Delivery
TP-2004-10	23	A	304 SS	Material Response (Dissected)
	24	B	316 SS	Material Response (Dissected)
	25	C	Ni 200	Material Response (Dissected)
	26	D	304 SS	Material Response (Dissected)
	27	E	316 SS	Material Response (Dissected)
	28	F	Ni 200	Material Response (Dissected)
TP-2004-12	29	A	C110 Cu	Material Response (Dissected)
	30	B	C110 Cu	Impact Pressure
	31	C	C110 Cu	Material Response (Dissected)
	32	D	1100 Al	Material Response (Dissected)
	33	E	1100 Al	Impact Pressure
	34	F	1100 Al	Material Response (Dissected)
	35	G	PMMA	Impact Pressure
	36	H	6061 Al	Impact Simultaneity

Test ID: TP-2004-06 Target Material: Aluminum 6061-T651 Date: 6/23/2004
Sample ID: A Flyer Material: N/A (Direct Spray)

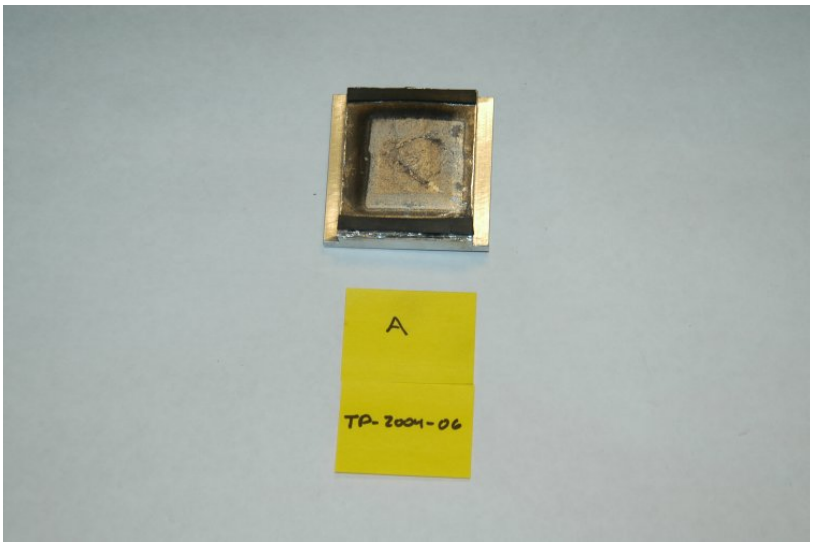

Test TP-2004-06 Sample A (Direct Spray Test)

Test Purpose

To evaluate the peak pressure developed on an aluminum surface directly from the SASN explosive detonation.

Performance Data

Areal Density	46.47	mg/cm^2	Predicted Vo:	N/A	cm/sec
			Predicted Impulse:	3247	taps
$V_{incident}$	N/A	m/sec			
$V_{rebound}$	N/A	m/sec	Measured Impulse:	2756	taps
Rebound Factor	N/A		Calculated Vo:	N/A	cm/sec
			% Measured of Predicted:	84.9%	

Ballistic Pendulum Parameters

Pendulum Mass	5085 (11.2)	gm (lbm.)	Impact Area	14.06 (2.25)	cm^2 (in^2)
String length	9.875	in.			

Notes

The areal density may be high due to overspray which does not take part in the impulse delivered

Sample ID: TP-2004-06 A Date: 6/23/2004

Pressure Data

Hugoniot Pressure:	N/A	kbar	Carbon Gage Constants		
Hydrocode Pressure:	N/A	kbar	Gage Resistance:	51.025	Ω
			Excitation Voltage:	45.0	volts
Carbon Gage			Line Resistance:	0.271	Ω
Peak Pressure:	6.83	kbar	Term Resistance:	74.76	Ω
Pulse Duration:		μs			
Impulse:		taps			

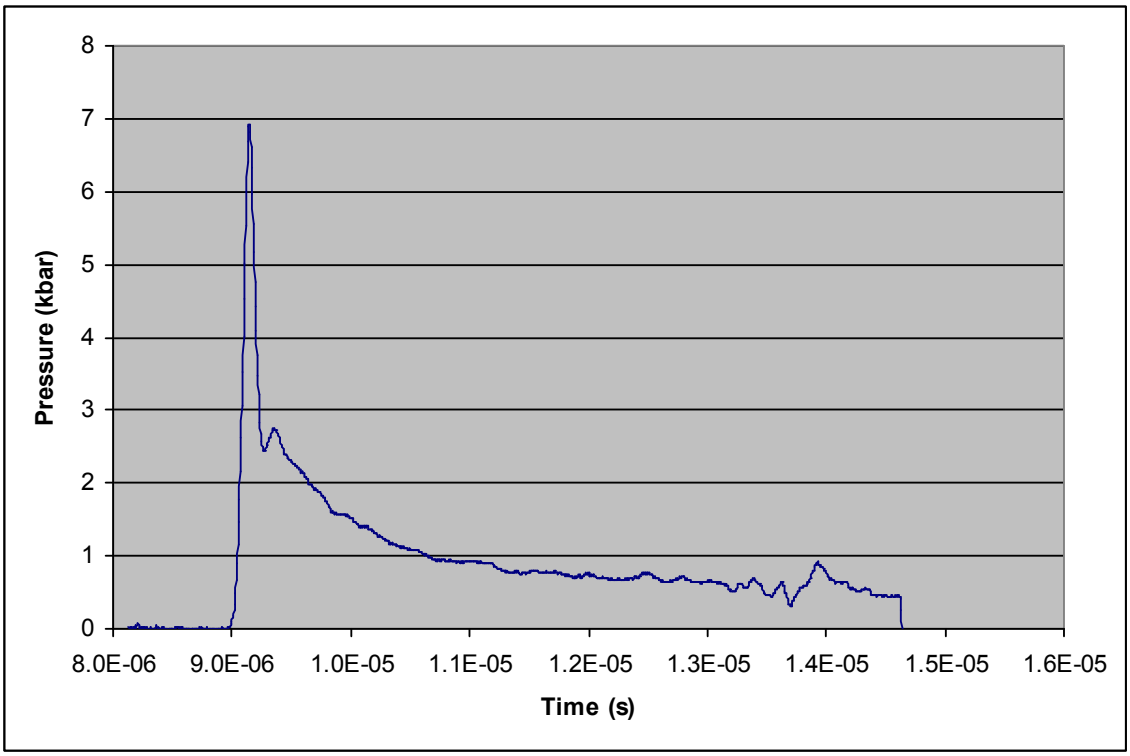

TP-2004-06 Sample A Pressure

Notes

Direct Spray on gage with no buffer. Peak pressure correct, but gage heating due to the explosive detonation causes the gage to read a higher pressure on the tail, and prevents the tail from returning to zero. The result is an incorrect pressure pulse shape, and a higher impulse than the actual.

Test ID: TP-2004-06 Target Material: LEXAN® Date: 6/23/2004
Sample ID: B Flyer Material: N/A (Direct Spray)

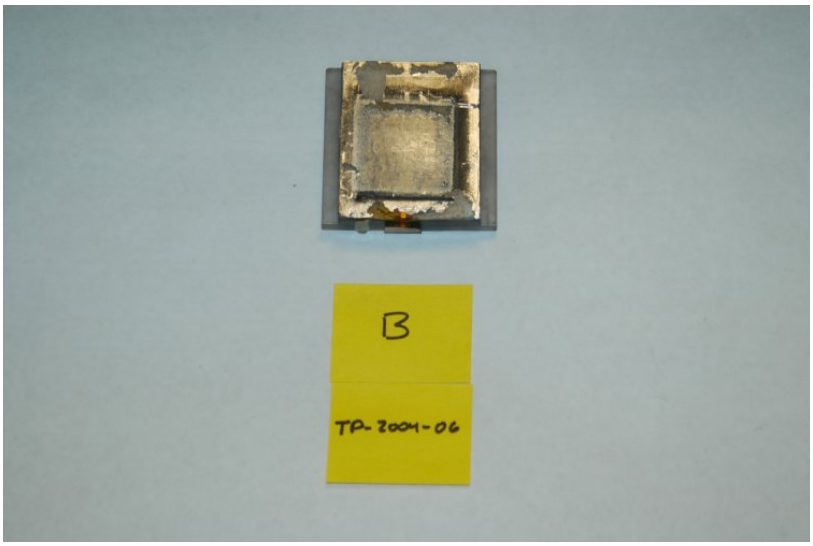

Test TP-2004-06 Sample B (Direct Spray Test)

Test Purpose

To evaluate the peak pressure developed on a LEXAN® surface directly from the SASN explosive detonation.

Performance Data

Areal Density	45.48	mg/cm^2	Predicted Vo:	N/A	cm/sec
			Predicted Impulse:	3166	taps
$V_{incident}$	N/A	m/sec			
$V_{rebound}$	N/A	m/sec	Measured Impulse:	2773	taps
Rebound Factor	N/A		Calculated Vo:	N/A	cm/sec
			% Measured of Predicted:	87.6%	

Ballistic Pendulum Parameters

Pendulum Mass	5085 (11.2)	gm (lbm.)	Impact Area	14.06 (2.25)	cm^2 (in^2)
String length	9.875	in.			

Notes

The areal density may be high due to overspray which does not take part in the impulse delivered

Sample ID: TP-2004-06 B Date: 6/23/2004

Pressure Data

Hugoniot Pressure:	N/A	kbar
Hydrocode Pressure:	N/A	kbar
Carbon Gage		
Peak Pressure:	3.75	kbar
Pulse Duration:	~9.34	μs
Impulse:	~5861	taps

Carbon Gage Constants		
Gage Resistance:	48.88	Ω
Excitation Voltage:	45.0	volts
Line Resistance:	0.271	Ω
Term Resistance:	74.76	Ω

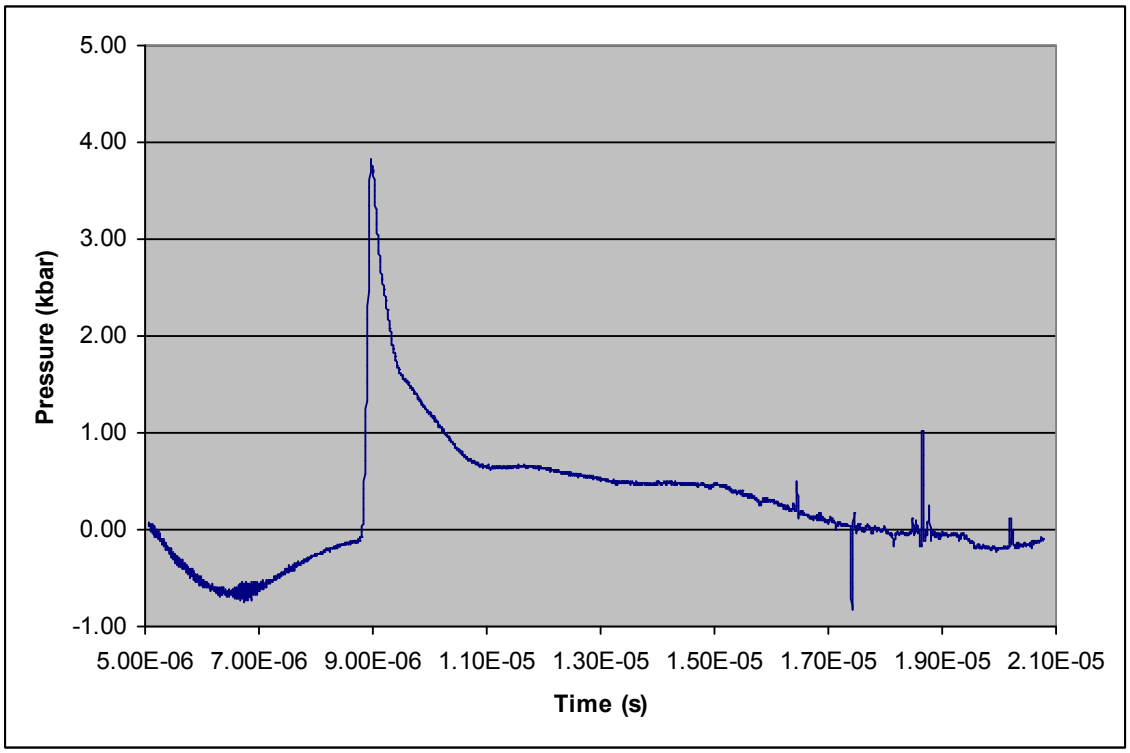

TP-2004-06 Sample B Pressure

Notes

Direct Spray on gage with no buffer. Peak pressure correct, but gage heating due to the explosive detonation causes the gage to read a higher pressure on the tail, and prevents the tail from correctly returning to zero. The result is an incorrect pressure pulse shape, and a higher impulse than the actual.

Test ID: TP-2004-06 Target Material: PMMA Date: 6/23/2004
Sample ID: C Flyer Material: N/A (Direct Spray)

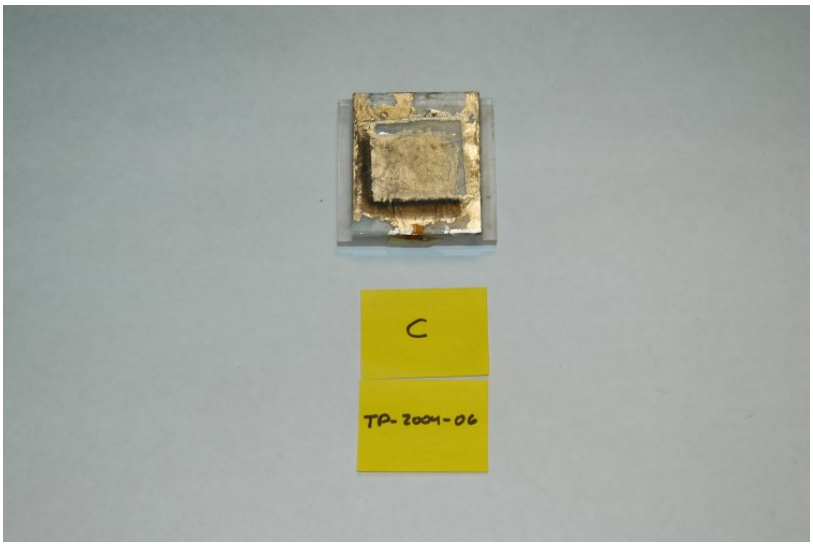

Test TP-2004-06 Sample C (Direct Spray Test)

Test Purpose

To evaluate the peak pressure developed on a PMMA surface directly from the SASN explosive detonation.

Performance Data

Areal Density	43.87	mg/cm^2	Predicted Vo:	N/A	cm/sec
			Predicted Impulse:	3033	taps
$V_{incident}$	N/A	m/sec			
$V_{rebound}$	N/A	m/sec	Measured Impulse:	2943	taps
Rebound Factor	N/A		Calculated Vo:	N/A	cm/sec
			% Measured of Predicted:	97.0%	

Ballistic Pendulum Parameters

Pendulum Mass	5085 (11.2)	gm (lbm.)	Impact Area	14.06 (2.25)	cm^2 (in^2)
String length	9.875	in.			

Notes

Sample ID: TP-2004-06 C Date: 6/23/2004

Pressure Data

Hugoniot Pressure:	N/A	kbar	Carbon Gage Constants		
Hydrocode Pressure:	N/A	kbar	Gage Resistance:	49.651	Ω
			Excitation Voltage:	45.0	volts
Carbon Gage			Line Resistance:	0.251	Ω
Peak Pressure:	3.53	kbar	Term Resistance:	74.76	Ω
Pulse Duration:	~6.1	μs			
Impulse:	~7766	taps			

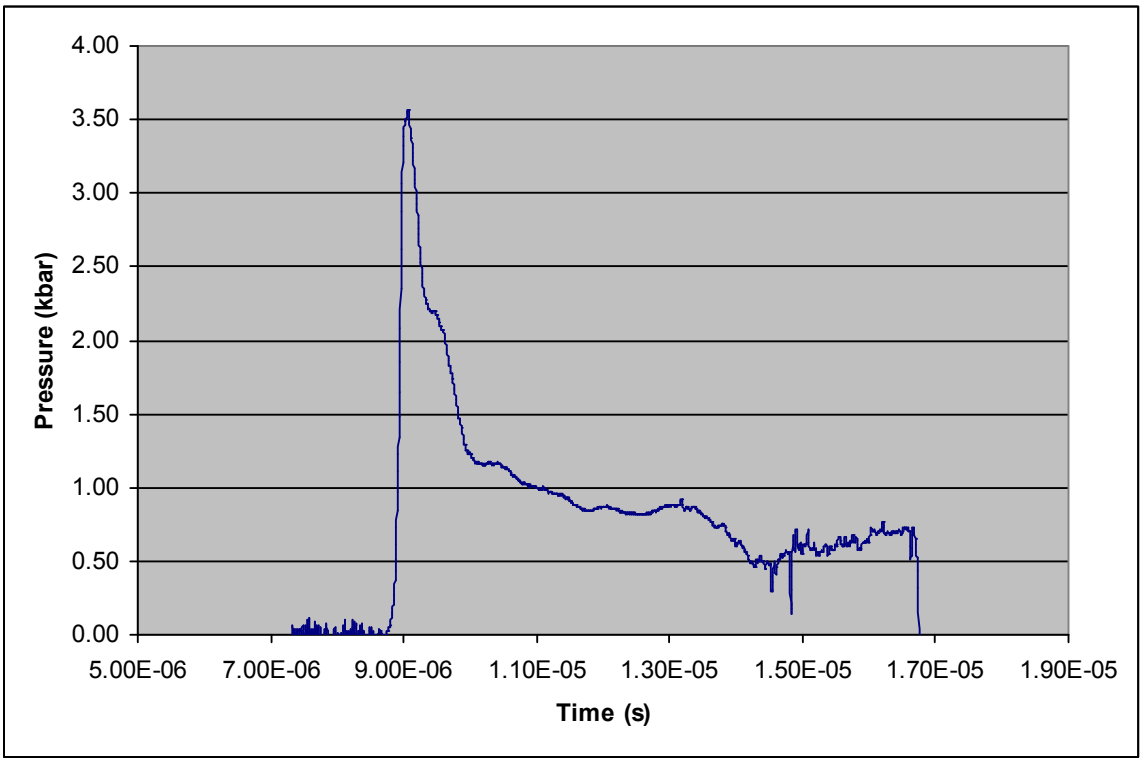

TP-2004-06 Sample C Pressure

Notes

Direct Spray on gage with no buffer. Peak pressure correct, but gage heating due to the explosive detonation causes the gage to read a higher pressure on the tail, and prevents the tail from returning to zero. The result is an incorrect pressure pulse shape, and a higher impulse than the actual.

Test ID:	TP-2004-06	Target Material:	6061-T651 Aluminum	Date:	6/23/2004
Sample ID:	D	Flyer Material:	1100 Aluminum		

Test TP-2004-06 Sample D (No Picture Available)

Test Purpose

First designed flyer test.

Performance Data

Areal Density	N/A	mg/cm^2	Predicted Vo:	N/A	cm/sec
			Predicted Impulse:	N/A	taps
$V_{incident}$	N/A	m/sec			
$V_{rebound}$	N/A	m/sec	Measured Impulse:	N/A	taps
Rebound Factor	N/A		Calculated Vo:	N/A	cm/sec
			% Measured to Predicted:	N/A	

Ballistic Pendulum Parameters

Pendulum Mass	5085 (11.2)	gm (lbm.)	Impact Area	N/A	cm^2 (in^2)
String length	9.875	in.			

Pressure Data

Hugoniot Pressure:	N/A	kbar
Hydrocode Pressure:	N/A	kbar
Carbon Gage:	No Used	

Notes

No Test. Flyer and spacer fell off of the target while on the backboard in the spray booth. The test was not able to be salvaged.

Test ID:	TP-2004-06	Target Material:	LEXAN®	Date:	6/23/2004
Sample ID:	E	Flyer Material:	Aluminum 1100		

Test TP-2004-06 Sample E

Test Purpose

To evaluate flyer assembly techniques, handling procedures, and firing procedures for conducting a one dimensional flyer experiment, as well as observe the material response of a flyer impact on a LEXAN® target.

Performance Data

Areal Density	45.82	mg/cm^2	Predicted Vo:	27326	cm/sec
			Predicted Impulse:	3006	taps
$V_{incident}$	273.0	m/sec			
$V_{rebound}$	62.6	m/sec	Measured Impulse:	2943	taps
Rebound Factor	1.23		Calculated Vo:	26753	cm/sec
			% Measured of Predicted:	97.9%	

Ballistic Pendulum Parameters

Pendulum Mass	5085 (11.2)	gm (lbm.)	Impact Area	14.06 (2.25)	cm^2 (in^2)
String length	9.875	in.			

Pressure Data

Hugoniot Pressure:	6.99	kbar
Hydrocode Pressure:	6.56	kbar
Carbon Gage:	Not Used	

Notes

Good Test. The LEXAN® showed a small spall area approximately 1 cm in diameter approximately 0.1 cm from the back surface. This result was not predicted by KOWIN, most likely due to the equation of state for LEXAN® which does not support tensile stresses.

Test ID: TP-2004-06 Target Material: PMMA Date: 6/23/2004
Sample ID: F Flyer Material: Aluminum 1100

Test TP-2004-06 Sample F

Test Purpose

To evaluate flyer assembly techniques, handling procedures, and firing procedures for conducting a one dimensional flyer experiment, as well as observe the material response of a flyer impact on a PMMA target.

Performance Data

Areal Density	42.78	mg/cm^2	Predicted Vo:	25577	cm/sec
			Predicted Impulse:	2900	taps
$V_{incident}$	256.0	m/sec			
$V_{rebound}$	68.4	m/sec	Measured Impulse:	2679	taps
Rebound Factor	1.27		Calculated Vo:	23625	cm/sec
			% Measured of Predicted:	92.4%	

Ballistic Pendulum Parameters

Pendulum Mass	5085 (11.2)	gm (lbm.)	Impact Area	14.06 (2.25)	cm^2 (in^2)
String length	9.875	in.			

Pressure Data

Hugoniot Pressure:	7.02	kbar
Hydrocode Pressure:	4.80	kbar
Carbon Gage:	No Used	

Notes

Good Test. The PMMA showed a oval shaped spall section removed from the back surface. The depth of the spall section was approximately 1 mm. This spall result was predicted by KOWIN.

Test ID: TP-2005-07 Target Material: Aluminum 6061-T651 Date: 7/16/2004
Sample ID: A Flyer Material: Aluminum 1100

Test TP-2004-07 Sample A

Test Purpose

Pressure measurement of an aluminum flyer impact on an aluminum target.

Performance Data

Areal Density	50.7	mg/cm^2	Predicted Vo:	30053	cm/sec
			Predicted Impulse:	3618	taps
$V_{incident}$	301.0	m/sec			
$V_{rebound}$	104.0	m/sec	Measured Impulse:	3617	taps
Rebound Factor	1.35		Calculated Vo:	30042	cm/sec
			% Measured to Predicted:	100.0%	

Ballistic Pendulum Parameters

Pendulum Mass	5085 (11.2)	gm (lbm.)	Impact Area	14.06 (2.25)	cm^2 (in^2)
String length	9.875	in.			

Notes

Excellent test, with 100% agreement between predicted impulse and measured impulse

Sample ID: TP-2004-07 A Date: 7/16/2004

Pressure Data

Hugoniot Pressure:	22.5	kbar	Carbon Gage Constants		
Hydrocode Pressure:	22.2	kbar	Gage Resistance:	48.5	Ω
			Excitation Voltage:	45.0	volts
Carbon Gage			Line Resistance:	0.271	Ω
Peak Pressure:	27.95	kbar	Term Resistance:	74.76	Ω
Pulse Duration:	1.96	μs			

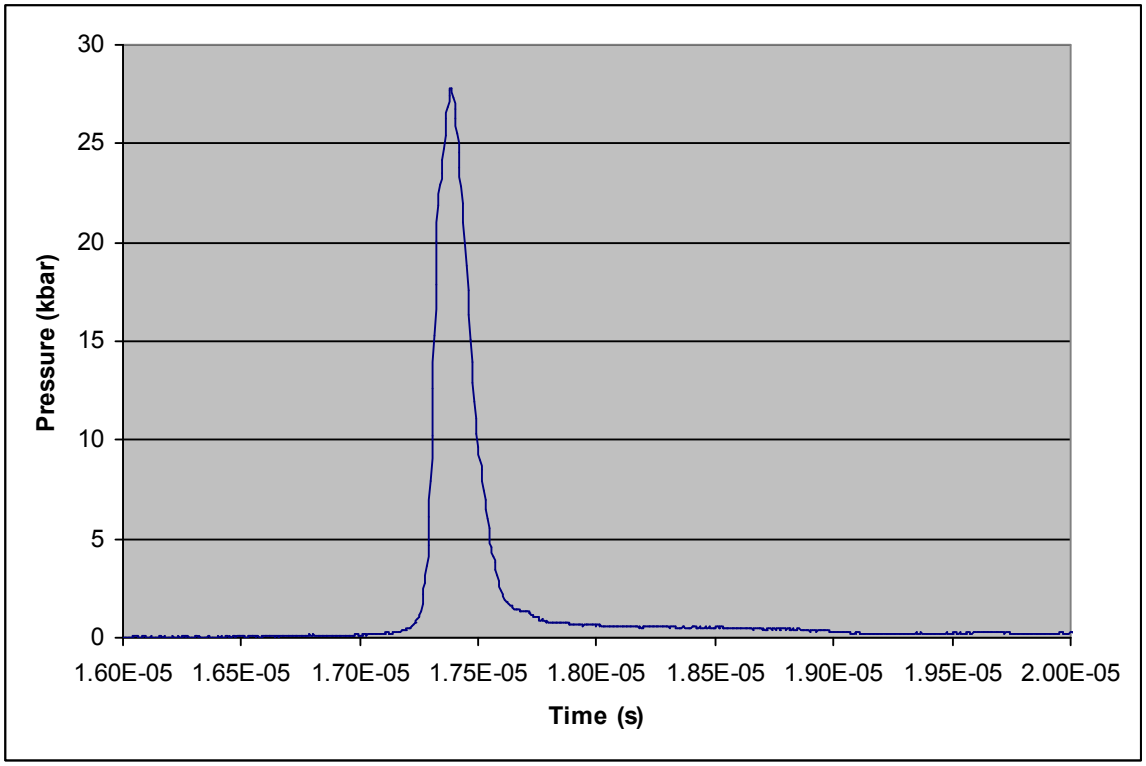

TP-2004-07 Sample A Pressure

Notes

Pressure Data is higher than predicted with either hugoniot or hydrocode measurements.

Test ID: TP-2005-07 Target Material: LEXAN® Date: 7/16/2004
Sample ID: B Flyer Material: Aluminum 1100

Test TP-2004-07 Sample B

Test Purpose

Pressure measurement of an aluminum flyer impact on a LEXAN® target.

Performance Data

Areal Density	50.7	mg/cm^2	Predicted Vo:	30053	cm/sec
			Predicted Impulse:	3241	taps
$V_{incident}$	301	m/sec			
$V_{rebound}$	61.8	m/sec	Measured Impulse:	3251	taps
Rebound Factor	1.21		Calculated Vo:	30140	cm/sec
			% Measured to Predicted:	100.3%	

Ballistic Pendulum Parameters

Pendulum Mass	5085 (11.2)	gm (lbm.)	Impact Area	14.06 (2.25)	cm^2 (in^2)
String length	9.875	in.			

Notes

Excellent test, with nearly 100% agreement between predicted impulse and measured impulse

Sample ID: TP-2004-07 B Date: 7/16/2004

Pressure Data

Hugoniot Pressure:	7.78	kbar	Carbon Gage Constants		
Hydrocode Pressure:	7.47	kbar	Gage Resistance:	46.8	Ω
			Excitation Voltage:	45.0	volts
Carbon Gage			Line Resistance:	0.271	Ω
Peak Pressure:	8.89	kbar	Term Resistance:	74.76	Ω
Pulse Duration:	2.02	μs			

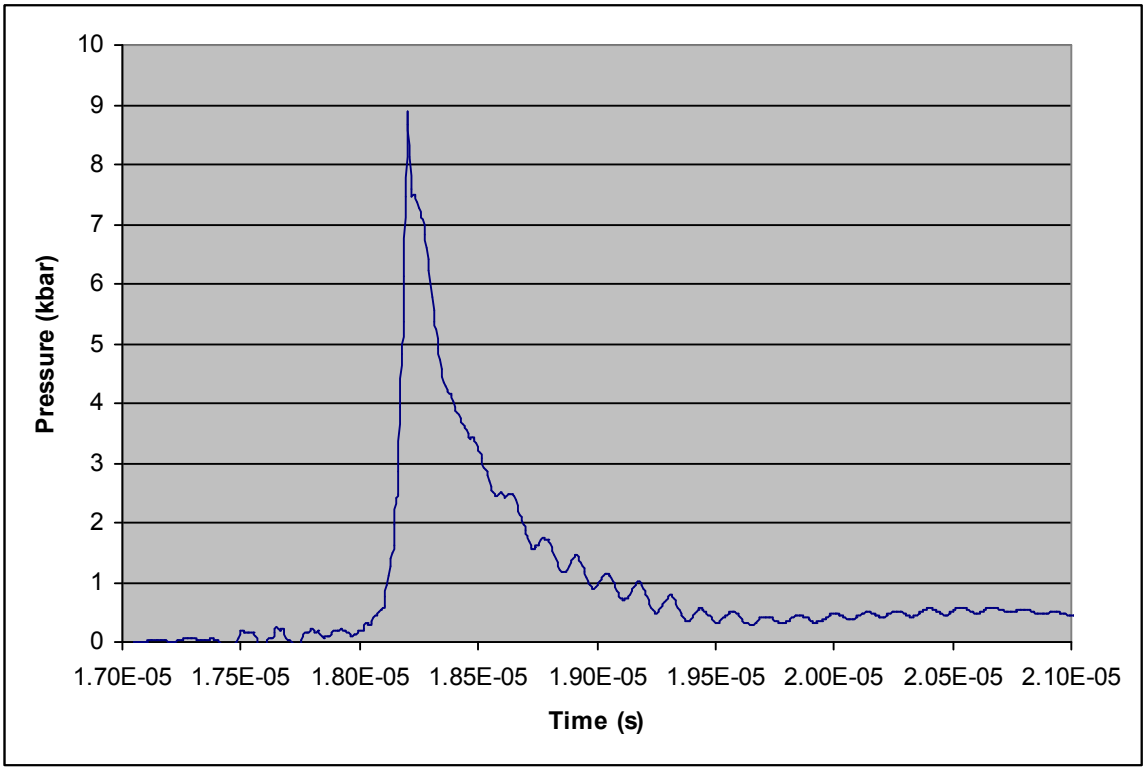

TP-2004-07 Sample B Pressure

Notes

The recording of the carbon gage data was quite noisy. It was found that the Rogoski coil instrumentation used to measure current from the capacitor bank, as well as trigger the instrumentation system, was nicked thereby exposing the coil to a large noise spike. This high frequency noise was transmitted to the carbon gage instrumentation. The pressure pulse was locally smoothed and filtered to remove as much noise as possible.

Test ID: TP-2005-07 Target Material: PMMA Date: 7/16/2004
Sample ID: C Flyer Material: Aluminum 1100

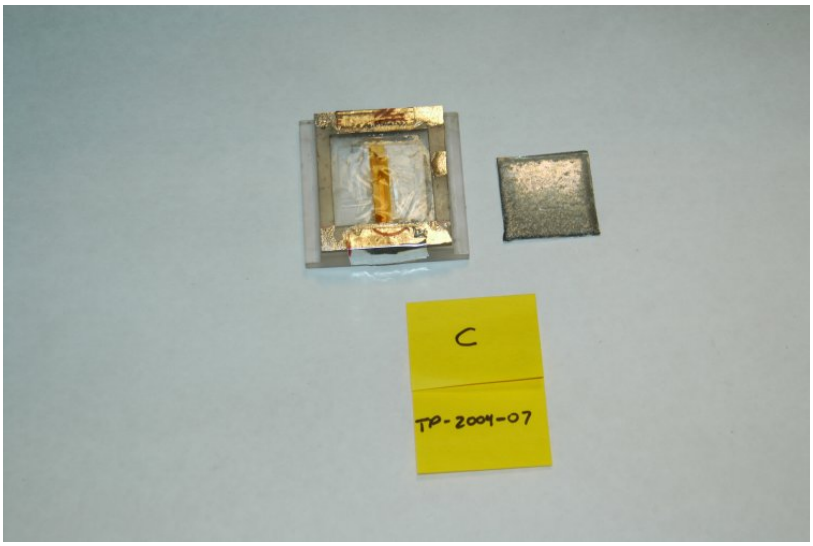

Test TP-2004-07 Sample C

Test Purpose

Pressure measurement of an aluminum flyer impact on a PMMA target.

Performance Data

Areal Density	50.7	mg/cm^2	Predicted Vo:	30053	cm/sec
			Predicted Impulse:	3322	taps
$V_{incident}$	301	m/sec			
$V_{rebound}$	70.8	m/sec	Measured Impulse:	2988	taps
Rebound Factor	1.24		Calculated Vo:	27035	cm/sec
			% Measured of Predicted:	90.0%	

Ballistic Pendulum Parameters

Pendulum Mass	5085 (11.2)	gm (lbm.)	Impact Area	14.06 (2.25)	cm^2 (in^2)
String length	9.875	in.			

Notes

Good test. Larger disagreement than observed in -06 tests

Sample ID: TP-2004-07 C Date: 7/16/2004

Pressure Data

Hugoniot Pressure:	8.40	kbar	Carbon Gage Constants		
Hydrocode Pressure:	5.98	kbar	Gage Resistance:	47.1	Ω
			Excitation Voltage:	45.0	volts
Carbon Gage			Line Resistance:	0.271	Ω
Peak Pressure:	10.28	kbar	Term Resistance:	74.76	Ω
Pulse Duration:	2.5	μs			

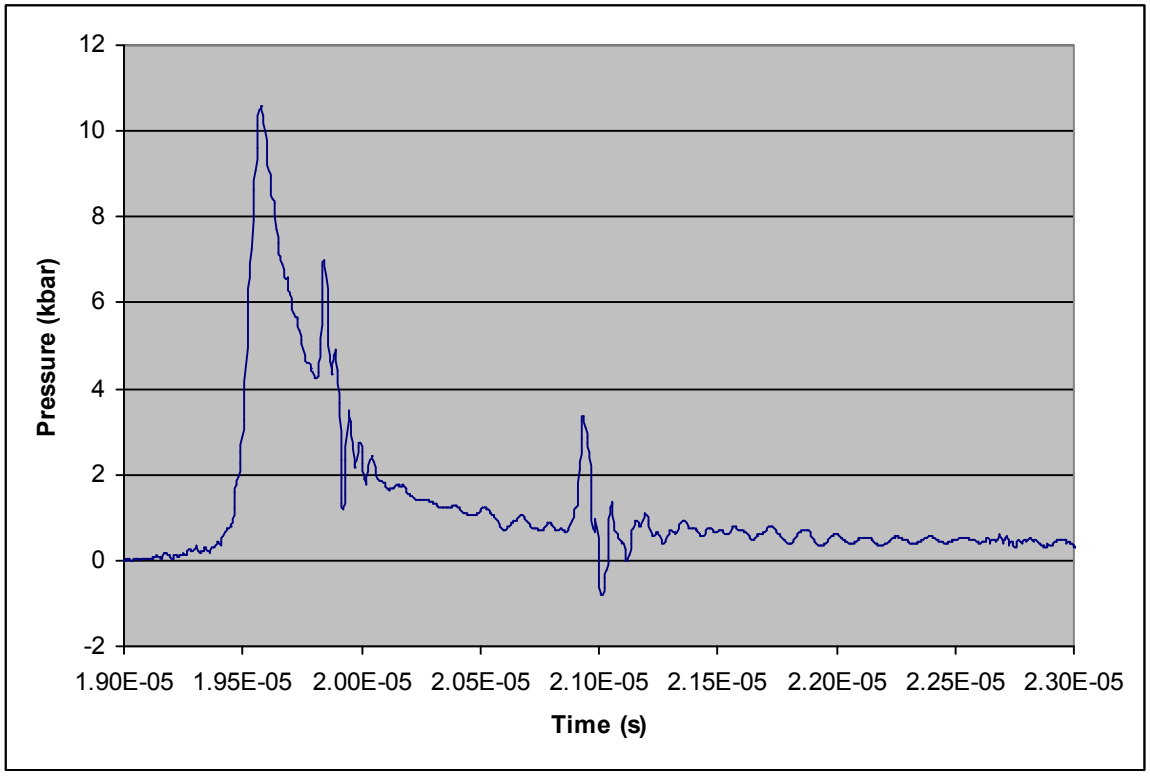

TP-2004-07 Sample C Pressure

Notes

The recording of the carbon gage data was quite noisy. It was found that the Rogoski coil instrumentation used to measure current from the capacitor bank, as well as trigger the instrumentation system, was nicked thereby exposing the coil to a large noise spike. This high frequency noise was transmitted to the carbon gage instrumentation. The pressure pulse was locally smoothed and filtered to remove as much noise as possible.

Test ID: TP-2005-07 Target Material: Aluminum 6061-T651 Date: 7/16/2004
Sample ID: D Flyer Material: Aluminum 1100

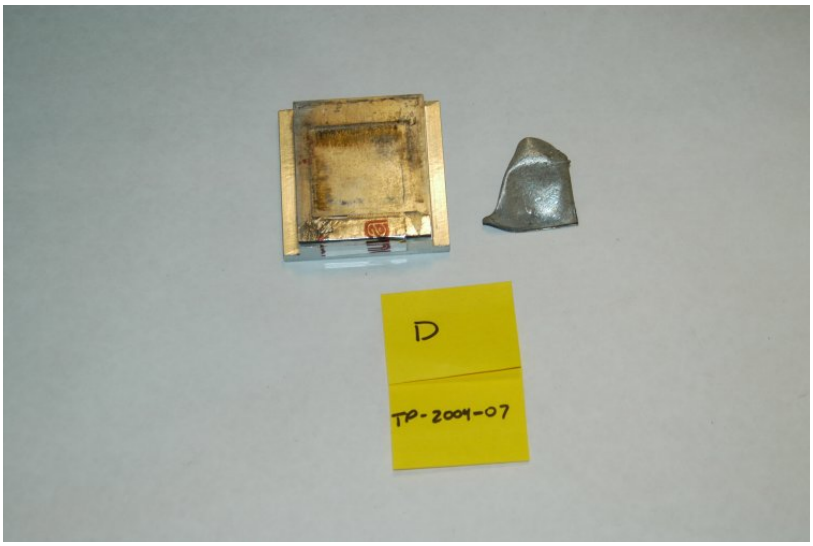

Test TP-2004-07 Sample D

Test Purpose
Material response test: Aluminum flyer impacting a 6061 aluminum target.

Performance Data

Areal Density	41.5	mg/cm^2	Predicted Vo:	24829	cm/sec
			Predicted Impulse:	3134	taps
$V_{incident}$	246.0	m/sec			
$V_{rebound}$	101.0	m/sec	Measured Impulse:	3439	taps
Rebound Factor	1.41		Calculated Vo:	27243	cm/sec
			% Measured of Predicted:	109.7%	

Ballistic Pendulum Parameters

Pendulum Mass	5085 (11.2)	gm (lbm.)	Impact Area	14.06 (2.25)	cm^2 (in^2)
String length	9.875	in.			

Pressure Data

Hugoniot Pressure:	18.3	kbar
Hydrocode Pressure:	17.3	kbar
Carbon Gage:	No Used	

Notes
Good Test. No major observations.

Test ID: TP-2005-07 Target Material: LEXAN® Date: 7/16/2004
Sample ID: E Flyer Material: Aluminum 1100

Test TP-2004-07 Sample E

Test Purpose
Material response test: Aluminum flyer impacting a LEXAN® target.

Performance Data

Areal Density	44.35	mg/cm^2	Predicted Vo:	26485	cm/sec
			Predicted Impulse:	2946	taps
$V_{incident}$	265	m/sec			
$V_{rebound}$	64.4	m/sec	Measured Impulse:	2894	taps
Rebound Factor	1.24		Calculated Vo:	26022	cm/sec
			% Measured of Predicted:	98.2%	

Ballistic Pendulum Parameters

Pendulum Mass	5085 (11.2)	gm (lbm.)	Impact Area	14.06 (2.25)	cm^2 (in^2)
String length	9.875	in.			

Pressure Data

Hugoniot Pressure:	6.75	kbar
Hydrocode Pressure:	6.28	kbar
Carbon Gage:	No Used	

Notes
Good Test. The LEXAN® target showed an interior spall in an oval shape near the center of impact.

Test ID: TP-2005-07 Target Material: PMMA Date: 7/16/2004
Sample ID: F Flyer Material: Aluminum 1100

Test TP-2004-07 Sample F

Test Purpose
Material response test: Aluminum flyer impacting a PMMA target.

Performance Data

Areal Density	41.05	mg/cm^2	Predicted Vo:	24564	cm/sec
			Predicted Impulse:	2802	taps
$V_{incident}$	246.0	m/sec			
$V_{rebound}$	67.6	m/sec	Measured Impulse:	2780	taps
Rebound Factor	1.27		Calculated Vo:	24367	cm/sec
			% Measured of Predicted:	99.2%	

Ballistic Pendulum Parameters

Pendulum Mass	5085 (11.2)	gm (lbm.)	Impact Area	14.06 (2.25)	cm^2 (in^2)
String length	9.875	in.			

Pressure Data

Hugoniot Pressure:	6.72	kbar
Hydrocode Pressure:	4.51	kbar
Carbon Gage:	No Used	

Notes
Good Test.
The PMMA target showed significant spall and greater damage than other PMMA targets to date. The Spall was oval in shape with cracks radiating out towards the edges of the target

Test ID: TP-2005-08 Target Material: 6061 Aluminum Date: 8/17/2004
Sample ID: A Flyer Material: 1100 Aluminum

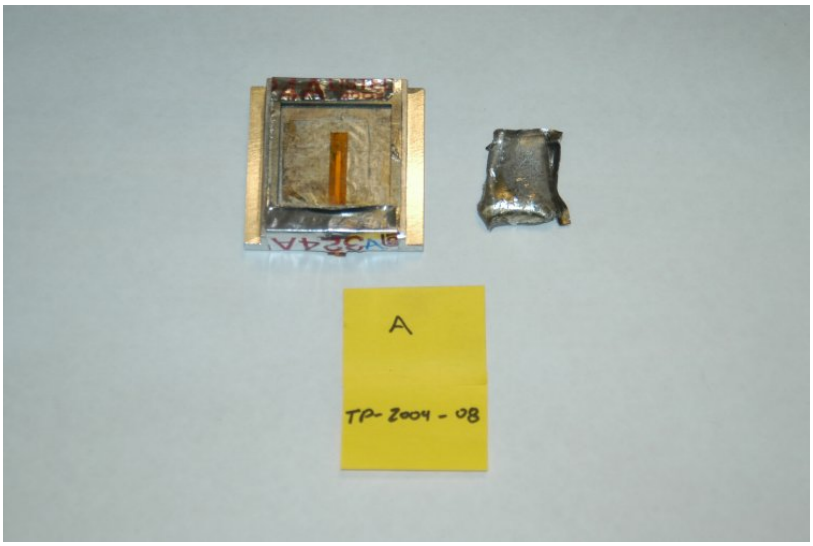

Test TP-2004-08 Sample A

Test Purpose

Pressure measurement of an aluminum flyer impact on an aluminum target. A repeat test of TP-2004-07 A.

Performance Data

Areal Density	50.8	mg/cm^2	Predicted Vo:	30108	cm/sec
			Predicted Impulse:	3625	taps
$V_{incident}$	301.0	m/sec			
$V_{rebound}$	104.0	m/sec	Measured Impulse:	3744	taps
Rebound Factor	1.35		Calculated Vo:	31096	cm/sec
			% Measured of Predicted:	103.3	

Ballistic Pendulum Parameters

Pendulum Mass	5085 (11.2)	gm (lbm.)	Impact Area	14.06 (2.25)	cm^2 (in^2)
String length	9.875	in.			

Pressure Data

Hugoniot Pressure:	22.57	kbar
Hydrocode Pressure:	22.3	kbar
Carbon Gage:	Not Recorded	

Notes

Functionally good test, though pressure was not recorded by the carbon gage instrumentation.

Test ID: TP-2005-08 Target Material: LEXAN® Date: 8/17/2004
Sample ID: B Flyer Material: 1100 Aluminum

Test TP-2004-08 Sample B

Test Purpose

Pressure measurement of an aluminum flyer impact on a LEXAN® target. A repeat test of TP-2004-07 B.

Performance Data

Areal Density	53.7	mg/cm^2	Predicted Vo:	31683	cm/sec
			Predicted Impulse:	3450	taps
$V_{incident}$	301	m/sec			
$V_{rebound}$	65.3	m/sec	Measured Impulse:	3825	taps
Rebound Factor	1.22		Calculated Vo:	35123	cm/sec
			% Measured of Predicted:	110.9%	

Ballistic Pendulum Parameters

Pendulum Mass	5085 (11.2)	gm (lbm.)	Impact Area	14.06 (2.25)	cm^2 (in^2)
String length	9.875	in.			

Pressure Data

Hugoniot Pressure:	7.78	kbar
Hydrocode Pressure:	7.49	kbar
Carbon Gage:	Not Recorded	

Notes

Functionally good test, though pressure was not recorded by the carbon gage instrumentation. The error was found in the triggering circuit for the carbon gage pulse power supply and corrected.

Test ID: TP-2005-08 Target Material: PMMA Date: 8/17/2004
Sample ID: C Flyer Material: 1100 Aluminum

Test TP-2004-08 Sample C

Test Purpose

Pressure measurement of an aluminum flyer impact on a PMMA target. Repeat of test TP-2004-07 C.

Performance Data

Areal Density	50.75	mg/cm^2	Predicted Vo:	30081	cm/sec
			Predicted Impulse:	3324	taps
$V_{incident}$	301	m/sec			
$V_{rebound}$	70.7	m/sec	Measured Impulse:	3753	taps
Rebound Factor	1.23		Calculated Vo:	33961	cm/sec
			% Measured of Predicted:	112.9%	

Ballistic Pendulum Parameters

Pendulum Mass	5085 (11.2)	gm (lbm.)	Impact Area	14.06 (2.25)	cm^2 (in^2)
String length	9.875	in.			

Notes

Sample ID: TP-2004-08 C Date: 8/17/2004

Pressure Data

Hugoniot Pressure:	8.41	kbar	Carbon Gage Constants		
Hydrocode Pressure:	5.99	kbar	Gage Resistance:	47.1	Ω
			Excitation Voltage:	45.0	volts
Carbon Gage			Line Resistance:	0.271	Ω
Peak Pressure:	10.7	kbar	Term Resistance:	74.76	Ω
Pulse Duration:	1.10	μs			

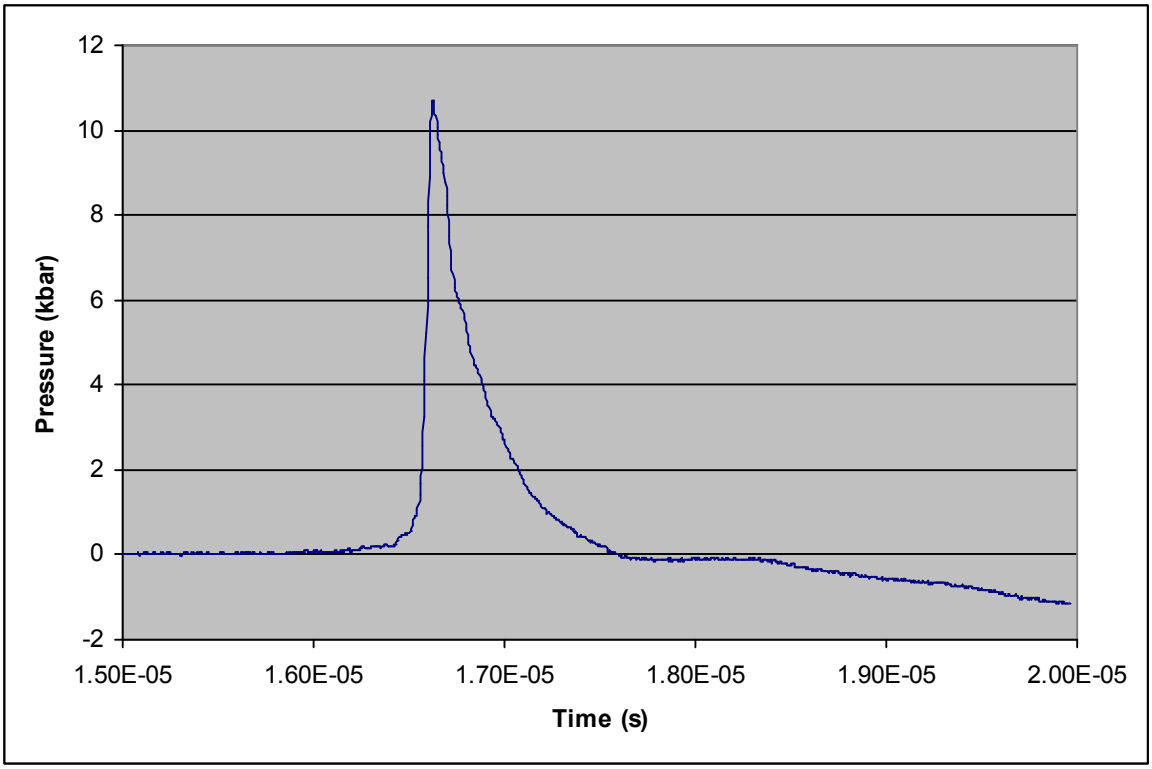

TP-2004-08 Sample C Pressure

Notes

Test ID: TP-2005-08 Target Material: LEXAN® Date: 8/17/2004
Sample ID: D Flyer Material: 1100 Aluminum

Test TP-2004-08 Sample D

Test Purpose

Material response test: Aluminum flyer impacting a LEXAN® target. A repeat of test TP-2004-07 E.

Performance Data

Areal Density	50.24	mg/cm^2	Predicted Vo:	29800	cm/sec
			Predicted Impulse:	3208	taps
$V_{incident}$	298	m/sec			
$V_{rebound}$	60.5	m/sec	Measured Impulse:	3210	taps
Rebound Factor	1.20		Calculated Vo:	29821	cm/sec
			% Measured of Predicted:	100.1%	

Ballistic Pendulum Parameters

Pendulum Mass	5085 (11.2)	gm (lbm.)	Impact Area	14.06 (2.25)	cm^2 (in^2)
String length	9.875	in.			

Pressure Data

Hugoniot Pressure:	7.70	kbar
Hydrocode Pressure:	7.40	kbar
Carbon Gage:	No Used	

Notes

Good test.

Test ID:	TP-2005-09	Target Material:	304 Stainless Steel	Date:	9/14/2004
Sample ID:	A	Flyer Material:	Aluminum 1100		

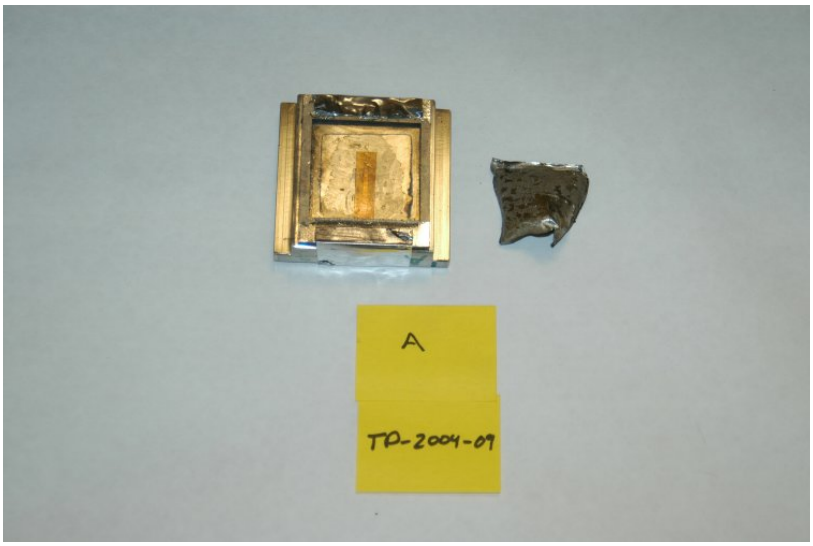

Test TP-2004-9 Sample A

Test Purpose

Pressure measurement of an aluminum flyer impact on a 304 Stainless Steel target.

Performance Data

Areal Density	54.65	mg/cm^2	Predicted Vo	32195	cm/sec
			Predicted Impulse	4419	taps
$V_{incident}$	322	m/sec	Measured Impulse	4379	taps
$V_{rebound}$	172	m/sec	Measured Vo	31900	cm/sec
Rebound Factor	1.53		% Difference	99.1%	

Ballistic Pendulum Data

Pendulum Mass	5085 (11.2)	gm (lbm.)	Impact Area	14.06 (2.25)	cm^2 (in^2)
String length	9.875	in.	Measured Impulse		taps

Notes

Test ID: TP-2005-09 Date: 9/14/2004

Pressure Data

Hugoniot Pressure:	34.9	kbar
Hydrocode Pressure:	31.6	kbar
Carbon Gage		
Peak Pressure:	35.0	kbar
Pulse Duration:	0.52	μs

Carbon Gage Constants

Gage Resistance:	47.3	Ω
Excitation Voltage:	45.0	volts
Line Resistance:	0.271	Ω
Term Resistance:	74.76	Ω

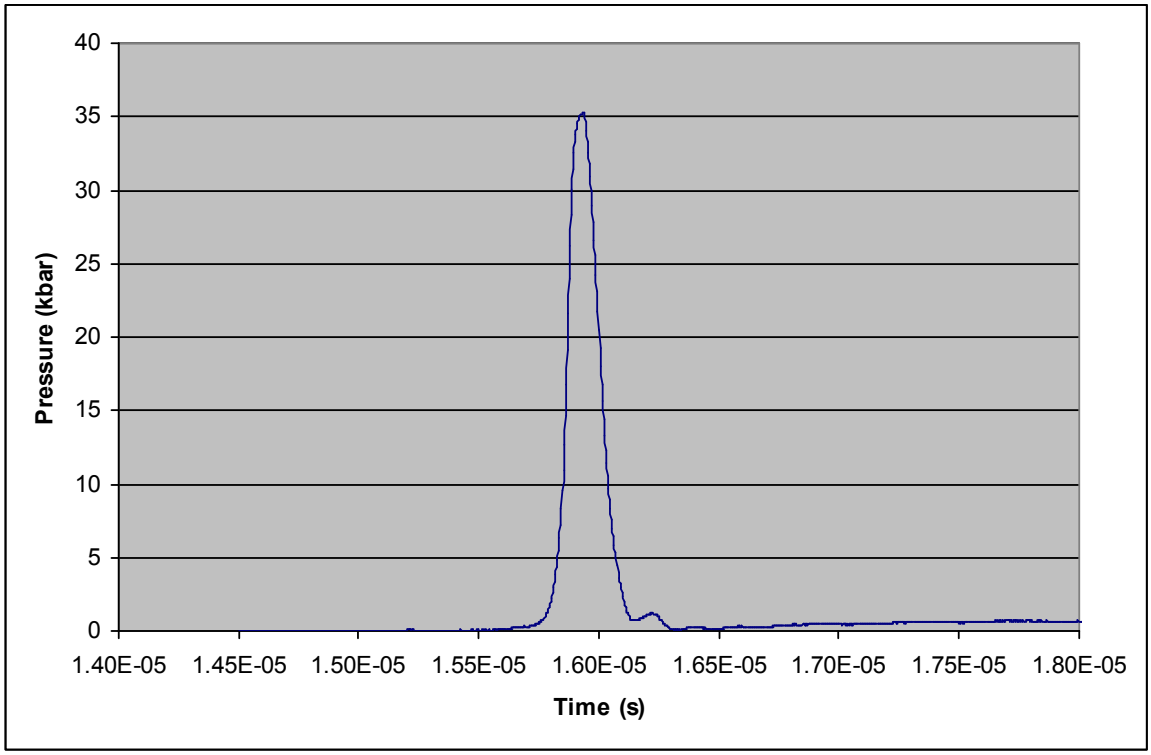

TP-2004-09 Sample A Pressure

Notes

Test ID:	TP-2005-09	Target Material:	316 Stainless Steel	Date:	9/14/2004
Sample ID:	B	Flyer Material:	Aluminum 1100		

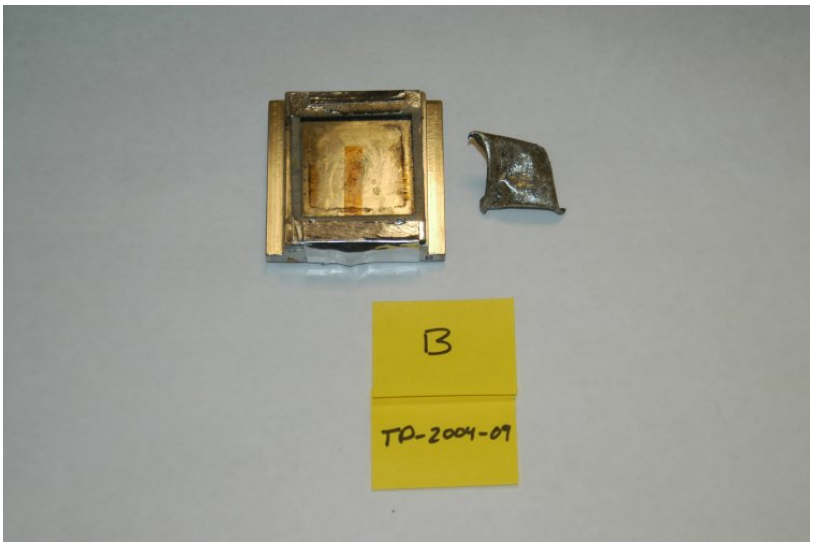

Test TP-2004-9 Sample B

Test Purpose

Pressure measurement of an aluminum flyer impact on a 316 Stainless Steel target.

Performance Data

Areal Density	54.65	mg/cm^2	Predicted Vo	32192	cm/sec
			Predicted Impulse	4419	taps
$V_{incident}$	322	m/sec	Measured Impulse	4281	taps
$V_{rebound}$	172	m/sec	Calculated Vo	31184	cm/sec
Rebound Factor	1.53		% Difference	96.9%	

Ballistic Pendulum Data

Pendulum Mass	5085 (11.2)	gm (lbm.)	Impact Area	14.06 (2.25)	cm^2 (in^2)
String length	9.875	in.			

Test Notes

Test ID: TP-2005-09 Date: 9/14/2004

Pressure Data

Hugoniot Pressure:	34.9	kbar
Hydrocode Pressure:	31.6	kbar
Carbon Gage		
Peak Pressure:	36.7	kbar
Pulse Duration:	0.54	μs

Carbon Gage Constants

Gage Resistance:	47.8	Ω
Excitation Voltage:	45.0	volts
Line Resistance:	0.271	Ω
Term Resistance:	74.76	Ω

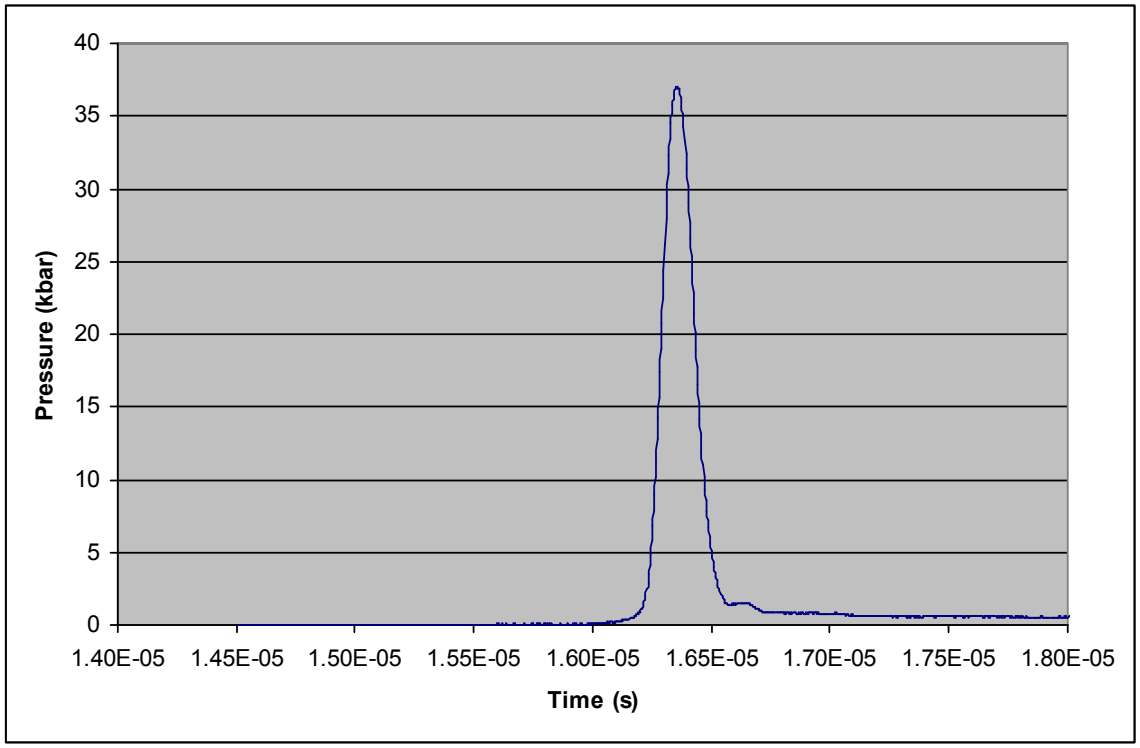

TP-2004-09 Sample B Pressure

Notes

Test ID:	TP-2005-09	Target Material:	Nickel 200	Date:	9/14/2004
Sample ID:	C	Flyer Material:	Aluminum 1100		

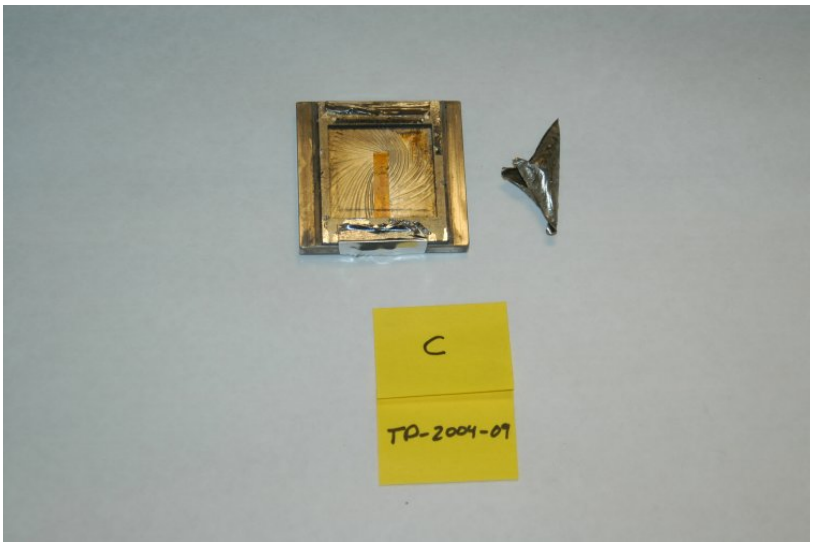

Test TP-2004-9 Sample C

Test Purpose

Pressure measurement of an aluminum flyer impact on a nickel 200 target.

Performance Data

Areal Density	54.65	mg/cm^2	Predicted Vo	32192	cm/sec
			Predicted Impulse	4527	taps
$V_{incident}$	322	m/sec	Measured Impulse	4496	taps
$V_{rebound}$	184	m/sec	Calculated Vo	31973	cm/sec
Rebound Factor	1.57		% Difference	99.3%	

Ballistic Pendulum Data

Pendulum Mass	5085 (11.2)	gm (lbm.)	Impact Area	14.06 (2.25)	cm^2 (in^2)
String length	9.875	in.			

Test Notes

Test ID: TP-2005-09 Date: 9/14/2004

Pressure Data

Hugoniot Pressure:	36.1	kbar
Hydrocode Pressure:	33.0	kbar
Carbon Gage		
Peak Pressure:	38.5	kbar
Pulse Duration:	0.52	μs

Carbon Gage Constants

Gage Resistance:	48.1	Ω
Excitation Voltage:	45.0	volts
Line Resistance:	0.271	Ω
Term Resistance:	74.76	Ω

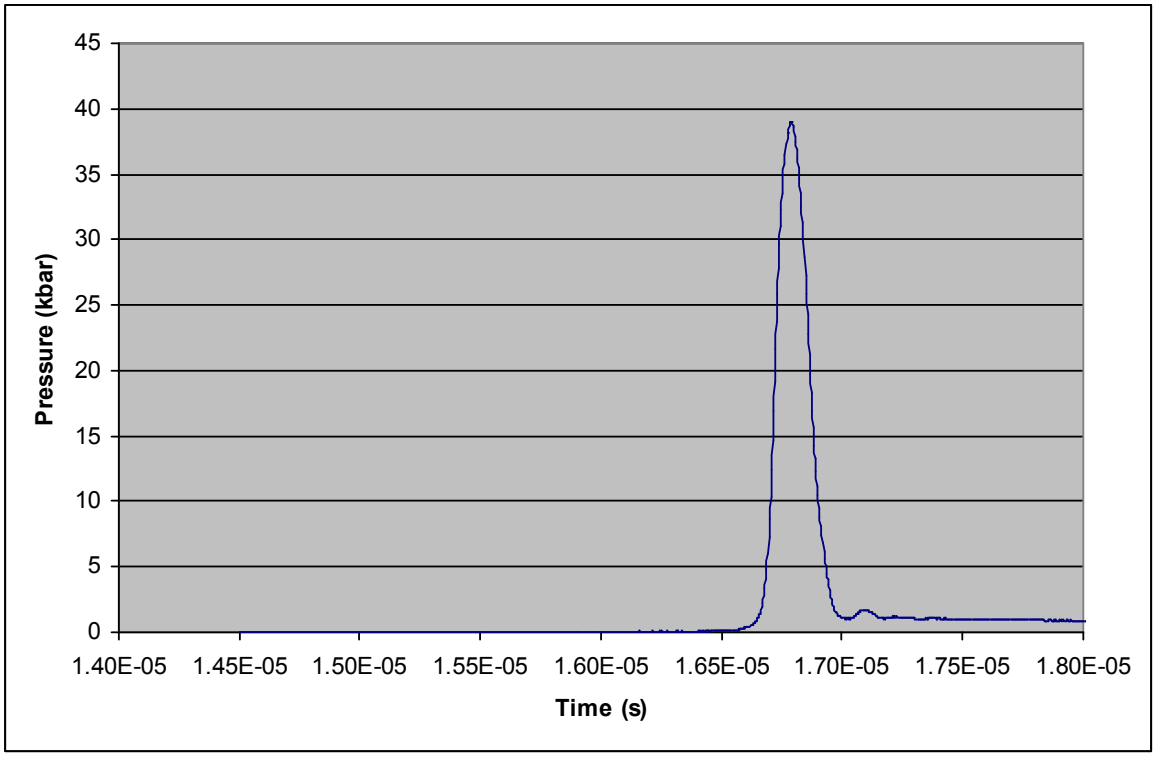

TP-2004-09 Sample C Pressure

Notes

Test ID:	TP-2005-09	Target Material:	304 Stainless Steel	Date:	9/14/2004
Sample ID:	D	Flyer Material:	Aluminum 1100		

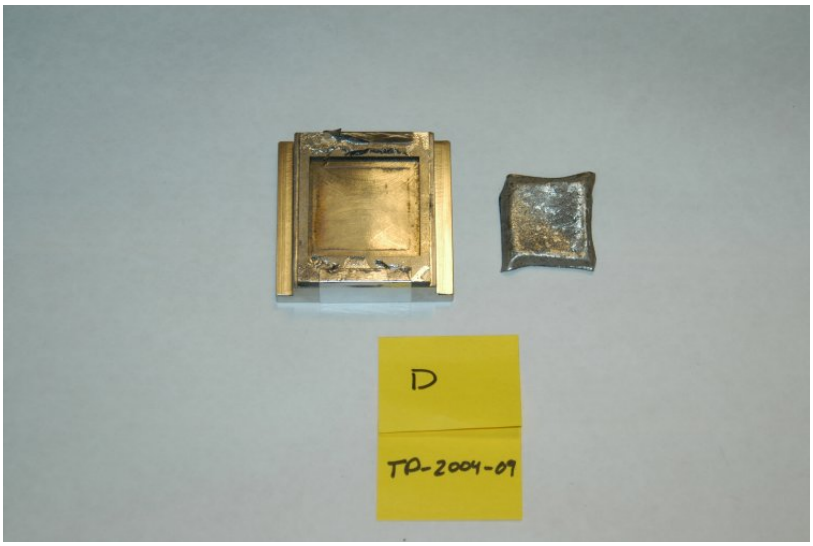

Test TP-2004-9 Sample D

Test Purpose

Material response test: Aluminum flyer impacting a 304 Stainless Steel target.

Performance Data

Areal Density	45.85	mg/cm^2	Predicted Vo	27343	cm/sec
			Predicted Impulse	3845	taps
$V_{incident}$	273	m/sec	Measured Impulse	3847	taps
$V_{rebound}$	156	m/sec	Calculated Vo	27359	cm/sec
Rebound Factor	1.57		% Difference	100.1%	

Ballistic Pendulum Data

Pendulum Mass	5085 (11.2)	gm (lbm.)	Impact Area	14.06 (2.25)	cm^2 (in^2)
String length	9.875	in.			

Pressure Data

Hugoniot Pressure:	29.43	kbar
Hydrocode Pressure:	27.10	kbar
Carbon Gage:	No Used	

Test Notes

Test ID:	TP-2005-09	Target Material:	316 Stainless Steel	Date:	9/14/2004
Sample ID:	E	Flyer Material:	Aluminum 1100		

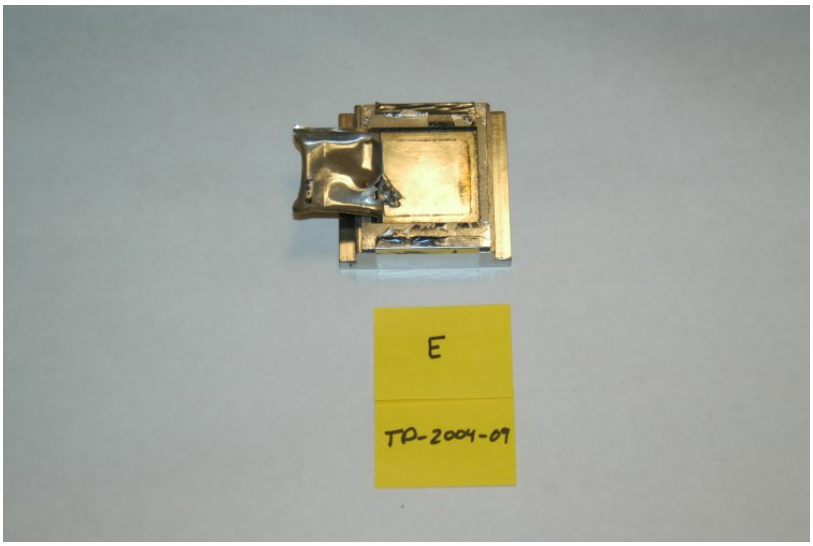

Test TP-2004-9 Sample E

Test Purpose

Material response test: Aluminum flyer impacting a 316 Stainless Steel target.

Performance Data

Areal Density	45.85	mg/cm^2	Predicted Vo	27343	cm/sec
			Predicted Impulse	3845	taps
$V_{incident}$	273	m/sec	Measured Impulse	3049	taps
$V_{rebound}$	156	m/sec	Calculated Vo	21685	cm/sec
Rebound Factor	1.57		% Difference	79.3%	

Ballistic Pendulum Data

Pendulum Mass	5085 (11.2)	gm (lbm.)	Impact Area	14.06 (2.25)	cm^2 (in^2)
String length	9.875	in.			

Pressure Data

Hugoniot Pressure:	29.43	kbar
Hydrocode Pressure:	27.10	kbar
Carbon Gage:	No Used	

Test Notes

Flyer plate found welded to target. The measured impulse was much lower than predicted. The weld caused the measured impulse to be low, which resulted in the calculated flyer velocity to be low.

Test ID:	TP-2005-09	Target Material:	Nickel 200	Date:	9/14/2004
Sample ID:	F	Flyer Material:	Aluminum 1100		

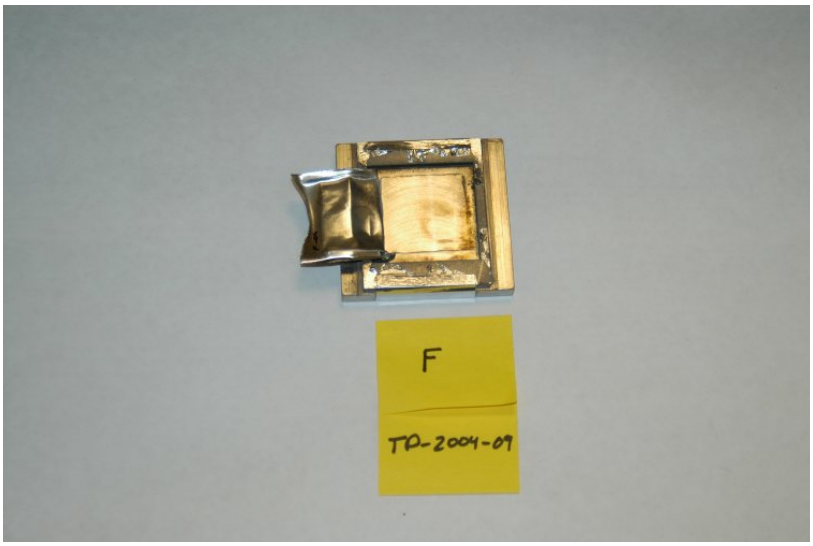

Test TP-2004-9 Sample F

Test Purpose

Material response test: Aluminum flyer impacting a nickel 200 target.

Performance Data

Areal Density	45.85	mg/cm^2	Predicted Vo	27343	cm/sec
			Predicted Impulse	3845	taps
$V_{incident}$	273	m/sec	Measured Impulse	3041	taps
$V_{rebound}$	166	m/sec	Calculated Vo	21136	cm/sec
Rebound Factor	1.61		% Difference	77.3%	

Ballistic Pendulum Data

Pendulum Mass	5085 (11.2)	gm (lbm.)	Impact Area	14.06 (2.25)	cm^2 (in^2)
String length	9.875	in.			

Pressure Data

Hugoniot Pressure:	30.44	kbar
Hydrocode Pressure:	27.1	kbar
Carbon Gage:	No Used	

Test Notes

Flyer plate found welded to target. The measured impulse was much lower than predicted. The weld caused the measured impulse to be low, which resulted in the calculated flyer velocity to be low.

Test ID: TP-2005-10 Target Material: 304 Stainless Steel Date: 9/29/2004
Sample ID: A Flyer Material: Aluminum 1100

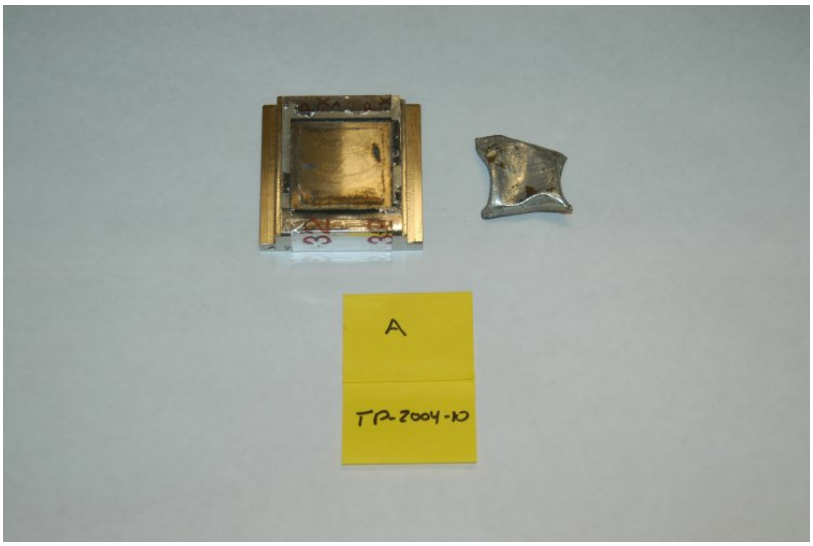

Test TP-2004-10 Sample A

Test Purpose
Material response test: Aluminum flyer impacting a 304 Stainless Steel target.

Performance Data

Areal Density	53.35	mg/cm^2	Predicted Vo:	31495	cm/sec
			Predicted Impulse:	4339	taps
$V_{incident}$	315	m/sec	Measured Impulse:	4145	taps
$V_{rebound}$	170	m/sec	Calculated Vo:	30088	cm/sec
Rebound Factor	1.54		% Measured of Predicted:	95.5%	

Ballistic Pendulum Parameters

Pendulum Mass	5085 (11.2)	gm (lbm.)	Impact Area	14.06 (2.25)	cm^2 (in^2)
String length	9.875	in.			

Pressure Data

Hugoniot Pressure:	34.1	kbar
Hydrocode Pressure:	31.9	kbar
Carbon Gage:	No Used	

Notes

Microhardness Testing

Station	1	2	3	4	5	6	7	8	9	10	Avg.
Standard	151	161	180	172	173	182	172	171	174	182	171.8
23-A	203	200	198	201	200	198	198	200	202	201	200.1
%	134.4	124.2	110.0	116.9	115.6	108.8	115.1	117.0	116.1	110.4	116.9

Macrohardness Testing

Scale		Rockwell B	HRB
	Standard	**Sample A (23)**	
Test	**Unshocked**	**Shocked**	**Unshocked**
1	78.05	86.82	76.12
2	78.27	84.31	77.77
3	79.13	85.70	77.66
4	78.64	88.44	78.04
5	78.24	86.66	79.23
6	78.66	87.51	
7	78.90	87.00	
8	78.78	84.71	
9	79.07	84.80	
10	78.96	86.76	
Average:	78.67	86.27	77.76
% of Standard:		109.7%	98.8%
% of Unshocked:		110.9%	

Notes

Test ID:	TP-2005-10	Target Material:	316 Stainless Steel	Date:	9/29/2004
Sample ID:	B	Flyer Material:	Aluminum 1100		

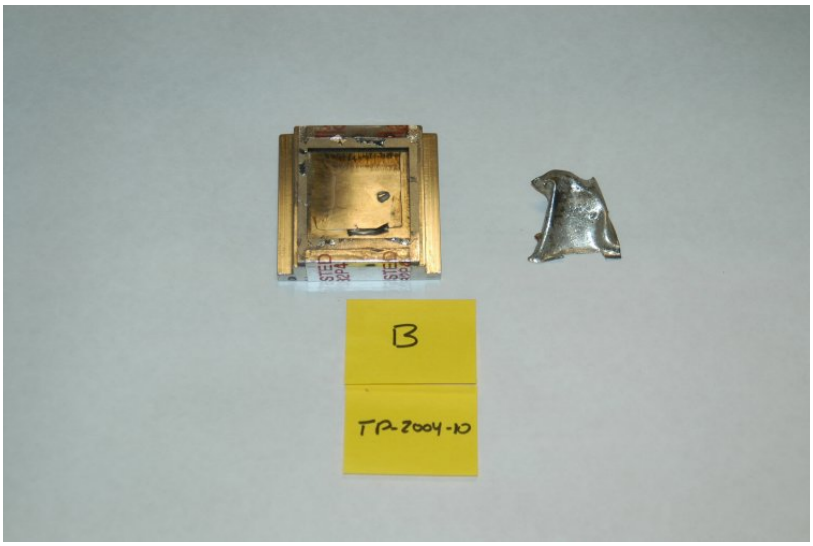

Test TP-2004-10 Sample B

Test Purpose

Material response test: Aluminum flyer impacting a 316 Stainless Steel target.

Performance Data

Areal Density	53.35	mg/cm^2	Predicted Vo:	31495	cm/sec
			Predicted Impulse:	4339	taps
$V_{incident}$	315	m/sec	Measured Impulse:	4064	taps
$V_{rebound}$	170	m/sec	Calculated Vo:	29495	cm/sec
Rebound Factor	1.54		% Measured of Predicted:	93.7%	

Ballistic Pendulum Parameters

Pendulum Mass	5085 (11.2)	gm (lbm.)	Impact Area	14.06 (2.25)	cm^2 (in^2)
String length	9.875	in.			

Pressure Data

Hugoniot Pressure:	34.1	kbar
Hydrocode Pressure:	31.9	kbar
Carbon Gage:	No Used	

Notes

Small welded portion of flyer left on target. The measured impulse was lower than expected. The resulting calculated flyer velocity was also low.

Microhardness Testing

Station	1	2	3	4	5	6	7	8	9	10	Avg.
Standard	185	182	181	184	185	185	186	184	184	184	184
24-B	167	167	166	166	165	164	165	165	166	165	165.6
%	90.3	91.8	91.7	90.2	89.2	88.6	88.7	89.7	90.2	89.7	90.0

Macrohardness Testing

Scale		Rockwell B	HRB
	Standard	**Sample 24 (B)**	
Test	**Unshocked**	**Shocked**	**Unshocked**
1	76.48	81.44	77.22
2	77.27	82.54	77.37
3	76.90	81.72	76.78
4	77.04	83.26	77.06
5	77.06	81.98	77.32
6	76.87	81.38	77.54
7	77.08	82.52	77.58
8	77.22	81.85	77.77
9	76.91	82.36	77.35
10		82.88	77.58
Average:	76.98	82.19	77.36
% of Standard:		106.8%	100.5%
% of Unshocked:		106.3%	

Notes

Test ID: TP-2005-10 Target Material: TYPE Nickel Date: 9/29/2004
Sample ID: C Flyer Material: Aluminum 1100

Test TP-2004-10 Sample C

Test Purpose

Material response test: Aluminum flyer impacting a nickel 200 target.

Performance Data

Areal Density	53.35	mg/cm^2	Predicted Vo:	31495	cm/sec
			Predicted Impulse:	4447	taps
$V_{incident}$	315	m/sec	Measured Impulse:	4422	taps
$V_{rebound}$	182	m/sec	Calculated Vo:	31322	cm/sec
Rebound Factor	1.58		% Measured of Predicted:	99.5%	

Ballistic Pendulum Parameters

Pendulum Mass	5085 (11.2)	gm (lbm.)	Impact Area	14.06 (2.25)	cm^2 (in^2)
String length	9.875	in.			

Pressure Data

Hugoniot Pressure:	35.3	kbar
Hydrocode Pressure:	32.2	kbar
Carbon Gage:	No Used	

Notes

Microhardness Testing

Station	1	2	3	4	5	6	7	8	9	10	Avg.
Standard	153	151	151	147	147	151	152	152	149	150	150.3
25-C	150	151	150	152	151	150	151	152	150	151	150.8
%	98.0	100.0	99.3	103.4	102.7	99.3	99.3	100.0	100.7	100.7	100.4

Macrohardness Testing

Scale		Rockwell B	HRB
	Standard	**Sample 25 (C)**	
Test	**Unshocked**	**Shocked**	**Unshocked**
1	48.23	60.73	47.04
2	48.55	61.94	46.85
3	48.59	61.52	46.50
4	49.63	61.89	48.25
5	49.39	60.84	47.64
6	49.30	58.75	
7	49.26	61.17	
8	48.86	61.38	
9	49.92	61.42	
10	48.90	62.04	
Average:	49.06	61.17	47.26
% of Standard:		124.7%	96.3%
% of Unshocked:		129.4%	

Notes

Test ID: TP-2005-10 Target Material: 304 Stainless Steel Date: 9/29/2004
Sample ID: D Flyer Material: Aluminum 1100

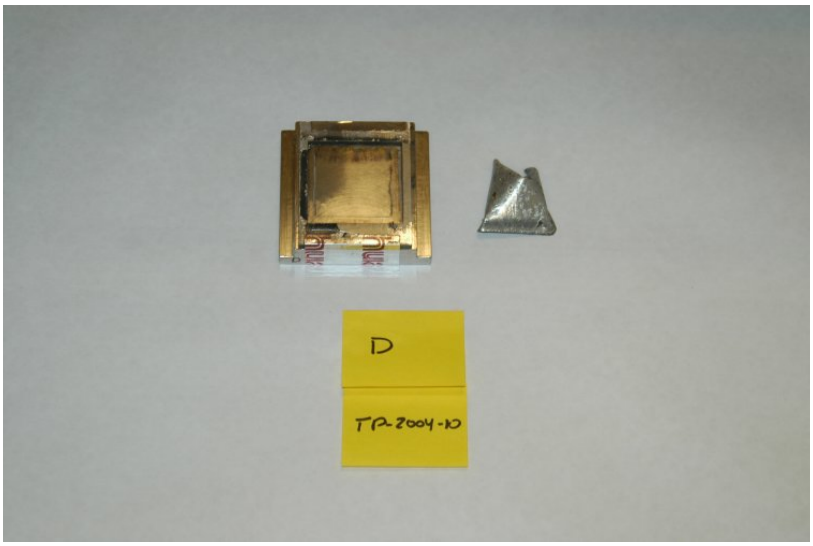

Test TP-2004-10 Sample D

Test Purpose
Material response test: Aluminum flyer impacting a 304 Stainless Steel target.

Performance Data

Areal Density	44.5	mg/cm^2	Predicted Vo:	26543	cm/sec
			Predicted Impulse:	3755	taps
$V_{incident}$	265	m/sec	Measured Impulse:	3756	taps
$V_{rebound}$	154	m/sec	Calculated Vo:	26547	cm/sec
Rebound Factor	1.58		% Measured of Predicted:	100.0%	

Ballistic Pendulum Parameters

Pendulum Mass	5085 (11.2)	gm (lbm.)	Impact Area	14.06 (2.25)	cm^2 (in^2)
String length	9.875	in.			

Pressure Data

Hugoniot Pressure:	28.5	kbar
Hydrocode Pressure:	25.9	kbar
Carbon Gage:	No Used	

Notes

Microhardness Testing

Station	1	2	3	4	5	6	7	8	9	10	Avg.
Standard	151	161	180	172	173	182	172	171	174	182	171.8
26-D	210	200	208	202	205	206	210	208	208	203	206
%	139.1	124.2	115.6	117.4	118.5	113.2	122.1	121.6	119.5	111.5	120.3

Macrohardness Testing

Scale		Rockwell B	HRB
	Standard	**Sample 26 (D)**	
Test	**Unshocked**	**Shocked**	**Unshocked**
1	78.05	83.03	77.44
2	78.27	83.03	78.30
3	79.13	83.03	78.16
4	78.64	83.03	78.27
5	78.24	83.03	78.87
6	78.66	83.03	
7	78.90	83.03	
8	78.78	84.86	
9	79.07	83.58	
10	78.96	83.86	
Average:	78.67	83.35	78.21
% of Standard:		106.0%	99.4%
% of Unshocked:		106.6%	

Notes

Test ID: TP-2005-10 Target Material: 316 Stainless Steel Date: 9/29/2004
Sample ID: E Flyer Material: Aluminum 1100

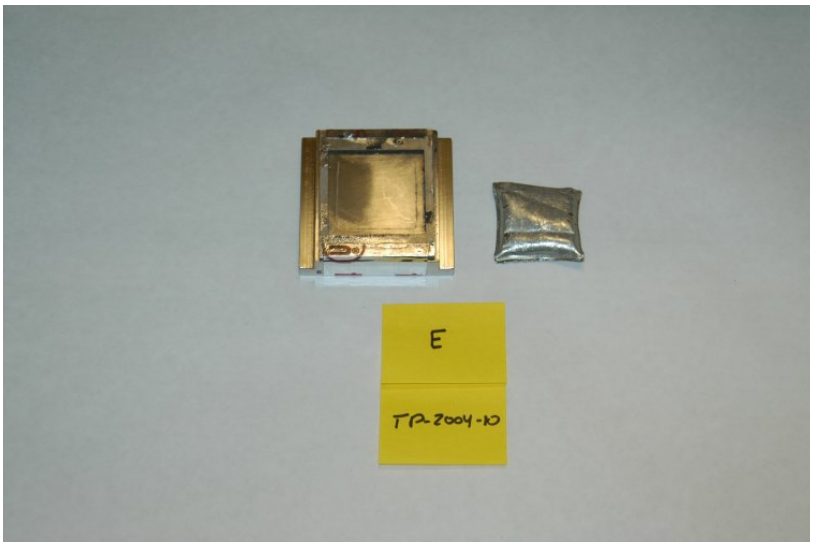

Test TP-2004-10 Sample E

Test Purpose

Material response test: Aluminum flyer impacting a 316 Stainless Steel target.

Performance Data

Areal Density	44.5	mg/cm^2	Predicted Vo:	26543	cm/sec
			Predicted Impulse:	3755	taps
$V_{incident}$	265	m/sec	Measured Impulse:	3105	taps
$V_{rebound}$	154	m/sec	Calculated Vo:	21945	cm/sec
Rebound Factor	1.58		% Measured of Predicted:	82.7%	

Ballistic Pendulum Parameters

Pendulum Mass	5085 (11.2)	gm (lbm.)	Impact Area	14.06 (2.25)	cm^2 (in^2)
String length	9.875	in.			

Pressure Data

Hugoniot Pressure:	28.5	kbar
Hydrocode Pressure:	25.9	kbar
Carbon Gage:	No Used	

Notes

Microhardness Testing

Station	1	2	3	4	5	6	7	8	9	10	Avg.
Standard	185	182	181	184	185	185	186	184	184	184	184
27-E	173	177	176	178	177	182	185	187	197	198	183
%	93.5	97.3	97.2	96.7	95.7	98.4	99.5	101.6	107.1	107.6	99.5

Macrohardness Testing

Scale		Rockwell B	HRB
	Standard	**Sample 27 (E)**	
Test	**Unshocked**	**Shocked**	**Unshocked**
1	76.48	80.36	76.43
2	77.27	80.63	75.65
3	76.90	80.67	76.45
4	77.04	80.89	76.53
5	77.06	81.28	76.41
6	76.87	82.31	76.23
7	77.08	83.13	76.72
8	77.22	81.83	
9	76.91	81.50	
10		81.64	
Average:	76.98	81.42	76.35
% of Standard:		105.8%	99.2%
% of Unshocked:		106.7%	

Notes

Test ID: TP-2005-10 Target Material: Nickel Date: 9/29/2004
Sample ID: F Flyer Material: Aluminum 1100

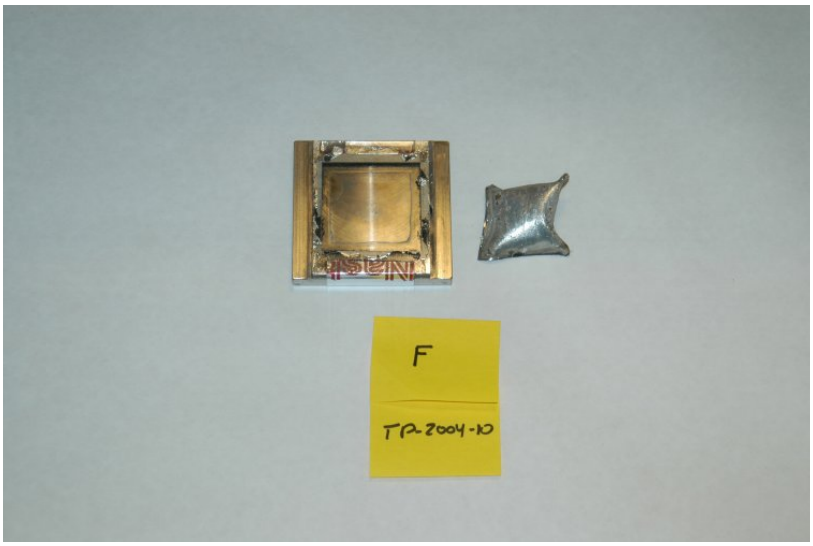

Test TP-2004-10 Sample F

Test Purpose

Material response test: Aluminum flyer impacting a nickel 200 target.

Performance Data

Areal Density	44.5	mg/cm^2	Predicted Vo:	26543	cm/sec
			Predicted Impulse:	3836	taps
$V_{incident}$	265	m/sec			
$V_{rebound}$	163	m/sec	Measured Impulse:	3332	taps
Rebound Factor	1.62		Calculated Vo:	23053	cm/sec
			% Measured of Predicted:	86.9%	

Ballistic Pendulum Parameters

Pendulum Mass	5085 (11.2)	gm (lbm.)	Impact Area	14.06 (2.25)	cm^2 (in^2)
String length	9.875	in.			

Pressure Data

Hugoniot Pressure:	29.5	kbar
Hydrocode Pressure:	25.8	kbar
Carbon Gage:	No Used	

Notes

Microhardness Testing

Station	1	2	3	4	5	6	7	8	9	10	Avg.
Standard	153	151	151	147	147	151	152	152	149	150	150.3
28-F	137	142	142	138	139	140	143	142	141	140	140.4
%	89.5	94.0	94.0	93.9	94.6	92.7	94.1	93.4	94.6	93.3	93.4

Macrohardness Testing

Scale		Rockwell B	HRB
	Standard	**Sample 28 (F)**	
Test	**Unshocked**	**Shocked**	**Unshocked**
1	48.23	59.05	45.88
2	48.55	60.33	45.55
3	48.59	59.65	47.70
4	49.63	59.90	45.88
5	49.39	59.79	46.98
6	49.30	60.13	
7	49.26	60.05	
8	48.86	60.61	
9	49.92	61.45	
10	48.90	60.89	
Average:	49.06	60.19	46.40
% of Standard:		122.7%	94.6%
% of Unshocked:		129.7%	

Notes

Test ID: TP-2005-12 Target Material: C110 Copper Date: 10/29/2004
Sample ID: A Flyer Material: Aluminum 1100

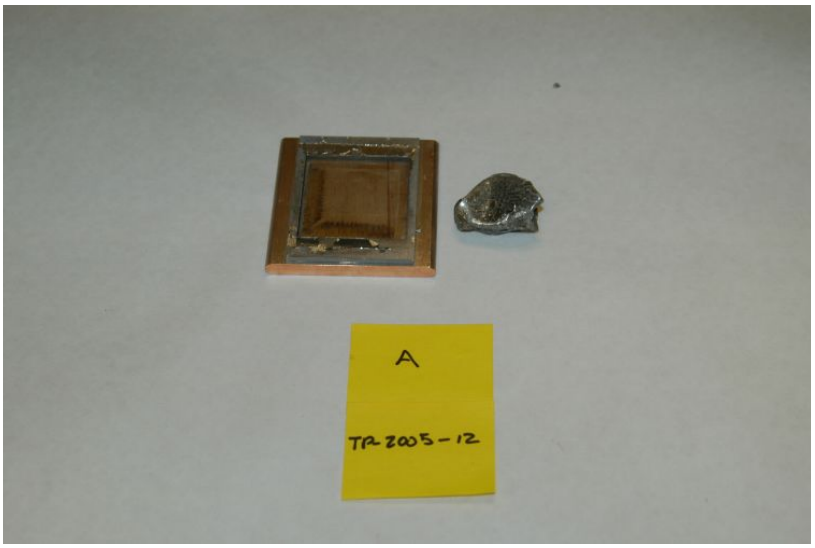

Test TP-2004-12 Sample A

Test Purpose
Material response test: Aluminum flyer impacting a C110 Copper target.

Performance Data

Areal Density	35.3	mg/cm^2	Predicted Vo:	21094	cm/sec
			Predicted Impulse:	3086	taps
$V_{incident}$	211	m/sec	Measured Impulse:	3059	taps
$V_{rebound}$	134	m/sec	Calculated Vo:	20907	cm/sec
Rebound Factor	1.64		% Measured of Predicted:	99.1%	

Ballistic Pendulum Parameters

Pendulum Mass	5085 (11.2)	gm (lbm.)	Impact Area	14.06 (2.25)	cm^2 (in^2)
String length	9.875	in.			

Pressure Data

Hugoniot Pressure:	22.3	kbar
Hydrocode Pressure:	20.1	kbar
Carbon Gage:	No Used	

Notes

Microhardness Testing

Station	1	2	3	4	5	6	7	8	9	10	Avg.
Standard	84.8	83.5	84.4	84.3	84.3	83.5	83.5	83.1	83.1	83	83.75
29-A	77.5	77.1	77.9	77.9	77.1	77.9	77.8	77.5	77.8	77.5	77.6
%	91.4	92.3	92.3	92.4	91.5	93.3	93.2	93.3	93.6	93.4	92.7

Macrohardness Testing

Scale		Rockwell F	HRF
	Standard	**Sample 29 (A)**	
Test	**Unshocked**	**Shocked**	**Unshocked**
1	32.68	54.01	27.56
2	33.89	54.11	28.19
3	34.89	54.48	29.61
4	35.22	52.78	32.91
5	33.76	54.36	30.49
6	33.52	53.98	
7	33.08	54.98	
8	33.42	55.75	
9	32.83	55.04	
10	35.22	57.72	
Average:	33.85	54.72	29.75
% of Standard:		161.7%	87.9%
% of Unshocked:		183.9%	

Notes

Test ID: TP-2005-12 Target Material: C110 Copper Date: 10/29/2004
Sample ID: B Flyer Material: Aluminum 1100

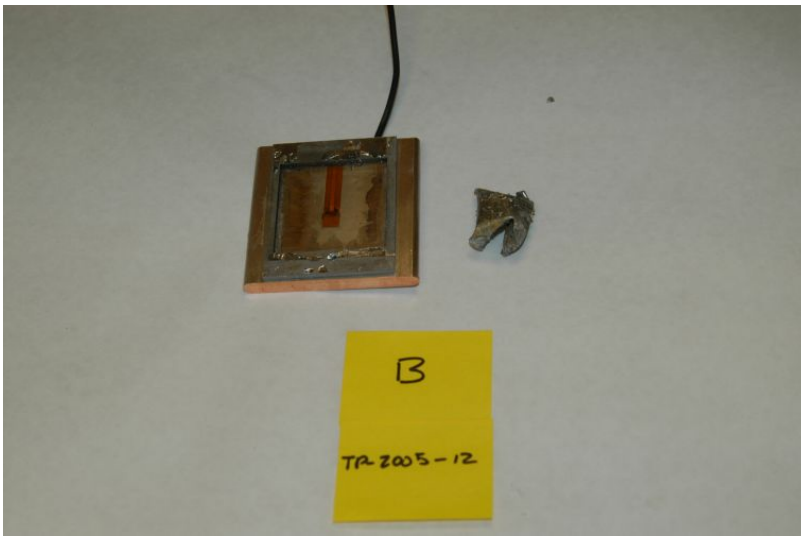

Test TP-2004-12 Sample B

Test Purpose

Impact pressure and impulse delivered test: Aluminum flyer impacting a C110 Copper target.

Performance Data

Areal Density	35.3	mg/cm^2	Predicted Vo:	21094	cm/sec
			Predicted Impulse:	3086	taps
$V_{incident}$	211	m/sec	Measured Impulse:	3128	taps
$V_{rebound}$	134	m/sec	Calculated Vo:	21380	cm/sec
Rebound Factor	1.64		% Measured of Predicted:	101.4%	

Ballistic Pendulum Parameters

Pendulum Mass	5085 (11.2)	gm (lbm.)	Impact Area	14.06 (2.25)	cm^2 (in^2)
String length	9.875	in.			

Notes

Sample ID: TP-2004-12 B Date: 10/29/2004

Pressure Data

Hugoniot Pressure:	22.3	kbar	Carbon Gage Constants		
Hydrocode Pressure:	20.1	kbar	Gage Resistance:	47.5	Ω
			Excitation Voltage:	45.0	volts
Carbon Gage			Line Resistance:	0.271	Ω
Peak Pressure:	22.6	kbar	Term Resistance:	74.76	Ω
Pulse Duration:	0.60	μs			

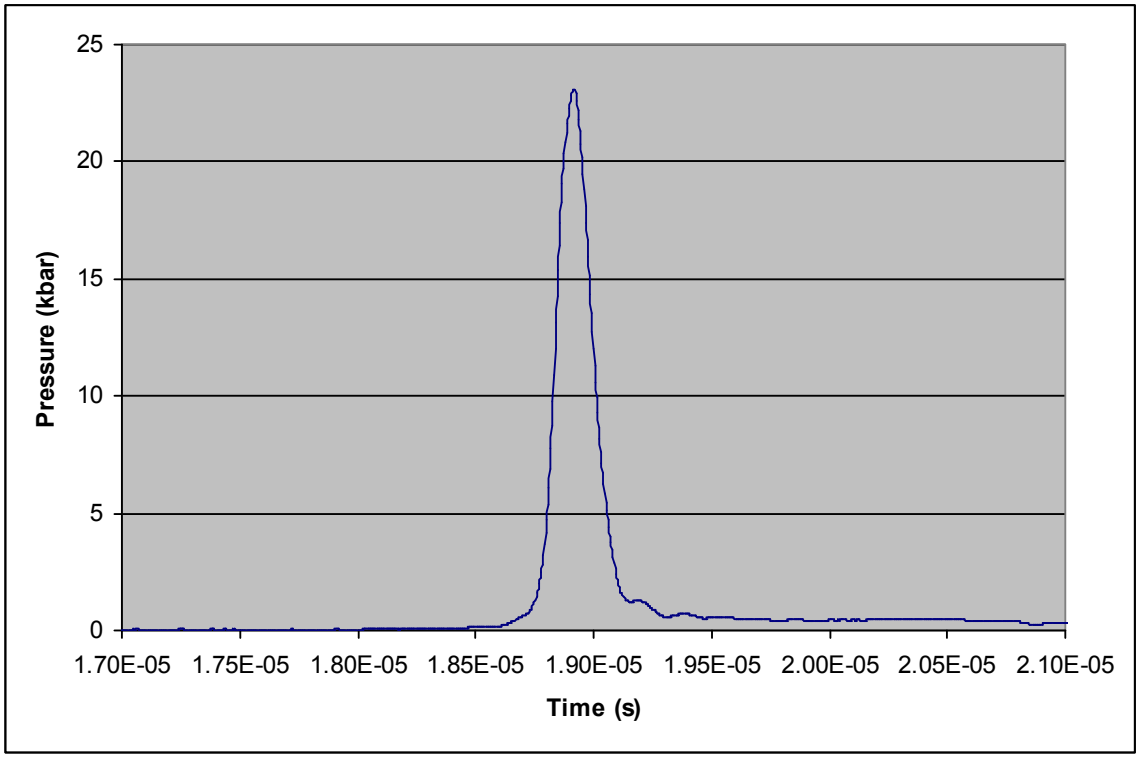

TP-2004-12 Sample B Pressure

Notes

Test ID: TP-2005-12 Target Material: C110 Copper Date: 10/29/2004
Sample ID: C Flyer Material: Aluminum 1100

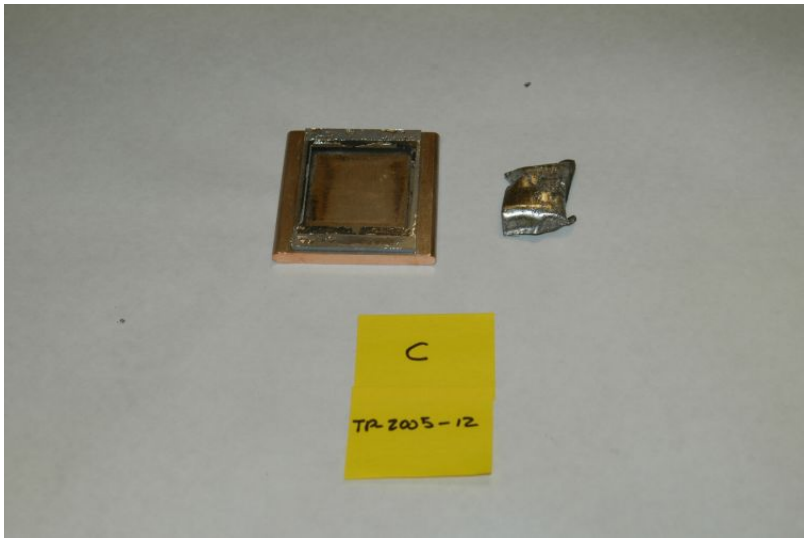

Test TP-2004-12 Sample C

Test Purpose
Material response test: Aluminum flyer impacting a C110 Copper target.

Performance Data

Areal Density	35.3	mg/cm^2	Predicted Vo:	21094	cm/sec
			Predicted Impulse:	3086	taps
$V_{incident}$	211	m/sec	Measured Impulse:	2972	taps
$V_{rebound}$	134	m/sec	Calculated Vo:	20311	cm/sec
Rebound Factor	1.64		% Measured of Predicted:	96.3%	

Ballistic Pendulum Parameters

Pendulum Mass	5085 (11.2)	gm (lbm.)	Impact Area	14.06 (2.25)	cm^2 (in^2)
String length	9.875	in.			

Pressure Data

Hugoniot Pressure:	22.3	kbar
Hydrocode Pressure:	20.1	kbar
Carbon Gage:	No Used	

Notes

Microhardness Testing

Station	1	2	3	4	5	6	7	8	9	10	Avg.
Standard	84.8	83.5	84.4	84.3	84.3	83.5	83.5	83.1	83.1	83	83.75
31-C	85.2	85.2	84.3	85.2	85.2	85.2	84.8	84.8	85.2	85.3	85.04
%	100.5	102.0	99.9	101.1	101.1	102.0	101.6	102.0	102.5	102.8	101.5

Macrohardness Testing

Scale		Rockwell F	HRF
	Standard	**Sample 31 (C)**	
Test	**Unshocked**	**Shocked**	**Unshocked**
1	32.68	52.18	28.05
2	33.89	53.77	30.18
3	34.89	55.16	30.34
4	35.22	55.23	29.38
5	33.76	51.88	
6	33.52	51.94	
7	33.08	57.89	
8	33.42	55.18	
9	32.83	55.23	
10	35.22	52.74	
Average:	33.85	54.34	29.49
% of Standard:		160.5%	87.1%
% of Unshocked:		184.3%	

Notes

Test ID: TP-2005-12 Target Material: 1100 Aluminum Date: 10/29/2004
Sample ID: D Flyer Material: 1100Aluminum

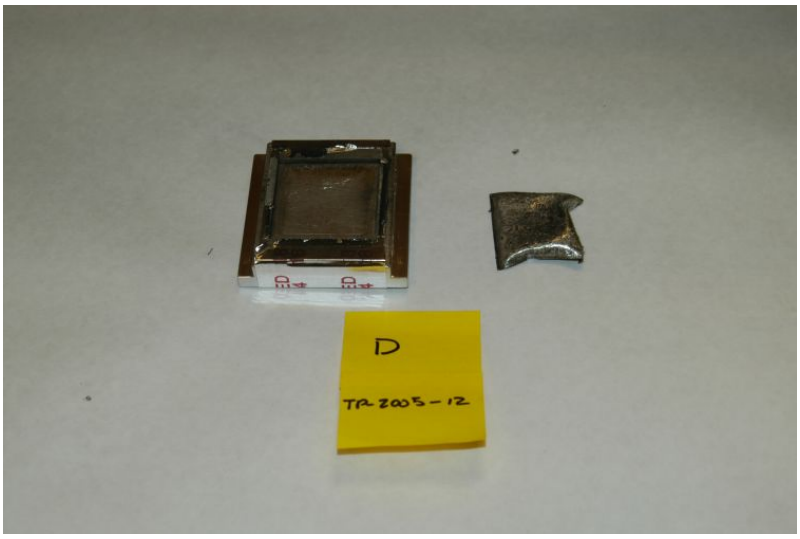

Test TP-2004-12 Sample D

Test Purpose
Material response test: Aluminum flyer impacting an 1100 aluminum target.

Performance Data

Areal Density	35.0	mg/cm^2	Predicted Vo:	20908	cm/sec
			Predicted Impulse:	2763	taps
$V_{incident}$	209	m/sec	Measured Impulse:	2798	taps
$V_{rebound}$	99.7	m/sec	Calculated Vo:	21170	cm/sec
Rebound Factor	1.48		% Measured of Predicted:	101.2%	

Ballistic Pendulum Parameters

Pendulum Mass	5085 (11.2)	gm (lbm.)	Impact Area	14.06 (2.25)	cm^2 (in^2)
String length	9.875	in.			

Pressure Data

Hugoniot Pressure:	15.5	kbar
Hydrocode Pressure:	13.6	kbar
Carbon Gage:	No Used	

Microhardness Testing

Station	1	2	3	4	5	6	7	8	9	10	Avg.
Standard	41.1	39.6	40.5	41.7	40.1	40	40.7	40.8	41	40.1	40.56
32-D	45.2	45.6	45.4	44.7	44.5	45.1	45.2	45.2	43.9	45.2	45
%	110	115	112	107	111	113	111	111	107	113	111

Macrohardness Testing

Scale		Rockwell E	HRE
	Standard	**Sample 32 (D)**	
Test	**Unshocked**	**Shocked**	**Unshocked**
1	30.92	35.95	33.59
2	31.90	36.05	33.85
3	32.16	36.29	33.63
4	31.53	37.12	33.17
5	31.82	36.97	32.93
6	31.94	36.64	31.73
7	32.02	38.04	33.63
8	31.79	38.04	33.89
9	31.81	38.37	33.49
10	32.38	37.61	
Average:	31.83	37.11	33.32
% of Standard:		116.6%	104.7%
% of Unshocked:		111.4%	

Notes

Test ID: TP-2005-12 Target Material: 6061 Aluminum Date: 10/29/2004
Sample ID: E Flyer Material: 1100Aluminum

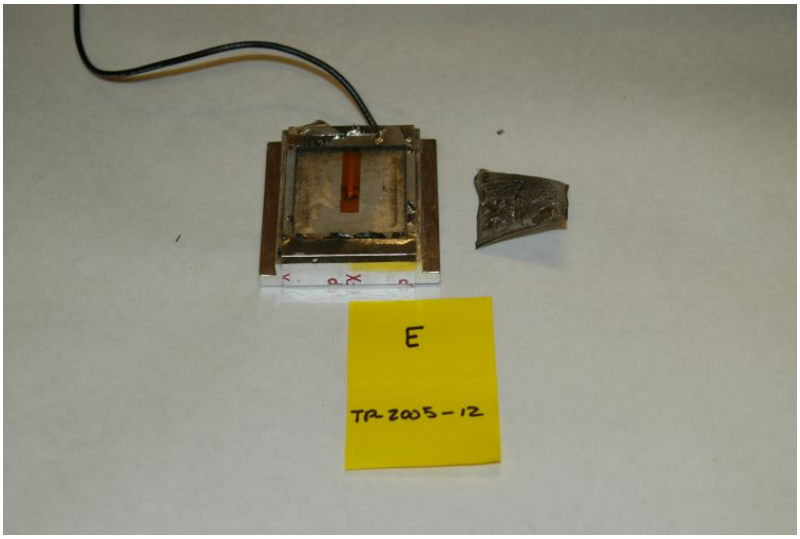

Test TP-2004-12 Sample E

Test Purpose

Impact pressure and impulse delivered test: Aluminum flyer impacting an 6061 aluminum target.

Performance Data

Areal Density	35.0	mg/cm^2	Predicted Vo:	20908	cm/sec
			Predicted Impulse:	2763	taps
$V_{incident}$	209	m/sec	Measured Impulse:	2645	taps
$V_{rebound}$	99.7	m/sec	Calculated Vo:	20008	cm/sec
Rebound Factor	1.48		% Measured of Predicted:	95.7%	

Ballistic Pendulum Parameters

Pendulum Mass	5085 (11.2)	gm (lbm.)	Impact Area	14.06 (2.25)	cm^2 (in^2)
String length	9.875	in.			

Notes

Sample ID: TP-2004-12 E Date: 10/29/2004

Pressure Data

Hugoniot Pressure:	15.5	kbar	Carbon Gage Constants		
Hydrocode Pressure:	13.6	kbar	Gage Resistance:	48.3	Ω
			Excitation Voltage:	45.0	volts
Carbon Gage			Line Resistance:	0.271	Ω
Peak Pressure:	14.6	kbar	Term Resistance:	74.76	Ω
Pulse Duration:	0.60	μs			

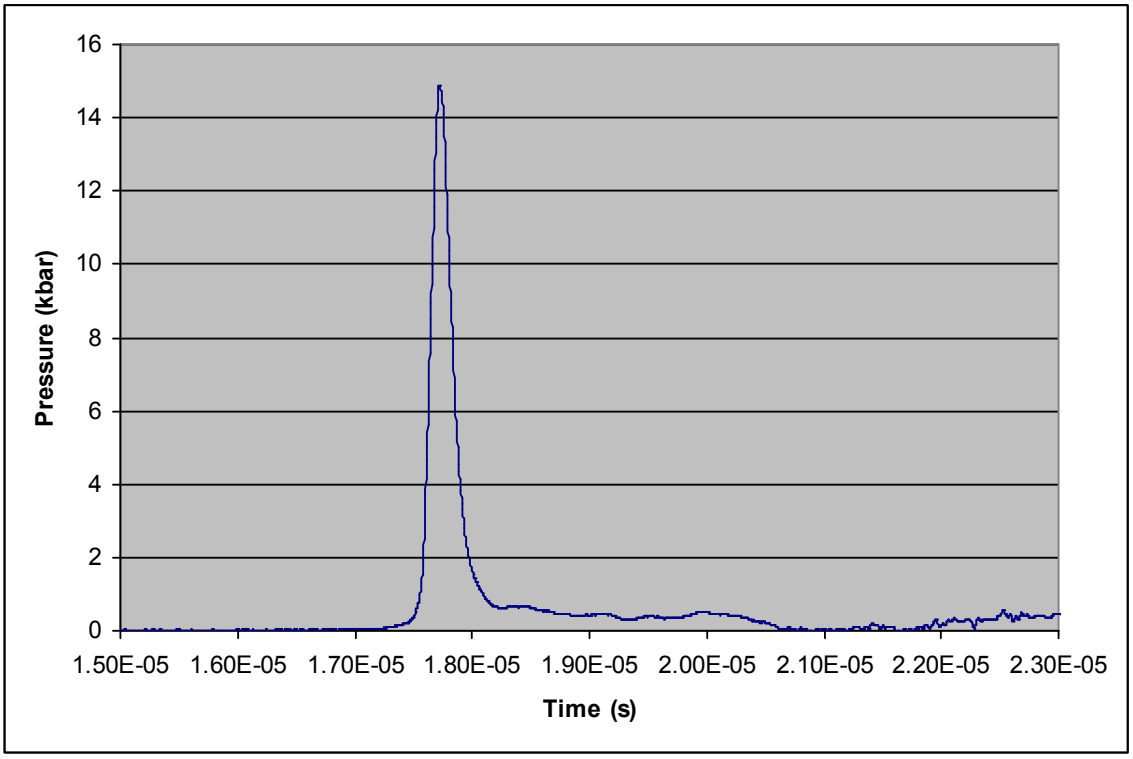

TP-2004-12 Sample E Pressure

Notes

Test ID: TP-2005-12 Target Material: 1100 Aluminum Date: 10/29/2004
Sample ID: F Flyer Material: 1100Aluminum

Test TP-2004-12 Sample F

Test Purpose

Material response test: Aluminum flyer impacting an 1100 aluminum target.

Performance Data

Areal Density	35.0	mg/cm^2	Predicted Vo:	20908	cm/sec
			Predicted Impulse:	2763	taps
$V_{incident}$	209	m/sec	Measured Impulse:	2363	taps
$V_{rebound}$	99.7	m/sec	Calculated Vo:	17880	cm/sec
Rebound Factor	1.48		% Measured of Predicted:	85.5%	

Ballistic Pendulum Parameters

Pendulum Mass	5085 (11.2)	gm (lbm.)	Impact Area	14.06 (2.25)	cm^2 (in^2)
String length	9.875	in.			

Pressure Data

Hugoniot Pressure:	15.5	kbar
Hydrocode Pressure:	13.6	kbar
Carbon Gage:	No Used	

Notes

Microhardness Testing

Station	1	2	3	4	5	6	7	8	9	10	Avg.
Standard	41.1	39.6	40.5	41.7	40.1	40	40.7	40.8	41	40.1	40.56
34-F	44.1	44.9	44.9	44.7	44.6	44.4	43.6	44.9	44.2	44.2	44.45
%	107	113	111	107	111	111	107	110	108	110	110

Macrohardness Testing

Scale		Rockwell E	HRE
	Standard	**Sample 34 (F)**	
Test	**Unshocked**	**Shocked**	**Unshocked**
1	30.92	36.34	32.88
2	31.90	36.58	33.13
3	32.16	37.30	33.11
4	31.53	36.95	32.95
5	31.82	35.76	32.92
6	31.94	37.85	33.44
7	32.02	38.57	34.53
8	31.79	38.41	35.15
9	31.81	38.14	35.27
10	32.38	37.31	35.27
Average:	31.83	37.32	33.87
% of Standard:		117.3%	106.4%
% of Unshocked:		110.2%	

Notes

Test ID: TP-2005-12 Target Material: PMMA Date: 10/29/2004
Sample ID: G Flyer Material: 1100Aluminum

Test TP-2004-12 Sample G

Test Purpose
Material response test: Aluminum flyer impacting an PMMA target.

Performance Data

Areal Density	35.3	mg/cm^2	Predicted Vo:	21094	cm/sec
			Predicted Impulse:	2503	taps
$V_{incident}$	211	m/sec	Measured Impulse:	2662	taps
$V_{rebound}$	68.8	m/sec	Calculated Vo:	22436	cm/sec
Rebound Factor	1.33		% Measured of Predicted:	106.4%	

Ballistic Pendulum Parameters

Pendulum Mass	5085 (11.2)	gm (lbm.)	Impact Area	14.06 (2.25)	cm^2 (in^2)
String length	9.875	in.			

Pressure Data

Hugoniot Pressure:	5.69	kbar
Hydrocode Pressure:	3.54	kbar
Carbon Gage:	Not Recorded	

Notes
Carbon gage data was not recorded due to a problem with the pulse power supply (PPS). It seems that the PPS triggered early, thus not providing power to the gage in the time of interest.

Test ID: TP-2005-12 Target Material: 6061 Aluminum Date: 10/29/2004
Sample ID: H Flyer Material: 1100Aluminum

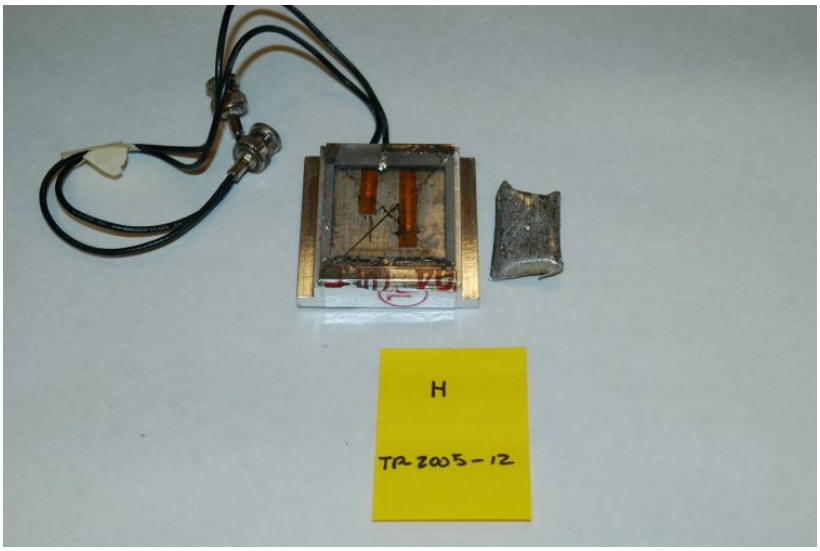

Test TP-2004-12 Sample H

Test Purpose

Impact pressure, impact simultaneity, and impulse delivered test: Aluminum flyer impacting a 6061 aluminum target.

Performance Data

Areal Density	35.3	mg/cm^2	Predicted Vo:	21094	cm/sec
			Predicted Impulse:	2782	taps
$V_{incident}$	211	m/sec			
$V_{rebound}$	100	m/sec	Measured Impulse:	2700	taps
Rebound Factor	1.47		Calculated Vo:	20468	cm/sec
			% Measured of Predicted:	97.0%	

Ballistic Pendulum Parameters

Pendulum Mass	5085 (11.2)	gm (lbm.)	Impact Area	14.06 (2.25)	cm^2 (in^2)
String length	9.875	in.			

Notes

Sample ID: TP-2004-12 H Date: 10/29/2004

Pressure Data

Hugoniot Pressure:	15.7	kbar
Hydrocode Pressure:	13.9	kbar

Carbon Gage

Peak Pressure:	15.0	16.1	kbar
Pulse Duration:	0.90	0.80	μs

Carbon Gage Constants	Gage 1	Gage 2	
Gage Resistance:	51.9	49.4	Ω
Excitation Voltage:	45.0	45.0	V
Line Resistance:	0.271	0.271	Ω
Term Resistance:	75.0	74.76	Ω

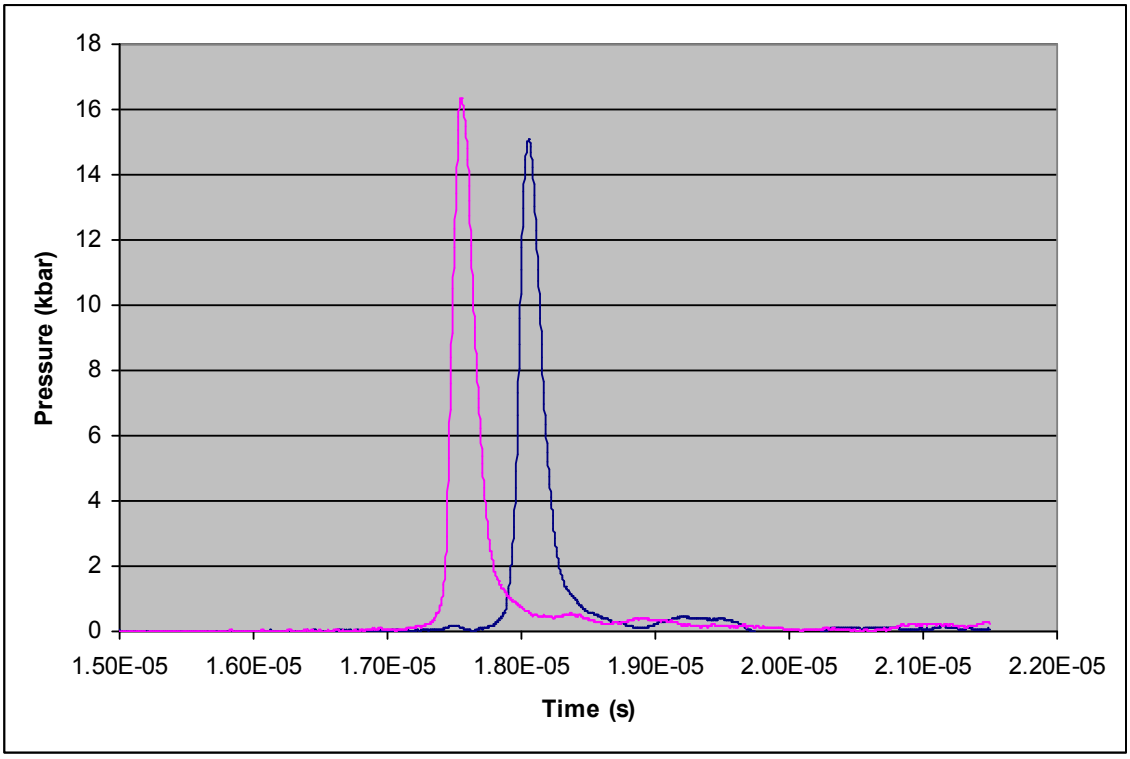

TP-2004-12 Sample H Pressure

Notes

15. APPENDIX C – TWO-DIMENSIONAL RING TESTS

- Simple Ring #1
- Composite Ring #2
- Simple Ring #3
- Simple Ring #4
- Simple Ring #5

Spray ID: TP-2005-14 Target Material: 6061 Aluminum Date: 2/3/2005
Sample ID: Ring #1 Flyer Material: 1100Aluminum

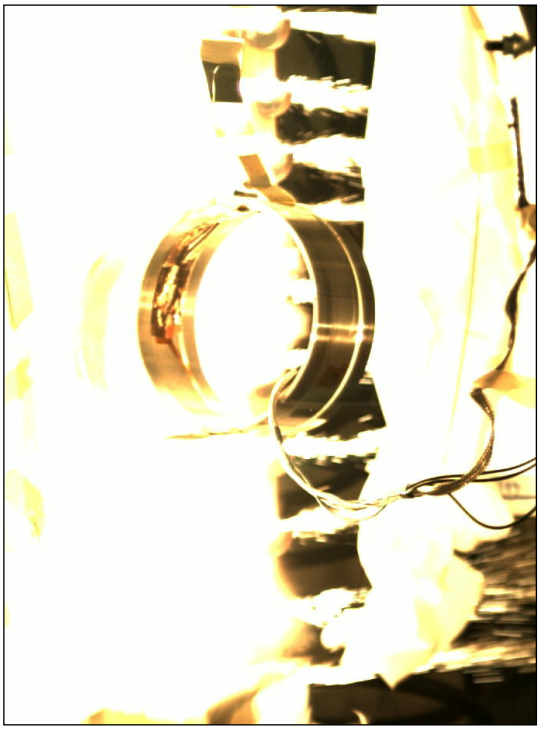

Ring #1 HS Video

Ring #1 Post-Test

Performance Data

Theta	75	60	45	30	15	0	-15	-30	-45	-60	-75
Gap (cm)	0.037	0.053	0.062	0.089	0.097	0.107	0.104	0.097	0.070	0.064	0.036
ρ_A (mg/cm^2)	12.1	19.64	24.1	27.54	29.65	30.91	29.89	27.82	24.66	18.56	10.04
Vel_{in} (cm/s)	5695	10109	12974	15154	16461	17230	16608	15329	13334	9439	4600
Vel_{out} (cm/s)	0.328	0.424	0.473	0.581	0.619	0.662	0.646	0.622	0.508	0.472	0.287
R_f	1.58	1.42	1.36	1.38	1.38	1.38	1.39	1.41	1.38	1.50	1.62
Transit (μs)	6.47	5.28	4.80	5.87	5.86	6.19	6.27	6.30	5.24	6.73	7.73
I_{sp} (taps)	**865**	**1383**	**1706**	**2020**	**2183**	**2298**	**2223**	**2077**	**1774**	**1365**	**720**

Notes

Sample ID: Ring #1 Date: 2/3/2005

X-Ray Rigid Body Motion

Exposure	Time (ms)
1	0.6
2	12.0
3	N/A

Ring Mass: 350 gm

Exposure	Delta t (ms)	Delta x (cm)	Vel. (cm/s)	Impulse (taps)
1-2	11.4	4.06	378.8	2180
1-3	N/A	N/A	N/A	N/A
2-3	N/A	N/A	N/A	N/A
		Average:	**378.8**	**2180**

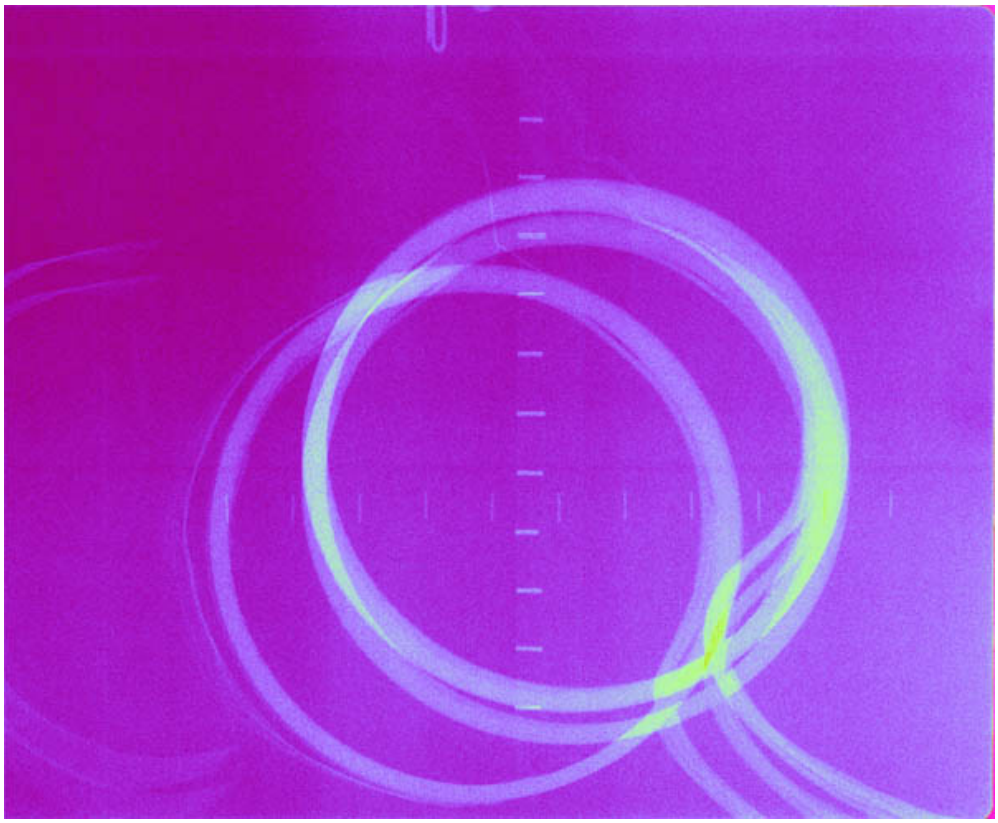

Ring #1 X-Ray Rigid Body Motion

Notes

X-ray head #3 pre-fired at 12.0 ms causing a double image at the second exposure time. No data recorded at exposure #3

No pressure gage data was recorded for this test due to a problem in triggering the pulse power supply (PPS) required for the carbon gage to function. Analysis of the problem, showed that the PPS was triggered earlier than expected. Because the PPS only delivers power to the gage for 100 μs, the impact event took place after the PPS had turned off. The solution is that the PPS must be triggered at the proper time.

Sample ID: Ring #1 Date: 2/3/2005

Ring Structural Strain Response

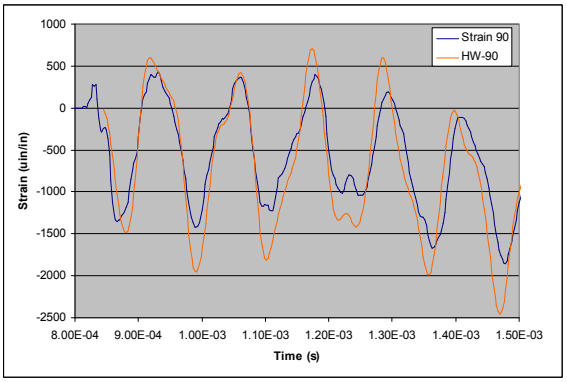

Ring #1 Early Time Strain 90º

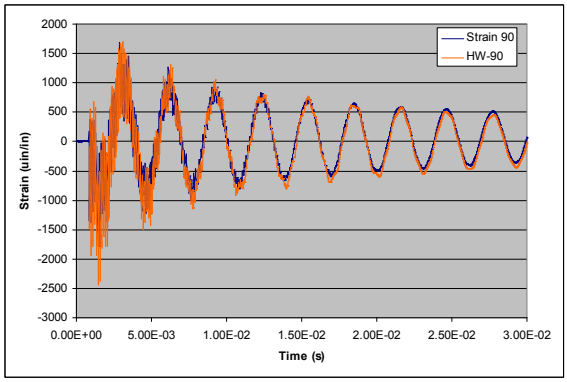

Ring #1 Late Time Strain 90º

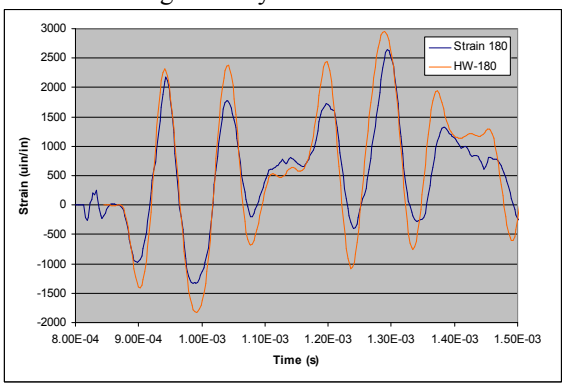

Ring #1 Early Time Strain 180º

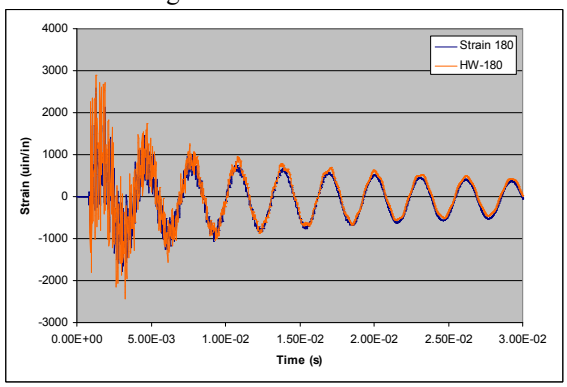

Ring #1 Late Time Strain 180º

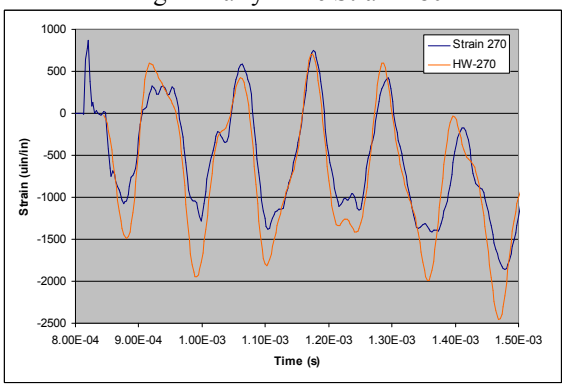

Ring #1 Early Time Strain 270º

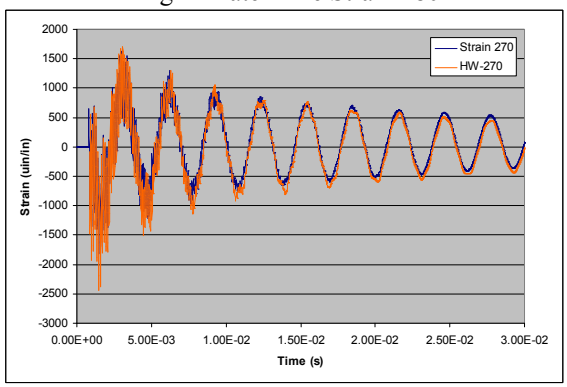

Ring #1 Late Time Strain 270º

Ring #1 Structural Strain Response

Calculated Peak I_{sp}: 2170 taps Measured Impulse: 2175 taps

Calculated Ring Vo: 378.8 cm/sec % of Sprayed Design: 103.3%

Notes

Spray ID: TP-2005-14 Target Material: Composite LEXAN® /Al Date: 2/3/2005
Sample ID: Ring #2 Flyer Material: 1100Aluminum

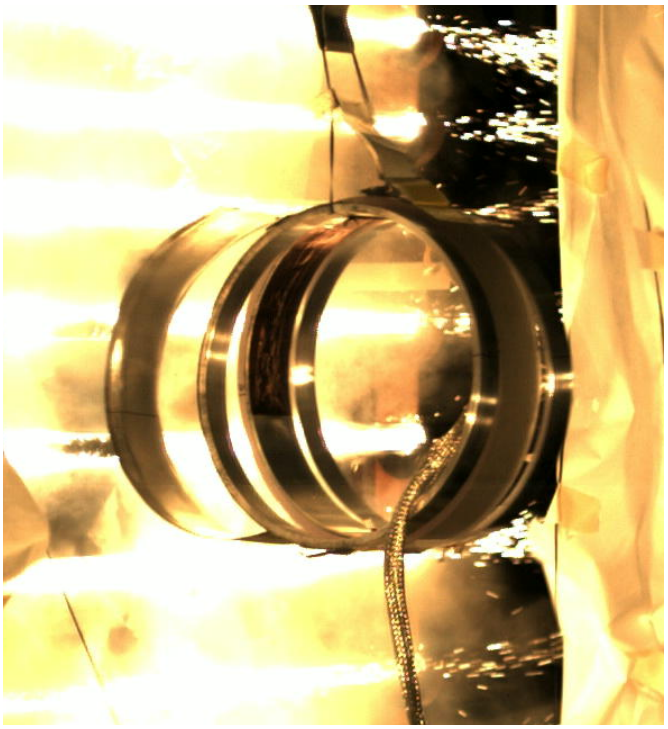

Ring #2 HS Video

Ring #2 Post-Test

Performance Data

Theta	75	60	45	30	15	0	-15	-30	-45	-60	-75
Gap (cm)	0.037	0.053	0.062	0.089	0.097	0.107	0.104	0.097	0.070	0.064	0.036
ρ_A (mg/cm^2)	12.1	19.64	24.1	27.54	29.65	30.91	29.89	27.82	24.66	18.56	10.04
Vel_{in} (cm/s)	5695	10109	12974	15154	16461	17230	16608	15329	13334	9439	4600
Vel_{out} (cm/s)	0.328	0.424	0.473	0.581	0.619	0.662	0.646	0.622	0.508	0.472	0.287
R_f	1.58	1.42	1.36	1.38	1.38	1.38	1.39	1.41	1.38	1.50	1.62
Transit (μs)	6.47	5.28	4.80	5.87	5.86	6.19	6.27	6.30	5.24	6.73	7.73
I_{sp} (taps)	**865**	**1383**	**1706**	**2020**	**2183**	**2298**	**2223**	**2077**	**1774**	**1365**	**720**

Notes

Sample ID: Ring #2 Date: 2/3/2005

X-Ray Rigid Body Motion

Exposure	Time (ms)
1	0.6
2	12.0
3	29.0
Ring Mass:	350 gm

Exposure	Delta t (ms)	Delta x (cm)	Vel. (cm/s)	Impulse (taps)
1-2	11.4	4.57	401.1	2012
1-3	28.4	9.53	335.4	1682
2-3	17.0	6.10	358.6	1799
		Average:	**365.0**	**1831**

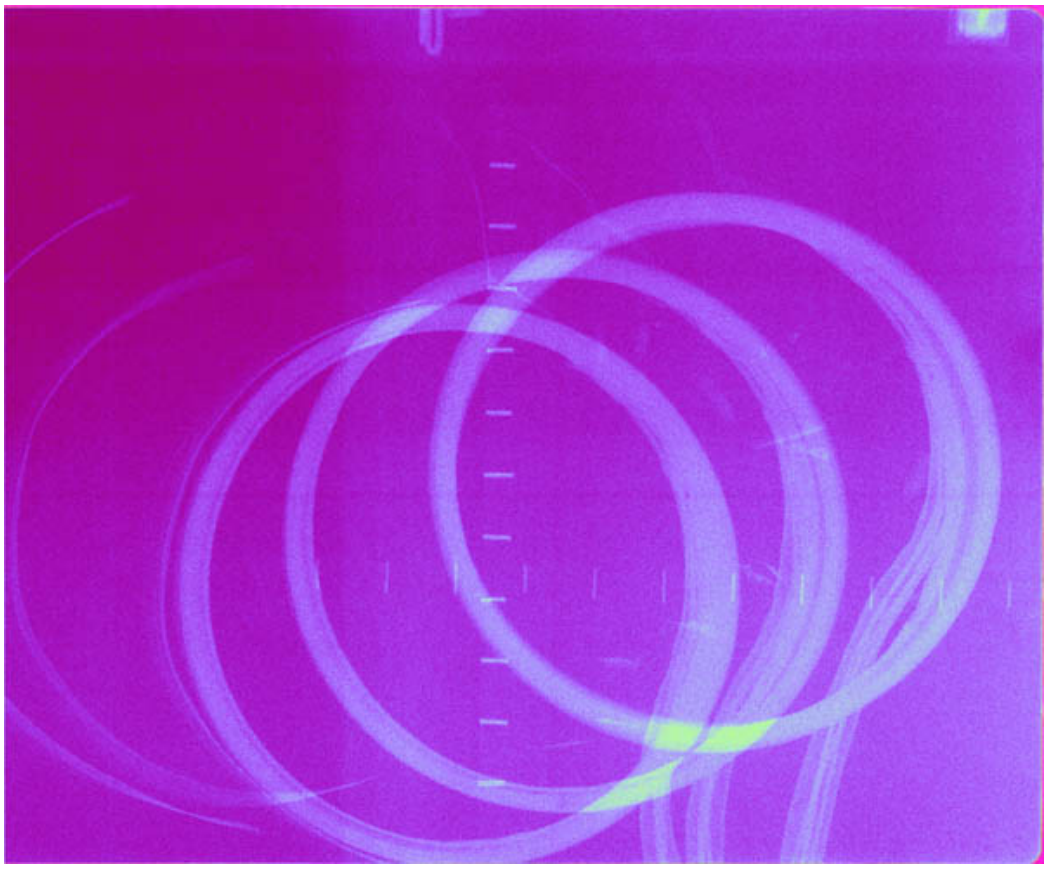

Ring #2 X-Ray Rigid Body Motion (Composite Ring)

Thin Film Carbon Pressure Gage

No carbon pressure gages were present on this test.

Notes

As has been seen before, the x-ray rigid body motion data seems to be consistently low in determining delivered impulse. No reason for this phenomenon has been determined.

Sample ID: Ring #2 Date: 2/3/2005

Ring Structural Strain Response

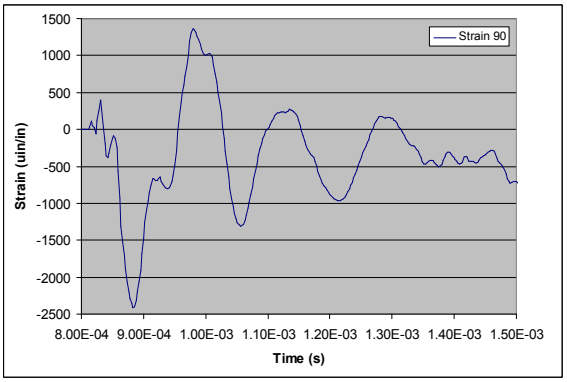

Ring #2 Early Time Strain 90º

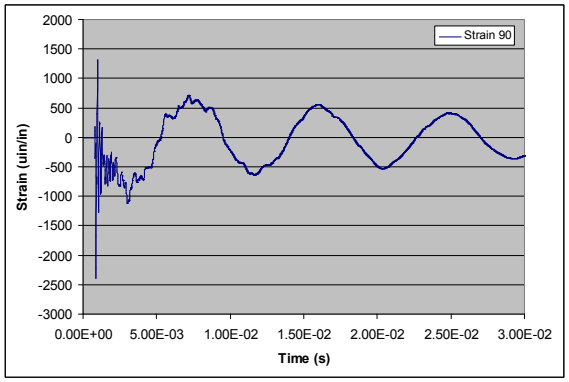

Ring #2 Late Time Strain 90º

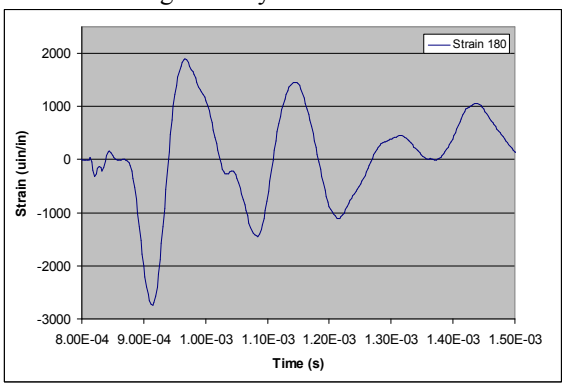

Ring #2 Early Time Strain 180º

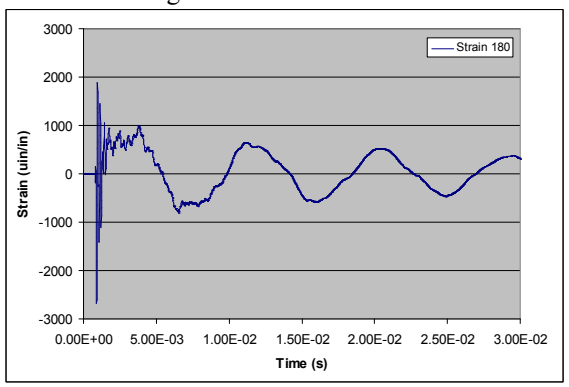

Ring #2 Late Time Strain 180º

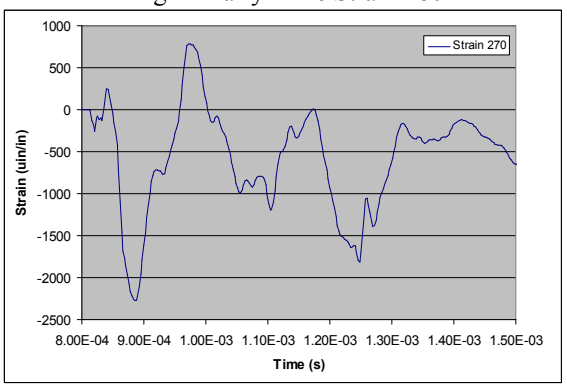

Ring #2 Early Time Strain 270º

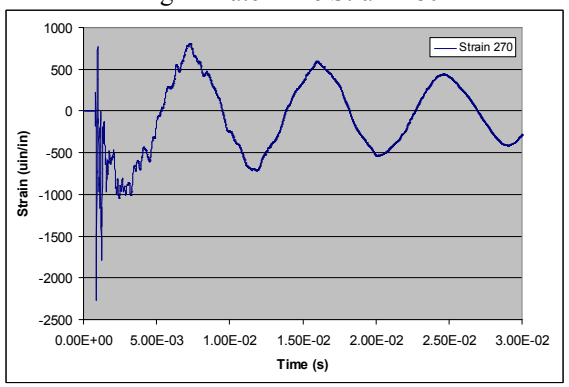

Ring #2 Late Time Strain 270º

Ring #2 Structural Strain Response

Calculated Peak I_{sp}: 2298 taps Measured Impulse: 2298 taps

Calculated Vo: 17,230 cm/sec % Difference: 0%

Notes

Spray ID: TP-2005-15 Target Material: 6061 Aluminum Date: 3/7/2005
Sample ID: Ring #3 Flyer Material: 1100Aluminum

No Video Image Available

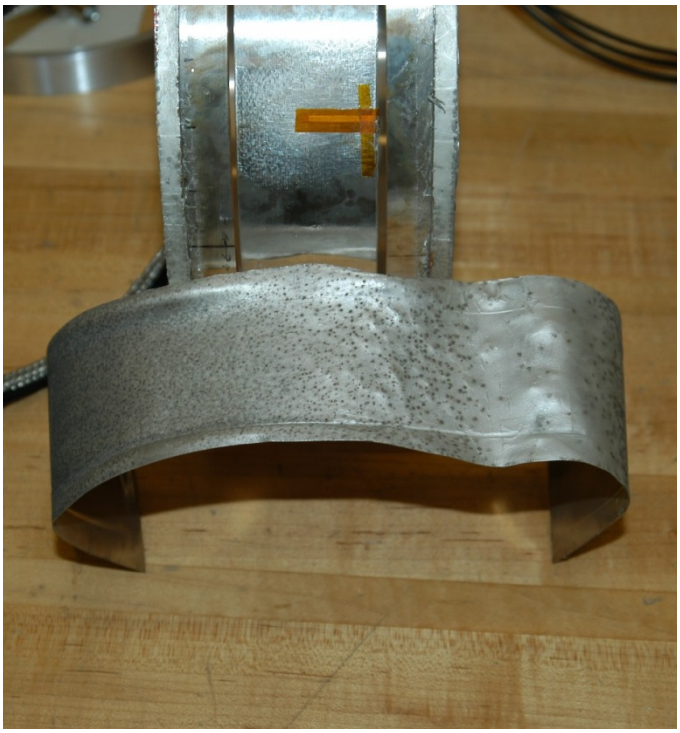

Ring #3 HS Video

Ring #3 Post-Test

Performance Data

Theta	**75**	**60**	**45**	**30**	**15**	**0**	**-15**	**-30**	**-45**	**-60**	**-75**
Gap (cm)	0.024	0.051	0.066	0.074	0.098	0.109	0.103	0.081	0.074	0.064	0.027
ρ_A (mg/cm^2)	10.56	18.31	24.07	28.14	30.1	31.3	30.21	28.34	24.77	17.96	10.24
Vel_{in} (cm/s)	4872	9286	12955	15528	16737	17467	16804	15652	13404	9072	4704
Vel_{out} (cm/s)	2550	4130	4940	5320	6260	6720	6470	5590	5240	4700	2670
R_f	1.52	1.44	1.38	1.34	1.37	1.38	1.39	1.36	1.39	1.52	1.57
Transit (μs)	4.95	5.47	5.10	4.74	5.84	6.25	6.12	5.19	5.50	7.00	5.67
I_{sp} (taps)	**715**	**1293**	**1725**	**2009**	**2216**	**2330**	**2243**	**2047**	**1797**	**1327**	**711**

Notes

Sample ID: Ring #3 Date: 3/7/2005

X-Ray Rigid Body Motion

Exposure	Time (ms)
1	0.6
2	12.0
3	29.0

Ring Mass: 350 gm

Exposure	Delta t (ms)	Delta x (cm)	Vel. (cm/s)	Impulse (taps)
1-2	11.4	3.94	345.4	1988
1-3	28.4	10.16	357.7	2059
2-3	17.0	6.22	366.1	2107
		Average:	**356.4**	**2051**

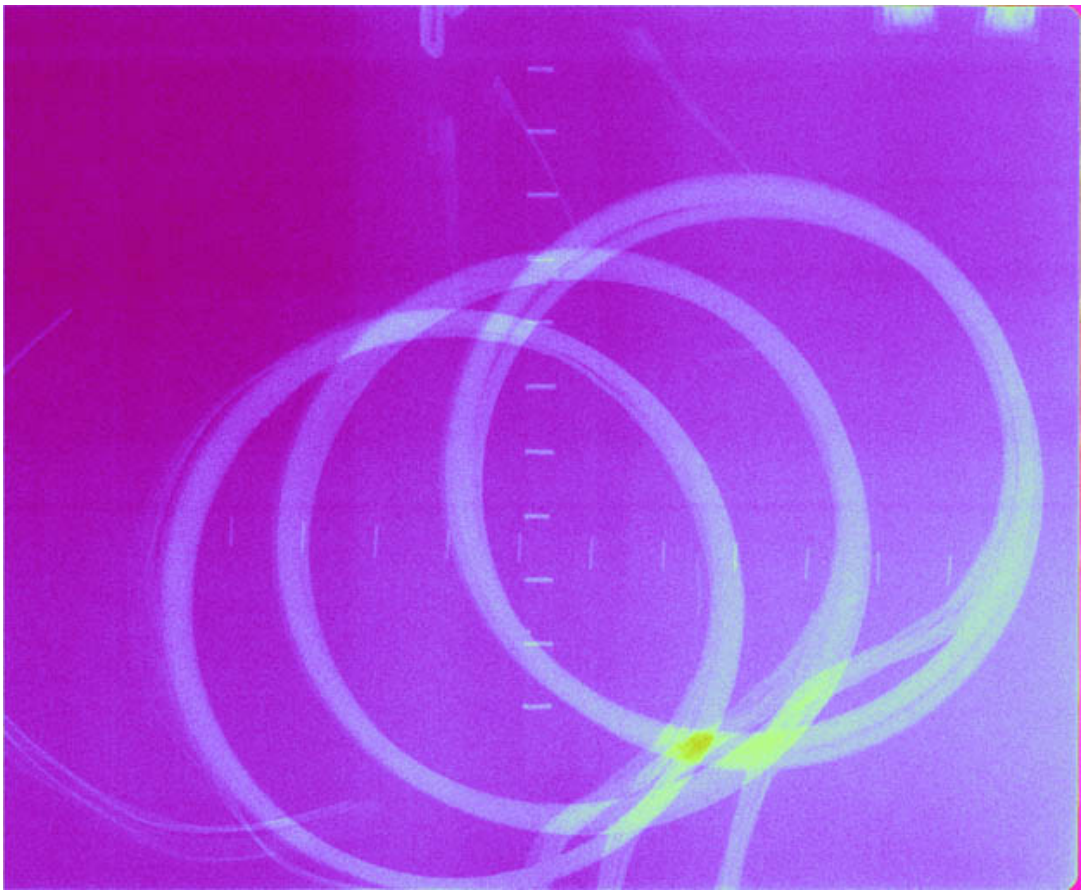

Ring #3 X-Ray Rigid Body Motion

Notes

Sample ID: Ring #3 Date: 3/7/2005

Thin Film Carbon Pressure Gage

Position	**-30º**		**0º**		**+30º**	
Peak Pressure	3.7	kbar	8.33	kbar	1.39	kbar
Pulse Duration	1.17	µs	0.75	µs	2.18	µs

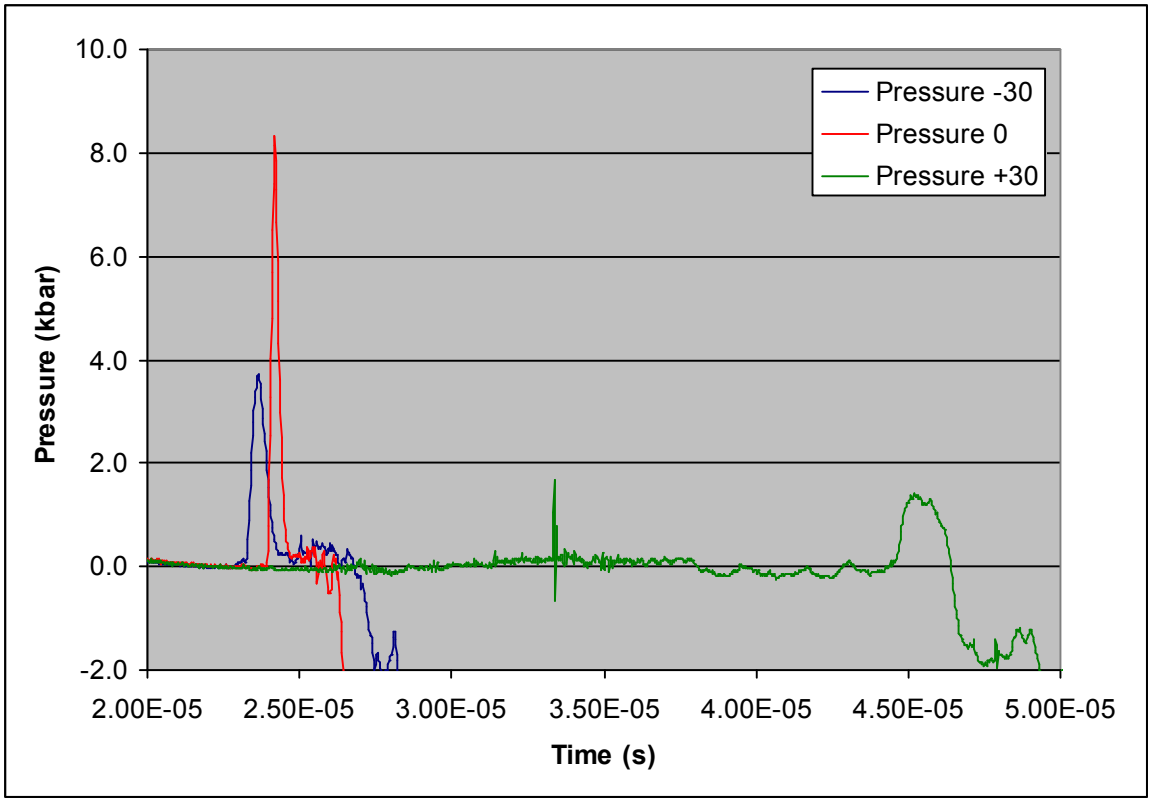

Ring #3 Impact Pressure

Notes

Sample ID: Ring #3 Date: 3/7/2005

Ring Structural Strain Response

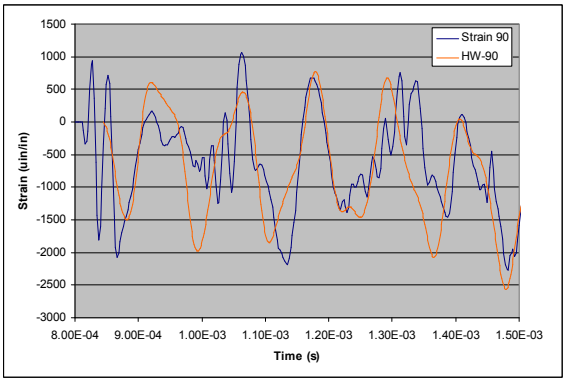

Ring #3 Early Time Strain 90º

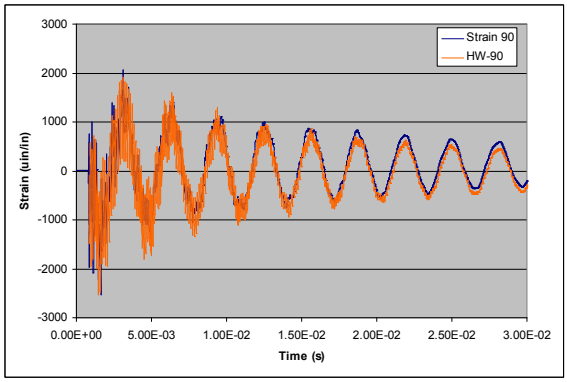

Ring #3 Late Time Strain 90º

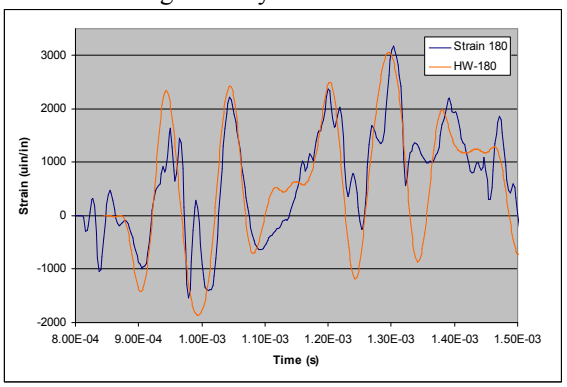

Ring #3 Early Time Strain 180º

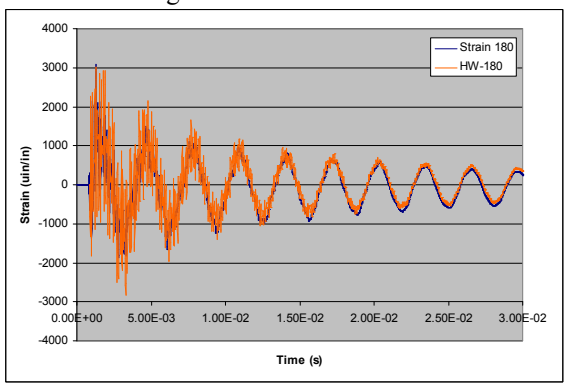

Ring #3 Late Time Strain 180º

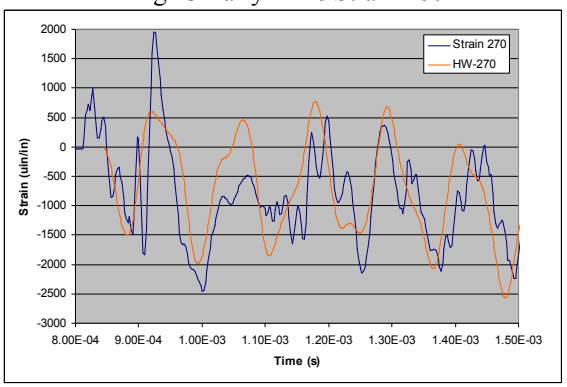

Ring #3 Early Time Strain 270º

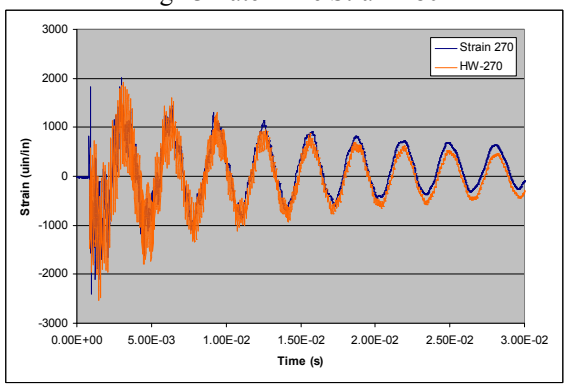

Ring #3 Late Time Strain 270º

Ring #3 Structural Strain Response

Calculated Peak I_{sp}: 2051 taps Measured Impulse: 2051 taps

Calculated Vo: 356.4 cm/sec % As Sprayed Design: 90%

Notes

Spray ID: TP-2005-15 Target Material: 6061 Aluminum Date: 3/7/2005
Sample ID: Ring #4 Flyer Material: 1100Aluminum

No Video Image Available

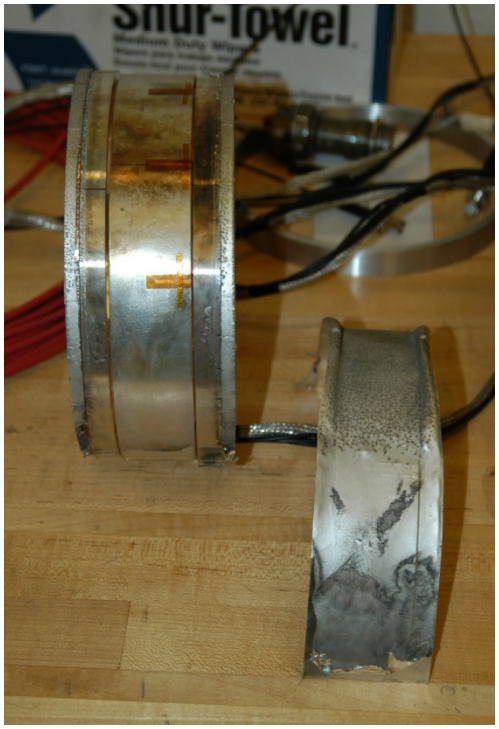

Ring #4 HS Video

Ring #4 Post-Test

Performance Data

Theta	**75**	**60**	**45**	**30**	**15**	**0**	**-15**	**-30**	**-45**	**-60**	**-75**
Gap (cm)	0.024	0.051	0.066	0.074	0.098	0.109	0.103	0.081	0.074	0.064	0.027
ρ_A (mg/cm^2)	10.56	18.31	24.07	28.14	30.1	31.3	30.21	28.34	24.77	17.96	10.24
Vel_{in} (cm/s)	4872	9286	12955	15528	16737	17467	16804	15652	13404	9072	4704
Vel_{out} (cm/s)	2550	4130	4940	5320	6260	6720	6470	5590	5240	4700	2670
R_f	1.52	1.44	1.38	1.34	1.37	1.38	1.39	1.36	1.39	1.52	1.57
Transit (μs)	4.95	5.47	5.10	4.74	5.84	6.25	6.12	5.19	5.50	7.00	5.67
I_{sp} (taps)	**715**	**1293**	**1725**	**2009**	**2216**	**2330**	**2243**	**2047**	**1797**	**1327**	**711**

Notes

Sample ID: Ring #4 Date: 3/7/2005

X-Ray Rigid Body Motion

Exposure	Time (ms)
1	0.6
2	12.0
3	29.0

Ring Mass: 350 gm

Exposure	Delta t (ms)	Delta x (cm)	Vel. (cm/s)	Impulse (taps)
1-2	11.4	4.06	356.5	2052
1-3	28.4	10.16	357.7	2059
2-3	17.0	6.10	358.6	2064
		Average:	**357.6**	**2058**

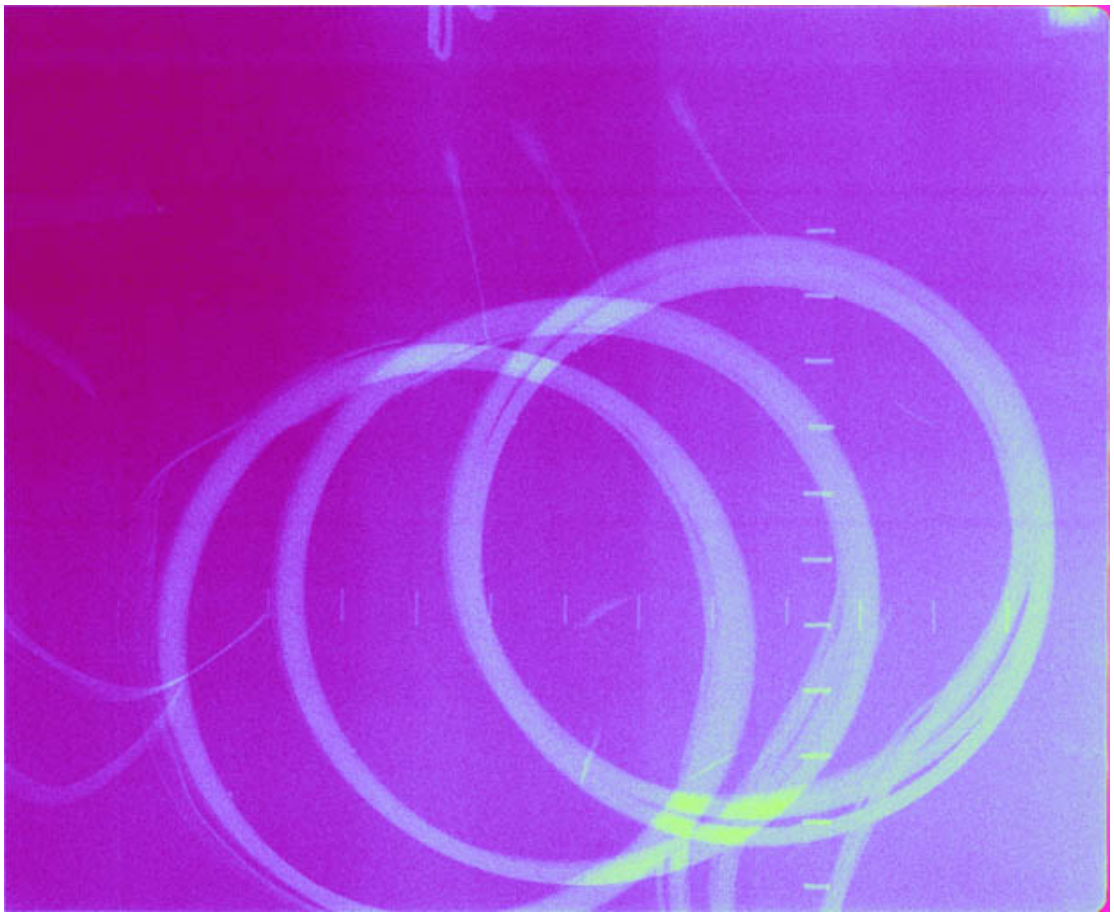

Ring #4 X-Ray Rigid Body Motion

Notes

Sample ID: Ring #4 Date: 3/7/2005

Thin Film Carbon Pressure Gage

Position	-30º		0º		+30º	
Peak Pressure	N/A	kbar	N/A	kbar	N/A	kbar
Pulse Duration	N/A	μs	N/A	μs	N/A	μs

Test Notes

Carbon gage pressure was not recorded.

Sample ID: Ring #4 Date: 3/7/2005

Ring Structural Strain Response

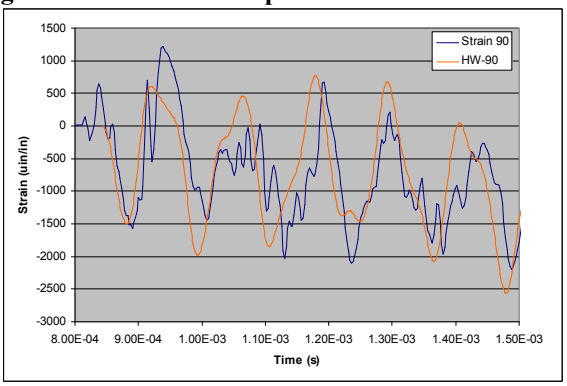

Ring #4 Early Time Strain 90º

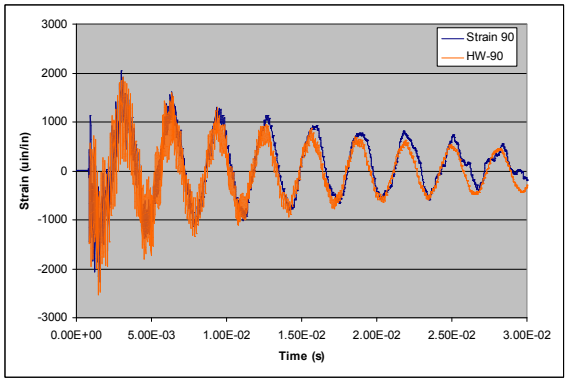

Ring #4 Late Time Strain 90º

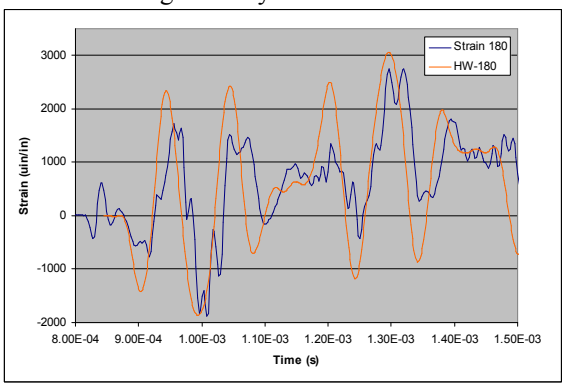

Ring #4 Early Time Strain 180º

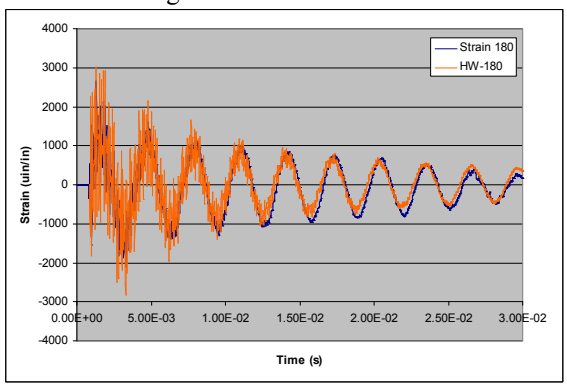

Ring #4 Late Time Strain 180º

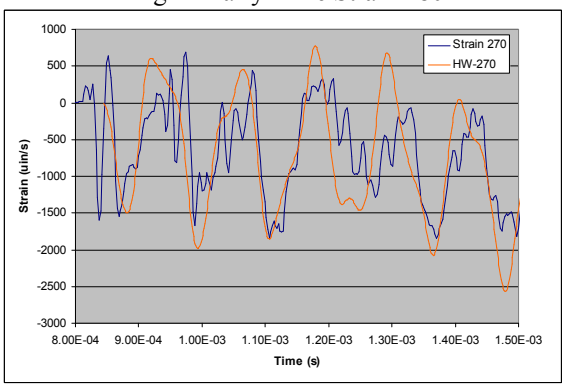

Ring #4 Early Time Strain 270º

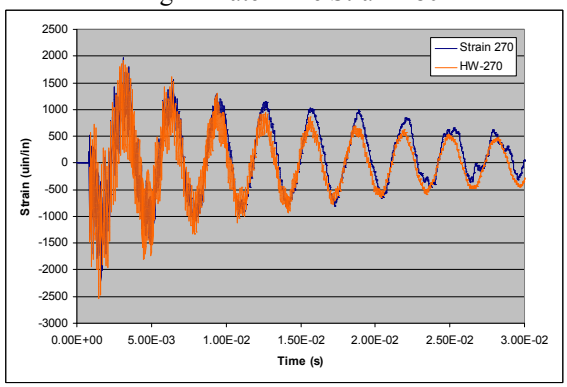

Ring #4 Late Time Strain 270º

Ring #4 Structural Strain Response

Calculated Peak I_{sp}: 2058 taps Measured Impulse: 2058 taps

Calculated Ring Vo: 357.6 cm/sec % as Sprayed Design: 90%

Notes

Spray ID: TP-2005-15 Target Material: 6061 Aluminum Date: 3/7/2005
Sample ID: Ring #5 Flyer Material: 1100Aluminum

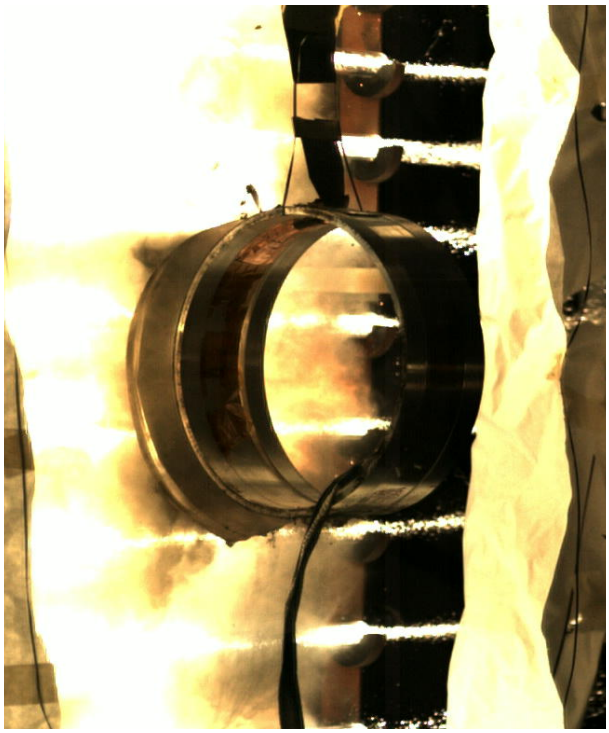

Ring #5 HS Video

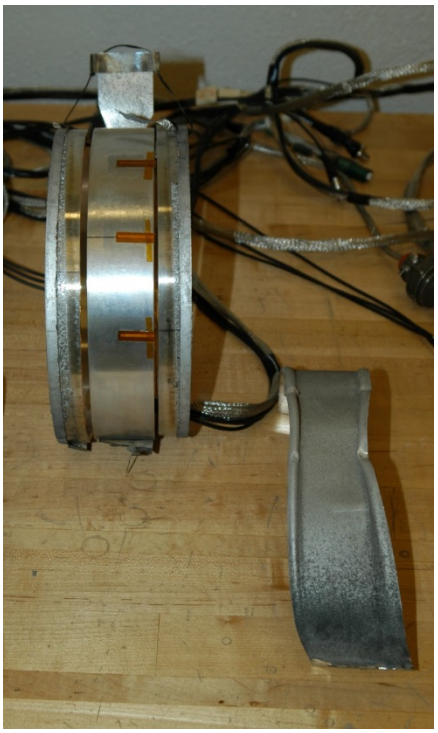

Ring #5 Post-Test

Performance Data

Theta	**75**	**60**	**45**	**30**	**15**	**0**	**-15**	**-30**	**-45**	**-60**	**-75**
Gap (cm)	0.024	0.051	0.066	0.074	0.098	0.109	0.103	0.081	0.074	0.064	0.027
ρ_A (mg/cm^2)	10.56	18.31	24.07	28.14	30.1	31.3	30.21	28.34	24.77	17.96	10.24
Vel_{in} (cm/s)	4872	9286	12955	15528	16737	17467	16804	15652	13404	9072	4704
Vel_{out} (cm/s)	2550	4130	4940	5320	6260	6720	6470	5590	5240	4700	2670
R_f	1.52	1.44	1.38	1.34	1.37	1.38	1.39	1.36	1.39	1.52	1.57
Transit (μs)	4.95	5.47	5.10	4.74	5.84	6.25	6.12	5.19	5.50	7.00	5.67
I_{sp} (taps)	**715**	**1293**	**1725**	**2009**	**2216**	**2330**	**2243**	**2047**	**1797**	**1327**	**711**

Notes

Sample ID: Ring #5 Date: 3/7/2005

X-Ray Rigid Body Motion

Exposure	Time (ms)
1	0.6 ms
2	12 ms
3	29 ms
Ring Mass:	365 gm

Exposure	Delta t (ms)	Delta x (cm)	Vel. (cm/s)	Impulse (taps)
1-2	11.4	4.32	378.8	2274
1-3	28.4	10.54	371.2	2228
2-3	17.0	6.35	373.5	2242
		Average:	**374.5**	**2248**

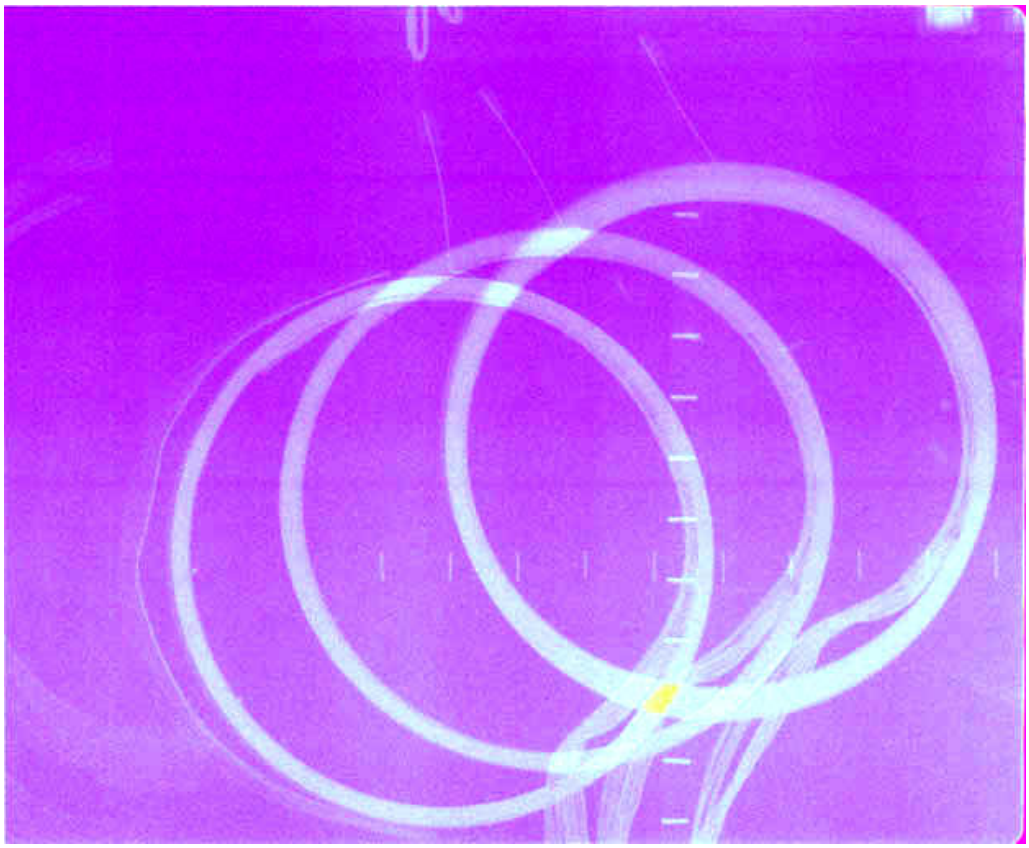

Ring #5 X-Ray Rigid Body Motion

Notes

Sample ID: Ring #5 Date: 3/7/2005

Thin Film Carbon Pressure Gage

	-30º		0º		+30º	
Peak Pressure	7.55	kbar	8.50	kbar	7.06	kbar
Pulse Duration	0.90	µs	1.00	µs	0.70	µs

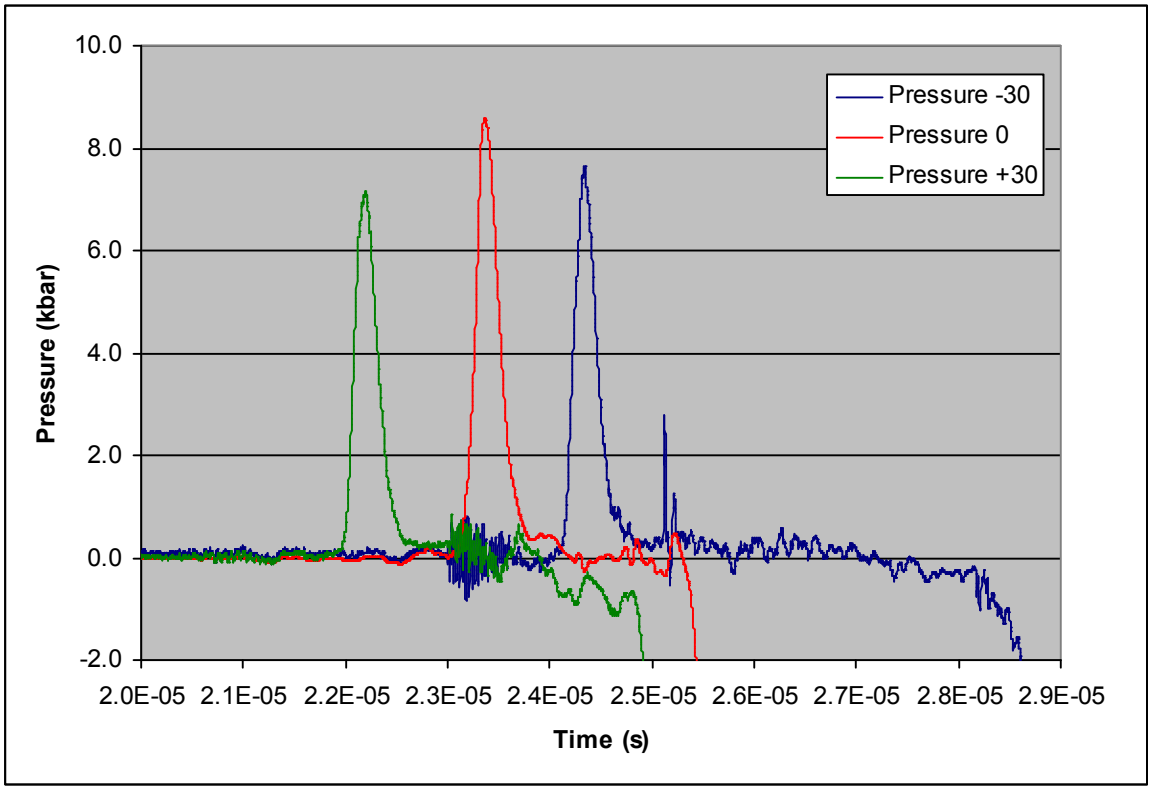

Ring #5 Impact Pressure Data

Notes

Sample ID: Ring #5 Date: 3/7/2005

Ring Structural Strain Response

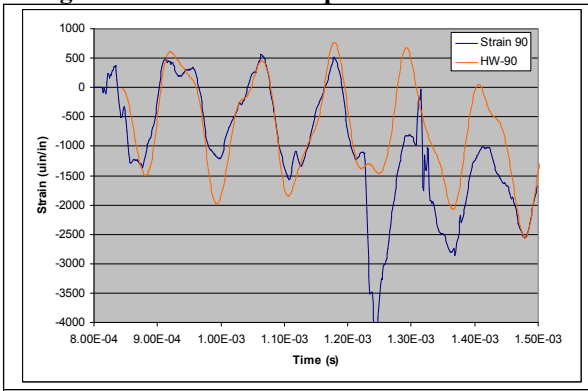

Ring #5 Early Time Strain 90º

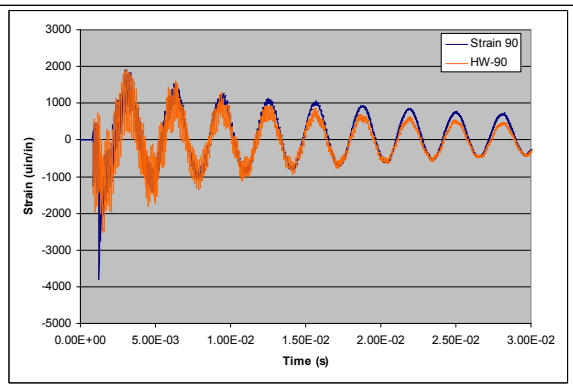

Ring #5 Late Time Strain 90º

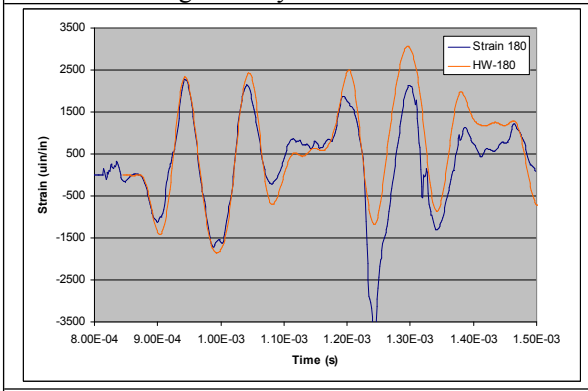

Ring #5 Early Time Strain 180º

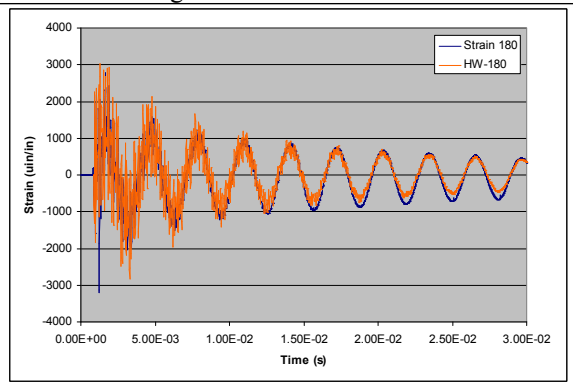

Ring #5 Late Time Strain 180º

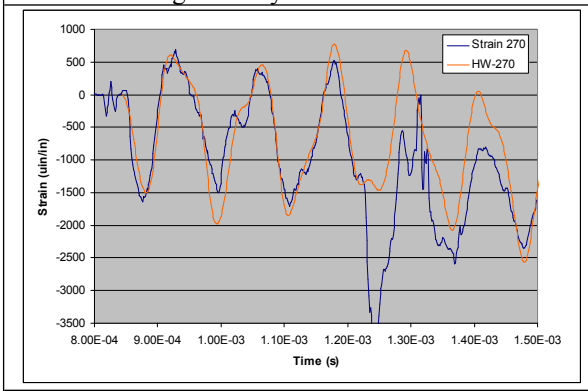

Ring #5 Early Time Strain 270º

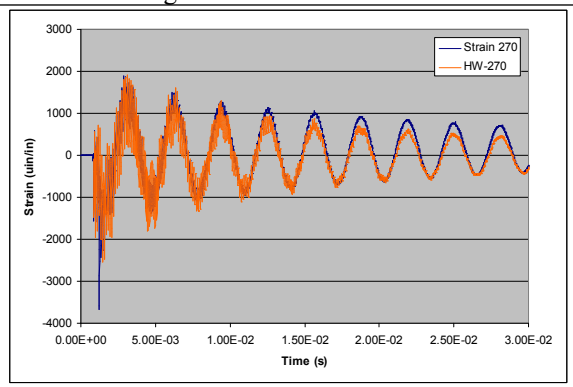

Ring #5 Late Time Strain 270º

Ring #5 Structural Strain Response

Calculated Peak I_{sp}: 2330 taps
Calculated Flyer Vo: 378.8 cm/sec
Measured Impulse: 2331 taps
% As Sprayed Design: 100%

Notes

Excellent Test!

16. DISTRIBUTION

1	MS0481	Nick Dereu	2222 (electronic copy)
1	MS0481	Chase Tagart	2222 (electronic copy)
1	MS0783	W. Gary Rivera	6615 (electronic copy)
1	MS1452	Marcus Chavez	2556 (electronic copy)
1	MS1453	Brad Elkin	2556 (electronic copy)
1	MS1454	Timothy Covert	2556 (electronic copy)
1	MS1454	Daniel Dow	2556 (electronic copy)
1	MS1454	John Liwski	2556 (electronic copy)
1	MS1454	Michael Willis	2556 (electronic copy)


Sandia National Laboratories